THE UNIVERSITY *of* EDINBURGH

Harnessing Coordination Cage Electrostatics to Unlock Bio-inspired Catalysis

王剪烛

Jianzhu Wang

THE UNIVERSITY *of* EDINBURGH

Degree of Doctor of Philosophy

University of Edinburgh

2021

For Mum and Dad

献给我的父亲和母亲

Own Work Declaration

I declare that this thesis was composed by myself, that the work contained herein is my own except where explicitly stated otherwise in the text, and that this work has not been submitted for any other degree or processional qualification except as specified.

Parts of this work have been published *in J. Am. Chem. Soc.* **2020**, *142*, 17743–17750.

Jianzhu Wang

Abstract

Synthetic supramolecular host molecules are able to mimic enzymes by using their cavities as an artificial active site. Previous research has shown that synthetic hosts are able to accelerate chemical transformations using mechanisms such as constrictive binding or enclosed proximity of reactants. These methods have generally led to modest activity and poor turnover.

This thesis will describe a different approach to coordination cage catalysis, one that utilises electrostatic effects to leverage activity. In Chapter 2 it will be shown that such mechanisms can be exploited to promote Michael addition, using a simple cationic Pd_2L_4 cage to stabilise anionic intermediates. These electrostatic effects dramatically increase the acidity of several pro-nucleophiles, such that catalysis spontaneously occurs through the release of hydronium ions. Reactivity can be further enhanced using 18-crown-6, which stabilises this conjugate acid. The cage also promotes high levels of diastereoselectivity for reactions that generate multiple stereoisomers. Counterintuitively, catalysis only occurs with weakly binding reactants, which also leads to broad substrate scope. In Chapter 3, the broad substrate scope has also been extended to Diels-Alder catalysis using similar Pd_2L_4 cages. In this study, transition state stabilisation was found to play an essential role in the rate enhancement and the enhanced diastereoselectivity that is observed for several Diels-Alder reactions.

Chapter 4 will describe the synthesis, characterisation, host-guest studies, and catalytic studies using several new Pd_2L_4 cages. These cages were designed to explore factors such as flexibility, cavity dimensions and an alternative palladium coordination site. Catalytic studies of the new Pd_2L_4 cages was investigated using the Diels-Alder and Michael addition reactions. It was found that the new cages exhibited lower activity than the Pd_2L_4 catalysts investigated in chapter 2 and 3. The influence that these structural modifications have on the catalysis is discussed.

Lay Summary

Enzymes that catalyse almost all the biological processes in living organisms are a type of naturally occurring supramolecules – typically large chemical structures that are folded using non-covalent interactions to produce a highly active species. By building artificial supramolecules that can imitate enzymes we can access and harness their remarkable catalytic power. These artificial supramolecules can be synthesised in a similar manner to children playing with building blocks. Large, complex supramolecular structures can be formed from carefully chosen molecular building blocks of small sizes and simple shapes.

Some of these supramolecules are hollow and can act as hosts holding smaller guests in the cavities. Guest molecules inside the host molecules often behave differently than those on the outside. This property has been successfully shown to accelerate the chemical reactions of the molecules inside.

The majority of this thesis focuses on investigating some specific approaches using supramolecular hosts to accommodate guest compounds and improve or alter their reactivity. Methods of improving the efficiency of supramolecular hosts are discussed by answering questions such as how the hosts behave when we modify their structures. The collective results in this research demonstrate that artificial supramolecules have comparable catalytic power to enzymes and have great potential for practical applications in daily life.

Acknowledgement

First of all, I would like to thank my supervisor Dr Paul Lusby for the opportunity to join the group and explore the Chemistry world. Thank you for all the freedom and encouragement to experiment with my own ideas and thank you for always being there to discuss my results. Most importantly, I have not only grown academically but also grown as a person through my PhD and I could not have done this without your support and guidance.

I owe a huge thank you to all the Lusby group members for the help, support and companionship. To Helen O'Connor, Sam Oldknow, Julia Vallejo Navarret, Bec Spicer, William Grantham, Patrick Boaler, Aaron Scott, Isis Middleton, Liam Spooner and Hang Zhou, thank you for all the quick chats about chemistry, they have really inspired me and I would not be the researcher I am today without you. A special thank you goes to Vicente Martí Centelles, for all the skills and knowledge you have passed on me and thank you for video chatting with me and answering my millions of questions even three years after you have left the group. Of course, thank you everybody for the daily shop/coffee breaks that keep me caffeinated and sane. Thank you all for being the fun, supportive and amazing lab mates that you are, and I have really enjoyed going into the office/lab every day because of you!

For my funding I would like to thank the University of Edinburgh for my Principal Career's Development Scholarship and my Edinburgh Global Research Scholarship.

A lot of this thesis would not be possible without the amazing technical departments. Thank you Dr Lorna Murray and Juraj Bella for all the help with the NMR spectroscopy. I am grateful for the many afternoons you spent helping me with my manual kinetic experiments. Thank you Dr Gary Nichol for solving all my crystal structures. I also owe a thank you to Dr Logan McKay, Dr Faye Cruickshank and Alan Taylor for their help with the Mass spectroscopy.

Some of this work could not have been achieved without our collaborators. I would like to thank Tom Young and Prof. Fernanda Duarte for their excellent computational calculations.

To all my friends, thank you for your support and the good times we shared in the past few years! To my wonderful flatmates Kriszti and Marina, Sam, the Edinburgh Karate Club, the Cowley group, my English grandma Mrs Day, my friends from home Xue, Fenghui, Zhenzhuo and Junjie, and many others, thank you for being in my life and I am very lucky to have you all. To Abi, thank you for all the post demonstration gym sessions that "accidentally" became drinking sessions. Thank you for the lockdown Zoom workouts, the walks, the delicious and beautiful cakes and the weekly ice cream trips that made the post lockdown life much better!

I would like to thank my family, especially my parents for their love and support throughout my whole life. I could only imagine the struggle you went through to let your only daughter go and study in a place that is half a world away from home. You gave me everything anyone could possibly ask for and much more!

Thank you to the Williams-Sandford family, Tania, Tony, Abbie, Paul and Christopher for looking after me and making my COVID-19 lockdown so easy. Thank you for making me feel safe and loved and keeping me very well fed. Thank you for the Marvel movie marathon and all the baking sessions; they were great fun!

Last but not least, thank you Martin for being an amazing partner. Words cannot express how much your love and support mean to me. You make me so happy, and you make me the best person I can be. I look forward to all the exciting adventures that we will share in the future!

Abbreviations

BArF	Tetrakis(3,5-bis(trifluoromethyl)phenyl]borate
COSY	Correlation spectroscopy
d	Doublet
DABCO	1,4-Diazabicyclo[2.2.2]octan
DBU	1,8-Diazabicyclo[5.4.0]undec-7-ene
DOSY	Diffusion ordered spectroscopy
h	Hour
HMBC	Heteronuclear multiple bond correlation
HSQC	Heteronuclear single quantum coherence
m	Multiplet
m/z	Mass to charge ratio
min	Minute
MS	Mass spectrometry
NMI	1-Methylimidazole
NMP	N-Methyl-2-pyrrolidone
NMR	Nuclear magnetic resonance
NOESY	Nuclear Overhauser effect spectroscopy
OTf	Trifluoromethanesulfonate
q	Quartet
r.t.	Room temperature
s	Singlet
t	Triplet
TLC	thin layer chromatography
TM	Transition metal
TS	Transition state
UV-vis	Ultraviolet-visible

Publications

Synergistic Non-covalent Catalysis Facilitates Base-Free Michael Addition

J. Wang, T. Young, F. Duarte, P. Lusby, *J. Am. Chem. Soc*., **2020**, *142*, 17743–17750.

Rationalizing the Activity of an "Artificial Diels-Alderase": Establishing Efficient and Accurate Protocols for Calculating Supramolecular Catalysis

T. Young, V. Martí-Centelles, J. Wang, P. Lusby, F. Duarte, *J. Am. Chem. Soc.*, **2020**, *142*, 1300–1310.

Navigated Self-assembly of a Pd_2L_4 Cage by Modulation of an Energy Landscape under Kinetic Control

T. Tateishi, S. Takahashi, A. Okazawa, V. Martí-Centelles, J. Wang, T. Kojima, P. Lusby, H. Sato, S. Hiraoka, *J. Am. Chem. Soc.*, **2019**, *141*, 19669–1976.

Conference Prizes

Royal Society of Chemistry Books Poster Prize

2019 Macrocyclic and Supramolecular Chemistry Meeting, Kent

"Using Enthalpy to Unpick Capsule Catalysis."

Royal Society of Chemistry ChemComm Talk Prize

2019 Macrocyclic and Supramolecular Chemistry Early Career Meeting, Lincoln

"Using Enthalpy to Avoid Product Inhibition."

Royal Society of Chemistry ChemComm Poster Prize

2018 Macrocyclic and Supramolecular Chemistry Meeting, Lancaster

"Catalytic Applications of Pd_2L_4 Assemblies."

Awards and Grants

Royal Society of Chemistry Researcher Mobility Grant – 2020

£3000 bursary grant for a PhD placement at ETH Zurich.

Principal Career Development Scholarship – PhD funding, 2017

Prestigious scholarship to cover ca. £4,000 annual UK rate tuition fees and living costs of £15,250 per year for three years.

Edinburgh Global Research Scholarship – PhD funding, 2017

Prestigious scholarship to cover ca. £16,000 difference between international and UK rate annual tuition fees for three years.

Table of Contents

Chapter 1

Supramolecular Catalysis with Coordination Cages

Chapter 1 Supramolecular Catalysis with Coordination Cages

1.1 Supramolecular cages and host-guest chemistry

Self-assembly is a ubiquitous process in nature, responsible for a vast number of biologically important structures and functions such as lipid bilayers and protein-RNA recognition. Self-assembly is driven by thermodynamic forces and uses "self-correction" to form globally or locally stable supramolecules held together by non-covalent interactions. Cage like architectures are of particular interest as they possess an internal cavity that creates a microenvironment for smaller molecules that can be encapsulated. In the past few decades, a great number of supramolecular cages have been reported, and the predominating type of cages are those built from the coordination of transition metals and organic ligands. The success of metal-organic cages can be attributed to their targeted design which is facilitated by the well-defined metal coordinating geometry and the easy modification of organic ligands. Furthermore, metal-ligand coordination is among the strongest non-covalent interactions and can construct relatively robust structures that are compatible with a wide range of applications.

Since the early studies using transition metals to drive self-assembly, the field has expanded rapidly and we now have access to numerous 2D and 3D structures.[1][2][3][4][5][6] Several review articles[7][8] have attempted to summarise bottom-up strategies that help to design supramolecular cages rationally. The core message is that the structural information of cages can be encoded into their building blocks. By using the correct combination of transition metals and organic ligands, self-assembly can achieve highly predictable cage structures. Therefore, the synthesis of metal-organic cages is significantly simpler in comparison to covalent receptor molecules, making metal-organic cages accessible to a wider chemistry community.

There has been a similarly rapid development of the molecular inclusion phenomenon since the earliest discoveries of crown ethers binding metal cations,[9] with receptors ranging from discrete covalent[10][11] and non-covalent[12] hosts in solution-state, as well as porous crystalline sponges in solid-state.[13][14] The host-guest chemistry of supramolecules has successfully demonstrated usefulness in numerous areas such as bio-imagining,[15] chemical sensing,[16][17] drug delivery,[18][19] reactive species stabilisation,[20][21] molecular magnetism[22] and molecular separation.[23] The resemblance of the cavities in molecular receptors to the active sites of enzymes also inspired chemists to explore the catalytic applications of supramolecules. In this chapter, catalysis based on guest encapsulation in coordination cages is discussed.

1.2 Early supramolecular catalysis and limitations

Before a large number of self-assembled cage molecules were accessed, early studies of supramolecular catalysis in the last century primarily relied on covalent hosts. A naturally-occurring oligosaccharide family, cyclodextrins, saw the first examples of supramolecular catalysis (Figure 1-1a). The early cyclodextrin catalysis research mainly focused on unimolecular transformations, such as the decarboxylation of cyanoacetic acids described, by Cramer and Kampe,[24] and the hydrolysis of phenyl esters, discussed by Bender[25][26]. Breslow reported one of the first bimolecular reactions catalysed by β-cyclodextrin, **1.R1**, showing a 2.5-fold rate enhancement for the Diels-Alder reaction of cyclopentadiene **1.1** and methyl vinyl ketone **1.2** (Figure 1-1b).[27] He attributed the catalysis to the high effective molarity resulting from the co-encapsulation of both substrates. The co-encapsulation is confirmed by experiments that showed a smaller host, α-cyclodextrin, **1.R2**, which can only bind one of the substrates, inhibited the reaction.[27] It is noteworthy that the "catalysis" was performed with 25 equivalents of β-cyclodextrin with respect to the limiting reagent **1.1**. Although the author did not provide kinetic profiles under catalytic conditions, some level of product inhibition is inferred by the superstoichiometric use of **1.R1**.

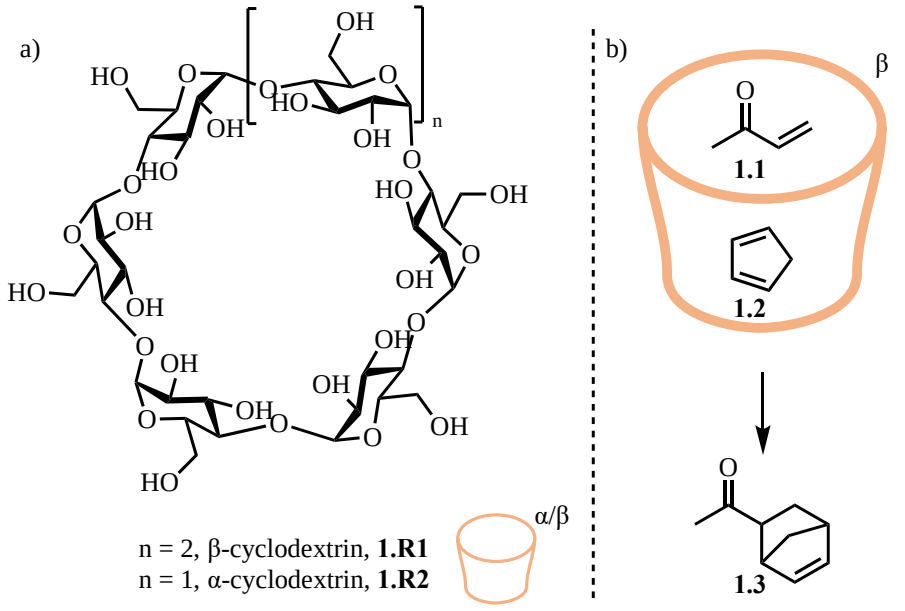

*Figure 1-1. a) Chemical structures of β/α-cyclodextrin, **1.R1** and **1.R2**. b) The Diels-Alder reaction of **1.1** and **1.2** in the presence of β-cyclodextrin.*

Sanders used a Zinc-porphyrin embedded macrocycle (Figure 1-2) to demonstrate the supramolecular catalysis approach using effective molarity. Unlike cyclodextrin, **1.R3** uses Zn coordinating sites to bind guests with pyridine groups (Figure 1-3).[28] The co-encapsulation brings the reactive centres of **1.4** and **1.5** into close proximity and promotes their Diels-Alder reaction by around 200-fold.[29] Moreover, the defined coordination geometry of Zn places the substrates **1.4** and **1.5** in a locked relative orientation, and the *exo* product, *exo* **1.6**, is exclusively formed (Figure 1-3). No rate acceleration was observed when a monomeric Zn-porphyrin unit, **1.7**, was used or a strong competitive inhibitor, **1.8**, was added (Figure 1-2). These control experiments confirm that the catalytic activity stems from the increased effective molarity in **1.R3** rather than the electronic effect of Zn-pyridine coordination. By using a smaller porphyrin trimer **1.R4**, the stereochemistry is completely reversed to be *endo* selective.[30] While **1.R3** demonstrates the ability to precisely control the stereo outcome of the Diels-Alder reaction of **1.4** and **1.5**, it has to be used in a stoichiometric amount. The product **1.6** is bound three orders of magnitude more strongly than either **1.4** or **1.5**, causing severe product inhibition. In the case of **1.R3**, replacing one bridging guest **1.6** with two "monotopically binding" guests **1.4** and **1.5** is entropically disfavoured.

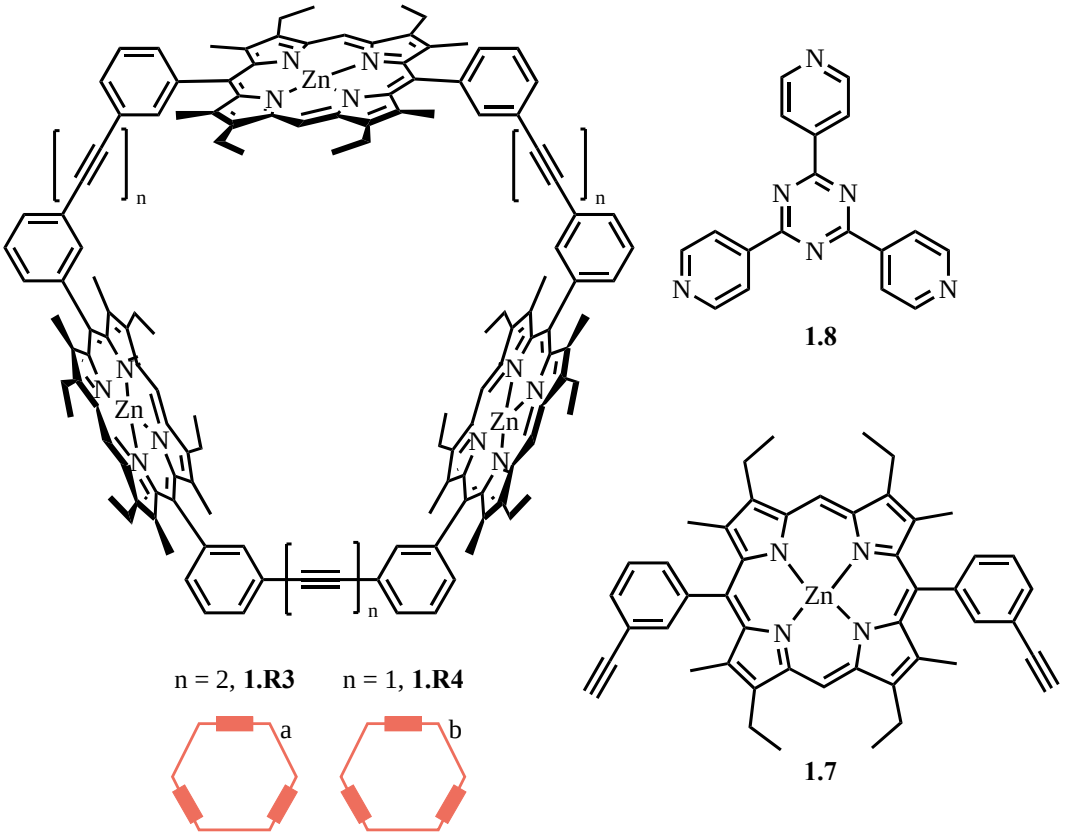

*Figure 1-2. Chemical structure of the Zn-porphyrin embedded macrocycle, **1.R3** and **1.R4**.*

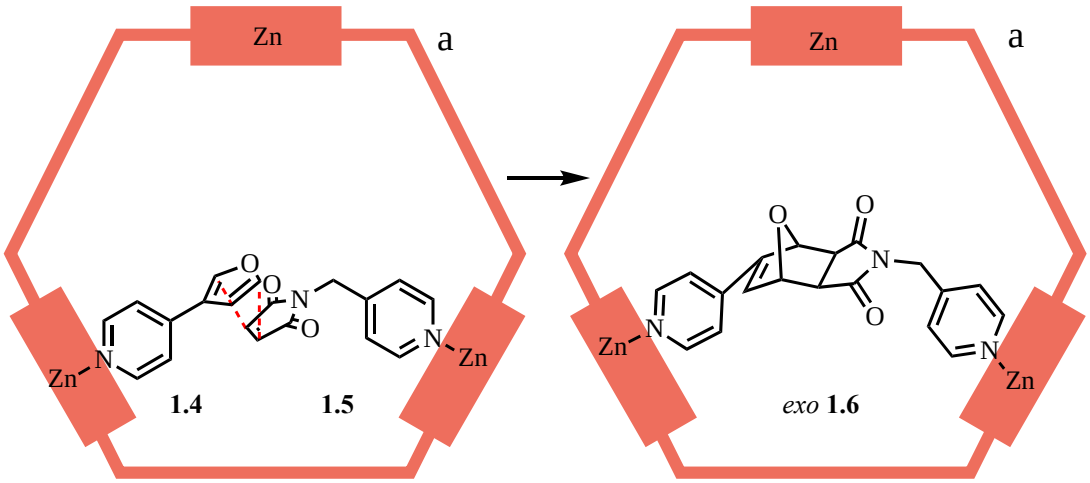

*Figure 1-3.The orientation of **1.4** and **1.5** in **1.R3** exclusively facilitates the formation of the exo product, **1.6**.*

Sanders was amongst the first to discuss the correlation between the type of reactions and product inhibition.[31] Product inhibition is a common problem intrinsic to the fusion reactions that use a co-encapsulation strategy to achieve high effective molarity.

[32][33][34][35] The fusion products are often more complementary to the supramolecular hosts than the starting materials and bind more strongly (Figure 1-4a). Equally, releasing one product molecule and including two substrate molecules causes a high entropic penalty. Conversely, unimolecular transformations, fission reactions and group transfer processes have entropically "neutral" or entropically favoured product release steps so are less prone to product inhibition (Figure 1-4a).

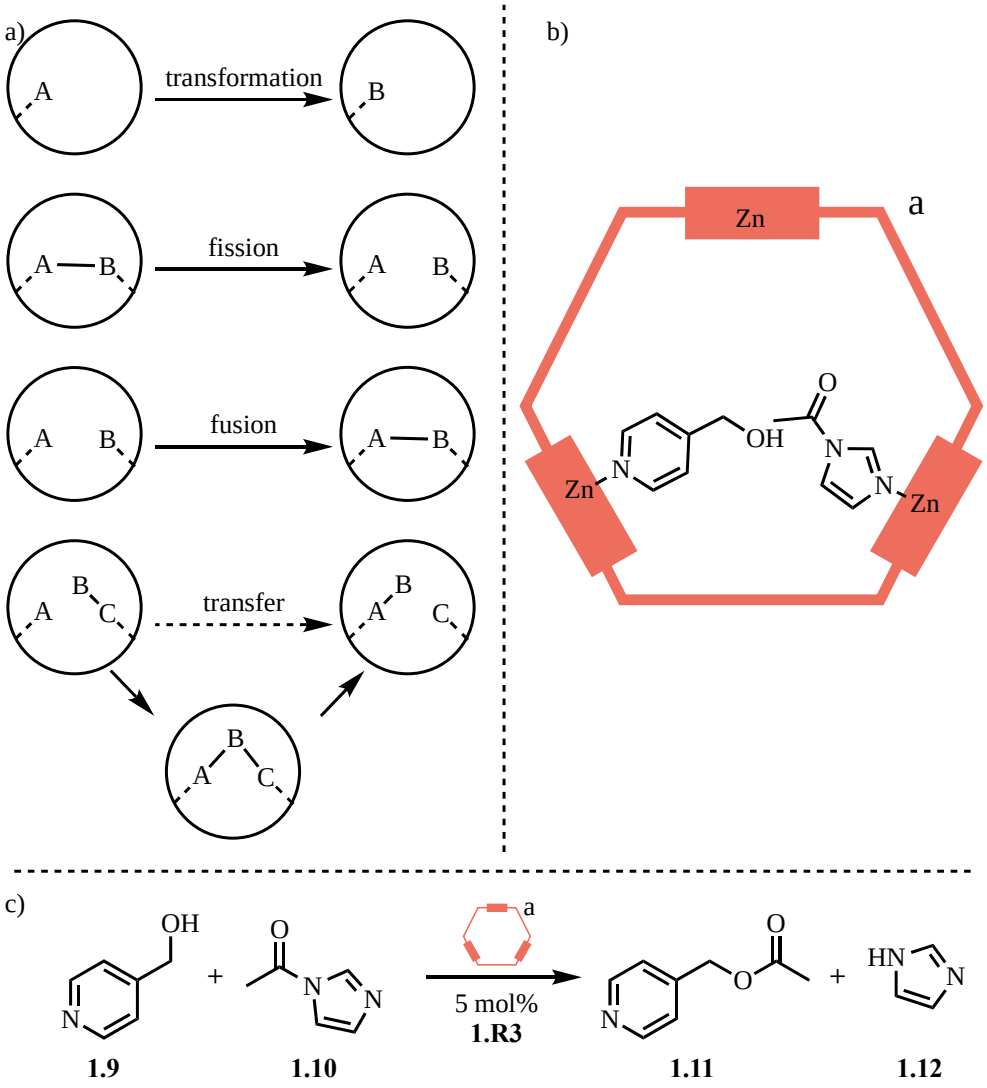

Figure 1-4. a) Chemical reactions that supramolecular hosts could catalyse. b) ***1.R3*** *stabilising the intermediate of the reaction between* ***1.9*** *and* ***1.10****. c) The acetyl transfer reaction between* ***1.9*** *and* ***1.10*** *catalysed by* ***1.R3****.*

Sanders experimentally demonstrated that the product inhibition is correlated to reaction type by using **1.R3**, previously shown as a stoichiometric promoter for Diels-

Alder reactions, to catalytically facilitate an acetyl transfer process between **1.9** and **1.10** (Figure 1-4c).[36] Similar to the Diels-Alder reactions, the 16-fold rate enhancement in **1.R3** stems from the preorganisation of the substrates (Figure 1-4b) rather than from the interactions with the Lewis acidic Zn^{2+} units. This is proved by the lack of catalysis in the presence of the monomer, **1.7**, or **1.R3** and a competitive inhibitor. More impressively, **1.R3** achieved a turnover number of 25, marking one of the first catalytic uses of supramolecular catalysts in a bimolecular reaction. It works because the products **1.11** and **1.12** have similar binding strength to **1.9** and **1.10**, and the release of two product molecules reduces the entropic barrier of turnover.

As the synthesis of supramolecules advanced, chemists advanced from using macrocycle receptors to using more complex, 3D cage structures to explore supramolecular catalysis. Rebek discovered the "softball" H-bond dimer **1.R5** constructed from two shape-complementary monomers **1.13** held together by carefully engineered H-bond donor and acceptor functionalities (Figure 1-5a,b). This "softball" capsule demonstrated efficient co-encapsulation of p-benzoquinone **1.14** and cyclohexadiene **1.15** in p-xylene (Figure 1-5c). A 170-fold initial rate enhancement was observed for the Diels-Alder reaction between **1.14** and **1.15** in the presence of **1.R5**.[37] Like the previous examples using co-encapsulation as a catalytic strategy, the Diels-Alder reaction in **1.R5** suffers from severe product inhibition. Although turnover can be achieved with selected substrates that form weaker binding products,[38] product inhibition remains a problem inherent to the co-encapsulation strategy that proves tricky to avoid systematically.

Closely examining the kinetics of the cycloaddition of **1.14** and **1.15** in the presence of **1.R5** reveals a potential limitation for only relying on the co-encapsulation method. Using the kinetic data reported by the Rebek group,[39] Houk and co-workers revealed that **1.R5** binds and stabilises the substrate pair (**1.14** & **1.15**) more favourably than

their transition state by + 0.4 kcal/mol.[i][40], creating a higher activation barrier for the reaction in the cavity. In other words, the rate acceleration in **1.R5** is merely due to the high effective concentration of the substrates, and **1.R5** is actually an anti-catalyst.

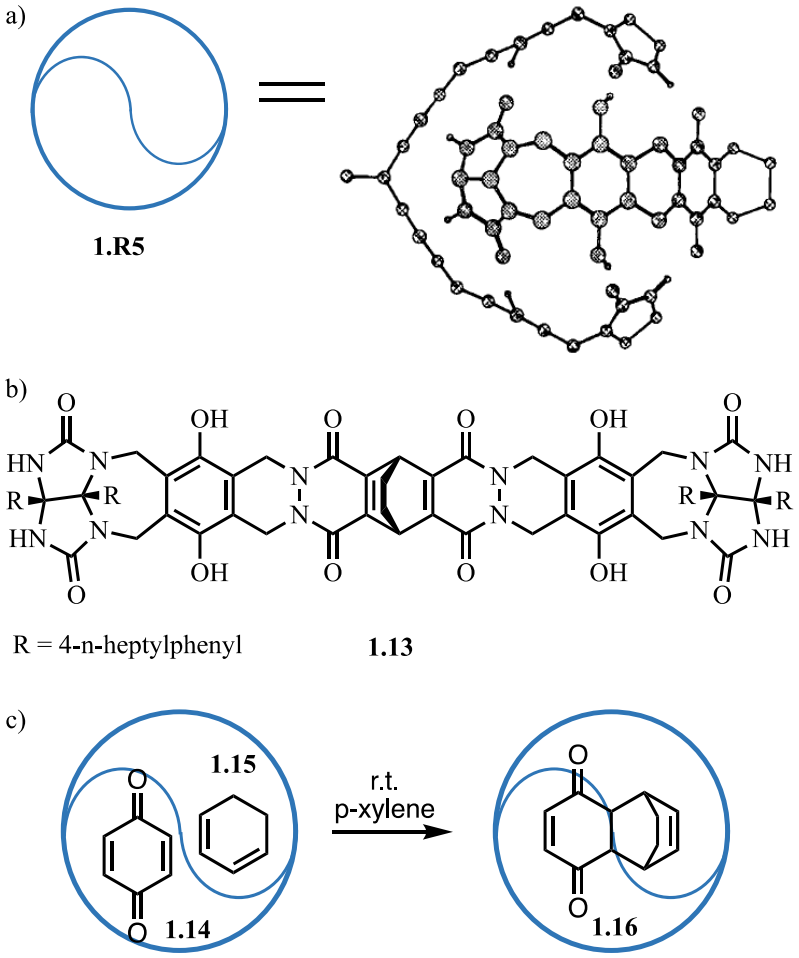

*Figure 1-5. a) "Softball" structure **1.R5** constructed by H-bond network. b) Chemical structure of the monomer, **1.13**. c) Co-encapsulation of **1.14** and **1.15** in **1.R5** leads to rate enhancement of their Diels-Alder reaction.*

[i] The value reported by Houk and co-workers is + 4.4 kcal/mol, although reproducing Houk's calculation gave the result of + 0.4 kcal/mol.

1.3 Coordination cage catalysis

Coordination cages have emerged as promising supramolecular catalysts. One way to apply coordination cages to catalysis is to use their cavities to modulate the properties of traditional catalysts such as transition metals (TM). For example, by binding both TM catalysts and substrates, coordination cages have shown the ability to improve the stability of the TM catalysts,[41][42] to enhance the reaction selectivity through cavity confinement,[43] and to increase the local concentration of the TM catalysts.[44] Another approach of coordination cage catalysis is to directly manipulate the reaction substrates, transition states, and intermediates through guest encapsulation. Without binding any traditional catalysts, coordination cages can exert catalytic functions on their own, drawing a close analogy to enzyme catalysis. This chapter will focus on such catalysis that is intrinsic to the cage cavities by discussing the common catalytic strategies.

1.3.1 Co-encapsulation method

The co-encapsulation method remains a powerful approach to achieve highly selective catalysis when using coordination cages. Fujita's palladium octahedron **1.C1** was one of the first coordination cages to be used as a "molecular flask" for Diels-Alder reactions (Figure 1-6). **1.C1** binds **1.17** and **1.18** through the hydrophobic effect and can precisely position the substrates in a restricted orientation through π-π stacking (Figure 1-7a).[45] The reaction between **1.17** and **1.18** naturally occurs at the 9,10-position in water. However, in the presence of stoichiometric **1.C1**, the 1,4-adduct, **1.19a**, was exclusively formed (Figure 1-7a).[45] The steric bulk of the cyclohexyl group on **1.17** is essential for placing the two desired reacting centres into close contact. When less sterically demanding N-substituents were used, only reactions across the 9,10-position were observed.[45]

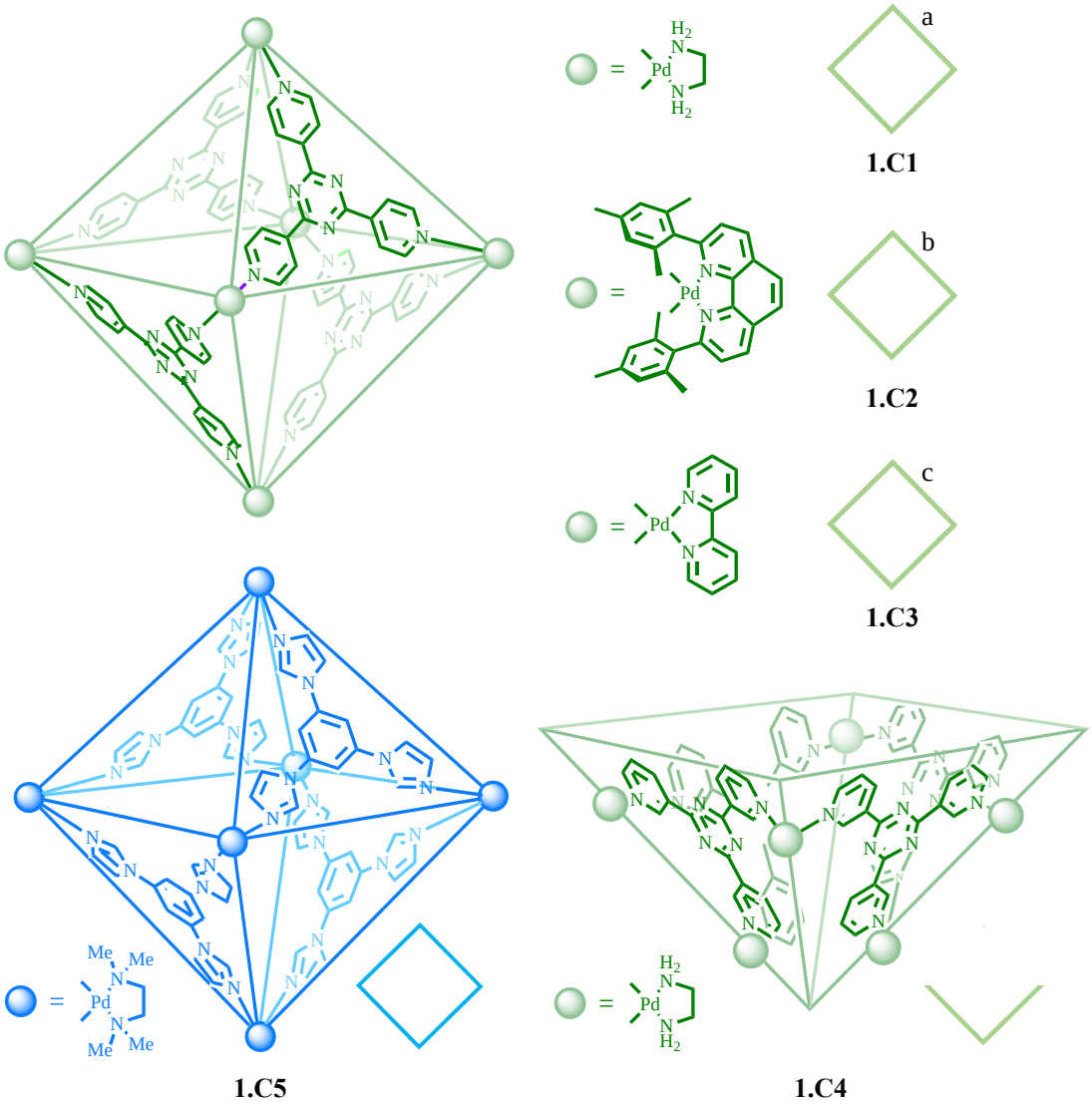

*Figure 1-6. Chemical structures of **1.C1**-**1.C5**.*

Impressively, encapsulation in **1.C1** was further shown to activate inherently inert aromatic compounds (Figure 1-7b). Naphthalene derivatives **1.20a-d** are relatively inactive compounds and do not react with **1.17** in the bulk phase. However, **1.21b-d** can be formed in the presence of stoichiometric **1.C1** because **1.20b-d** and **1.17** are bound in close proximity, further demonstrating the power of co-encapsulation.[46] The strict binding conformation in **1.C1** also leads to unusual regio- and stereoselectivity, and in all cases, **1.17** is added across the less electron rich ring and, unlike common Diels-Alder reactions, yields *exo* products.[46] It is noteworthy that when **1.20a** was used as the diene, even though a ternary complex was observed, no Diels-Alder

reaction occurred.[46] This shows that "togetherness" on its own does not necessarily provide substrates activation, and TS stabilisation is required. The catalysis weakens as the steric bulk of the alkyl chains reduces; the yield of **1.21** is the highest for propyl substituted **1.20d,** and the lowest for methyl substituted **1.20b**.[46] This trend demonstrates that in the co-encapsulation method, catalysis can be tuned by engineering the substrate preorganisation. Similarly, the smaller naphthalenes (**1.20a**, **1.20b**) can be efficiently activated by using a modified Pd_6L_4 octahedron cage, **1.C2** (Figure 1-6), with a contracted cavity volume that matches the Diels-Alder transition states when using maleimide derivative **1.22** (Figure 1-7c).[47] In fact, the use of **1.C1** as Diels-Alder "molecular flasks" has proved to be highly versatile, accessing a range of inert aromatic structures.[48][49]

Despite the impressive activation for otherwise unfavoured reaction pathways, the Diels-Alder reactions in **1.C1** require a stoichiometric amount of host. However, some factors can help to achieve cage catalyst turnover when adopting the co-encapsulation method. For example, Fujita's more open, bowl-shaped structure, **1.C4**, allows turnover of the reaction of **1.17** and **1.18,** which forms the conventional product **1.19b** (Figure 1-6, Figure 1-7a).[45] Similarly, Mukherjee used a more open, cylinder-shaped Pd_6L_4 **1.C5** to catalyse the formation of **1.19b** with 10 mol% loading (Figure 1-6, Figure 1-7a).[50] In both cases, the formation of **1.19b** bends the planar aromatic surface of anthracene and weakens the host-guest π stacking interactions, leading to the auto exclusion of the product.[45][50] Although these examples demonstrate that it is possible to achieve turnover, product-host shape mismatch remains notoriously difficult to engineer and product inhibition still heavily affiliates supramolecular catalysis using the co-encapsulation method.

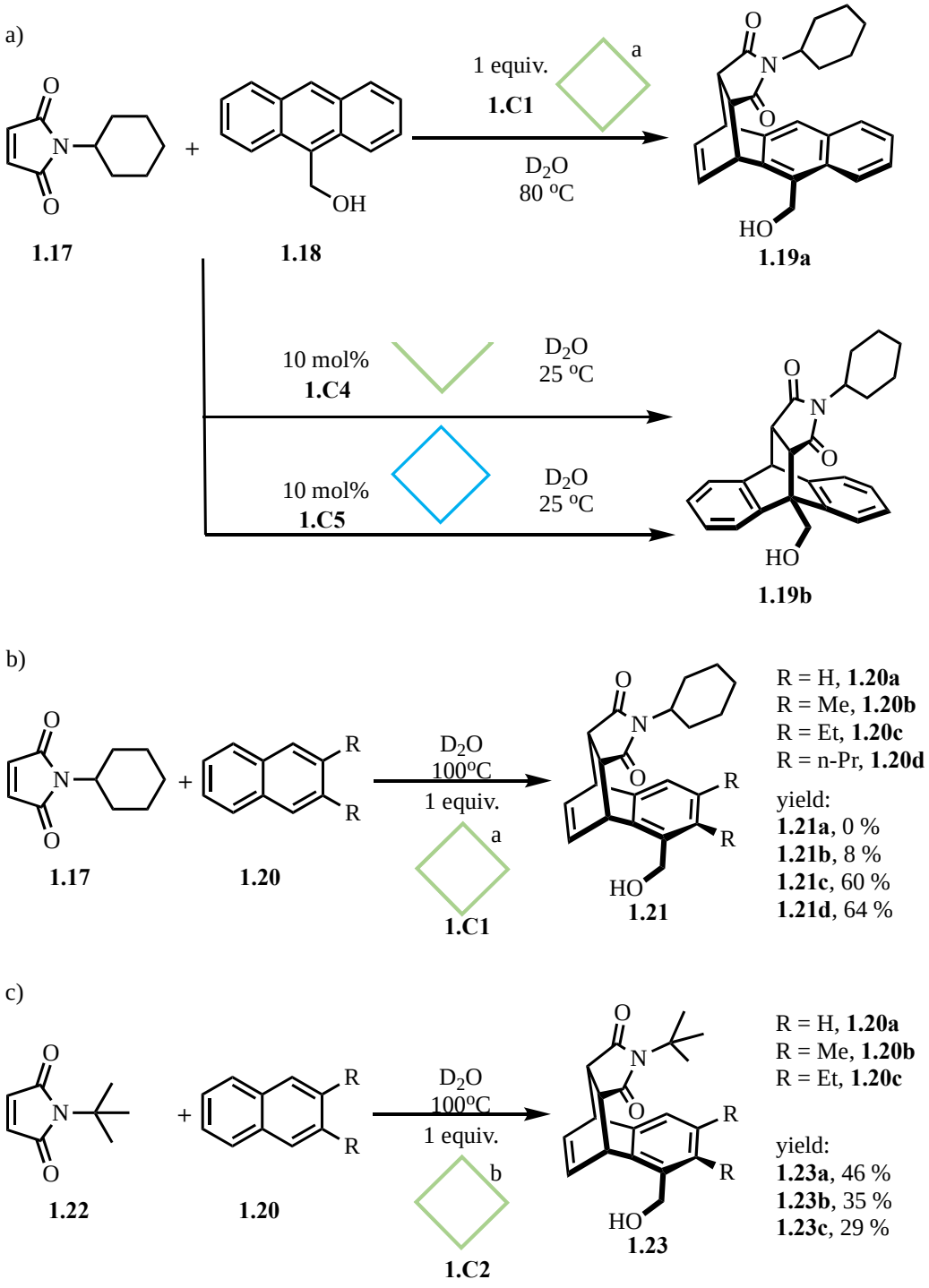

*Figure 1-7. a) Stochiometric **1.C1** promotes unusual regio-selectivity. **1.C4** and **1.C5** catalytically promotes the reaction of **1.17** and **1.18**. b) and c) Cavity of **1.C1,** and **1.C2** activate inert naphthalene compounds **1.20**.*

1.3.2 Constrictive binding method

Constrictive binding refers to the mechanism where a single substrate is forced into a reactive conformation through host-guest binding. The bound ground state substrate has fewer rotational degrees of freedom and consequently experiences a lower entropic penalty leading to the transition state. Constrictive binding methods achieve rate enhancement through substrate preorganisation, and it does not involve transition state or intermediate stabilisation.

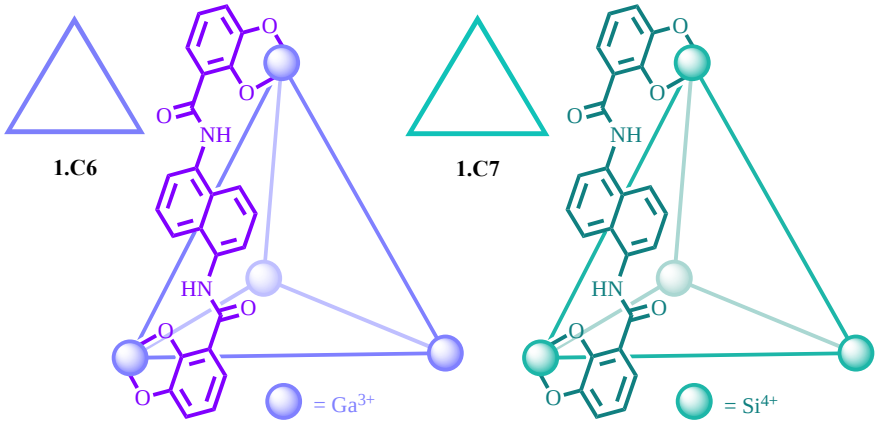

*Figure 1-8. Chemical structures of the Ga^{3+} cage **1.C6** and the Si^{4+} analogue **1.C7**.*

The Raymond group showcased the effectiveness of such a supramolecular catalysis strategy. The tetrahedron cage **1.C6** (Figure 1-8) is constructed with 4 Ga^{3+} ions and 6 bis-bidentate catechol ligands, giving **1.C6** an overall 12^- charge. The naphthyl linker ensures the hydrophobicity of the cavity. These factors render **1.C6** an ideal host for many organic cations, including cationic substrates and cationic intermediates,[51][52] and **1.C6** is one of the most widely studied coordination cage catalysts. **1.C6** was shown to catalytically promote the aza-cope rearrangement reactions of ammonium species **1.24** (Figure 1-9).[53] The iminium product **1.25** hydrolyses in the bulk phase to the aldehyde **1.26,** whose neutral charge weakens the host-guest binding and ensures the cavity remains free for efficient turnover.[53] The catalysis arises from the ability of **1.C6** to bind **1.24** in the reactive chair conformation that resembles the transition state (Figure 1-9). Such substrate preorganisation is supported by the NOE peaks in the ^{1}H NMR spectrum between the protons on the two ends of the encapsulated **1.24c**, which is not observed for the unbound molecule.[53] The possibility of the hydrophobic

effect facilitated catalysis is ruled out, as the rearrangement of **1.24** does not show any solvent dependency.[53] Although coulombic interactions facilitate the binding of **1.24**, they do not contribute to the rate enhancement. This was shown by that the rate constant for the rearrangement of **1.24b** in **1.C6** is almost identical to that in an analogous structure **1.C7** (Figure 1-8) that bears a reduced charge (8^-).[54] The lack of columbic contribution to the catalysis is perhaps because the substrate **1.24**, the transition state and the product **1.25** are all cationic, and there is no selective binding of any of these species.

It is noteworthy that the rate acceleration in **1.C6** varies drastically, ranging from 5- to 850-fold for **1.24a-d** of different sizes (Figure 1-9).[53] The larger compounds, such as **1.24c** and **1.24d**, are bound in a more tightly packed conformation and have smaller entropic cost for rearrangement, although further increasing the substituent to n-butyl appears to weaken the binding restriction. The small **1.24a** molecule displays weak catalysis (k_{cat}/k_{uncat} = 5) because its loose encapsulation in the cavity allows bond rotation and leads to poor substrate preorganisation. Interestingly, the *cis* and *trans* isomers, **1.24b** and **1.24c** also show notably different rate enhancement (90- and 140-fold, respectively), highlighting the importance of the shape complementarity of the substrate and the cavity for the constrictive binding method.

Kinetic studies also confirm that the catalysis stems from substrate preorganisation. The encapsulation of **1.24b-d** in **1.C6** leads to a significant decrease in the entropic activation energy ($\Delta\Delta S^{\ddagger}$ up to 10 cal mol^{-1} K^{-1}) (Figure 1-9).[55] Conversely, the enthalpic barrier is very similar for the catalysed and background reactions, with $\Delta\Delta H^{\ddagger}$ being less than -1.2 kcal mol^{-1} (Figure 1-9).[55] While the rate acceleration of bound **1.24b-d** is largely due to lowering the entropic barrier, the small yet non-negligible reduced enthalpic cost suggest that the encapsulation in **1.C6** may introduce some strain on **1.24b-d**.

Tetrahedron cages constructed from bis-bidentate ligands and metal centres with octahedral coordination geometry exhibit intrinsic helical chirality at each vertex, Δ and Λ. Homochiral ΔΔΔΔ-**1.C6** can be isolated from its enantiomeric counterpart and was shown to induce chirality on the aza-cope rearrangements of **1.24 (**Figure 1-9**)**.[56]

Again, the highest enantiomeric excess was observed for the mid-sized **1.24d**, highlighting its tight packing in the high complementarity cavity of **1.C6**.

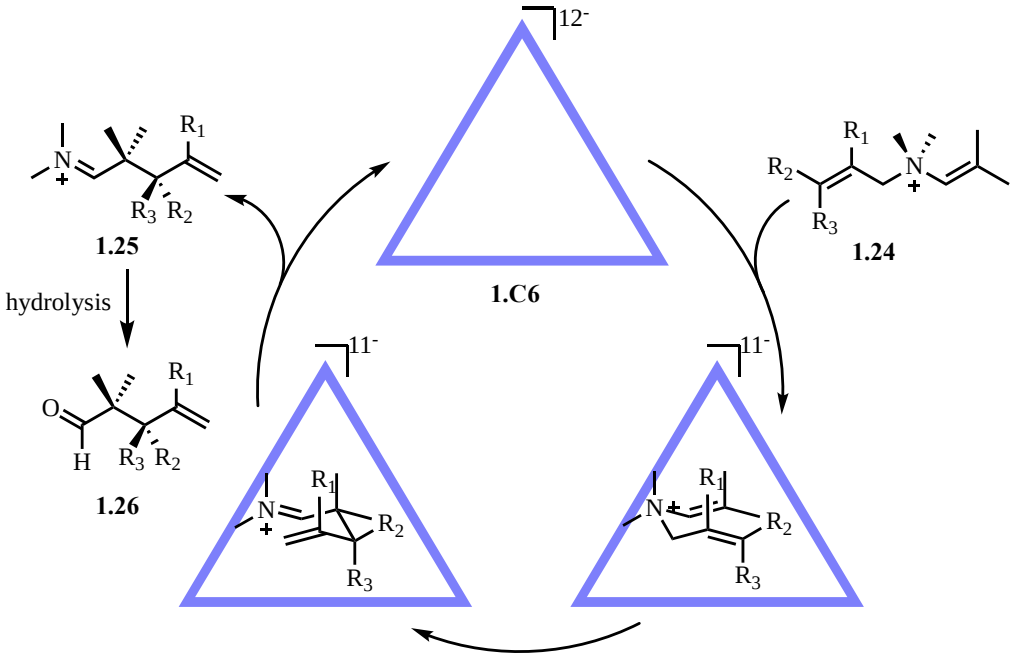

		k_{cat}/k_{uncat}[a]	$\Delta\Delta H^{\ddagger}$[a]	$\Delta\Delta S^{\ddagger}$[a]	ee[b]
1.24a	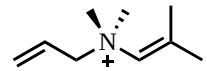	5	ND	ND	0
1.24b	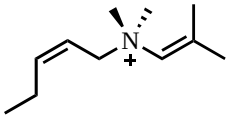	90	-1.2	5	64
1.24c	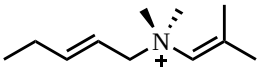	140	-0.1	10	25
1.24d	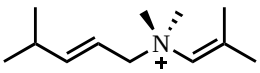	854	-1	10	60, 78[c]
1.24e	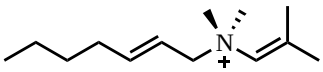	56	ND	ND	6[d]

[a] Parameters obtained with racemic **1.C6** as the catalyst.
[b] Reaction condition: 20 mol% ΔΔΔΔ-**1.C6**, D_2O, 50 °C.
[c] ee at 5°C. [d] 50 mol% catalyst loading

*Figure 1-9. (top) The constrictive binding of **1.24** by **1.C6** leads to the aza-cope catalysis, and the iminium product undergoes rapid hydrolysis in the bulk phase. (bottom) Rate enhancement and thermodynamic parameters for racemic **1.C6** catalysed aza-cope rearrangement, and the enantioselectivity of ΔΔΔΔ-**1.C6** catalysed reactions.*

1.3.3 Electrostatic interaction method

Both the co-encapsulation and the constrictive binding methods facilitate reactions by reducing the entropic barriers. However, substrate preorganisation has been found to play a less significant role in enzyme catalysis. In contrast, highly efficient enzyme catalysis has shown to have an electrostatic basis.[57][58][59] For example, enzymes are able to modify the basicity of their substrates through intricate H-bond networks and electrostatic interactions,[60][61] leading to significant pK_a changes.[62] Although covalent receptors have also shown the ability to shift the pK_a values of their bound guests,[63][64] coordination cages are prime candidates for using electrostatic interactions to mimic enzyme catalysis, not least because of their permanent charges. Examples of coordination cage catalysis using electrostatic interactions to stabilise intermediates and transition states are discussed in this section.

1.3.3.1 Coulombic interaction method

The Raymond group used the coulombic attraction and hydrophobicity of **1.C6** to stabilise transient iminium cations.[65] These prospects of **1.C6** were also shown to facilitate the binding of protonated orthoformate molecules **1.27**, resulting in a p*K*a shift up to 4 units for the conjugate acids **1.27**H^+ (Figure 1-10). The pK_a modulation allows the hydrolysis of **1.27** under basic conditions (pH = 11) with highly impressive rate acceleration (k_{cat}/k_{uncat} up to 3900), even though such reactions are usually catalysed by acid.[66] The cavity of **1.C6** is proven to facilitate the hydrolysis of **1.27** by the size-sensitive substrate scope and the competitive inhibition experiments. Cage **1.C6** also shows high catalyst turnover with only 1 mol% of cage required due to the higher hydrophilicity of **1.28,** which facilitates the product release.[66] Orthoformate hydrolysis usually proceeds with an A-1 mechanism where the protonation of the substrates is rapid. Interestingly, kinetic investigations reveal that the cage catalysed hydrolysis undergoes an A-S_E2 mechanism with the catalyst resting state being **1.C6** binding neutral **1.27** (Figure 1-10).[67] The proton transfer to **1.27** becomes the rate determining step, possibly due to the increased pK_a of H_3O^+ in **1.C6**. It is worth noting that after the initial hydrolysis step, the subsequent hydrolyses can occur inside or

outside the cavity. In similar studies, the ability of **1.C6** to alter the pK_a of bound guests was also used to facilitate the hydrolysis of acetyl compounds in basic media.[68][69]

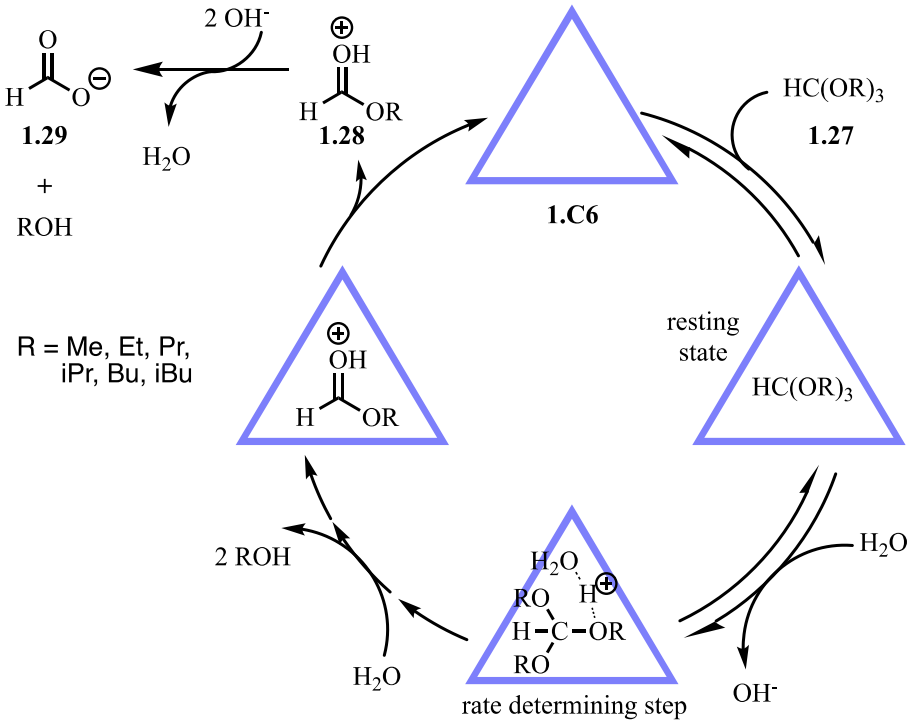

*Figure 1-10. Mechanism of **1.C6** catalysed hydrolysis of orthoformate **1.27**.*

Positively charged coordination cages have also shown catalysis by stabilising anionic intermediates through coulombic interactions. The Fujita group showed that **1.C1** can facilitate the Knoevenagel reaction of **1.30** and **1.31**, forming **1.33** in 96% yield while only 4% of the product was generated without **1.C1** (Figure 1-11).[70] The reaction turns over efficiently with only 1 mol% **1.C1** required due to the product-host size discrepancy. The authors speculated a mechanism where only one of the substrates, **1.30**, is bound in **1.C1** and is attacked by the enolate form of **1.31** in the bulk phase. However, given the large cavity volume and precedent co-encapsulation of multiple guests,[71][72] it is possible that a transient ternary complex **1.30** & **1.31**⊂**1.C1** exists. It is also possible that the deprotonated **1.31** interacts with the exterior of **1.C1** through the ion-pairing effect, bringing the substrates into close proximity. Nevertheless, the oxyanion intermediate **1.32** is stabilised by the 12^+ charged **1.C1** regardless of the

binding of **1.31**. The subsequent dehydration of **1.32** after proton transfer is facilitated by the hydrophobic environment in the **1.C1** core.

A control experiment showed that the bowl shaped **1.C4** has very little influence on the condensation of **1.30** and **1.31** (17% yield).[70] This is interesting as **1.C4** possesses the same amount of charge and also binds **1.30**, suggesting the necessity of a specific cage geometry. It was hypothesised that the portals in **1.C1** can stabilise **1.32** with their three surrounding Pd^{2+} centres.[70] A few other designs of Pd^{2+} cages were found by Mukherjee and co-workers to catalyse Knoevenagel reactions of similar substrates.[50][73][74] These structures all have portals surrounded by $Pd^{2+,}$ and the Knoevenagel reactions may proceed by a similar mechanism.

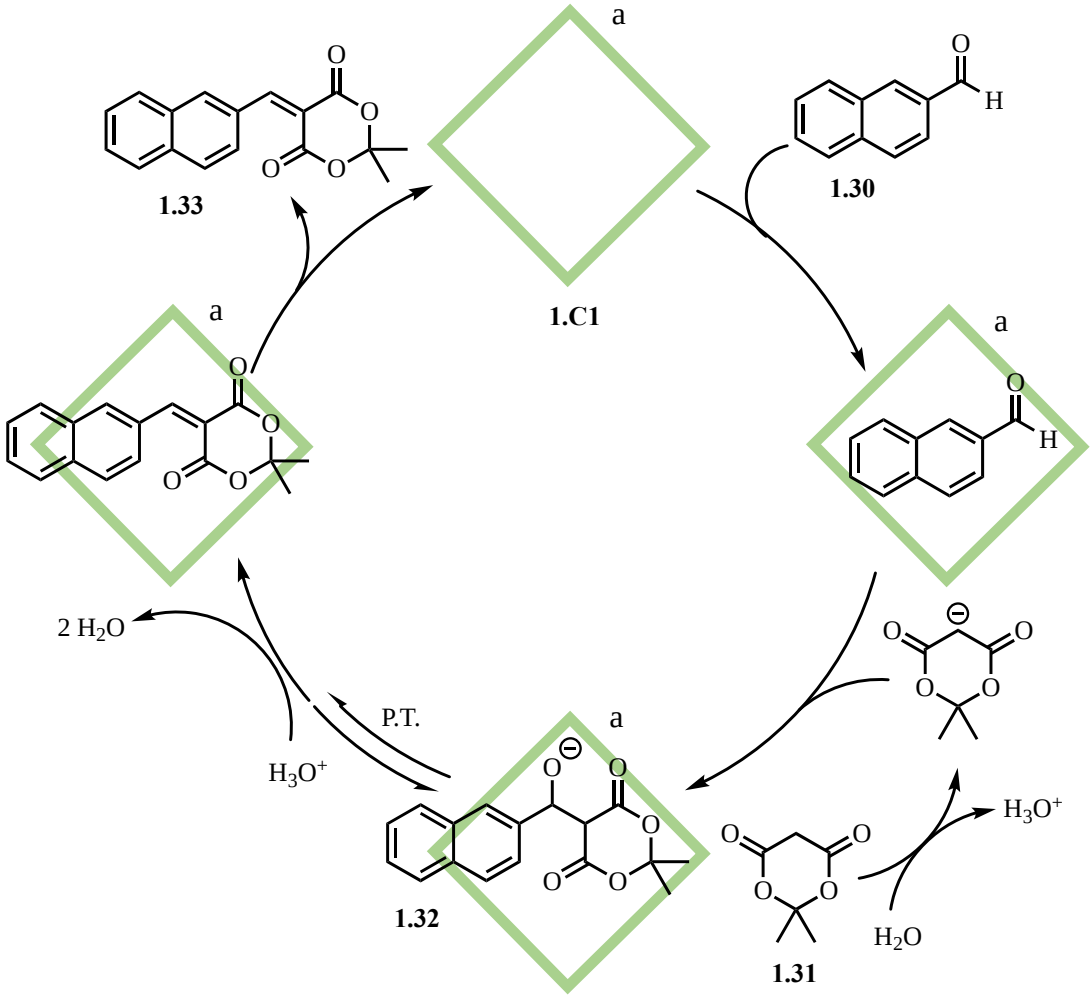

*Figure 1-11. Mechanism of **1.C1** catalysed Knoevenagel reaction of **1.30** and **1.31**.*

Another cationic cage showing catalytic properties is the Fe^{2+} tetrahedron, **1.C8** (Figure 1-12a), developed by the Nitschke group. 1 mol% cage can efficiently catalyse the hydrolysis of dichlorvos **1.34**, giving methyl phosphoric acid **1.35** as the major product and dichlorovinylmethyl phosphoric acid **1.36** as the minor product (Figure 1-12b).[75] Both **1.35** and **1.36** are more hydrophilic than **1.34**, which is believed to aid the catalyst turnover. The authors did not discuss the potential mechanism for the hydrolysis of **1.34**, only speculating that the reaction occurs inside the cavity. It is plausible that the oxyanion intermediate is stabilised by the cavity of the 8^+ charged cage (Figure 1-12b). However, the intermediate can also possibly be stabilised by the outside of **1.C8** through hydrogen bonding and/or the ion-pairing effect, in a similar manner to the binding and hydrolysis of **1.34** on the exterior of a $[Co_8L_{12}]^{16+}$ cage, **1.C9** (Figure 1-13a), reported by Ward and co-workers.[76] Another possible mechanism is that hydroxide ions are coulombically attracted to the outside of **1.C8**, creating higher effective molarity, promoting the hydrolysis in a similar manner as outlined in section 1.3.3.2 .

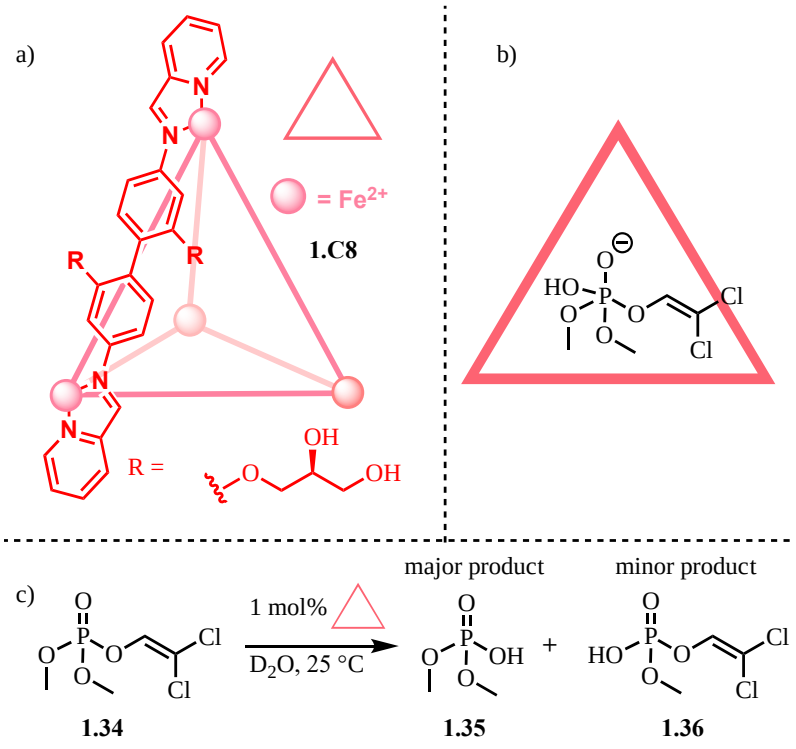

*Figure 1-12. a) The chemical structure of **1.C8**. b) Possible oxyanion stabilisation in the cavity of **1.C8**. c) **1.C8** aided hydrolysis of **1.34**.*

1.3.3.2 Ionic sphere modulation

Coulombic interactions can affect not only the bound guests (substrates, intermediates and transition states) but also the charged species associated on the outside of the coordination cages. Ward and co-workers demonstrated that the Kemp elimination of **1.37** can be catalysed by an altered ionic sphere caused by the ion-pairing effect of **1.C9** (Figure 1-13). At pD = 8.5 and in the presence of **1.C9**, an impressive rate enhancement was observed (k_{cat}/k_{uncat} = 2×10^5) for the Kemp elimination.[77] Benzisoxazole **1.37** binds in the hydrophobic core of **1.C9**, and simultaneously, the 16^+ charge of the cage attracts hydroxide ions on the exterior of **1.C9** holding them at an optimal position for eliciting the N=CH protons of **1.37** (Figure 1-13c).[77] The catalysis arises as a result of an increased local concentration of hydroxide ions. Competitive inhibition experiments support this hypothesis, and the addition of either cycloundecanon that blocks the cavity or chloride that binds on the outside leads to a retarded rate of reaction. The observation that the **1.C9** catalysed Kemp elimination showed pD independency between pD = 8.5 and pD = 11.4 also indicates the external hydroxide binding saturates at pD = 8.5.[77] The authors also note that the highly hydrophobic environment has poorer stabilisation for the negative charge building on the transition state than H_2O in the bulk phase, indicating that the internal binding is anti-catalytic and that the rate enhancement solely stems from the high hydroxide concentration.[77] The Kemp elimination turns over efficiently, owing to the thermodynamic preference for the hydrophilic cyanophenolate product to bind in water outside **1.38**.

Interestingly, in the presence of chloride ions, the cage catalysed Kemp elimination of **1.37** appears to be autocatalytic.[78] This behaviour results from the preferable binding of the product ions **1.38** over chloride (Figure 1-13b). This is supported by experiments that showed the addition of other phenolate compounds further enhanced the catalysis of **1.C9**. When adding phenolates of various basicity to the reaction, the catalysis can be tuned; a phenolate of higher pK_a leads to a more accelerated rate.[78] This observation again supports that the catalysis of **1.37** arises from external ion-pairing of **1.C9**.

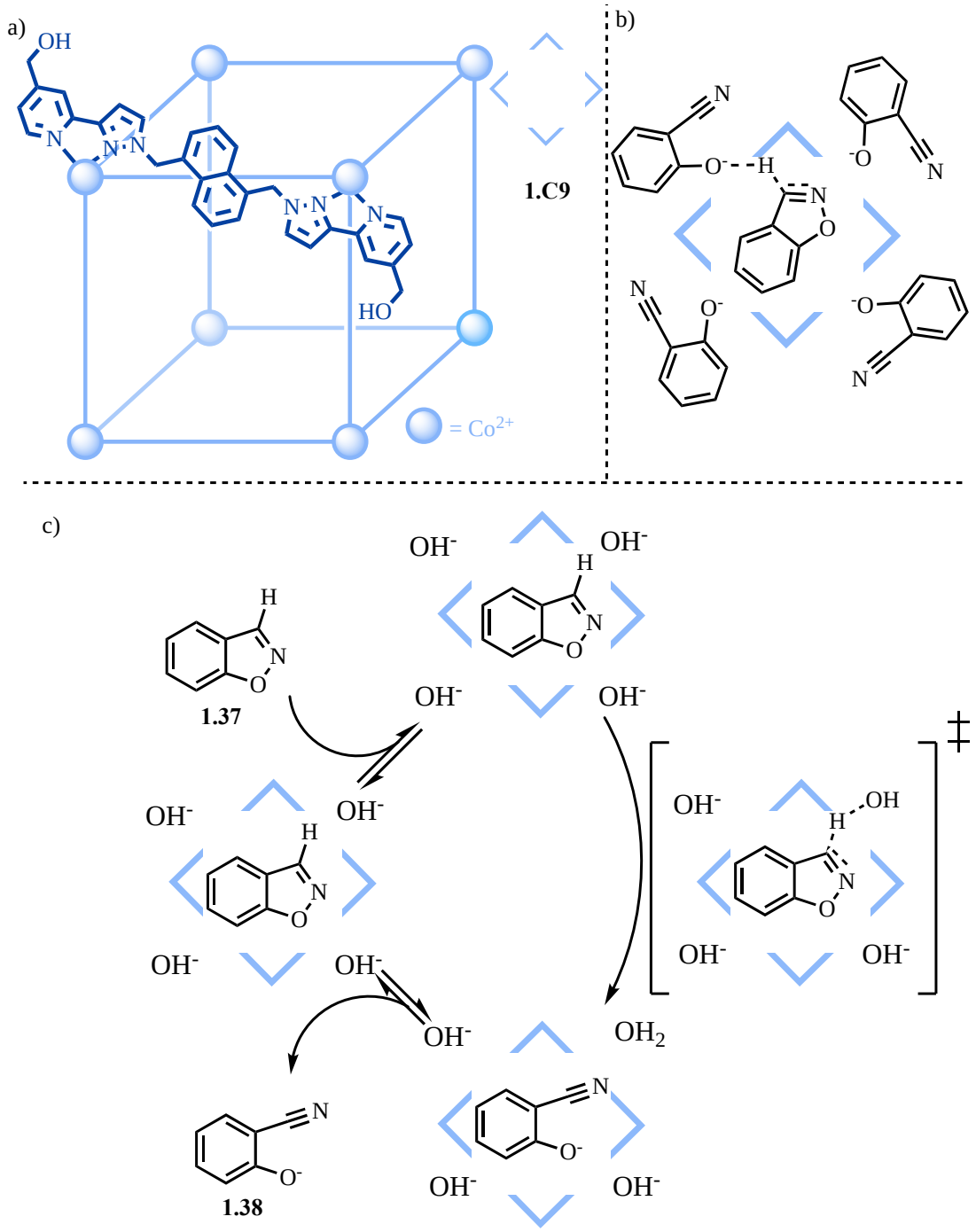

*Figure 1-13. a) The chemical structure of **1.C9**. b) Autocatalysis pathway: **1.C9** binds product **1.37** on the exterior, and **1.37** elicits proton from **1.38**. c) Proposed mechanism of **1.C9** catalysed Kemp elimination of **1.37**.*

1.3.3.3 Non-coulombic electrostatic method

While non-coulombic electrostatic forces are generally weaker interactions, they prove to be extremely useful in catalysis, both in nature and in synthetic catalysts. For

example, small molecule H-bond catalysts have been shown to electronically activate substrate in a similar manner to a Lewis acid, and to stabilise anionic intermediates.[79][80] One advantage of H-bond catalysis over the coulombic attraction method is that neutral transition states, such as the Diels-Alder transition state, can also be stabilised. π-ion interactions have also seen an increasing application in organocatalysis where small molecules with electron-rich or deficient aromatic surfaces stabilise cationic or anionic intermediates.[81][82]

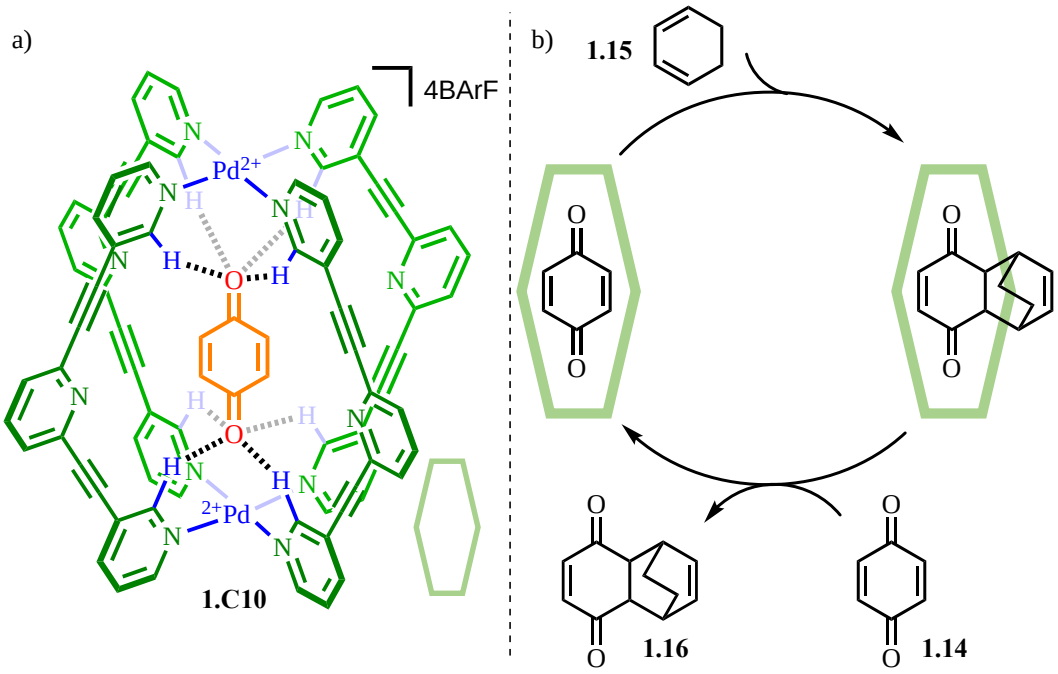

Figure 1-14. a) ***1.C10*** *binds* ***1.14*** *through polarised ortho-pyridyl C-H bonds. b) Single-species-to-single-species turnover mechanism for the* ***1.C10*** *catalysed Dield-Alder reaction of* ***1.14*** *and* ***1.15****.*

The Lusby group has expanded the use of non-coulombic electrostatic interactions to coordination cage catalysis, using the Pd_2L_4 structure **1.C10** (Figure 1-14a). The Pd^{2+} ions significantly polarise the ortho-pyridyl C-H bonds, rendering them effective H-bond donors.[83] Highly complimentary guest **1.14** binds strongly by positioning its carbonyl groups into both H-bond pockets. The carefully designed polar interactions are maximised using the apolar solvent, CD_2Cl_2, and the large non-interacting anions, BArF. **1.C10** catalyses the Diels-Alder reactions of **1.14** and a broad range of dienes highly efficiently with k_{cat}/k_{uncat} up to 1000 (Figure 1-14b).[84] The catalysis can be

switched off by the addition of a competitive inhibitor, pentacenedione, proving that the activity stems from the cage cavity. Unlike the majority of the supramolecular Diels-Alder catalysts, **1.C10** only binds one substrate **1.14** and not the diene **1.15**. Rather than relying on increased molarity of substrates in the cavity, **1.C10** electronically activates **1.14** through the hydrogen bond interactions lowering its LUMO.[84] **1.C10** also displays efficient stabilisation towards the transition state of **1.14** and **1.15**, resulting in the high catalytic activity.[84][85]

The Diels-Alder reactions catalysed by **1.C10** also shows very low product inhibition, with a turnover number up to 1000. This is significant as the system can release a bimolecular fusion product without engineering guest shape/size discrepancy. Because the catalysis does not involve binding the diene **1.15**, only one molecule of **1.14** is required to displace on a molecule of **1.16** (Figure 1-14b), allowing an entropically neutral turnover step.

1.3.4 Enclosed reactivity

Coordination cages can act as non-covalent protective groups by shielding the reactive functionalities in their cavities. This was demonstrated by the Fujita group using a *cis*-cap Pd^{2+} cage **1.C3** (Figure 1-6). The nucleophilic substitution of aryl-substituted allylic chloride **1.39a** yields the terminal product **1.40a** and the internal product **1.40b** in a 56:44 ratio in D_2O (Figure 1-15). However, when charged with 50 mol% **1.C3**, the terminal/internal ratio of the substitution reaction increases to 71:29, favouring **1.40a**.[86] The addition of the strongly binding 1-adamentanol suppresses the regioselectivity, confirming the essential role of the cage cavity. **1.C3** is likely to favour the formation of **1.40a** by shielding the internal sites with the cavity and exposing the external site through the cage portals. This is supported by the observation that the terminal methylene group on **1.39a** exhibits the smallest shielding effect on the ^{1}H NMR of the host-guest complex **1.39a⊂1.C3**. Impressively, the branched allylic chloride **1.39b** showed an inverted terminal/internal ratio from 38:62 under the uncatalysed condition to the 52:48 in the presence of **1.C3** (Figure 1-15).[86] In a relevant study, the authors also demonstrated that **1.C1** can bind a long, linear terpenoid chain into a U-shaped conformation with the terminal C=C bond exposed

through cage portals and the two internal C=C shielded in the cavity, leading to highly selective electrophilic addition at the terminal site.[87]

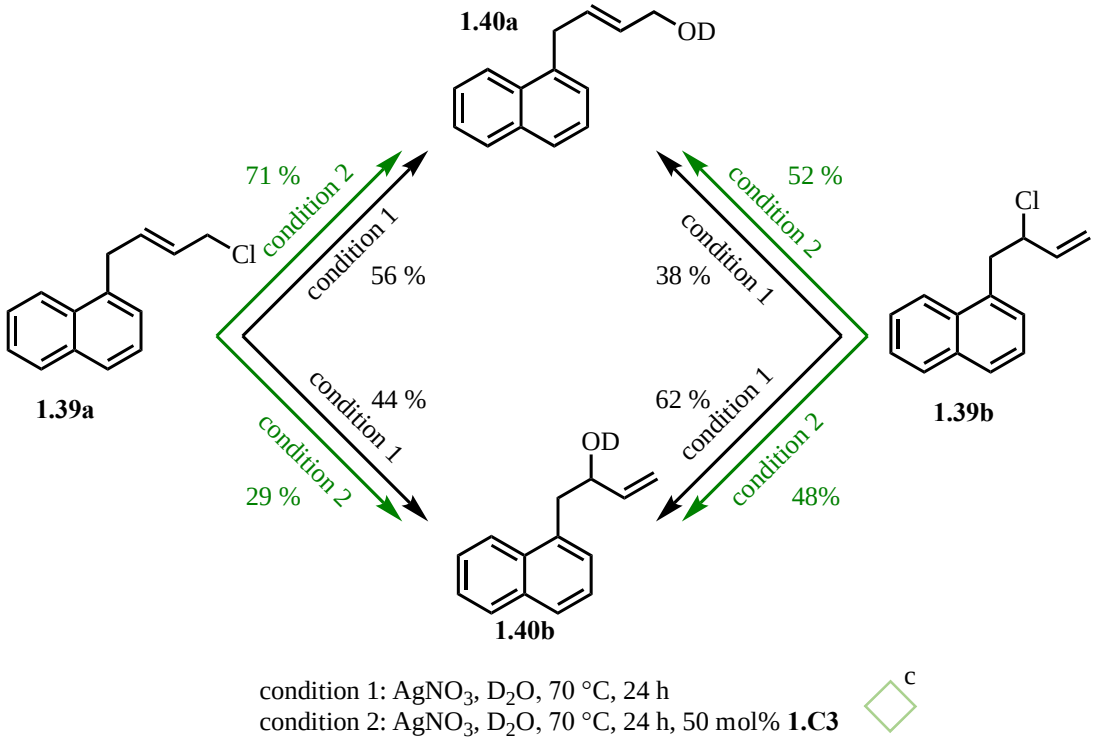

*Figure 1-15. The nucleophilic substitution of aryl-substituted allylic chloride **1.39a** and **1.39b**.*

Coordination cages can also facilitate the pathways to form short-lived, kinetic products through guest binding. "Ship-in-bottle" type syntheses of cyclic oligomers of trialkoxysilanes were described by Fujita and co-workers where cage **1.C3** binds multiple substrate molecules and kinetically traps the products because the sizes of the products are larger than the cage portals. While the monomer **1.41** self-condenses rapidly and participates (possibly via **1.42**), **1.C3** directs a clean formation of **1.42** in only all *cis* conformers and provides significant stabilisation, even under acid conditions (Figure 1-16).[88] Although the reaction requires stoichiometric cage, it shows the confined cavity of coordination cages can mediate highly selective processes. Further studies demonstrate that the sizes of the oligomers can be fine-tuned by using Pd^{2+} cages of suitable sizes and geometries.[89][90]

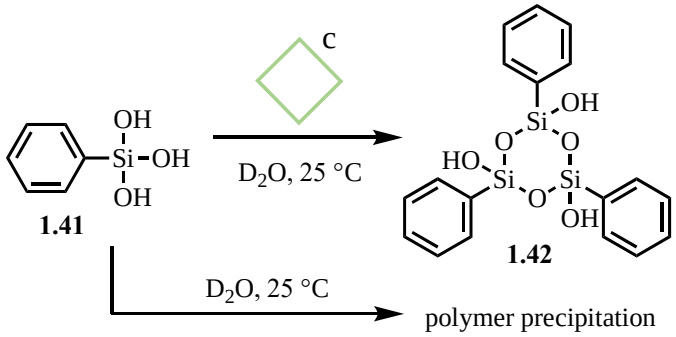

*Figure 1-16. Selective formation of **1.42** in the cavity of **1.C3** while **1.41** forms insoluble siloxane polymers.*

1.3.5 Hybrid methods

Coordination cages often simultaneously possess multiple characteristics such as a confined hydrophobic core, charged vertices, and ligands capable of interacting with the guests. These factors can collectively contribute to the catalysis in the cavity using a combination of entropic and enthalpic activation methods.

For example, the Raymond group used **1.C6** to accelerate the Nazarov cyclisation of **1.43** by 2 million fold,[91][92] demonstrating the power of a hybrid mechanism. The 12^- charged cage **1.C6** facilitates the protonation of **1.43**, likely by stabilising the resulting cationic intermediates **1.44** and/or **1.45** (Figure 1-17). Constrictive binding of the substrate **1.43** and/or intermediates **1.44** and **1.45** leads to a U-shaped conformation that is optimal for the electrocyclisation.[91] Analysis of the energetics of the catalysed and uncatalysed Nazarov cyclisation also revealed significant transition state stabilisation by **1.C6**.[93] In a further study, the authors observed a 680-fold decrease in the k_{obs} of the Nazarov reaction of **1.43** when using the less charged Si^{4+} cage **1.C7**,[54] demonstrating the contribution of coulombic attraction in the intermediate/transition state stabilisation. It is noteworthy that pentamethylcyclopentadiene **1.46** strongly binds in **1.C6,** similar to many supramolecular catalysis examples where the products resemble transition state geometries,. However, turnover of the Nazarov reaction can be achieved by trapping **1.46** with **1.47** to form a less complimentary guest **1.48** (Figure 1-17).[91]

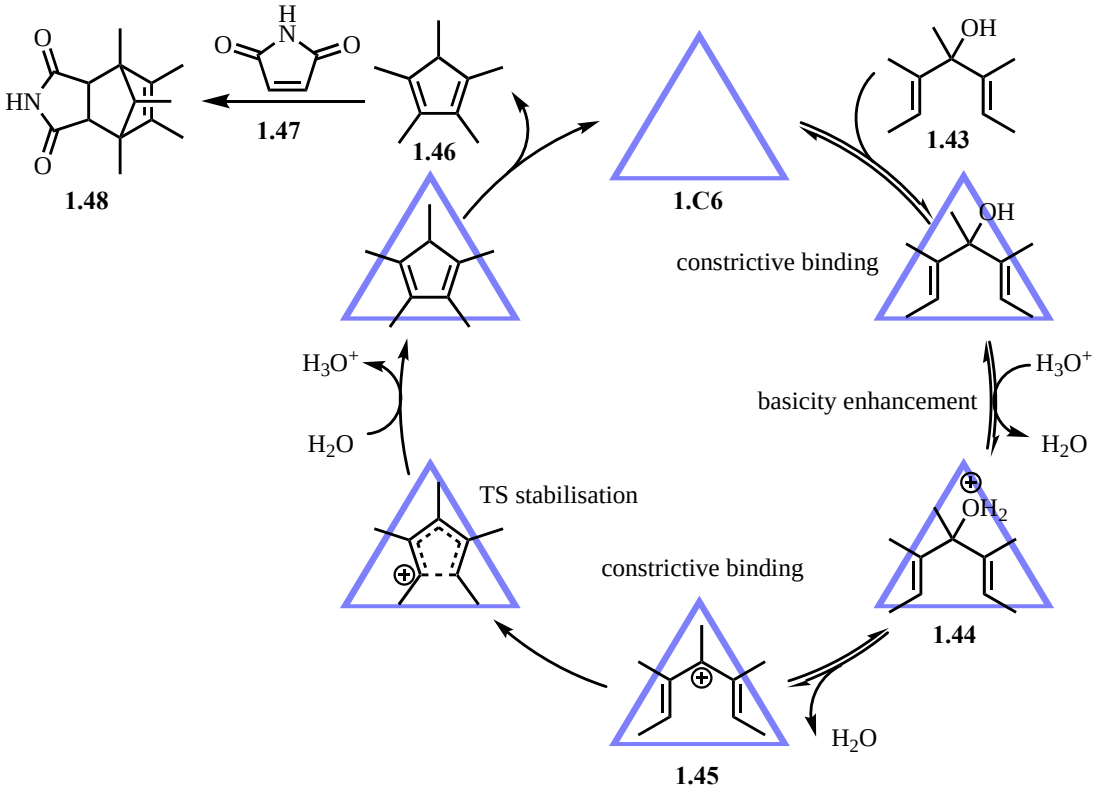

*Figure 1-17. The proposed mechanism of the **1.C6** catalysed Nazarov cyclisation of **1.43**.*

A similar example combining coulombic stabilisation and constrictive binding is the cyclisation of citronellal **1.49** (Figure 1-18). This reaction proceeds 5×10^4 times faster in the presence of **1.C6** than in phosphate buffer solutions.[94][95] The rate enhancement results from the ability of anionic **1.C6** to promote the protonation of **1.49** by stabilising the resulting cation. It is also possible that the guest binding pre-organises **1.49**H^+ into a reactive conformation which leads to a lowered entropic barrier proceeding the intermediate **1.50**.

In addition to rate enhancement, the microenvironment of **1.C6** gives rises to otherwise unfavoured reaction pathways (Figure 1-18). In the aqueous bulk phase, the carbocation intermediate **1.50** is captured by H_2O, forming the major product **1.51** (91 %). However, the highly hydrophobic cavity of **1.C6** excludes H_2O and allows the hydride eliminating pathway that generates **1.52** as the main product (97%).[94] Relevant studies also show that the restrictive chiral environment of enantiopure **1.C6**

can induce chirality to the cyclisation products and that adaptation of the cage spacers can alter the catalysis efficiency and diastereoselectivity. [95][96]

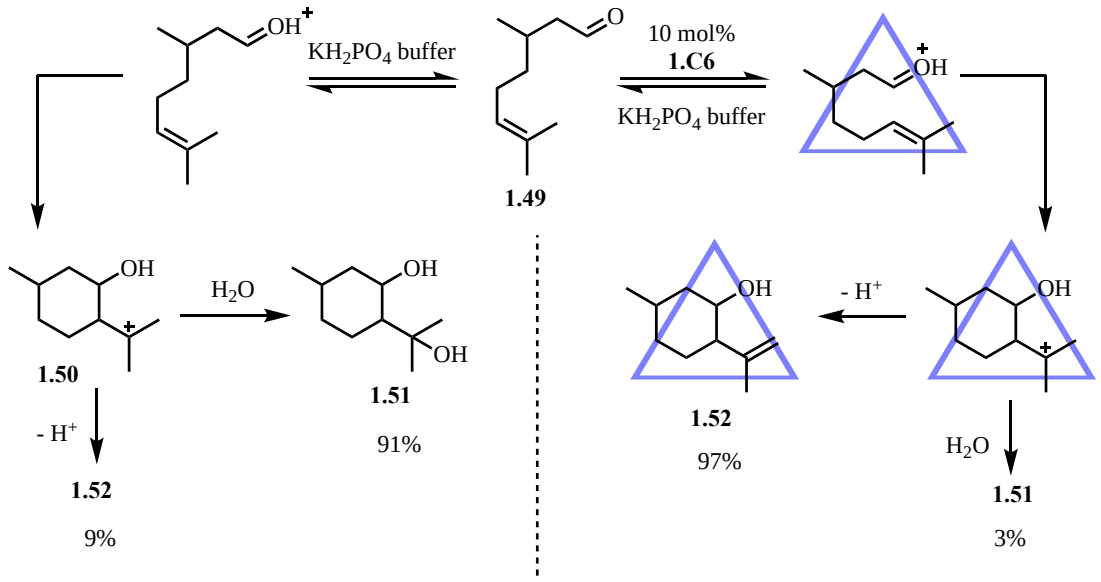

*Figure 1-18. The cavity of **1.C6** expels H_2O and facilitates the otherwise unfavoured formation of **1.52**.*

A similar reaction pathway divergent effect of **1.C6** was observed with the aza-Prins cyclisation of **1.53**. The conformation of the iminium intermediate **1.54** following the condensation of **1.53** with formaldehyde plays a determining role in the reaction mechanism. In the absence of **1.C6**, **1.53** cyclises *via* the transition state geometry where the doubly substituted C=C bond adopts the less hindered equatorial position (**1.54a**) (Figure 1-19, left pathway). The resulting carbocation **1.55** is subsequently quenched by H_2O, giving **1.56** as the product. On the contrary, constrictive binding of **1.C6** causes **1.54** to favour the more compact transition state with the C=C bond occupying the axial position (**1.54b**) (Figure 1-19, left pathway).[97] Cyclisation of **1.54b** then generates **1.57** that places the carbocation in proximity to the N-methyl group, promoting a 1,5-hydride shift that exclusively forms **1.58**.

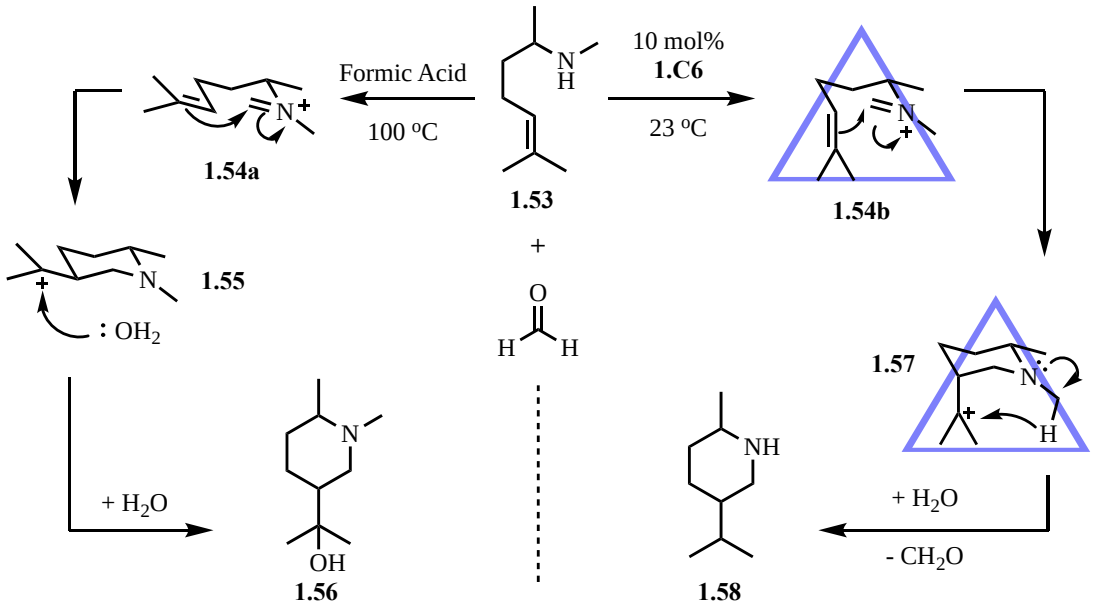

Figure 1-19. ***1.C6*** *favours the more "compact" transition state* ***1.54b****, leading to a 1,5-hydride shift of the cabocation intermediate* ***1.57****.*

1.4 Summary and Outlook

The intrinsic catalytic function of hollow coordination cages bears the potential to mimic enzymatic activities and has attracted rising attention. Substrate preorganisation provides an effective method to reduce the entropic activation barriers and to induce reaction selectivity through the confinement effect. The permanent charges of coordination cages deliver electrostatic interactions exerting intermediates and transition state stabilisation that underpins highly efficient enzyme-like activity. Multiple prospects of coordination cages could also work in tandem, leading to complex catalysis where both entropic and enthalpic factors of the reactions are modulated.

Unimolecular processes, such as rearrangement reactions, in coordination cages, have been shown to catalytically turnover due to the entropically neutral product-starting material exchange. However, product inhibition remains a challenge for fusion reactions that rely on co-encapsulation of the substrate, although cage-product size and shape discrepancy can be used to avoid product inhibition in isolated cases. The single species turnover approach provides one way to promote catalytic fusion reactions. However, there is still a need for the development of systems that unpicks product inhibition.

Coordination cage catalysis is still an underdeveloped field, and a systematic methodology to expand its reaction scope is yet to be established. A common approach adopted by many research groups has been to first identify strong binding guests for the archetypical cage structures and then to “screen” amongst these guests for the substrates that may undergo chemical reactions in the presence of the cages. While this approach could be efficient for discovering unimolecular transformation catalysis, it may fail to identify suitable fusion reactions whose intermediates or transition states have drastically different geometries or charge state to the starting materials. It is thus essential for researchers to develop a deep understanding of coordination cage catalytic mechanisms in order to design and optimise cage catalysts. Furthermore, the cage catalysis research will undoubtedly transition from searching for reactions that suit the

catalysts to rationally designing supramolecular cage catalysts based on the reactions of interest.

1.5 Thesis Aims

The aim of this thesis is to investigate the catalytic potential of simple Pd_2L_4 structures and to understand their catalytic mechanisms. This thesis focuses on utilising electrostatic host-guest interactions to influence reaction intermediates and transition states to develop highly efficient, enzyme-mimicking supramolecular cage catalysts. This work also aims to unpick product inhibition that is often associated with cage catalysed bimolecular fusion reactions.

The aim of chapter 2 is to develop a new catalysis approach that takes advantage of efficient coulombic interactions in Pd_2L_4 cages. It investigates how binding carbanions can unlock C-C forming Michael addition reactions.

Chapter 3 investigates how Pd_2L_4 cages bind guests through hydrogen bonds, and how they can influence the neutral transition states of Diels-Alder reactions. It branches away from previous research in the Lusby group to expand the substrate scope and gain a deeper understanding of the mechanistic subtlety.

Chapter 4 expands our portfolio of Pd_2L_4 cages and investigates how varying the size and shape can affect the structure-activity relationship. By understanding how the 3D environment affects the cage in catalysis, we can build towards rationally designing cage catalysts for specific applications.

1.6 References

[1] M. Fujita, *Chem. Soc. Rev.* **1998**, *27*, 417–425.
[2] M. Han, D. M. Engelhard, G. H. Clever, *Chem. Soc. Rev.* **2014**, *43*, 1848–1860.
[3] M. M. J. Smulders, I. A. Riddell, C. Browne, J. R. Nitschke, *Chem. Soc. Rev.* **2013**, *42*, 1728–1754.
[4] M. D. Ward, P. R. Raithby, *Chem. Soc. Rev.* **2013**, *42*, 1619–1636.
[5] T. R. Cook, P. J. Stang, *Chem. Rev.* **2015**, *115*, 7001–7045.
[6] S. Saha, I. Regeni, G. H. Clever, *Coord. Chem. Rev.* **2018**, *374*, 1–14.
[7] D. L. Caulder, K. N. Raymond, *Acc. Chem. Res.* **1999**, *32*, 975–982.
[8] R. Chakrabarty, P. S. Mukherjee, P. J. Stang, *Chem. Rev.* **2011**, *111*, 6810–6918.
[9] C. J. Pedersen, H. K. Frensdorff, *Angew. Chem. Int. Ed. Engl.* **1972**, *11*, 16–25.
[10] S. Liu, C. Ruspic, P. Mukhopadhyay, S. Chakrabarti, P. Y. Zavalij, L. Isaacs, *J. Am. Chem. Soc.* **2005**, *127*, 15959–15967.
[11] S. M. Biros, J. Julius Rebek, *Chem. Soc. Rev.* **2007**, *36*, 93–104.
[12] F. J. Rizzuto, L. K. S. von Krbek, J. R. Nitschke, *Nat. Rev. Chem.* **2019**, *3*, 204–222.
[13] Y. Inokuma, S. Yoshioka, J. Ariyoshi, T. Arai, Y. Hitora, K. Takada, S. Matsunaga, K. Rissanen, M. Fujita, *Nature* **2013**, *495*, 461–466.
[14] Y. Inokuma, M. Kawano, M. Fujita, *Nat. Chem.* **2011**, *3*, 349–358.
[15] B. P. Burke, W. Grantham, M. J. Burke, Gary. S. Nichol, D. Roberts, I. Renard, R. Hargreaves, C. Cawthorne, S. J. Archibald, P. J. Lusby, *J. Am. Chem. Soc.* **2018**, *140*, 16877–16881.
[16] R. A. Tromans, T. S. Carter, L. Chabanne, M. P. Crump, H. Li, J. V. Matlock, M. G. Orchard, A. P. Davis, *Nat. Chem.* **2019**, *11*, 52–56.
[17] A. J. Plajer, E. G. Percástegui, M. Santella, F. J. Rizzuto, Q. Gan, B. W. Laursen, J. R. Nitschke, *Angew. Chem. Int. Ed.* **2019**, *58*, 4200–4204.
[18] J. E. M. Lewis, E. L. Gavey, S. A. Cameron, J. D. Crowley, *Chem. Sci.* **2012**, *3*, 778–784.
[19] B. Therrien, G. Süss-Fink, P. Govindaswamy, A. K. Renfrew, P. J. Dyson, *Angew. Chem. Int. Ed.* **2008**, *47*, 3773–3776.
[20] M. Yamashina, Y. Sei, M. Akita, M. Yoshizawa, *Nat. Commun.* **2014**, *5*, 4662.
[21] P. Mal, B. Breiner, K. Rissanen, J. R. Nitschke, *Science* **2009**, *324*, 1697–1699.
[22] A. J. Scott, J. Vallejo, A. Sarkar, L. Smythe, E. R. Martí, G. S. Nichol, W. T. Klooster, S. J. Coles, M. Murrie, G. Rajaraman, S. Piligkos, P. J. Lusby, E. K. Brechin, *Chem. Sci.* **2021**, *12*, 5134–5142.
[23] D. Zhang, T. K. Ronson, Y.-Q. Zou, J. R. Nitschke, *Nat. Rev. Chem.* **2021**, *5*, 168–182.
[24] F. Cramer, W. Kampe, *J. Am. Chem. Soc.* **1965**, *87*, 1115–1120.
[25] V. T. D'Souza, M. L. Bender, *Acc. Chem. Res.* **1987**, *20*, 146–152.
[26] R. L. VanEtten, J. F. Sebastian, G. A. Clowes, M. L. Bender, *J. Am. Chem. Soc.* **1967**, *89*, 3242–3253.
[27] D. C. Rideout, R. Breslow, *J. Am. Chem. Soc.* **1980**, *102*, 7816–7817.
[28] H. L. Anderson, J. K. M. Sanders, *J. Chem. Soc. Chem. Commun.* **1989**, 1714–1715.

[29] C. J. Walter, H. L. Anderson, J. K. M. Sanders, *J. Chem. Soc. Chem. Commun.* **1993**, 458–460.
[30] Z. Clyde-Watson, A. Vidal-Ferran, L. J. Twyman, C. J. Walter, D. W. J. McCallien, S. Fanni, N. Bampos, R. S. Wylie, J. K. M. Sanders, *New J. Chem.* **1998**, *22*, 493–502.
[31] J. K. M. Sanders, *Chem. – Eur. J.* **1998**, *4*, 1378–1383.
[32] J. Chen, J. Rebek, *Org. Lett.* **2002**, *4*, 327–329.
[33] W. L. Mock, T. A. Irra, J. P. Wepsiec, T. L. Manimaran, *J. Org. Chem.* **1983**, *48*, 3619–3620.
[34] M. Marty, Z. Clyde-Watson, L. J. Twyman, M. Nakash, J. K. M. Sanders, *Chem. Commun.* **1998**, 2265–2266.
[35] Ronald. Breslow, Tao. Guo, *J. Am. Chem. Soc.* **1988**, *110*, 5613–5617.
[36] L. G. Mackay, R. S. Wylie, J. K. M. Sanders, *J. Am. Chem. Soc.* **1994**, *116*, 3141–3142.
[37] J. Kang, J. Rebek, *Nature* **1997**, *385*, 50–52.
[38] J. Kang, J. Santamaría, G. Hilmersson, J. Rebek, *J. Am. Chem. Soc.* **1998**, *120*, 7389–7390.
[39] J. Kang, G. Hilmersson, J. Santamaría, J. Rebek, *J. Am. Chem. Soc.* **1998**, *120*, 3650–3656.
[40] S. P. Kim, A. G. Leach, K. N. Houk, *J. Org. Chem.* **2002**, *67*, 4250–4260.
[41] Z. J. Wang, C. J. Brown, R. G. Bergman, K. N. Raymond, F. D. Toste, *J. Am. Chem. Soc.* **2011**, *133*, 7358–7360.
[42] C. J. Brown, G. M. Miller, M. W. Johnson, R. G. Bergman, K. N. Raymond, *J. Am. Chem. Soc.* **2011**, *133*, 11964–11966.
[43] D. H. Leung, R. G. Bergman, K. N. Raymond, *J. Am. Chem. Soc.* **2007**, *129*, 2746–2747.
[44] R. Gramage-Doria, J. Hessels, S. H. A. M. Leenders, O. Tröppner, M. Dürr, I. Ivanović-Burmazović, J. N. H. Reek, *Angew. Chem. Int. Ed.* **2014**, *53*, 13380–13384.
[45] M. Yoshizawa, M. Tamura, M. Fujita, *Science* **2006**, *312*, 251–254.
[46] T. Murase, S. Horiuchi, M. Fujita, *J. Am. Chem. Soc.* **2010**, *132*, 2866–2867.
[47] Y. Fang, T. Murase, M. Fujita, *Chem. Lett.* **2015**, *44*, 1095–1097.
[48] S. Horiuchi, Y. Nishioka, T. Murase, M. Fujita, *Chem. Commun.* **2010**, *46*, 3460–3462.
[49] S. Horiuchi, T. Murase, M. Fujita, *Chem. – Asian J.* **2011**, *6*, 1839–1847.
[50] D. Samanta, S. Mukherjee, Y. P. Patil, P. S. Mukherjee, *Chem. – Eur. J.* **2012**, *18*, 12322–12329.
[51] D. L. Caulder, R. E. Powers, T. N. Parac, K. N. Raymond, *Angew. Chem. Int. Ed.* **1998**, *37*, 1840–1843.
[52] D. L. Caulder, C. Brückner, R. E. Powers, S. König, T. N. Parac, J. A. Leary, K. N. Raymond, *J. Am. Chem. Soc.* **2001**, *123*, 8923–8938.
[53] D. Fiedler, R. G. Bergman, K. N. Raymond, *Angew. Chem. Int. Ed.* **2004**, *43*, 6748–6751.
[54] C. M. Hong, M. Morimoto, E. A. Kapustin, N. Alzakhem, R. G. Bergman, K. N. Raymond, F. D. Toste, *J. Am. Chem. Soc.* **2018**, *140*, 6591–6595.

[55] D. Fiedler, H. van Halbeek, R. G. Bergman, K. N. Raymond, *J. Am. Chem. Soc.* **2006**, *128*, 10240–10252.
[56] C. J. Brown, R. G. Bergman, K. N. Raymond, *J. Am. Chem. Soc.* **2009**, *131*, 17530–17531.
[57] A. Warshel, P. K. Sharma, M. Kato, Y. Xiang, H. Liu, M. H. M. Olsson, *Chem. Rev.* **2006**, *106*, 3210–3235.
[58] A. Warshel, *Proc. Natl. Acad. Sci.* **1978**, *75*, 5250–5254.
[59] J. Villà, M. Štrajbl, T. M. Glennon, Y. Y. Sham, Z. T. Chu, A. Warshel, *Proc. Natl. Acad. Sci.* **2000**, *97*, 11899–11904.
[60] N.-C. Ha, M.-S. Kim, W. Lee, K. Y. Choi, B.-H. Oh, *J. Biol. Chem.* **2000**, *275*, 41100–41106.
[61] W. W. Cleland, P. A. Frey, J. A. Gerlt, *J. Biol. Chem.* **1998**, *273*, 25529–25532.
[62] S. Száraz, D. Oesterhelt, P. Ormos, *Biophys. J.* **1994**, *67*, 1706–1712.
[63] J. Mohanty, A. C. Bhasikuttan, W. M. Nau, H. Pal, *J. Phys. Chem. B* **2006**, *110*, 5132–5138.
[64] H. Bakirci, A. L. Koner, T. Schwarzlose, W. M. Nau, *Chem. – Eur. J.* **2006**, *12*, 4799–4807.
[65] V. M. Dong, D. Fiedler, B. Carl, R. G. Bergman, K. N. Raymond, *J. Am. Chem. Soc.* **2006**, *128*, 14464–14465.
[66] M. D. Pluth, R. G. Bergman, K. N. Raymond, *Science* **2007**, *316*, 85–88.
[67] M. D. Pluth, R. G. Bergman, K. N. Raymond, *J. Am. Chem. Soc.* **2008**, *130*, 11423–11429.
[68] M. D. Pluth, R. G. Bergman, K. N. Raymond, *Angew. Chem. Int. Ed.* **2007**, *46*, 8587–8589.
[69] M. D. Pluth, R. G. Bergman, K. N. Raymond, *J. Org. Chem.* **2009**, *74*, 58–63.
[70] T. Murase, Y. Nishijima, M. Fujita, *J. Am. Chem. Soc.* **2012**, *134*, 162–164.
[71] S. H. A. M. Leenders, R. Becker, T. Kumpulainen, B. de Bruin, T. Sawada, T. Kato, M. Fujita, J. N. H. Reek, *Chem.- Eur. J.* **2016**, *22*, 15468–15474.
[72] K. Takaoka, M. Kawano, T. Ozeki, M. Fujita, *Chem. Commun.* **2006**, 1625–1627.
[73] P. Das, A. Kumar, P. Howlader, P. S. Mukherjee, *Chem. – Eur. J.* **2017**, *23*, 12565–12574.
[74] D. Samanta, P. Sarathi Mukherjee, *Chem. Commun.* **2013**, *49*, 4307–4309.
[75] J. L. Bolliger, A. M. Belenguer, J. R. Nitschke, *Angew. Chem. Int. Ed.* **2013**, *52*, 7958–7962.
[76] C. G. P. Taylor, A. J. Metherell, S. P. Argent, F. M. Ashour, N. H. Williams, M. D. Ward, *Chem. – Eur. J.* **2020**, *26*, 3065–3073.
[77] W. Cullen, M. C. Misuraca, C. A. Hunter, N. H. Williams, M. D. Ward, *Nat. Chem.* **2016**, *8*, 231–236.
[78] W. Cullen, A. J. Metherell, A. B. Wragg, C. G. P. Taylor, N. H. Williams, M. D. Ward, *J. Am. Chem. Soc.* **2018**, *140*, 2821–2828.
[79] Z. Zhang, P. R. Schreiner, *Chem. Soc. Rev.* **2009**, *38*, 1187–1198.
[80] A. G. Doyle, E. N. Jacobsen, *Chem. Rev.* **2007**, *107*, 5713–5743.
[81] C. R. Kennedy, S. Lin, E. N. Jacobsen, *Angew. Chem. Int. Ed.* **2016**, *55*, 12596–12624.
[82] Y. Zhao, Y. Cotelle, L. Liu, J. López-Andarias, A.-B. Bornhof, M. Akamatsu, N. Sakai, S. Matile, *Acc. Chem. Res.* **2018**, *51*, 2255–2263.

[83] D. P. August, G. S. Nichol, P. J. Lusby, *Angew. Chem. Int. Ed.* **2016**, *55*, 15022–15026.
[84] V. Martí-Centelles, A. L. Lawrence, P. J. Lusby, *J. Am. Chem. Soc.* **2018**, *140*, 2862–2868.
[85] T. A. Young, V. Martí-Centelles, J. Wang, P. J. Lusby, F. Duarte, *J. Am. Chem. Soc.* **2020**, *142*, 1300–1310.
[86] Y. Kohyama, T. Murase, M. Fujita, *Chem. Commun.* **2012**, *48*, 7811–7813.
[87] H. Takezawa, T. Kanda, H. Nanjo, M. Fujita, *J. Am. Chem. Soc.* **2019**, *141*, 5112–5115.
[88] M. Yoshizawa, T. Kusukawa, M. Fujita, K. Yamaguchi, *J. Am. Chem. Soc.* **2000**, *122*, 6311–6312.
[89] M. Yoshizawa, T. Kusukawa, M. Fujita, S. Sakamoto, K. Yamaguchi, *J. Am. Chem. Soc.* **2001**, *123*, 10454–10459.
[90] Y. Yamauchi, M. Fujita, *Chem. Commun.* **2010**, *46*, 5897–5899.
[91] C. J. Hastings, M. P. Backlund, R. G. Bergman, K. N. Raymond, *Angew. Chem. Int. Ed.* **2011**, *50*, 10570–10573.
[92] C. J. Hastings, M. D. Pluth, R. G. Bergman, K. N. Raymond, *J. Am. Chem. Soc.* **2010**, *132*, 6938–6940.
[93] C. J. Hastings, R. G. Bergman, K. N. Raymond, *Chem. – Eur. J.* **2014**, *20*, 3966–3973.
[94] W. M. Hart-Cooper, K. N. Clary, F. D. Toste, R. G. Bergman, K. N. Raymond, *J. Am. Chem. Soc.* **2012**, *134*, 17873–17876.
[95] W. M. Hart-Cooper, C. Zhao, R. M. Triano, P. Yaghoubi, H. L. Ozores, K. N. Burford, F. D. Toste, R. G. Bergman, K. N. Raymond, *Chem. Sci.* **2015**, *6*, 1383–1393.
[96] C. Zhao, Q.-F. Sun, W. M. Hart-Cooper, A. G. DiPasquale, F. D. Toste, R. G. Bergman, K. N. Raymond, *J. Am. Chem. Soc.* **2013**, *135*, 18802–18805.
[97] D. M. Kaphan, F. D. Toste, R. G. Bergman, K. N. Raymond, *J. Am. Chem. Soc.* **2015**, *137*, 9202–9205.

Chapter 2

Synergistic non-covalent catalysis facilitates base-free Michael addition

Chapter 2 Synergistic Non-covalent Catalysis Facilitates Base-free Michael Addition

Parts of this chapter was published in J. Am. Chem. Soc. ***2020****, 142, 17743–17750.*

Computational experiments in this chapter were carried out by Tom A. Young and Dr Fernanda Duarte at the Chemistry Research Laboratory, University of Oxford, Mansfield Road, Oxford, OX1 3TA, UK.

2.1 Introduction

The organisation of charge within an active site, which selectively stabilises intermediates and transition states using electrostatic forces, is the basis for highly efficient enzyme catalysis.[1] This mode of reactivity provides a blueprint for developing synthetic catalysts that use only non-covalent interactions.[2][3][4] Self-assembled coordination cages are prime candidates for mimicking biological catalysts because (a) they provide a well-defined microenvironment distinct from the bulk phase, and (b) they invariably possess well-defined permanent charge. For reactions involving ionic species, cage catalysis can be categorised by whether a negatively charged catalyst stabilises cationic intermediates or the opposite. The former has been demonstrated by Raymond, Bergman, and Toste on numerous occasions, who used a dodeca-anionic gallium tetrahedron to catalyse reactions that involve various cationic intermediates, such as oxonium[5] and iminium species,[6] carbocations,[7] and positively charged transition metal complexes.[8]

Anionic coordination cages are relatively rare compared to the vast number of cationic coordination assemblies that are built from transition metal ions and neutral ligands.[9][10][11][12][13][14][15][16] It seems somewhat surprising then that reports of catalysis that involve the stabilisation of reactive anionic species within cationic cages are exceedingly rare.[17][18][19][20] There are several possible explanations for this apparent anomaly. Many cationic cage compounds are effective hosts because they bind apolar substrates in water using the hydrophobic effect, while the associated

anions are strongly hydrated and loosely associated with the cage periphery.[20] Unlike their cationic equivalents, anionic intermediates can also be strongly coordinating and thus have the potential to disrupt the cage structure. Finally, anionic intermediates – again unlike cations – are also likely to be less well stabilised by the flat aromatic surfaces that define the cavity of a typical coordination cage. It should be noted, though, that highly electron deficient aromatic systems can be used to achieve catalysis by the stabilisation of negatively charged intermediates, as exemplified by the work of Matile using organo-naphthodiimide and C_{60} structures.[21][22][23] While it is difficult to identify the precise reasons for the lack of anion-stabilising processes, what is clear is that being able to realise this apparently simple concept could open up the field of cage catalysis to a raft of new transformations, not least considering the plethora of C-C bond-forming reactions that involve the deprotonation of weakly acidic C-H compounds.

Furthermore, the majority of supramolecular catalysis examples investigate hydrolysis[5][26][18][20] or unimolecular processes such as rearrangement,[24][25] and ring-opening/closing reactions.[7][27][19][28][29][30] The rare research on bimolecular or multicomponent reactions has been limited to Diels-Alder additions with very few exceptions.[17][6][31] One possible explanation is that supramolecular structures are usually optimised to strongly bind one substrate, making it difficult to activate all the reagents. Paradoxically, though, increased effective molarity by simultaneously binding both substrates often leads to severe product inhibition, albeit accelerating the reactions. With the "sweet spot" between substrate activation, intermediates/transition state stabilisation and easy product release being unobvious, the supramolecular approach to facilitate more synthetically relevant bimolecular fusion reactions is currently lacking. Herein, I demonstrate the full effectiveness of anion stabilising using a simple cationic host system to catalyse Michael addition with remarkable efficiency.

2.2 Aims and objectives

The Lusby group has previously shown that simple Pd_2L_4 coordination cages,[12][13][14][15][16] like **C1** and **C2** (Figure 2-1), can act as highly efficient catalysts.[32][33][34] The catalytic properties of these cages do not stem from entropic effects, such as the dual encapsulation[35][36][37] or constrictive binding[24] mechanisms that have dominated earlier bioinspired approaches. Instead, the activity of **C1** and **C2** arises because they can enthalpically stabilise polar intermediates and transition states. This stabilisation is facilitated using large non-coordinating BArF counteranions, which are unable to access the cavity and leave a charge-dense interior that is Coulombically frustrated. Furthermore, the cationic Pd ions polarise the adjacent C-H bonds, creating pockets of H-bond donor atoms (Figure 2-1, shown in blue) that can provide additional interactions. The BArF counteranions also impart solubility in apolar solvents, such as dichloromethane, leading to a poorly solvated inner microenvironment, further increasing the recognition of polar, reactive intermediates. Conversely, traditional small non-coordinating anions such as BF_4, PF_6, and OTf bind tightly inside the cage, especially in apolar solvents, significantly reducing the affinity toward other species.[38] This work investigates reactions involving encapsulated anionic intermediates using **C1** or **C2** as catalysts, with Michael addition chosen as a representative reaction.

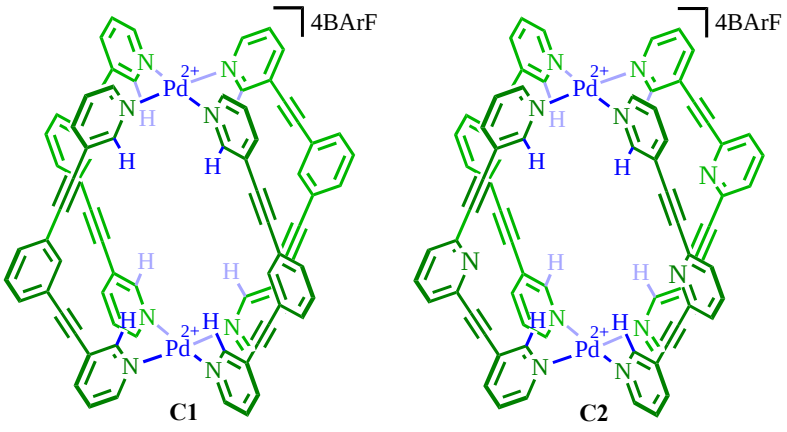

*Figure 2-1. Chemical structure of **C1** and **C2**. Large, non-coordinating BArF counteranions create a highly polar, coulombically frustrated cavity that can provide significant reactive intermediate and transition state stabilisation.*

2.3 Exploration on single substrate binding approach

It has previously been shown that **C1**/**C2** can encapsulate and electronically activate quinone type molecules through interactions with the polarised ortho-pyridyl C-H bonds.[38][32] Hence, quinones were initially chosen as Michael acceptors. The H-bond pockets of **C1** were also expected to bind and stabilise the oxyanion intermediate. Furthermore, an "entropically neutral" turnover step was envisaged, where one quinone would replace one product molecule (Figure 2-2a). This method was thought to be favourable and had successfully aided turnover in previous studies.[ii]

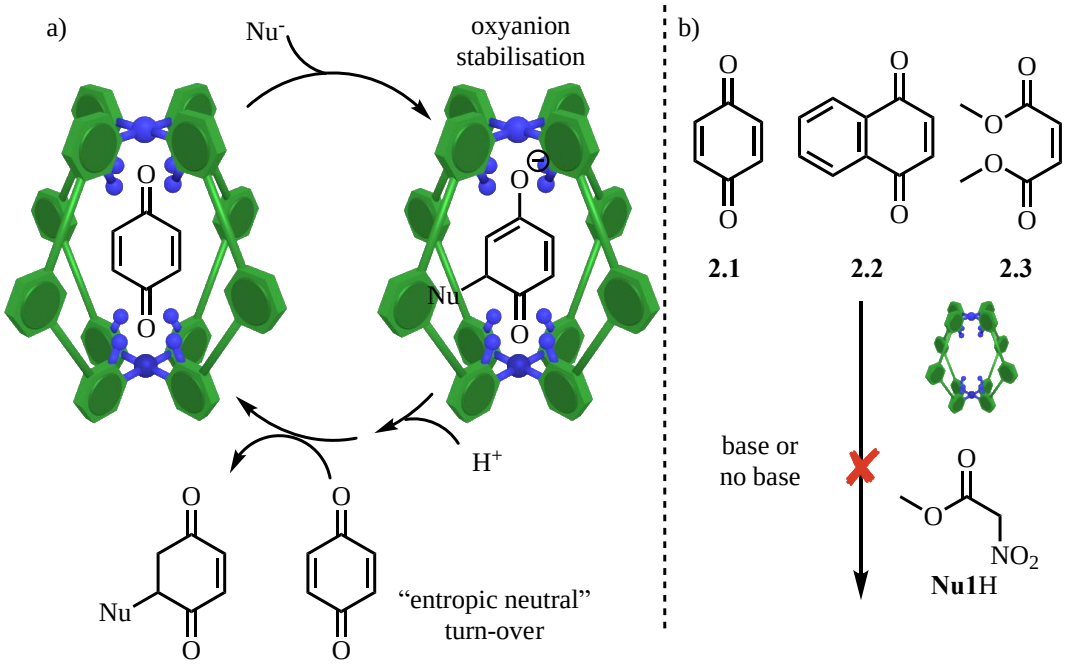

*Figure 2-2. a) Proposed mechanism of **C1** facilitated Michael addition of **2.1** and **Nu1H**. b) Complementary electrophile, weakly binding pro-nucleophile: no catalytic Michael addition.*

However, when reacting **2.1** or **2.2** and an acidic pro-nucleophile **Nu1**H (pK_a = 5.7)[39] with 20 mol% **C1**, no identifiable Michael addition products were observed. More disappointingly, even with an additional 10 mol% organic base, DBU (pK_a between

[ii] Single-species-to-single-species turnover will also be discussed in detail in Chapter 3.

11 and 12 for $DBUH^+$)[40][41], no 1,4-adduct was yielded. Similar results were found for guest **2.3**, where **C1** led to no reactivity between **2.3** and **Nu1**H, with or without DBU. However, the analysis of the NMR spectra shed light on the reason for the lack of catalysis. Upon addition of DBU, **C1** peaks split into two sets with the new ortho-pyridyl signal significantly deshielded. This is indicative of a strong binding guest that undergoes slow in-out kinetics with the cage. Given the reaction mixture's composition, the slow exchange species is likely to be **Nu1**$^-$⊂**C1**. With **2.3** peaks observed to shift back towards the unbound state (Figure 2-3), it is inferred that **Nu1**$^-$ simply displaces the bound electrophile rather than adding to the 1,4-position.

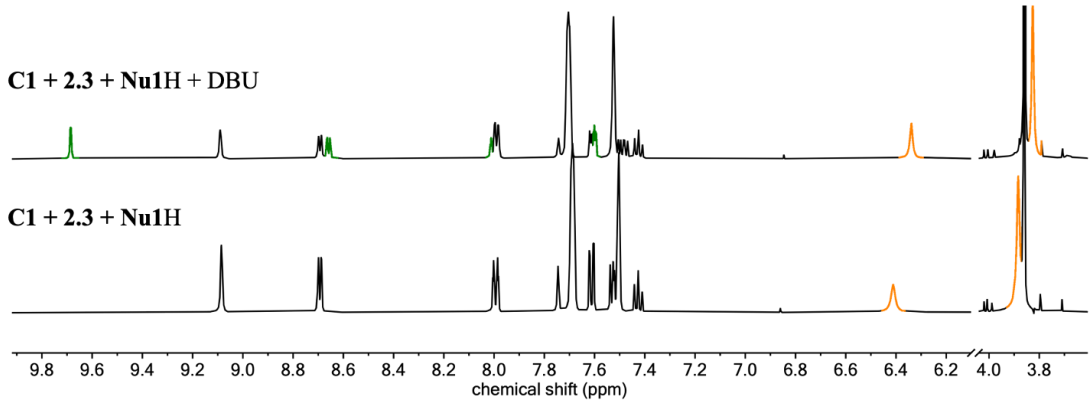

*Figure 2-3. ^1H NMR spectra (CD_2Cl_2, 500 MHz) of the reaction mixture of **2.3** and **Nu1**H with 20 mol% **C1** and 10 mol% DBU. Green: A second set of cage peaks was observed in the presence of DBU. Orange: Peask of **2.3** shift to the unbound state in the presence of DBU.*

Another approach was attempted where complementarily bound 1,3-dicarbonyl compounds were used as Michael donors. The positively charged cage was thought to facilitate the enolization of **2.4** and enhance its pro-nucleophilicity. The turnover step would involve the proton transfer between the neutral pro-nucleophile and the anionic intermediate (Figure 2-4a).

However, no Michael catalysis was observed for the reaction of **E1** and 20 mol% **C1** with **2.4**, **2.5** or **2.6**. ^{1}H NMR only showed one set of cage signals, indicating **2.4**$^-$⊂**C1** was generated at a concentration below the limit of detection for NMR. 10 mol% DBU was introduced to the reaction along with 20 mol% **C1** in order to investigate whether the low pro-nucleophilicity enhancement or the subsequent steps were responsible for the lack of reactivity. Even with increased concentration of nucleophilic anions,

evidenced by the slow exchange signals of **2.4**$^{-}$⊂**C1**, **2.5**$^{-}$⊂**C1** and **2.6**$^{-}$⊂**C1**, no catalytic 1,4-addition occurred. In fact, addition of **C1** appeared to inhibit the background reaction of **2.5** and **E1** with DBU, indicating the bound nucleophile is unreactive.

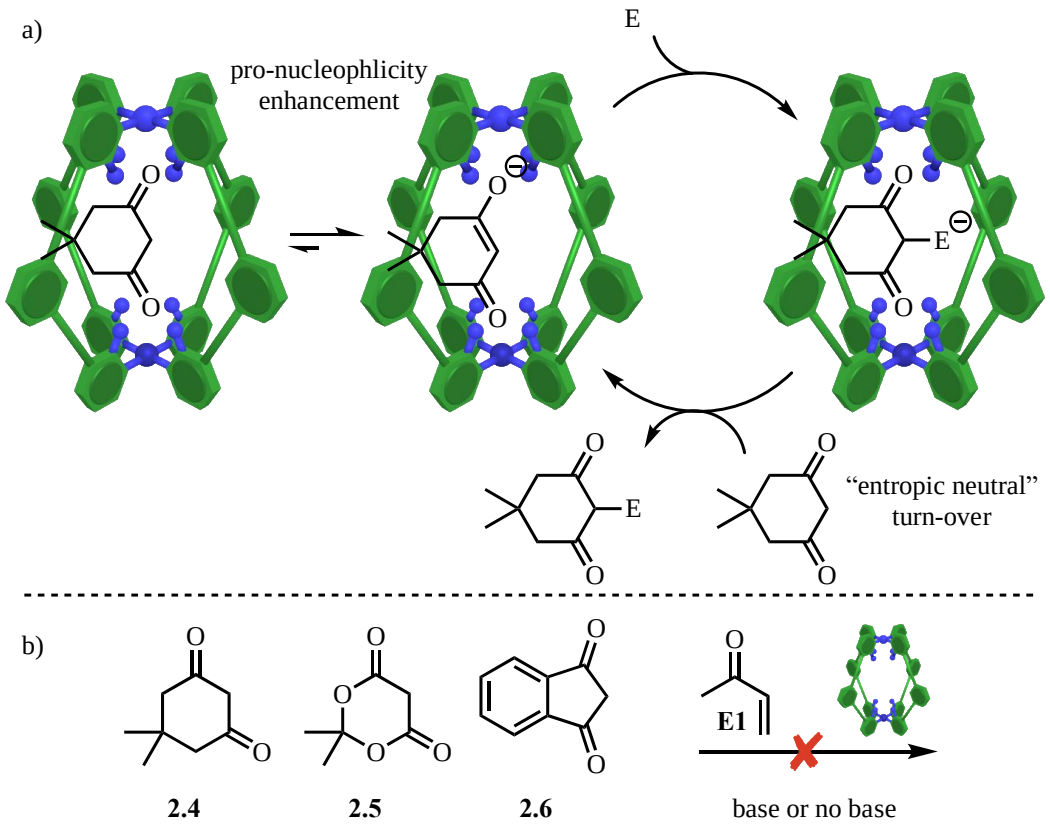

Figure 2-4. a) Proposed Michael addition catalysis via pro-nucleophile binding strategy. b) Complementary pro-nucleophile, weakly binding electrophile: no catalytic Michael addition.

These negative results led me to reconsider the strategy for discovering Michael addition reactivity. In both unsuccessful approaches, I tried to take advantage of the strong binding of complementary guests, either electrophile or pro-nucleophile, that interact with both H-bond pockets in **C1** (e.g. K_A = 8000 M^{-1} for **2.1** and K_A = 1100 M^{-1} for **2.3**). The lack of activity led me to reason that the dual interaction of both substrates might be necessary, such that I should expand the search to poorly complementary, weakly binding guests.

2.4 Catalysis by co-encapsulation of weak substrates

2.4.1 Enhancing pro-nucleophilicity through guest binding

Nu1H ($K_A \approx 30$ M^{-1}) and **E1** ($K_A < 30$ M^{-1}) were chosen as a pair because they are both small, weak guests that would hopefully allow simultaneous binding of both substrates in the cage. I was pleased to find that Michael product **P1** was formed when charging a mixture of **Nu1**H and **E1** with 20 mol% **C1** without any organic base (blue squares, Figure 2-5). A series of control reactions were performed in order to prove that the catalysis stems from the cage cavity. Firstly, no reaction occurred when only the substrates were combined, even after 150 hours. Secondly, no Michael adduct was observed when $Pd(pyridine)_4(BArF)_2$ was present, confirming the rate acceleration is unlikely due to Lewis acid catalysis by free Pd^{2+} ions. Furthermore, the introduction of a strong competitive binder ($K_A = 10^8$ M^{-1}) to the cage-mediated process completely halted the reaction, confirming that the catalytic properties stem from the microenvironment of **C1** rather than from the periphery of the cage or some other extraneous effect (Figure 2-5).

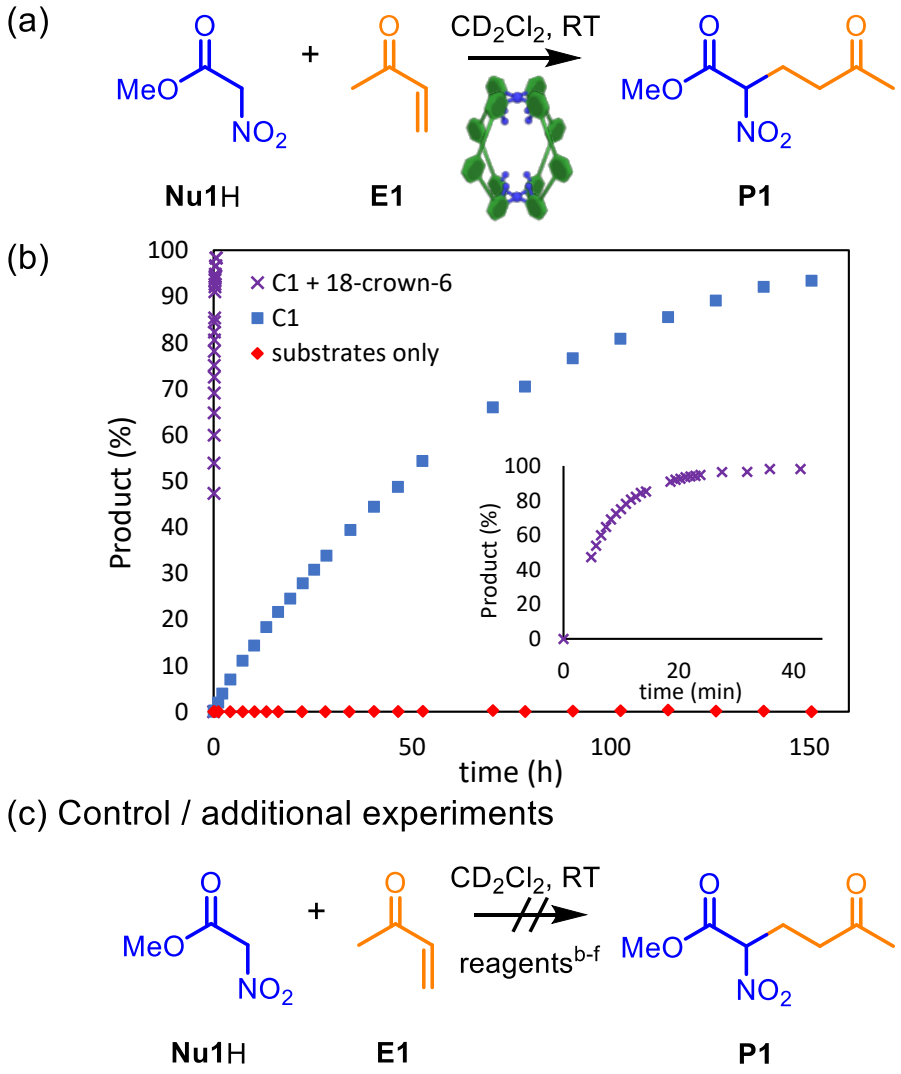

[b]**C1** + pentacenedione (Inhibitor, K_a = 10^8 M^{-1}); [c][Pd(pyridine)$_4$](BArF)$_2$; [d]**C2**; [e]18-crown-6 only; [f][Pd(pyridine)$_4$](BArF)$_2$ + 18-crown-6

Figure 2-5. Base-free Michael addition catalysis.[iii]

[iii] General reaction conditions: **C1** (0.25 mM, 20 mol%), **Nu1**H (12.5 mM), **E1**(2.5 mM), 18-crown-6 (2.5 mM), CD_2Cl_2, R.T.

Michael addition has been shown to proceed with transition metal Lewis acid catalysts without additional basic reagents.[42] **C1**, on the other hand, promotes the reaction of **Nu1**H and **E1** through the cavity rather than directly using the Pd^{2+} components. **C1** also does not bear any Brønsted basic functional group, in contrast to the small molecule H-bond catalysts.[43][44][45][46][47] This indicates that the residual H_2O in CD_2Cl_2 is likely to perform as the base to deprotonate **Nu1**H (Figure 2-6). However, this could not be tested directly due to the poor solubility of **C1** in anhydrous dichloromethane. It is interesting to note the pK_a values of **Nu1**H (+5.7) and H_3O^+ (–1.7). These values are measured in water, and the translation into CD_2Cl_2 needs to be treated with caution. Nonetheless, it is clear that the cage significantly increases the acidity of the pro-nucleophile through a combination of coulombic attraction and other H-bonding interactions.[48]

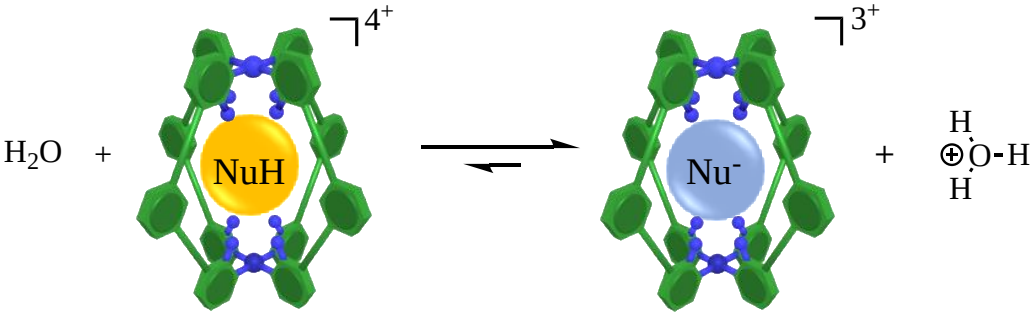

*Figure 2-6. Acidity enhancement by **C1**; H_2O serves as Brønsted base.*

Interestingly, the reaction of **Nu1**H and **E1** did not proceed with **C2**, a close structural analogue. As the driving force for pK_a shift is the coulombic encapsulation, it is reasonable to infer that **C1** has a higher affinity towards anions than **C2**. This hypothesis echoes the study that shows **C1** can increase the redox potential of quinone guests by stabilising semiquinone radical anions, whereas **C2** is inactive.[34] Electrostatic potential (ESP) analysis reveals that **C1** indeed displays a higher positive potential, while the central nitrogen lone pairs significantly neutralise the electric field within the central portion of **C2** (Figure 2-7**)**.

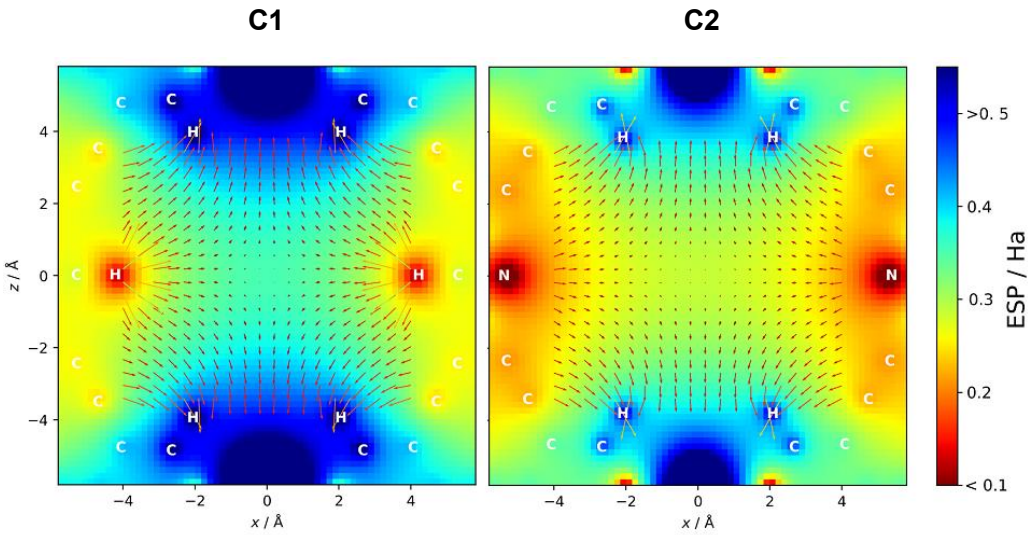

*Figure 2-7.Electrostatic potential (ESP) slices of cages **C1** and **C2** on the xz plane containing two opposing ligands and two metal centres. Positive values (red) indicate increases in the electron density, while negative values (blue) indicate electron density reductions. Arrows represent the electric field defined from negative to positive (∇ESP), and the length corresponds to the magnitude.*

2.4.2 Improving catalysis through synergistic activation

The base-free Michael addition catalysis with **C1** was also validated with another pro-nucleophile, benzoylnitromethane, **Nu2**H. The reaction of **Nu2**H and **E1** proceeded to completion under 70 hours. The faster reaction rate is in accordance with the higher acidity of **Nu2**H (pK_a = +5.0).[49]

However, attempts to expand the substrate scope to less acidic pro-nucleophiles and less reactive electrophiles were unsuccessful. Revisiting the acid-base equilibrium shown in Figure 2-6, it is clear that while coulombic attraction stabilises Nu$^-$⊂**C1**, the resulting hydronium ions are high in energy in an apolar environment: CD_2Cl_2. The negative charges are diffused across the BArF anions, and the stability of the loose ion pair of $H_3O^+BArF^-$ is likely the limiting factor of the acidification ability of **C1**. Although residual water and H_3O^+ molecules are likely to exist in lower energy clusters in CD_2Cl_2, it was hypothesised that the addition of the commercially available 18-crown-6 might provide stabilisation to the resultant hydronium ions[50][51][52] and shift the equilibrium towards the charge separated state (Figure 2-8).

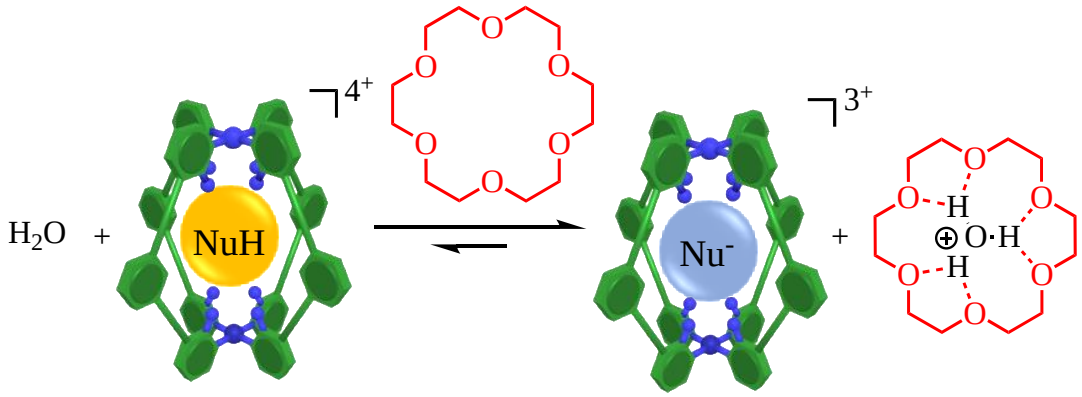

Figure 2-8. 18-crown-6 stabilises hydronium ion, lowering the energy of the whole system (considering both cage and the bulk phase).

It was exciting to observe that when **Nu1**H and **E1** were reacted with 20 mol% **C1** and one equivalent of 18-crown-6, the reaction time dramatically reduced from 150 hours to under 40 minutes. No product was formed after several days when 18-crown-6 was used as the sole catalyst, highlighting that synergistic binding of both charged species (i.e. **Nu1**$^-$ and H_3O^+) is essential for optimal catalysis. The control experiment with

the mononuclear complex, $Pd(pyridine)_4(BArF)_2$, and crown ether also gave no reactivity. Although $Pd(pyridine)_4(BArF)_2$ decomposed notably in the presence of 18-crown-6, it was clear that free Pd^{2+} and pyridine base did not contribute to the synergistic pro-nucleophile activation. **C1**, on the other hand, retained structural integrity when mixed with crown ether. The stability of **C1** is in accordance with the cooperativity displayed in the lantern-shaped architectures. Pentacenedione again inhibited the reaction with cage and crown ether, highlighting the necessity of the cavity (Figure 2-5). Interestingly, **C2** also showed latent catalytic activity to **Nu1**H and **E1** in the presence of 18-crown-6, albeit diminished (> 98% yield at 90 hours). This rate acceleration shows the hydronium stabilisation compensates for the weak acidity enhancement of **C2**, further supporting the collective activation paradigm.

The **C1**/18-crown-6 system was also tested on a preparative scale. After stirring **E1**, **Nu1**H, **C1** and 18-crown-6 at room temperature for 44 hours, 72 mg of **P1** was isolated at 91% yield, which is comparable to the NMR scale reaction. This result is particularly exciting as large-scale supramolecular catalysis is rare[53], and only as low as 2 mol% **C1** was used. Moreover, only a catalytic amount of 18-crown-6 was required (10 mol%), supporting that 18-crown-6 binds the one equivalent of H_3O^+ released by the formation of **Nu1**$^-$⊂**C1** (assuming the affinity of hydronium ions in 18-crown-6 is sufficiently high in CD_2Cl_2).

Armed with this combined non-covalent method, I turned to a wider scope (Scheme 2-1) of both different electrophiles (**E2-4**) and pro-nucleophiles (**Nu3-5**H). Methyl acrylate, **E2**, is seen as a challenging electrophile, much less reactive and difficult to activate than **E1**, yet product **P3** is generated in excellent yield under catalytic conditions. Also, products **P3-5** demonstrates that the cage can activate the electrophiles with a range of different functional groups. This functional group tolerance also applies to different pro-nucleophiles, with nitrile-containing **Nu4**H and **Nu5**H giving products **P7** and **P8**, also in excellent yields. It is also worth noting that pro-nucleophiles **Nu3-5** are significantly less acidic than either **Nu1**H or **Nu2**H based on their reported pK_a values (~10-11), further highlighting the remarkable acidification "power" of this combined non-covalent catalytic method.

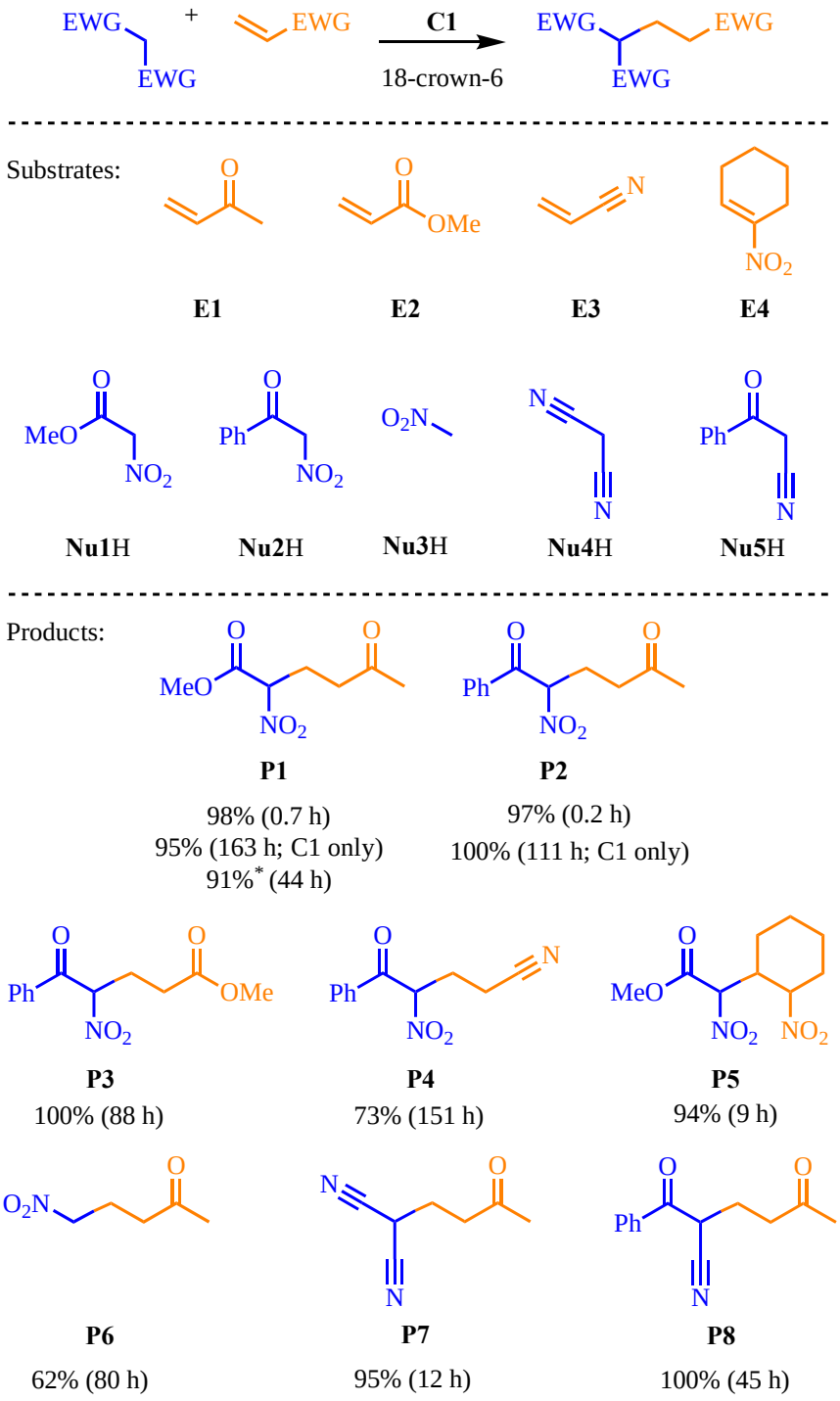

Scheme 2-1. Substrate scope for synergistic base-free Michael addition catalysis.[iv]

In order to further probe the role 18-crown-6 plays in the Michael addition catalysis, a few ether compounds were tested as cation stabilisers. 15-crown-5 has been shown to associate with hydronium ions to a lesser extent than 18-crown-6 due to its symmetry mismatch with H_3O^+.[54][55] THF, lacking the macrocyclic effect, is predicted to display even poorer hydronium stabilisation. As expected, reduced cation affinity led to diminished Michael addition catalysis. In the presence of **C1**, both model reactions (**Nu2**H/**E3** and **Nu5**H/**E1**) (Scheme 2-2) progressed slower with 15-crown-5 than 18-crown-6, and THF did not appear to contribute to the rate acceleration (Table 2-1).

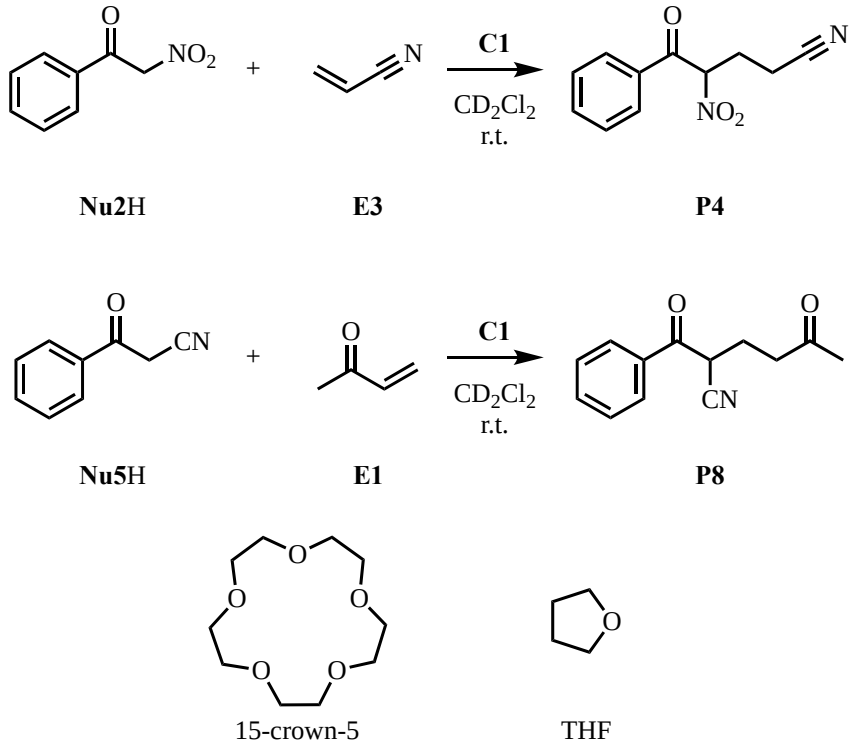

*Scheme 2-2. **C1** catalysed the formation of **P4** and **P8** and the chemical structure of 15-crown-5 and THF.*

[iv] Conditions: 0.5 mM **C1**, 2.5 mM 18-crown-6, 2.5 mM electrophile, 12.5 mM pro-nucleophile, CD_2Cl_2, R.T.. Yield determined by ^{1}H NMR spectroscopy. *isolated yield using **E1** (0.42 mmol), **Nu1**H (0.63 mmol), **C1** (8.4 μmol, 2 mol%), and 18-crown-6 (42 μmol, 10 mol%), CD_2Cl_2 (70 ml), R.T., 44 h.

*Table 2-1. Michael catalysis with **C1** and various hydronium ion stabilisers.*

Entry	Pro-nucleophile	Electrophile	Cage	Additive	Yield at t = 40 h
1	**Nu5**H	**E1**	**C1**	18-crown-6	> 98%
2	**Nu5**H	**E1**	**C1**	15-crown-5	19 %
3	**Nu5**H	**E1**	**C1**	THF	No reaction
4	**Nu2**H	**E3**	**C1**	18-crown-6	45 %
5	**Nu2**H	**E3**	**C1**	15-crown-5	14 %
6	**Nu2**H	**E3**	**C1**	THF	No reaction

The "power" of the combined activation can be further boosted by adjusting the proton carrier. Since **C1** and 18-crown-6 stabilise the charge separation, the limiting factor of the acid-base equilibrium shown in Figure 2-8 becomes the basicity of H_2O. Organic ammonium ions have also shown binding in 18-crown-6[56][57], and it is reasoned that using an amine instead of H_2O with **C1** can more effectively deprotonate mildly acid substrates. As aliphatic amines rapidly decompose the cage, aniline was chosen as an appropriate proton elicitor (Figure 2-9).

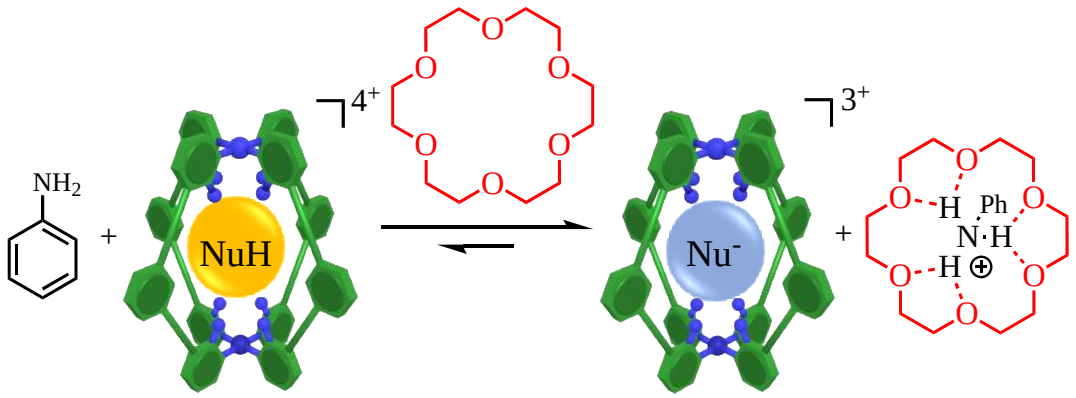

*Figure 2-9. **C1** enhances pro-nucleophlicity with aniline eliciting protons and 18-crown-6 stabilising the ammonium cation.*

As shown in Figure 2-10, **Nu3**H and **E1** did not react with just 10 mol% aniline and 20 mol% **C1**, and the conjugate addition was only initiated by adding 18-crown-6. This observation is consistent with the broadening of the aniline peaks (shown in red, Figure 2-10) upon the addition of the crown ether, which is attributed to the protonation of

the amine group and the binding of the resulting aminium ion. A significant enhancement of the catalysis was observed using the additional amine: the **C1**/18-crown-6/aniline catalysed reaction yielded 20% Michael product (orange, Figure 2-10) after 0.3 hours, and conversely, the **C1**/18-crown-6 promoted process only converted 2% after 1.3 hours. However, in the presence of aniline, side reactions were found to compete with the Michael addition. Although **C1**/18-crown-6 on their own only generate **P6** as the sole product, the addition of aniline led to the polymerisation of **E1** (product shown in pink), leaving the final yield of **P6** to be 20%. While the exact cause of the polymerisation remains unclear, some basic species is likely responsible. One plausible explanation is that with the synergistic acidification effect, the H_2O molecules bound in **C1** could be deprotonated by aniline and form free OH^-. The generation of hydroxide ions is also consistent with the slight disassembling of **C1** (free ligand shown in blue). **C1** is compatible with either aniline or 18-crown-6 on its own but degrades in the presence of both additives, possibly caused by the formation of a coordinating species, OH^- (Figure 2-11). Interestingly, cage degradation is more pronounced in the absence of a mildly acidic guest. OH^- ions likely have a higher affinity to Pd^{2+} whereas the carbanion Nu^- preferably binds in **C1** cavity. It is noteworthy that aniline alone is not basic enough to carry out the Michael addition, with its conjugate acid's pK_a equals 4.9.[58] However, a reasonably basic condition can be achieved through collective non-covalent interactions of benign reagents.

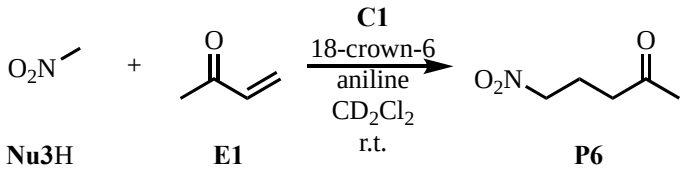

Scheme 2-3. ***C1****, 18-crown-6 and aniline catalysed reaction of* ***Nu3****H and* ***E1****.*

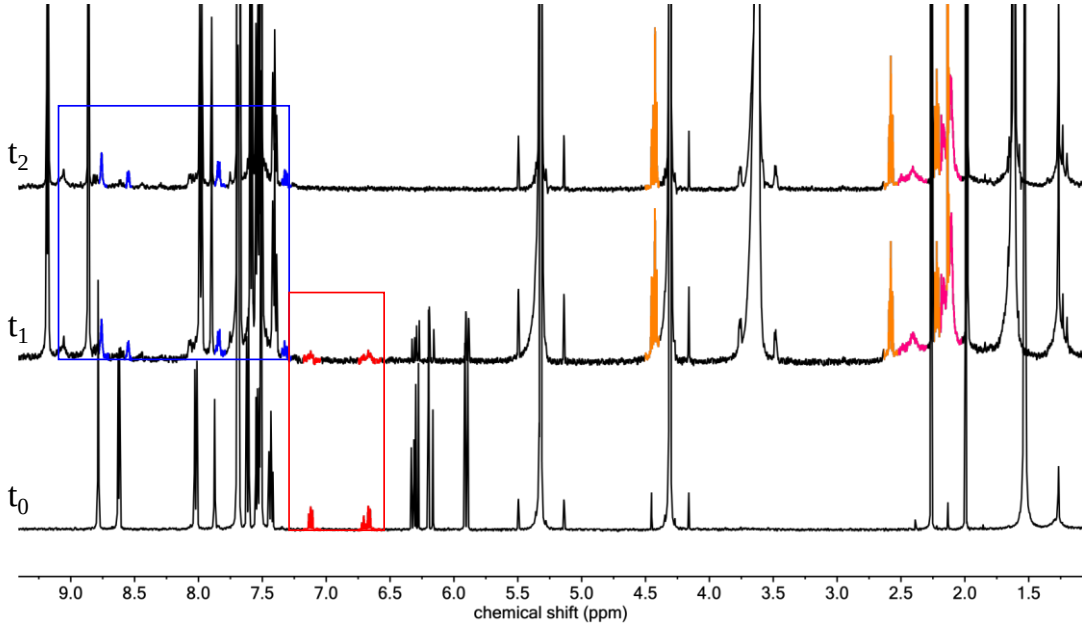

Figure 2-10. ^{1}*H NMR (*CD_2Cl_2*, 500 MHz) of the Michael addition of* ***Nu3****H and* ***E1****. Mixture components at* t_0*:* ***Nu3****H,* ***E1****,* ***C1*** *and aniline. Mixture components at* t_1 *(0.3 h) and* t_2 *(1.3 h):* ***Nu3****H,* ***E1****,* ***C1****, aniline and 18-crown-6. Species are coloured as follows: free ligand (blue), aniline (red),* ***P6*** *(orange) and oligomer (pink).*

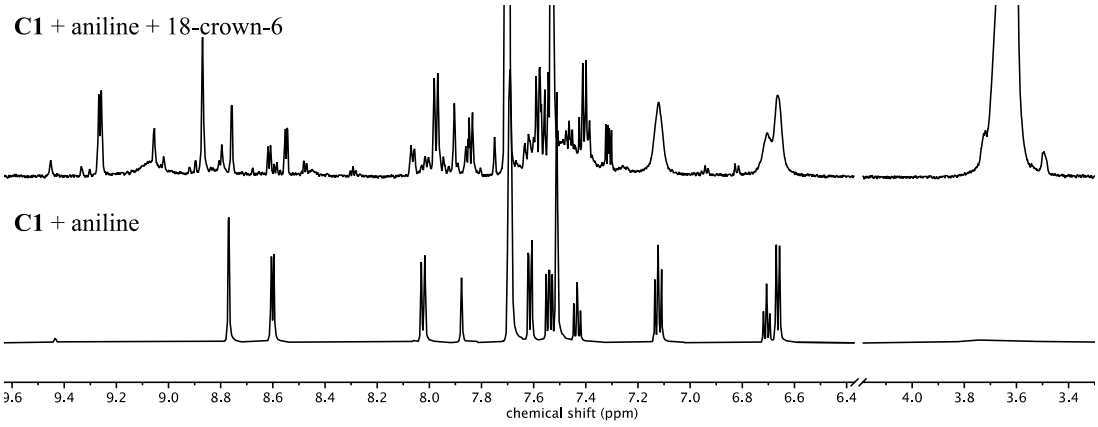

Figure 2-11. Significant degradation of ***C1*** *in the presence of only aniline and 18-crown-6.*

2.4.3 Advantages over traditional H-bond catalysts

In order to better evaluate the "power" of the **C1**/18-crown-6 system, a comparison was sought with other non-covalent catalysts. Surprisingly, there is virtually no literature relating to the catalytic formation of **P2-8**. In fact, **P3-5** and **P8** were previously unreported compounds whose identification was achieved by synthesising the authentic samples. No formation of **P2** under catalytic condition was found, and literature reported homogenous promotion of **P6-7** is large limited to the usage of aqueous media or metal catalysts.[59][60][61][62][63] However, a few examples have been described where the catalytic use of organic bases facilitated the formation of **P6** and **P1**. For example, Kisanga *et al.* observed that **P6** was generated at 78% yield in 0.15 hours using 10 mol% of a Verkade base (proazaphosphatrane) at -63 °C in isobutyronitrile.[64] Machetti and co-workers discussed the quantitative formation of **P1** with organic bases including DABCO, NMP, NMI and DBU (10 mol% catalyst, chloroform, 60 °C, 18 h).[65] Nevertheless, the most comparable non-covalent system is perhaps the bifunctional Brønsted-base-hydrogen-bond catalyst (Figure 2-12) discussed by the Vicario group. 2 mol% of the reported quinine-squaramide was sufficient to mediate the formation of **P1** at room temperature in toluene. However, it is noteworthy that this small molecule organic catalyst approach uses about two orders of magnitude higher concentrations compared to the **C1**/18-crown-6 system. As host-guest binding is largely affected by the substrate concentrations, it is appropriate to directly compare the **C1**/18-crown-6 system and organocatalyst under similar conditions.

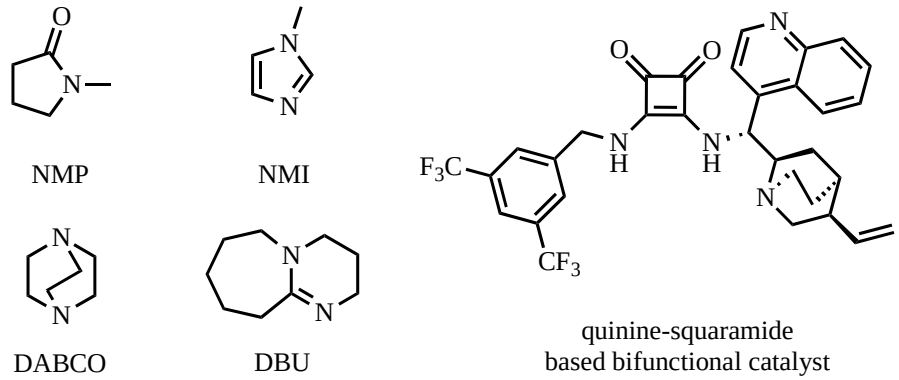

Figure 2-12. Chemical structures of organic bases (NMP, NMI, DABCO and DBU) and the bifunctional organocatalyst.

The reactivity of **Nu1**H and **E1** was tested with two representative small molecule non-covalent catalysts: a squaramide derivative **NC1** and the Schreiner's catalyst **NC2** (Scheme 2-4). No reaction occurred when **NC1**/**NC2** was used as the catalyst with or without 18-crown-6 (entry 5-8, Table 2-2), in contrast to the **C1** and **C1**/18-crown-6 systems. The lack of reactivity is attributed to the absence of pro-nucleophilicity enhancement in the traditional H-bond catalysts. Adding DBU, which is sufficiently basic (estimated pK_a of $DBUH^+$ is 12) to deprotonate **Nu1**H (pK_a = 5.7), to the H-bond catalysts does generate a small amount of **P1**. However, the yields with **NC1** or **NC2** and DBU are worse than that with DBU on its own (entry 9-11, Table 2-2). **NC2** also decomposes in the presence of DBU. Interestingly, the combination of 20 mol% **C1** and 10 mol% DBU is not only stable through the course of the reaction but also produces significant rate acceleration: 98% yield with **C1**/DBU compared to the 2% yield with only DBU at t = 1h (entry 11 and entry 12, Table 2-2). It is perhaps not surprising that adding DBU further speeds up the **C1** catalysed reaction (entry 12 and entry 1, Table 2-2). However, it is worth noting that the **C1**/18-crown-6 system performs almost the same as the **C1**/DBU catalyst (entry 3 and entry 12, Table 2-2), highlighting the high effectiveness of 18-crown-6 that is similar to a strong organic base.

Similarly, while **C2** alone does not promote the reaction of **Nu1**H and **E1**, the addition of 18-crown-6 or DBU provides a notable improvement in the reactivity (entry 2, 4 and 13, Table 2-2). Compared to the reaction with only DBU, **C2** also offers extra

acceleration, albeit to a lesser degree than **C1** (entry 3, 4, 12, and 13, Table 2-2). As DBU can deprotonate **Nu1**H anyway, the improved catalysis by **C1**/**C2** suggests that the cages may play a more prominent role than just enhancing the acidity of the pro-nucleophile.

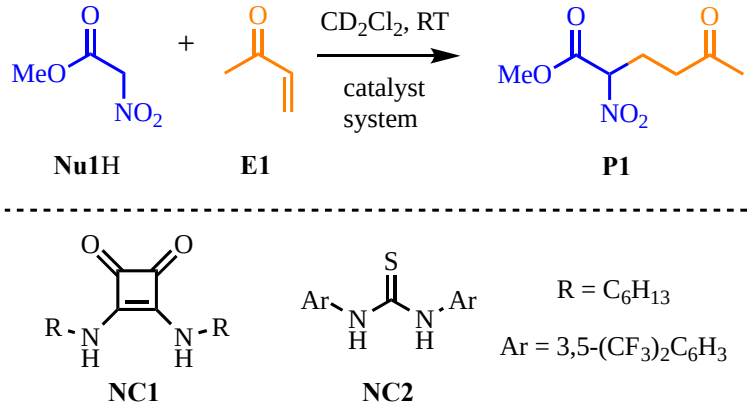

*Scheme 2-4. The reaction of **Nu1**H and **E1** and the chemical structures of non-covalent catalysts, **NC1** and **NC2** .*

*Table 2-2. Comparison of the **C1**/18-crown-6 method with other non-covalent catalyst systems.*[v]

Entry	Catalyst system	Yield at t = 1 h	Yield at t = 52 h
1	**C1**	2%	54%
2	**C2**	No reaction	No reaction
3	**C1**/18-crown-6	> 98%	> 98%
4	**C2**/18-crown-6	15%	95%
5	**NC1**	No reaction	No reaction
6	**NC2**	No reaction	No reaction
7	**NC1**/18-crown-6	No reaction	No reaction
8	**NC2**/18-crown-6	No reaction	No reaction
9	**NC1**/DBU	1%	38%
10	**NC2**/DBU	0%	15%
11	DBU	2%	44%
12	**C1**/DBU	> 98%	> 98%
13	**C2**/DBU	14%	80%

[v] Conditions: **Nu1**H (12.5 mM), **E1** (2.5 mM), catalyst (20 mol%), DBU (10 mol%), 18-crown-6 (2.5 mM), CD_2Cl_2 (500 µL). Yields determined by ^{1}H NMR spectroscopy.

2.4.4 Discussion on the origin of the Pd_2L_4 Michael catalysis

As discussed in the previous section, evidence suggests that **C1** plays more catalytic roles than substrate acidification and that simultaneous binding of both the nucleophile and electrophile is essential. It is possible that the binding sites in **C1** interact with the carbonyl group of **E1** and lower the LUMO of the electrophile in the same manner where H-bond catalysts act like Lewis acids.[66][44][32][38] The possibility of **C1** stabilising an "electron flow" is also considered. As discussed in section 2.3, when one of the substrates (nucleophile or electrophile) binds to both H-bond pockets, the Michael addition catalysis does not occur even though the formation of $Nu^-\subset$**C1** is observed. Take the reaction of **2.4** and **E1,** for example (Figure 2-13b), the nucleophilic attack requires electrons to flow away from the positively charged **C1** cavity, which is disfavoured. In contrast, the binding sites in **C1** are spaced almost perfectly to place the reactive centres of **Nu1**$^-$ and **E1** in close proximity. The electrons then could move from bound **Nu1**$^-$ to bound **E1**, moving from one charged Pd^{2+} pocket to the other (Figure 2-13a).

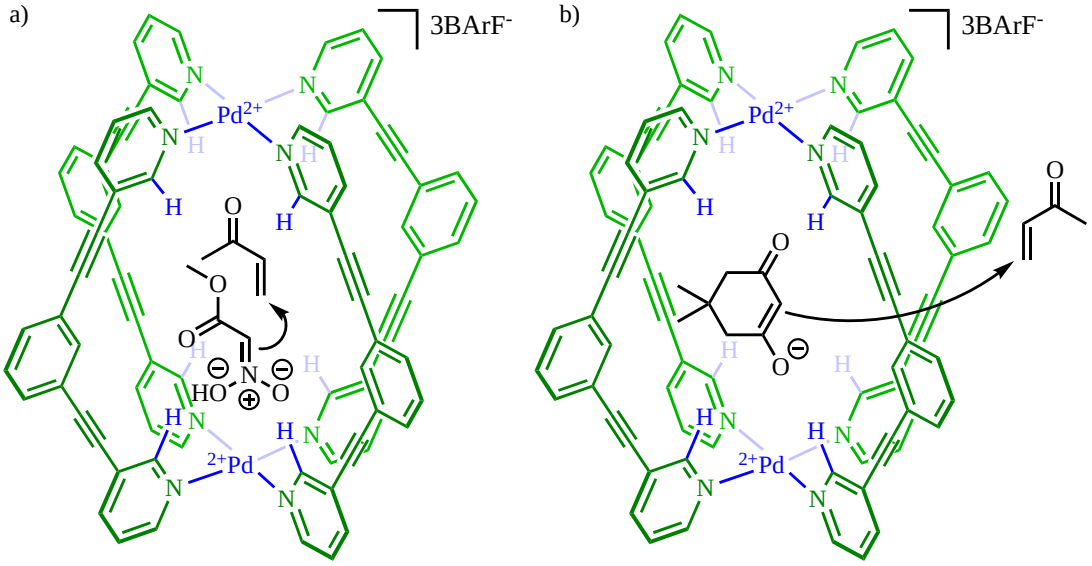

*Figure 2-13. a) Hypothesised co-encapsulation of **Nu**$^-$ and **E1**. b) Unfavoured electron flow away from positively charged **C1**.*

It is important to note that because remote substituents of the substrates can protrude into the cage windows between adjacent ligands, guest binding in **C1** is dominated by the complementarity of polar interactions rather than the overall size (this directly

contrasts many host systems where the proportion of the ratio of guest to host volume is thought to be key).[67] Hence, molecules with functional groups that interact with both H-bond sites simultaneously demonstrate the highest affinities (e.g. quinones). However, for the reactions successfully catalysed by **C1**/18-crown-6, all the reactive electrophiles have only one H-bond acceptor group, and the reactive pro-nucleophiles possess relatively weak H-bond accepting functionalities (nitro and nitrile)[68] that are misaligned for optimal binding (**Nu3**H, **Nu4**H and **Nu5**H). Although these substrates are considered to be poor guests, they all showed high reactivity. The resulting Michael adducts **P1**-**P8,** which bear a structural similarity to the transition states, fulfil complementarity to the two polar interacting sites in **C1**, and it is likely that **C1** catalyses their formation by stabilising the corresponding intermediates and/or transition state.

The complementary recognition of the Michael addition intermediates and/or transition states is further examined in detail using the reaction of **Nu1**H and **E1**. While the composing fragments **Nu1**H and **E1** weakly bind in **C1** ($K_A \leq 30$ M^{-1} for both compounds), **P1** displays a higher association constant of 150 M^{-1}due to its "bridging" of both H-bond sites. This indicates the preferential binding of the intermediates and/or transition states over the substrates. The binding mode of P1 ⊂ C1 also supports such intermediate/TS stabilisation observed in the crystal structures obtained by slow evaporation from dichloromethane. (Figure 2-14). Three H-bond acceptor groups from **P1** that originate from both **Nu1**H and **E1** are simultaneously located in the two binding sites. The nitro group occupies one pocket through four H-bonds, with the C-O distances range from 3.5 Å to 3.6 Å. The C-O distances between the ortho-pyridyl carbons and the keto oxygen are 3.2 Å and 3.3 Å, and the C-O distances are 3.3 Å and 3.4 Å from the ester group to the cage pocket. The H-bond network of **P1** ⊂ **C1** shows extremely high complementarity, and it strongly suggests that the Michael rate acceleration is realised by the recognitions of key reactive intermediates and/or transition states by polar interactions with **C1**. This is usually considered the hallmark of enzymatic reactivities and sets the cage promoted Michael reactions apart from the

many examples of supramolecular catalysis that rely on strong substrate binding.[17][18][19]

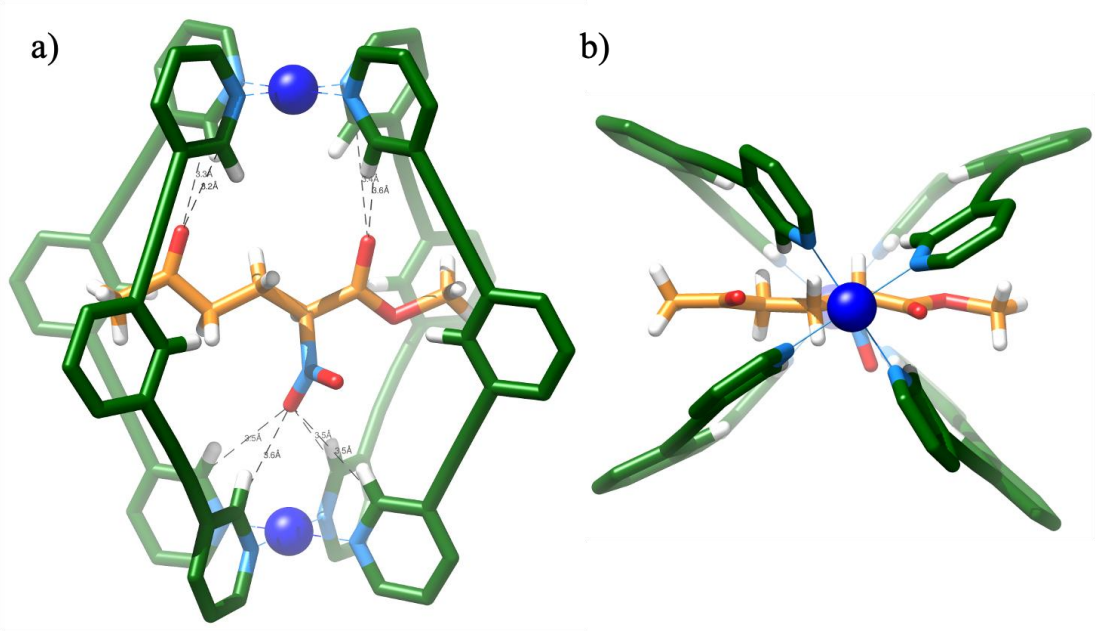

*Figure 2-14. X-ray crystallographic structure of **P1** ⊂**C1** with side view (a) and top view (b). Counteranions, solvent molecules, non-interaction protons and disorder omitted for clarity. Colour code: C of **C1**: green, C of **P1**: orange, N: light blue, Pd: blue, O: red, H: white.*

2.5 Stereoselectivity of cage promoted Michael addition reactions

Supramolecular catalysts have the potential to incur unusual reaction selectivity because their confined microenvironments can influence the substrates or transition states through steric or electronic effects. In the case of **C1**/18-crown-6 promoted Michael reactions, the combination of **Nu1**H and **E4** is particularly interesting. **P5** has three contiguous chiral centres and hence four diastereoisomers, **P5a-d**. When an organic base, DBU, was the catalyst, a mixture of an approximately equal amount of all four isomers was formed. In contrast, the reaction showed complete selectivity towards the anti- isomers when **C1** and 18-crown-6 were used.

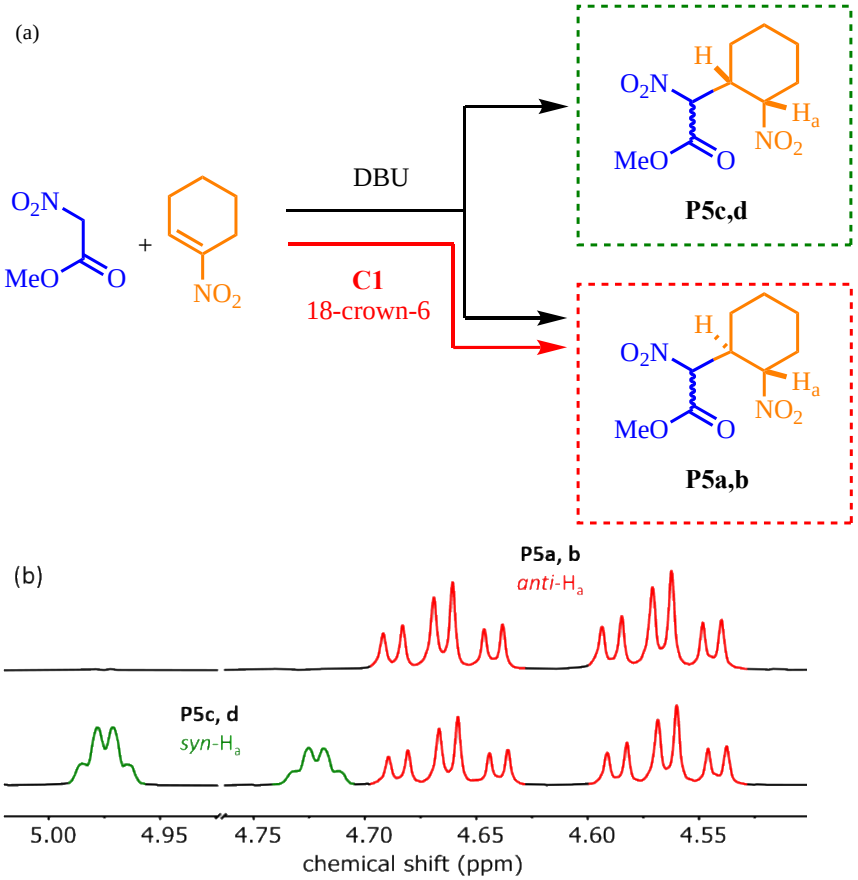

*Figure 2-15. (a) Diastereoselectivity with DBU or **C1**/18-crown-6 as catalysts. (b) partial ^{1}H NMR (CD_2Cl_2, 500 MHz) of the **Nu1**H/**E4** reaction mixture with (top) **C1**/18-crown-6 and with (bottom) DBU.*

The host-guest chemistry of **P5a-d** and **C1** was examined in order to investigate the driving force of the bias for the two anti-isomers. The separation of the four products proved to be challenging. Hence a pseudo titration was performed with a mixture of approximately 1:1:1:1 **P5a**,**b**,**c**,**d** that was obtained from a reaction solely catalysed by DBU. The partial ^{1}H NMR spectra shown in Figure 2-16 present the resonances most affected by binding to the H-bond pockets, namely the ortho-pyridyl protons of **C1** and H_a of **P5** (the cyclohexyl proton adjacent to the **E1** nitro group, shown in Figure 2-15). As the host concentration increases, signals of both **C1** and **P5** shift downfield, indicating the formation of **P5⊂C1** complex. It was observed that both **P5a,b** (anti-products) signals exhibited significant shift, whereas one of the syn-isomers, **P5c,d**, showed almost no interaction with **C1** (peak at *ca.* 4.97). Due to the solubility limit of **C1**, data with higher host equivalents was not obtained. Nevertheless, the qualitative host-guest analysis reveals that **C1** is able to recognise different P5 isomers selectively. This result is in good accordance with the calculated **P5⊂C1** energies at the SMD(DCM)-M06-2X/def2-TZVP//PBE0-D3BJ/def2-SVP level of theory, where encapsulation destabilises **P5c** and **P5d**, raising the energy relative to the lowest energy diastereoisomer from 2.3 kcal mol^{-1} and 6.3 kcal mol^{-1} to 2.4 kcal mol^{-1} and 8.8 kcal mol^{-1} respectively (Figure 2-17). The lowest energy orientation of the bound **P5** also supports the upfield shift in H_a signals because the cyclohexyl nitro group is shown to interact with **C1** through hydrogen bonding.

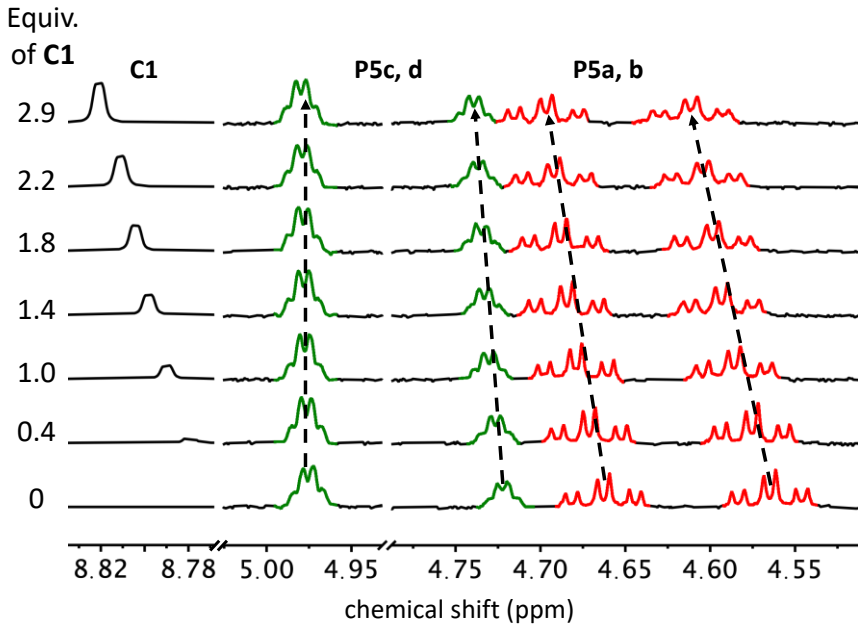

*Figure 2-16. Partial ^{1}H NMR (CD_2Cl_2, 500 MHz) spectra for the pseudo titration of **C1** into **P5a-d**. The intensity of **C1** peaks is normalised to match those of **P5**.*

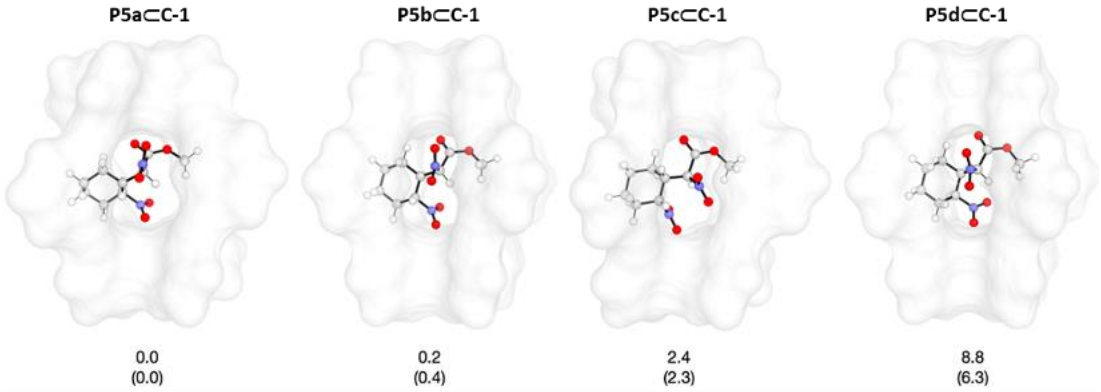

*Figure 2-17. Relative energies in kcal mol^{-1} and 3D geometries of **P5** diastereomers within **C1** calculated at the SMD(DCM)-M06-2X/def2-TZVP//PBE0-D3BJ/def2-SVP level of theory. Energies for unencapsulated species at the same level of theory are shown in parentheses.*

The bias in the binding of **P5a-d** led to the consideration of thermodynamic control in the diastereoselectivity. Thermodynamic effects were considered unlikely to be the reason because then a stoichiometric amount of **C1** would be required to achieve 100% anti selectivity, while catalytic loading of **C1** proved sufficient. In order to confirm this theory, experiments were carried out to probe the reversibility of **P5** formation and the possibility of interconversion between the syn and anti isomers. A mixture of **P5a-d** was added to a **C1**/18-crown-6 catalysed reaction of **Nu1**H and **E4** shortly after it started. New **P5a,b** compounds were exclusively generated, and no consumption of **P5c** or **P5d** was observed for up to 100 hours. Therefore, it was concluded that although **C1** can selectively recognise the anti isomers, the preference in **P5a,b** formation was not caused by thermodynamic effects.

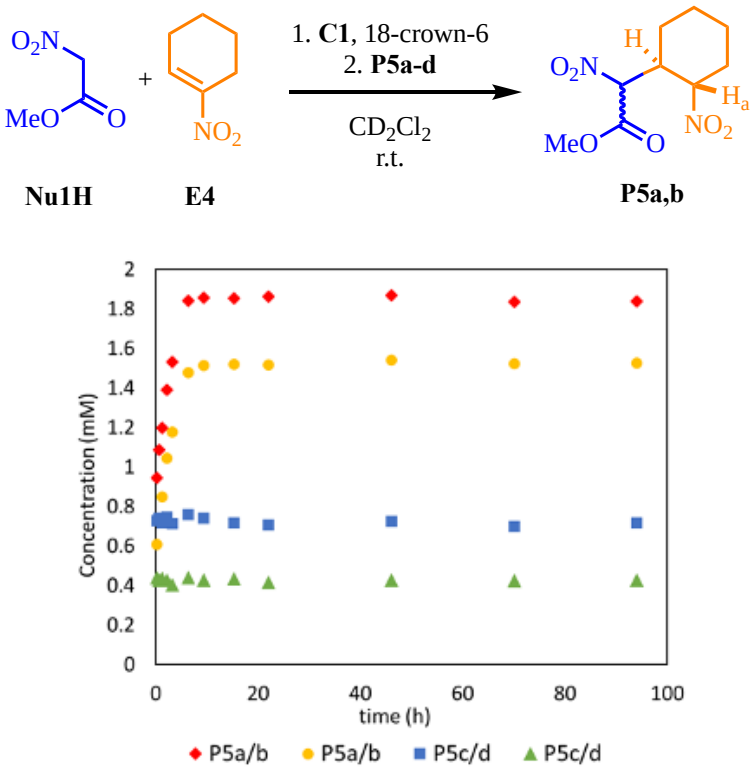

*Figure 2-18. Kinetic profiles of Michael addition between of nitromethylacetate **Nu1**H (12.5 mM) and 1-nitrocyclohexene **E4** (2.5 mM) with **C1** (0.5 mM) and 18-crown-6 (2.5 mM) with A mixture of **P5a-d** (**P5a/b**: 0.6 mM and 0.9 mM, **P5c/d**: 0.7 mM and 0.4 mM) introduced after reaction initiation. The concentration of **P5a/b**: red diamond and yellow circle. Concentration **P5c/d**: blue square and green triangle.*

The kinetic effects responsible for the diastereoselectivity were then considered, and the attention was focused on calculating the key intermediate **P5-I1**$^{-}$. **P5-I1**$^{-}$ undergoes epimerisation at the nitronate group on the central C6 ring, and it exists as one diastereoisomeric pair and four enantiomers: **P5-Ia1**$^{-}$ (*R*,*R*) and **P5-Ia'1**$^{-}$ (*S*,*S*); **P5-Ib1**$^{-}$ (*R*,*S*) and **P5-Ib'1**$^{-}$ (*S*,*R*). Each diastereoisomer has the nitroester-methine group either at the pseudoequatorial (**P5-Ia1**$^{-}$ and **P5-Ib1**$^{-}$) or pseudoaxial positions (**P5-Ia'1**$^{-}$ and **P5-Ib'1**$^{-}$). As unbound species, the two conformations of the two diastereoisomers have similar stability, with the largest difference to be 3.5 kcal mol^{-1}. In the presence of **C1**, however, four **P5-I1**$^{-}$ intermediates show a significantly larger energy spread. Compared to the most favoured conformation, **P5-Ib'1**$^{-}$**⊂C1**, the energy calculated for **P5-Ib1**$^{-}$**⊂C1** is 12.8 kcal mol^{-1} higher. This destabilisation is rationalised with the loss of an O···H–C interaction between the ester group and **C1** binding sites. Even **P5-Ia1**$^{-}$**⊂C1**, the second stable bound species is 4.8 kcal mol^{-1} higher in energy than **P5-Ib'1**$^{-}$**⊂C1**; hence it is inferred that the possible pathway is to go through **P5-Ib'1**$^{-}$**⊂C1**.

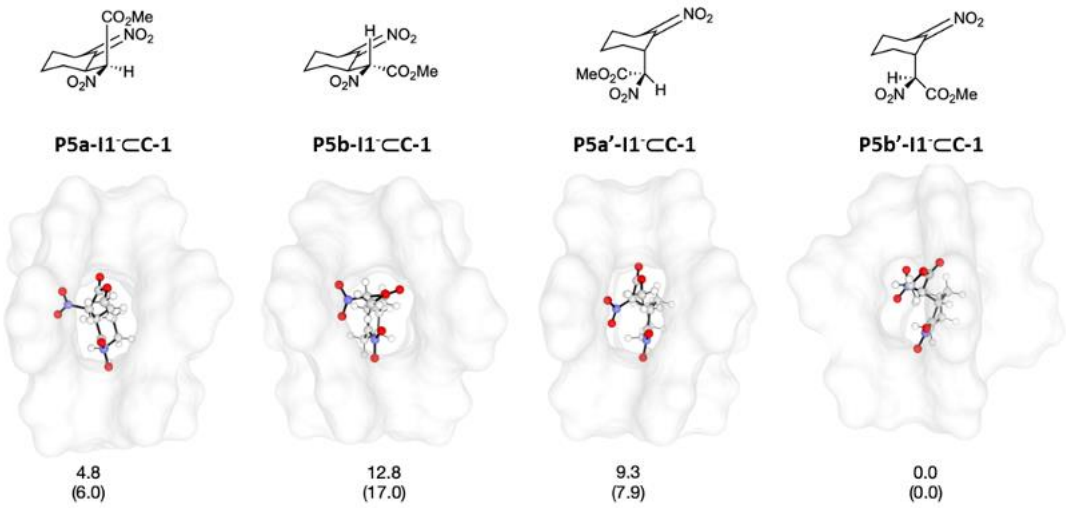

*Figure 2-19. Relative energies in kcal mol-1 and 3D geometries of the **P5-I1**$^{-}$**⊂ C1** intermediate complexes, calculated at the SMD(DCM)-M06-2X/def2-TZVP//PBE0-D3BJ/def2-SVP level of theory.*

Examination of **P5-Ib'1**$^{-}$**⊂C1** reveals the origin of the anti isomer bias in the **C1** catalysed reaction of **Nu1**H and **E4**. With the nitroester-methine group adopting the

pseudoaxial position, the acid proton (alpha- to both the nitro and ester group) is delivered to the nitronate from the same face, generating **P5-I2**$^-$ solely in the configuration where two cyclohexyl C-H bonds are in anti- positions. Further calculation reveals that such proton transfer is likely mediated by H_2O (21.7 kcal mol^{-1}) rather than going through a four-membered ring transition state. Note that the water-assisted proton transfer process was calculated for the unbound reaction due to the difficulty of locating the transition state in **C1** (composed of ~100 atoms including Pd^{2+} ions). Interestingly, the proton transfer from **P5-I1**$^-$ to **P5-I2**$^-$ causes planarization at the nitroester-methine group, meaning any stereoselectivity in the nucleophilic attack step will not be represented in the final product. It is also inferred that the protonation of P**5-I2**$^-$ to give **P5** is not stereoselective, for both anti isomers were observed in a roughly 1:1 ratio.

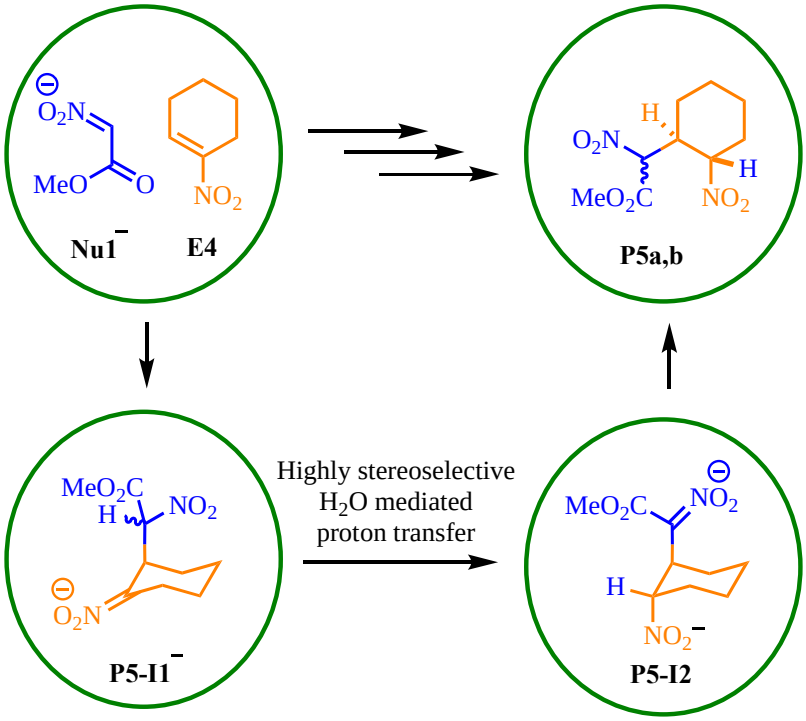

Figure 2-20. Stereoselectivity catalytic pathway. Initial H_2O proton transfer would generate the observed anti diastereoselectivity.

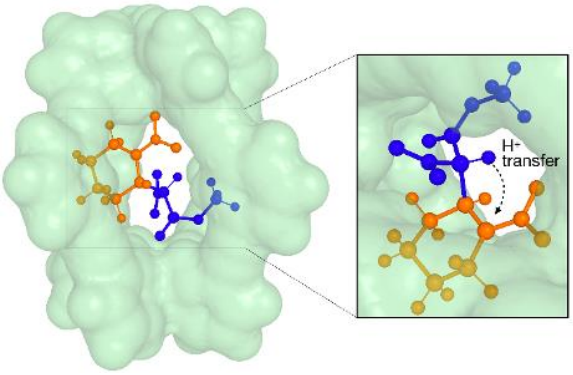

Figure 2-21. Most stable encapsulated diastereomeric conformer of ***P5-I1***$^{-}$ *calculated at the SMD(DCM)-M06-2X/def2-TZVP//PBE0-D3BJ/def2-SVP level of theory.*

2.6 **Conclusion**

Michael addition has been successfully demonstrated to be promoted by a simple Pd_2L_4 architecture. This approach marks a significant step in supramolecular catalysis in that it achieves rate acceleration through anion stabilisation which is exceedingly rare despite the prevalence of cationic cages. Furthermore, **C1** does not possess any Brønsted basic functionalities or metal Lewis acid, making the condition relatively mild. The introduction of a second macrocyclic receptor, 18-crown-6, significantly enhances the "power" of this cage catalysis method by providing synergistic stabilisation of the charge separation state.

Unlike most supramolecular catalysts based on strong guest encapsulation, the **C1**/18-crown-6 method demonstrates high activity with a broad scope of poorly binding substrates while showing no reaction promotion towards strong guests. The successful combinations of nucleophiles and electrophiles are those which yield products able to bridge both binding sites of **C1**, indicating the catalytic behaviour stems from the recognition of the key intermediates and/or the transition states. The preference in binding specific intermediate conformers also leads to a highly diastereoselective pathway, demonstrating the advantage of catalysis in a confined space.

2.7 Experimental

2.7.1 General information

2.7.1.1 Materials and methods

Unless otherwise stated, all reagents and solvents were purchased from Alfa Aesar, VWR, Fluorochem or Sigma Aldrich and used without further purification. Column chromatography was carried out using Geduran Si60 (40-63 μm) as the stationary phase and TLC was performed on precoated Kieselgel 60 plates (0.20 mm thick, 60F254. Merck, Germany) and observed under UV light at 254 nm. All reactions were carried out under air and at room temperature, unless otherwise stated.

All ^{1}H and ^{13}C NMR spectra were recorded on either a 500 MHz Bruker AV III equipped with a DCH cryo-probe (Ava500), a 400MHZ Bruker AV III equipped with BBFO+ probe (Ava400), a 500 MHz Bruker AV IIIHD equipped with a Prodigy cryo-probe (Pro500) or a 600 MHz Bruker AV IIIHD equipped with a TCI cryo-probe (Ava600) at a constant temperature of 300 K. Chemical shifts are reported in parts per million. Coupling constants (J) are reported in hertz (Hz). Standard abbreviations indicating multiplicity were used as follows: m = multiplet, q = quartet, t = triplet, d = doublet, s = singlet. All analysis was performed with MestReNova, Version 14.0.0. All assignments were confirmed using a combination of COSY, NOESY, HMBC and HSQC NMR spectra.

2.7.1.2 Synthesis

Cages **C1** and **C2** were synthesized according to known literature procedures.[38]

2.7.2 Michael addition reactions monitoring

2.7.2.1 General procedure for monitoring Michael addition reactions using 1H NMR Spectroscopy

Prior to NMR scale reactions, starting materials were purified as follows: Methyl vinyl ketone **E1**, methyl acrylate **E2**, acrylonitrile **E3**, 1-nitrocyclohexene **E4** and nitromethane **Nu3**H were purified by distillation. Malononitrile **Nu4**H and nitromethylacetate **Nu1**H were purified by silica plug (eluent: CH_2Cl_2).

Benzoylnitromethane **Nu2**H and benzoylacetonitrile **Nu5**H were recrystallized from ^{i}PrOH. 18-crown-6 was purified by sublimation.

For catalysis reactions using **C1** or **C2** with 18-crown-6: To an NMR tube was introduced a solution containing the cage compound (450 µL of a 0.56 mM CD_2Cl_2 stock solution), the Michael donor (20 µL of a 312.5 mM CD_2Cl_2 stock solution), the Michael acceptor (10 µL of a 125 mM CD_2Cl_2 stock solution), and the internal standard tetrakis(trimethylsilyl)silane (10 µL of a 15.6 mM CD_2Cl_2 stock solution). The Michael addition was started by the addition of 18-crown-6 (10 µL of a 125 mM CD_2Cl_2 stock solution).

For catalysis reactions using **C1** or **C2** with DBU: To an NMR tube was introduced a solution containing the cage compound (450 µL of a 0.56 mM CD_2Cl_2 stock solution), the Michael donor (20 µL of a 312.5 mM CD_2Cl_2 stock solution), the Michael acceptor (10 µL of a 125 mM CD_2Cl_2 stock solution), and the internal standard tetrakis(trimethylsilyl)silane (10 µL of a 15.6 mM CD_2Cl_2 stock solution). The Michael addition was started by the addition of DBU (10 µL of a 12.5 mM CD_2Cl_2 stock solution).

For reactions with only 18-crown-6: To an NMR tube was introduced a solution containing 450 µL CD_2Cl_2), the Michael donor (20 µL of a stock solution 312.5 mM in CD_2Cl_2), the Michael acceptor (10 µL of a stock solution 125 mM in CD_2Cl_2), and the internal standard tetrakis(trimethylsilyl)silane (10 µL of a stock solution 15.6 mM in CD_2Cl_2). 18-crown-6 (10 µL of a 125 mM CD_2Cl_2 stock solution) was added last.

For reactions with only DBU: To an NMR tube was introduced a solution containing 450 µL CD_2Cl_2, the Michael donor (20 µL of a stock solution 312.5 mM in CD_2Cl_2), the Michael acceptor (10 µL of a stock solution 125 mM in CD_2Cl_2), and the internal standard tetrakis(trimethylsilyl)silane (10 µL of a stock solution 15.6 mM in CD_2Cl_2). The Michael addition was started by the addition of DBU (10 µL of a 12.5 mM CD_2Cl_2 stock solution).

For reactions with only **C1** or **C2**: To an NMR tube was introduced a solution containing the cage compound (450 µL of a 0.56 mM CD_2Cl_2 stock solution), the

Michael donor (20 µL of a 312.5 mM CD_2Cl_2 stock solution), the Michael acceptor (10 µL of a 125 mM CD_2Cl_2 stock solution), and the internal standard tetrakis(trimethylsilyl)silane (10 µL of a 15.6 mM CD_2Cl_2 stock solution). The solution was made up to 500 µL by the addition of 10 µL CD_2Cl_2.

For reactions with substrates only: To an NMR tube was introduced a solution containing 460 µL CD_2Cl_2, the Michael donor (20 µL of a stock solution 312.5 mM in CD_2Cl_2), the Michael acceptor (10 µL of a stock solution 125 mM in CD_2Cl_2), and the internal standard tetrakis(trimethylsilyl)silane (10 µL of a stock solution 15.6 mM in CD_2Cl_2).

For competitive inhibition reactions: To an NMR tube was introduced a solution containing the cage compound (450 µL of a 0.56 mM CD_2Cl_2 stock solution). Pentacenedione (0.4 mg, 1.29 µmol) was added as solid to the NMR tube prior to the addition of the Michael acceptor (10 µL of a 125 mM CD_2Cl_2 stock solution), the Michael donor (20 µL of a 312.5 mM CD_2Cl_2 stock solution), the internal standard tetrakis(trimethylsilyl)silane (10 µL of a 15.6 mM CD_2Cl_2 stock solution) and 10 µL CD_2Cl_2.

For reactions showing stereoselectivity: To an NMR tube was introduced 440 µL CD_2Cl_2, the Michael donor (10 µL of a stock solution 2.5 M in CD_2Cl_2), the Michael acceptor (20 µL of a stock solution 250 mM in CD_2Cl_2), and the internal standard tetrakis(trimethylsilyl)silane (10 µL of a stock solution 15.6 mM in CD_2Cl_2). For the **C1**/18-crown-6 catalyzed reactions, the cage compound (2.4 mg, 0.5 µmol, added as solid), 18-crown-6 (10 µL of a 500 mM CD_2Cl_2 stock solution) and another 10 µL CD_2Cl_2 were added. For the DBU control reactions, DBU (20 µL of a 50 mM CD_2Cl_2 stock solution) was added.

For re-introducing **P5a-d** into an ongoing kinetic experiment: To an NMR tube was introduced a solution containing CD_2Cl_2 (430 µL), the cage compound **C1** (1.2 mg, 0.25 µmol, added as solid), the Michael donor (20 µL of a 312.5 mM CD_2Cl_2 stock solution), the Michael acceptor (10 µL of a 125 mM CD_2Cl_2 stock solution), and the internal standard tetrakis(trimethylsilyl)silane (10 µL of a 15.6 mM CD_2Cl_2 stock

solution). The Michael addition was started by the addition of 18-crown-6 (10 µL of a 125 mM CD_2Cl_2 stock solution). A mixture of **P5a-d** (20 µL of a 72 mM CD_2Cl_2 stock solution) was added to the same NMR sample after the initiation of the reaction.

For reactions with only $[Pd(py)_4](BArF)_2$: To an NMR tube was introduced a solution containing 440 µL CD_2Cl_2, the Michael donor (20 µL of a stock solution 312.5 mM in CD_2Cl_2), the Michael acceptor (10 µL of a stock solution 125 mM in CD_2Cl_2), and the internal standard tetrakis(trimethylsilyl)silane (10 µL of a stock solution 15.6 mM in CD_2Cl_2). $[Pd(py)_4](BArF)_2$ (20 µL of a 12.5 mM CD_2Cl_2 stock solution) was added last.

For reactions with $[Pd(py)_4](BArF)_2$ and 18-crown-6: To an NMR tube was introduced a solution containing 430 µL CD_2Cl_2, the Michael donor (20 µL of a stock solution 312.5 mM in CD_2Cl_2), the Michael acceptor (10 µL of a stock solution 125 mM in CD_2Cl_2), the internal standard tetrakis(trimethylsilyl)silane (10 µL of a stock solution 15.6 mM in CD_2Cl_2) and $[Pd(py)_4](BArF)_2$ (20 µL of a 12.5 mM CD_2Cl_2 stock solution). 18-crown-6 (10 µL of a 125 mM CD_2Cl_2 stock solution) was added last.

For reactions with only Squaramide **NC1** or Schreiner's catalyst **NC2**: To an NMR tube was introduced a solution containing 440 µL CD_2Cl_2, the Michael donor (20 µL of a stock solution 312.5 mM in CD_2Cl_2), the Michael acceptor (10 µL of a stock solution 125 mM in CD_2Cl_2) and the internal standard tetrakis(trimethylsilyl)silane (10 µL of a stock solution 15.6 mM in CD_2Cl_2). Squaramide **NC1** or Schreiner's catalyst **NC2** (20 µL of a 12.5 mM CD_2Cl_2 stock solution) was added last.

For reactions with Squaramide **NC1** or Schreiner's catalyst **NC2** and 18-crown-6: To an NMR tube was introduced a solution containing 430 µL CD_2Cl_2, the Michael donor (20 µL of a stock solution 312.5 mM in CD_2Cl_2), the Michael acceptor (10 µL of a stock solution 125 mM in CD_2Cl_2), the internal standard tetrakis(trimethylsilyl)silane (10 µL of a stock solution 15.6 mM in CD_2Cl_2) and Squaramide **NC1** or Schreiner's catalyst **NC2** (20 µL of a 12.5 mM CD_2Cl_2 stock solution). 18-crown-6 (10 µL of a 125 mM CD_2Cl_2 stock solution) was added last.

For reactions with Squaramide **NC1** or Schreiner's catalyst **NC2** and DBU: To an NMR tube was introduced a solution containing 430 µL CD_2Cl_2, the Michael donor (20 µL of a stock solution 312.5 mM in CD_2Cl_2), the Michael acceptor (10 µL of a stock solution 125 mM in CD_2Cl_2), the internal standard tetrakis(trimethylsilyl)silane (10 µL of a stock solution 15.6 mM in CD_2Cl_2) and Squaramide **NC1** or Schreiner's catalyst **NC2** (20 µL of a 12.5 mM CD_2Cl_2 stock solution). DBU (10 µL of a 12.5 mM CD_2Cl_2 stock solution) was added last.

All the reactions were kept at 298 K and ^{1}H NMR spectra were recorded at regular intervals until sufficient data was collected. Kinetic NMR data were processed using the MestreNova 14.0.0 software and the concentrations of all chemical species were determined using NMR integration against the internal standard at each reaction time point.

2.7.2.2 Product Identification

The products of each NMR scale reaction were identified by comparing the spectra to either previously reported ^{1}H NMR spectroscopic data or to the data obtained from authentically synthesised products (data see section 2.7.6).

The literature data for **P6** is found in the following source[69]:

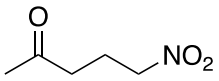

J. Am. Chem. Soc. **2017**, 139, 8110-8113

2.7.3 Substrate scope and NMR scale reaction yields

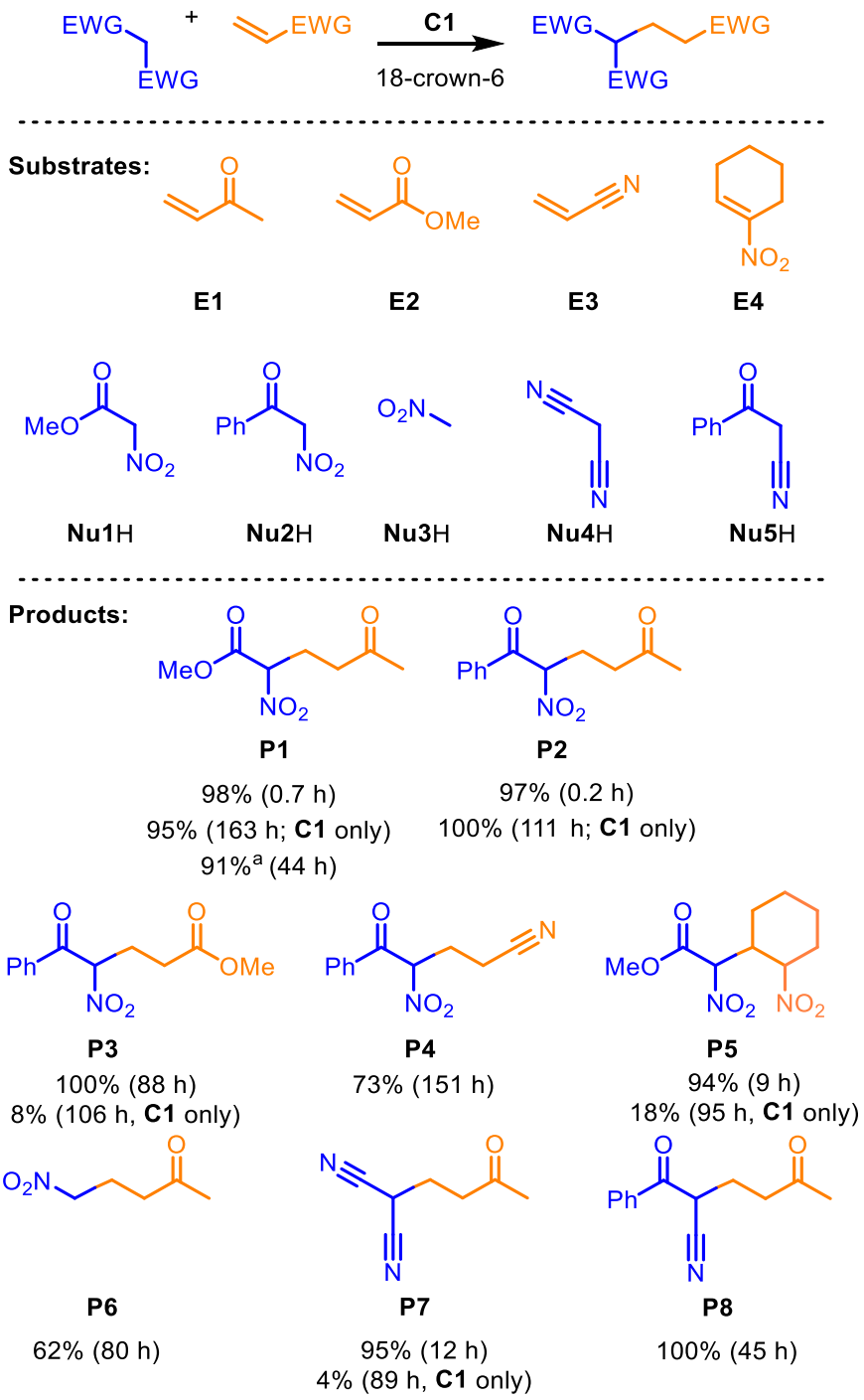

*Figure 2-22. Cage catalyzed Michael reaction substrate scope and NMR scale reaction yields under the following conditions: 0.5 mM **C1**, 2.5 mM 18-crown-6, 2.5 mM Michael acceptor, 12.5 mM Michael donor, CD_2Cl_2, r.t.. Yield determined by ^1H NMR spectroscopy integration against internal standard, tetrakis(trimethylsilyl)silane. aIsolated yield using 2 mol% **C1**, 10 mol% 18-crown-6, CH_2Cl_2, r.t, 44 h.*

2.7.4 Kinetic profiles of Michael addition reactions

2.7.4.1 Michael addition between nitromethylacetate Nu1H and methyl vinyl ketone E1 with C1

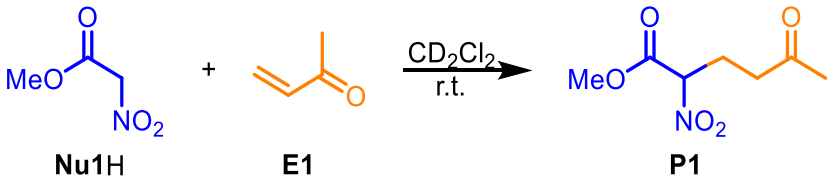

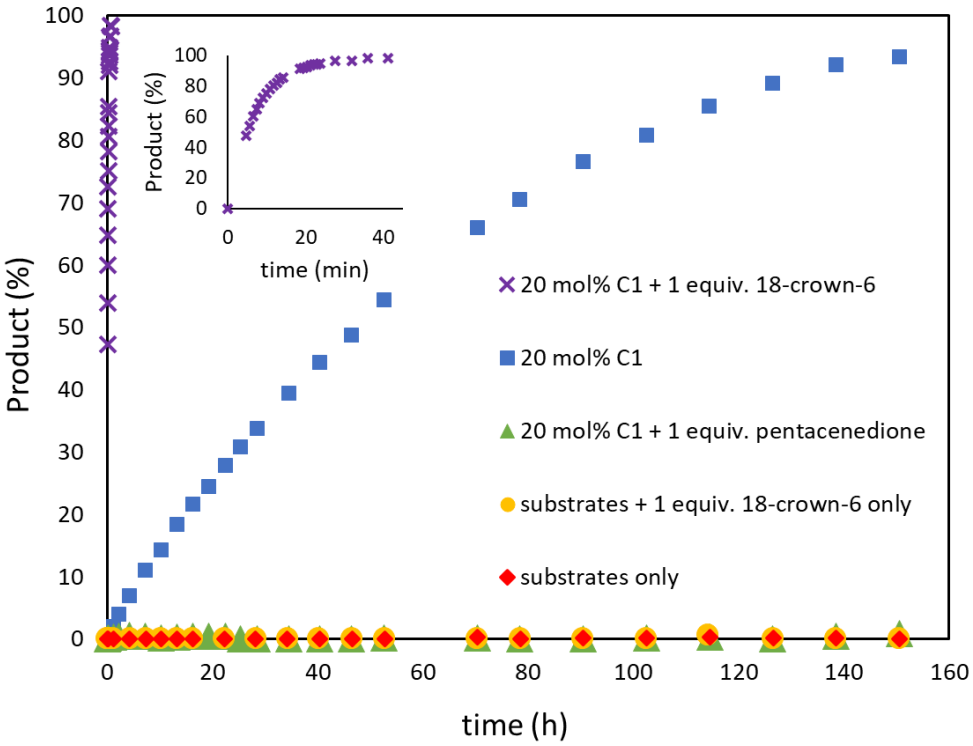

*Figure 2-23. Kinetic profiles of Michael addition between 2.5 mM methyl vinyl ketone **E1** and 12.5 mM nitromethylacetate **Nu1**H with 2.5 mM 18-crown-6 and 0.5 mM **C1** (purple cross), with 0.5 mM **C1** (blue square), with 0.5 mM **C1** and 2.5 mM pentacenedione (green triangle), with 2.5 mM 18-crown-6 (yellow circle) or on their own (red diamond).*

2.7.4.2 Michael addition between nitromethylacetate Nu1H and methyl vinyl ketone E1 with C2 and comparison to C1.

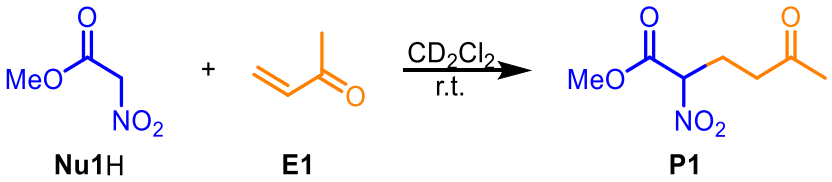

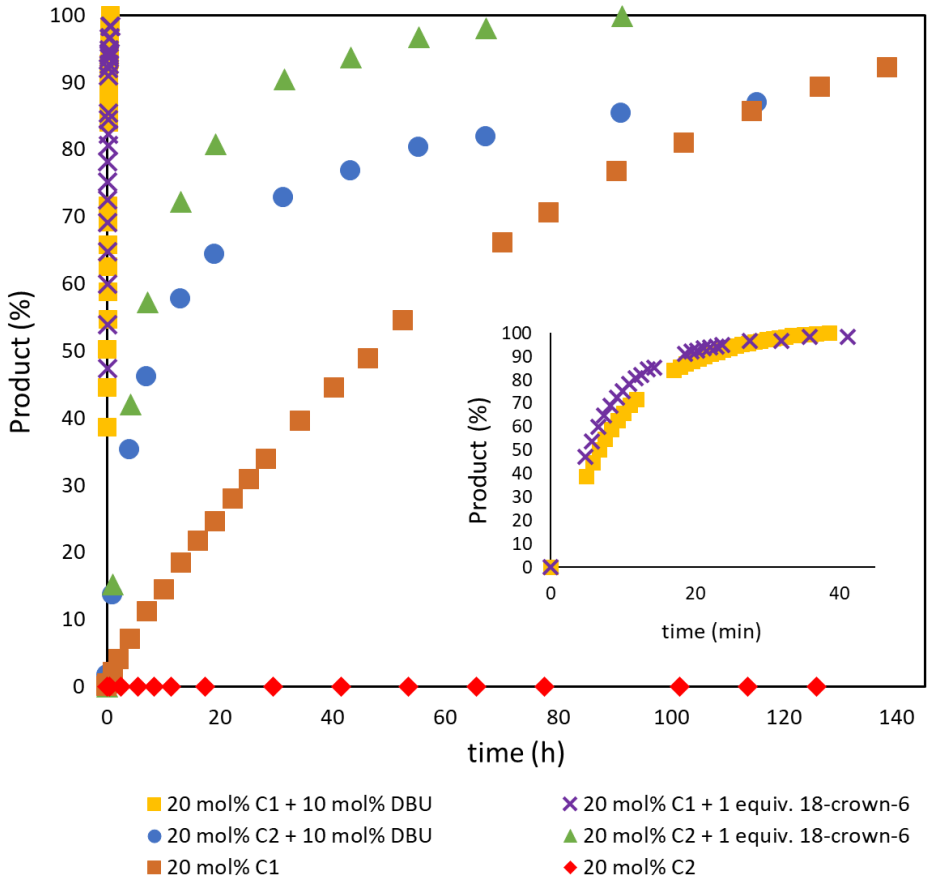

*Figure 2-24. Kinetic profiles of Michael addition between 2.5 mM methyl vinyl ketone **E1** and 12.5 mM nitromethylacetate **Nu1**H with 2.5 mM 18-crown-6 and 0.5 mM **C1** (purple cross), with 0.25 mM DBU and 0.5 mM **C1** (yellow square), with 2.5 mM 18-crown-6 and 0.5 mM **C2** (green triangle), with 0.25 mM DBU and 0.5 mM **C2** (blue circle), with only 0.5 mM **C1** (orange square) and with only 0.5 mM **C2** (red diamond).*

2.7.4.3 Michael addition between nitromethylacetate Nu1H and methyl vinyl ketone E1 with 18-crown-6 and Schreiner's catalyst NC2 or Squaramide NC1

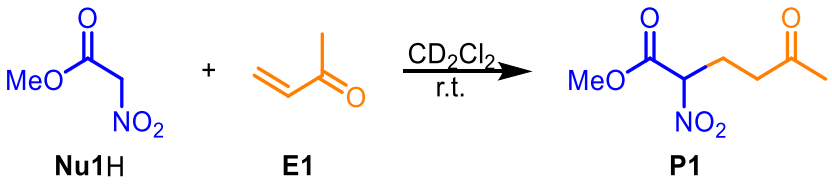

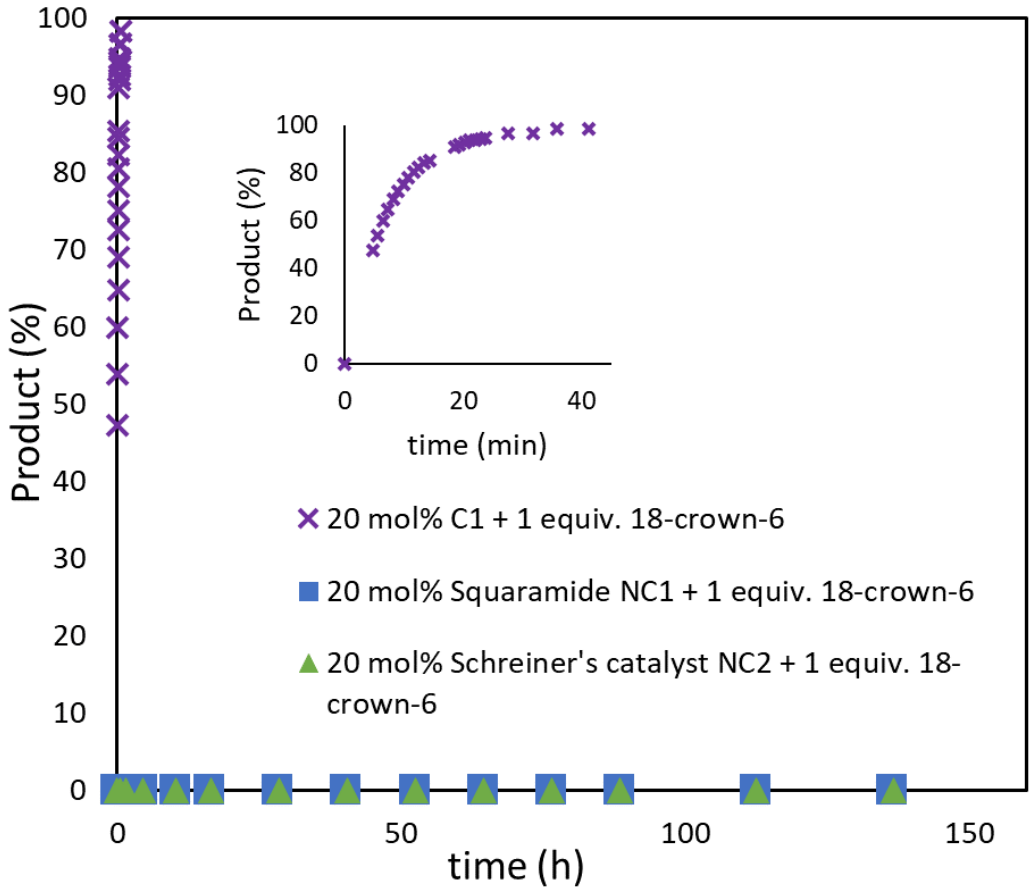

*Figure 2-25. Kinetic profiles of Michael addition between 2.5 mM methyl vinyl ketone **E1** and 12.5 mM nitromethylacetate **Nu1**H with 2.5 mM 18-crown-6 and 0.5 mM **C1** (purple cross), with 2.5 mM 18-crown-6 and 0.5 mM Squaramide **NC1** (blue square) and with 2.5 mM 18-crown-6 and 0.5 mM Schreiner's catalyst **NC2** (green triangle).*

2.7.4.4 Michael addition between nitromethylacetate Nu1H and methyl vinyl ketone E1 with DBU and Schreiner's catalyst NC2 or Squaramide NC1

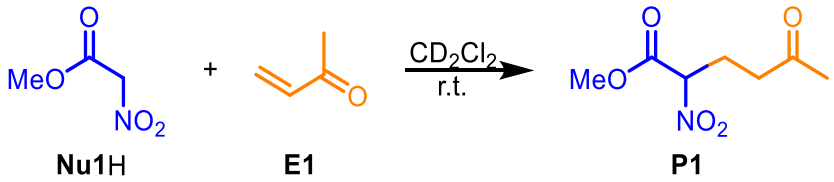

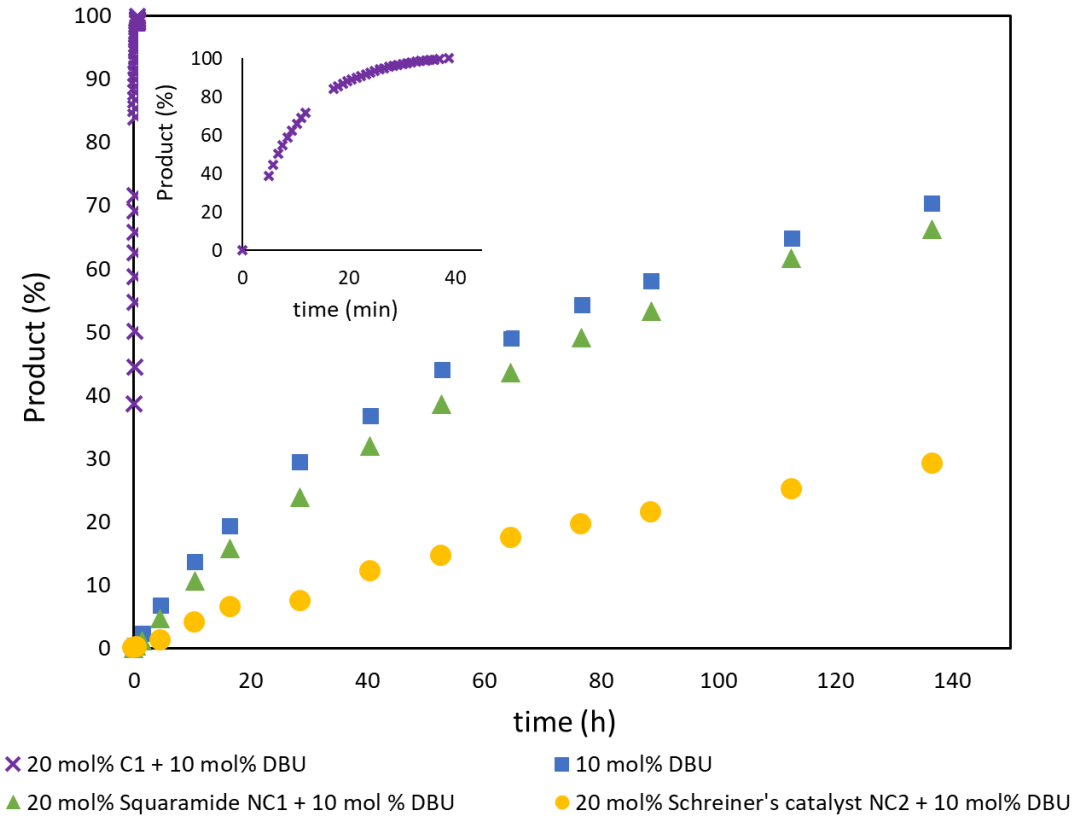

*Figure 2-26. Kinetic profiles of Michael addition between 2.5 mM methyl vinyl ketone **E1** and 12.5 mM nitromethylacetate **Nu1**H with 0.25 mM DBU and 0.5 mM **C1** (purple cross), with 0.25 mM DBU (blue square), with 0.25 mM DBU and 0.5 mM Squaramide **NC1** (green triangle) and with 0.25mM DBU and 0.5 mM Schreiner's catalyst **NC2** (yellow circle).*

2.7.4.5 Michael addition between nitromethylacetate Nu1H and methyl vinyl ketone E1 with Schreiner's catalyst NC2 or Squaramide NC1

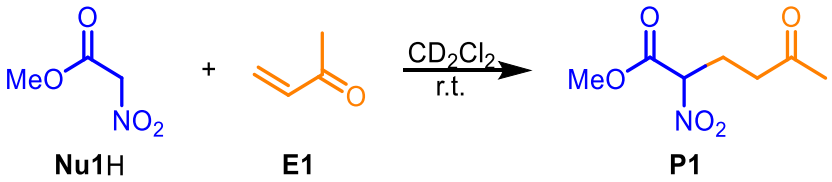

Nu1H **E1** **P1**

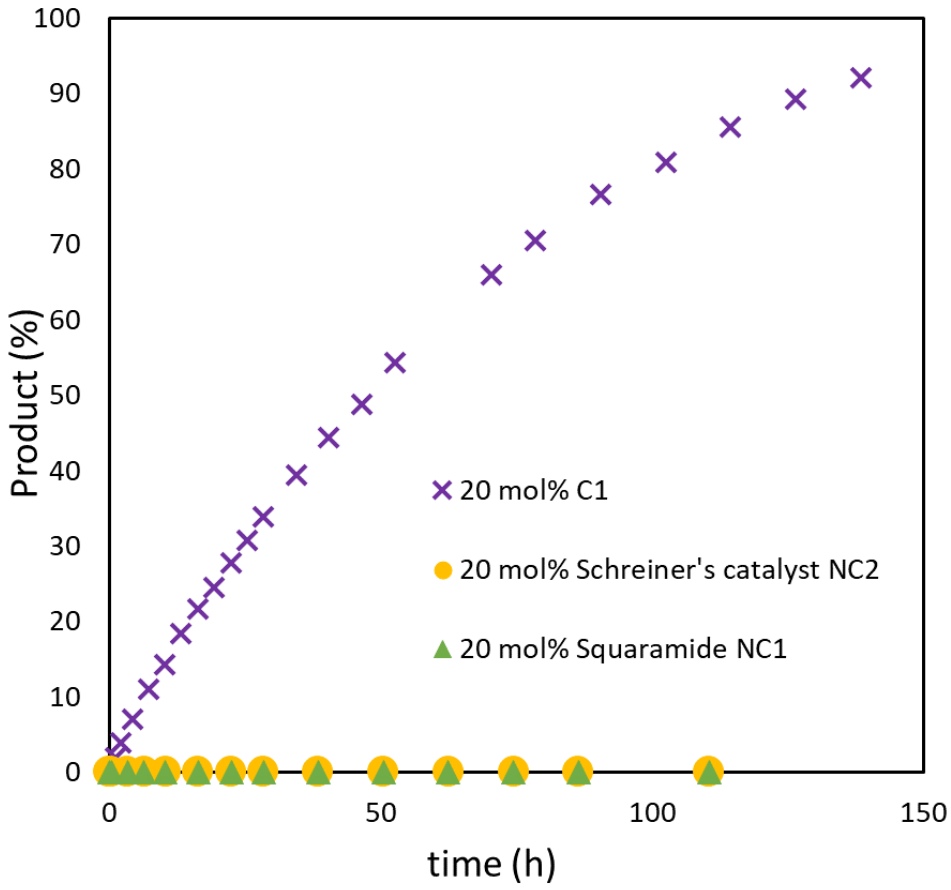

*Figure 2-27. Kinetic profiles of Michael addition between 2.5 mM methyl vinyl ketone **E1** and 12.5 mM nitromethylacetate **Nu1**H with 0.5 mM C1 (purple cross), with 0.5 mM Squaramide **NC1** (green triangle) and with 0.5 mM Schreiner's catalyst **NC2** (yellow circle).*

2.7.4.6 $[Pd(py)_4](BArF)_2$ control reactions for Michael addition between nitromethylacetate Nu1H and methyl vinyl ketone E1

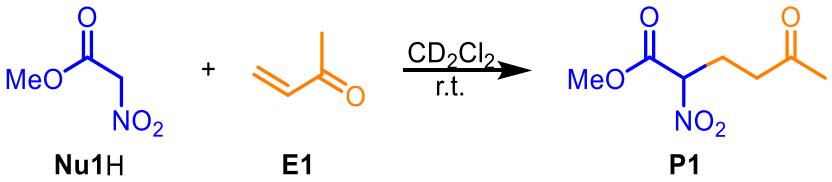

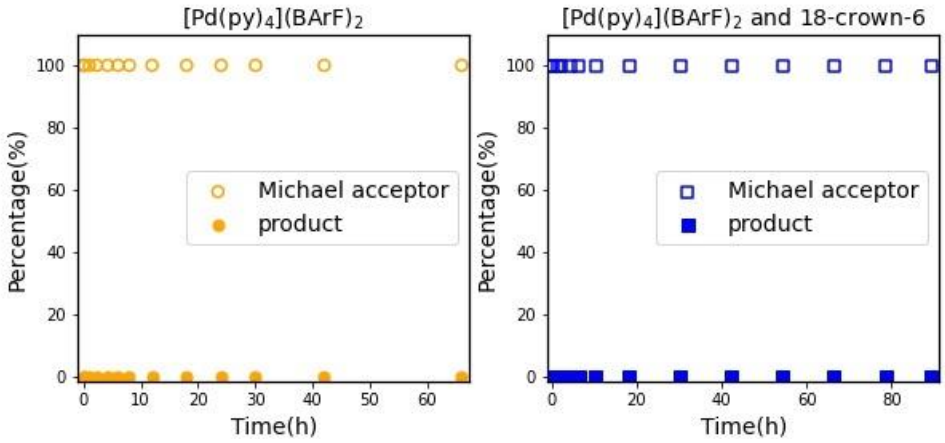

*Figure 2-28. Kinetic profiles of Michael addition between 2.5 mM methyl acrylate **E2** and 12.5 mM nitromethylacetate **Nu2H** with 0.5 mM $[Pd(py)_4](BArF)_2$ (left) or 2.5 mM 18-crown-6 and 0.5 mM $[Pd(py)_4](BArF)_2$ (right).*

2.7.4.7 Michael addition between benzoylnitromethane Nu2H and methyl vinyl ketone E1

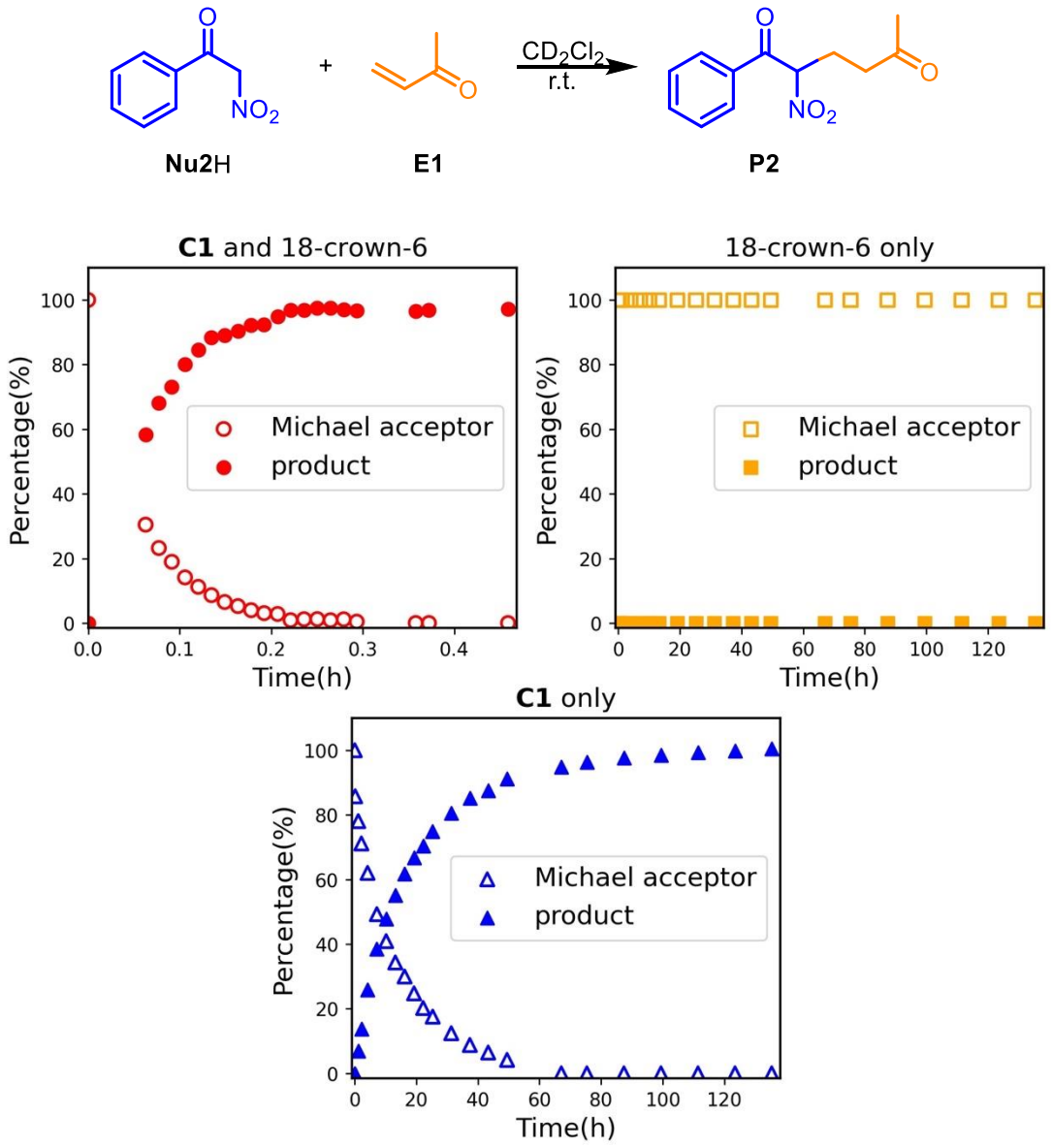

*Figure 2-29. Kinetic profiles of Michael addition between 2.5 mM methyl vinyl ketone **E1** and 12.5 mM benzoylnitromethane **Nu2H** with 2.5 mM 18-crown-6 and 0.5 mM **C1** (top left), 2.5 mM 18-crown-6 (top right) or 0.5 mM **C1** (bottom).*

2.7.4.8 Michael addition between benzoylnitromethane Nu2H and methyl acrylate E2

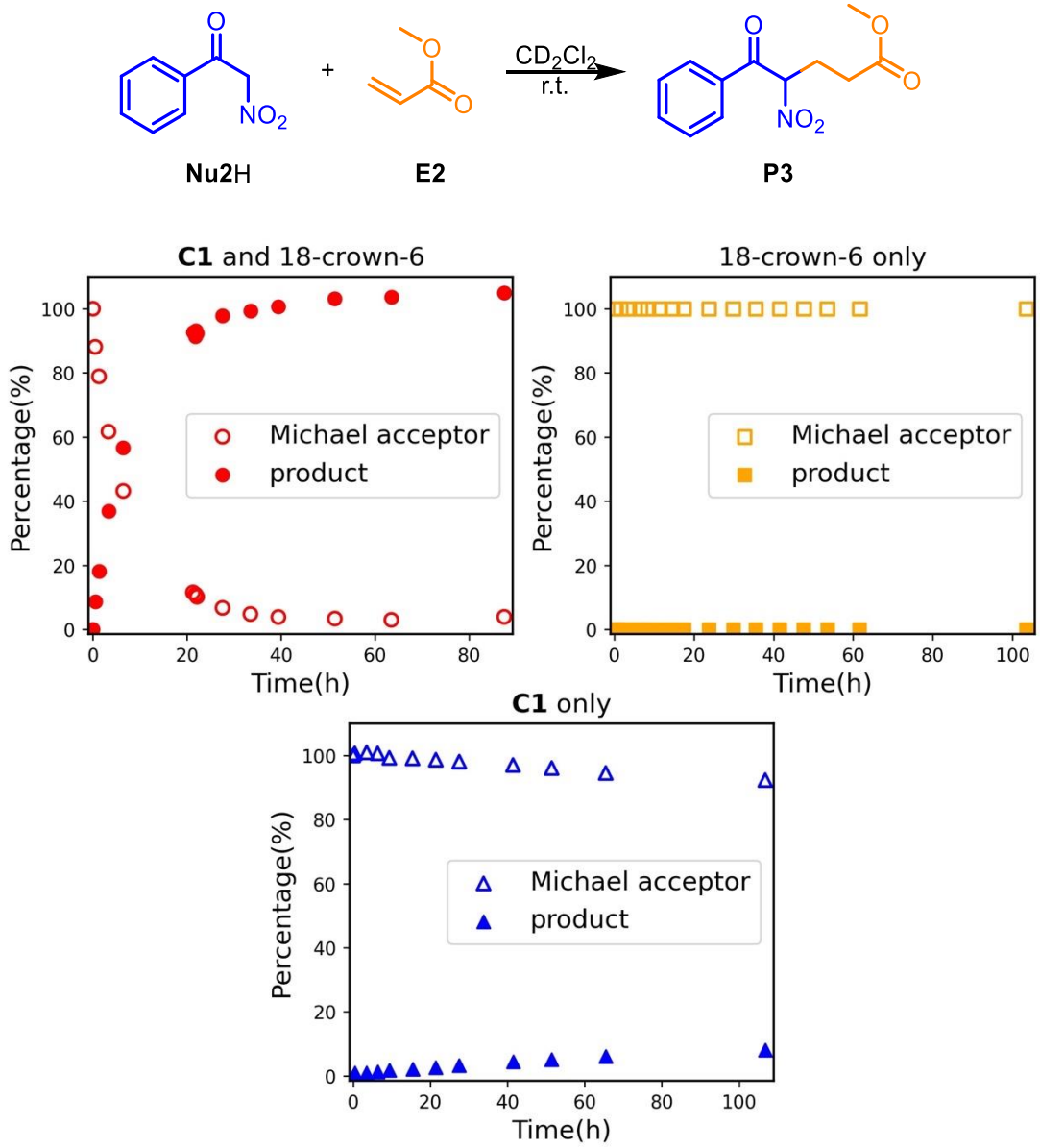

*Figure 2-30. Kinetic profiles of Michael addition between 2.5 mM methyl acrylate **E2** and 12.5 mM benzoylnitromethane **Nu2**H with 2.5 mM 18-crown-6 and 0.5 mM **C1** (top left), 2.5 mM 18-crown-6 (top right) or 0.5 mM **C1** (bottom).*

2.7.4.9 Michael addition between benzoylnitromethane Nu2H and acrylonitrile E3

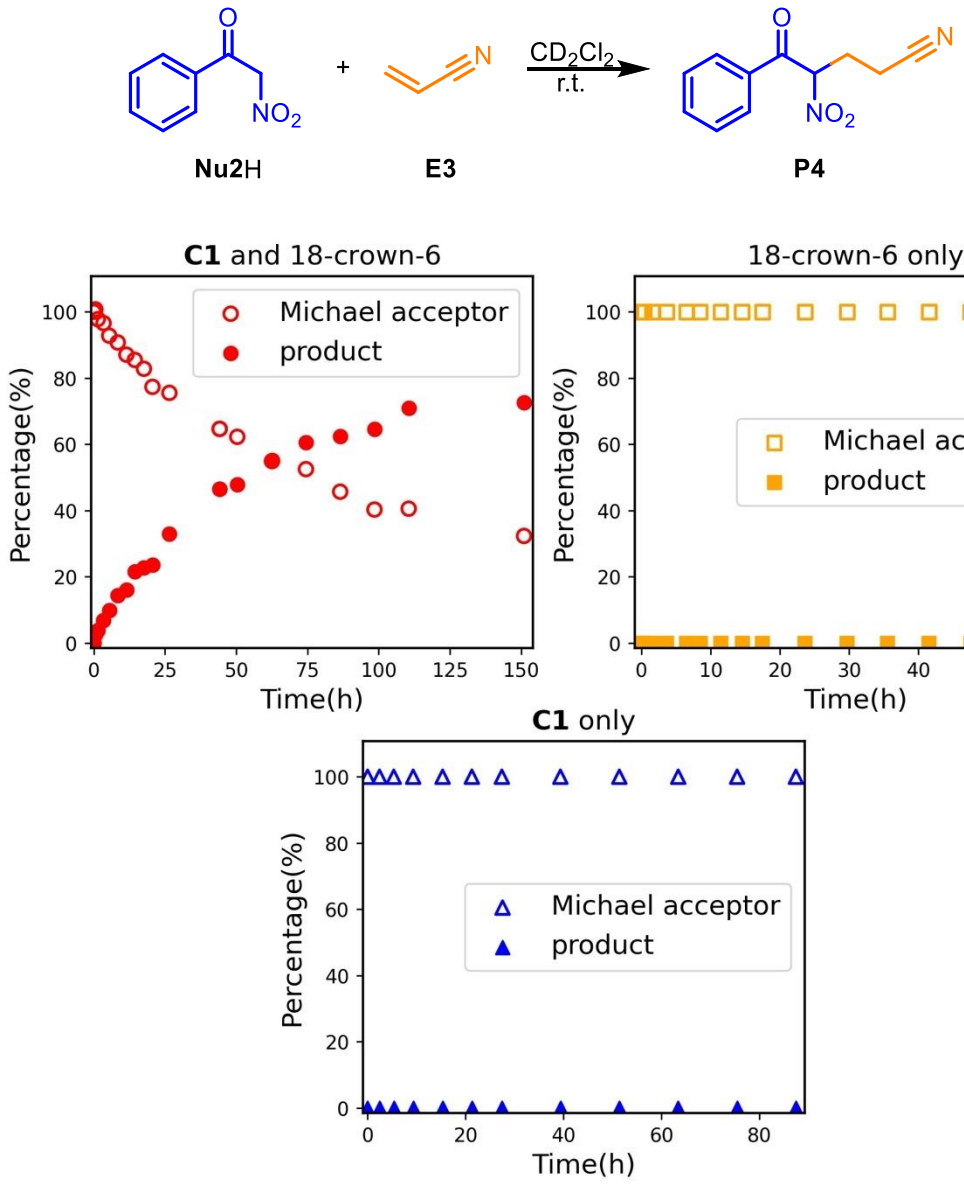

*Figure 2-31. Kinetic profiles of Michael addition between 2.5 mM acrylonitrile **E3** and 12.5 mM benzoylnitromethane **Nu2**H with 2.5 mM 18-crown-6 and 0.5 mM **C1** (top left), 2.5 mM 18-crown-6 (top right) or 0.5 mM **C1** (bottom).*

2.7.4.10 Michael addition between nitromethylacetate Nu1H and 1-nitrocyclohexene E4

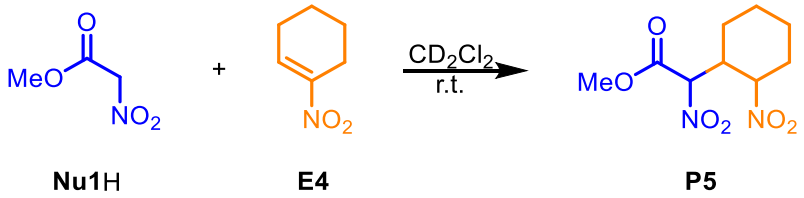

Nu1H **E4** **P5**

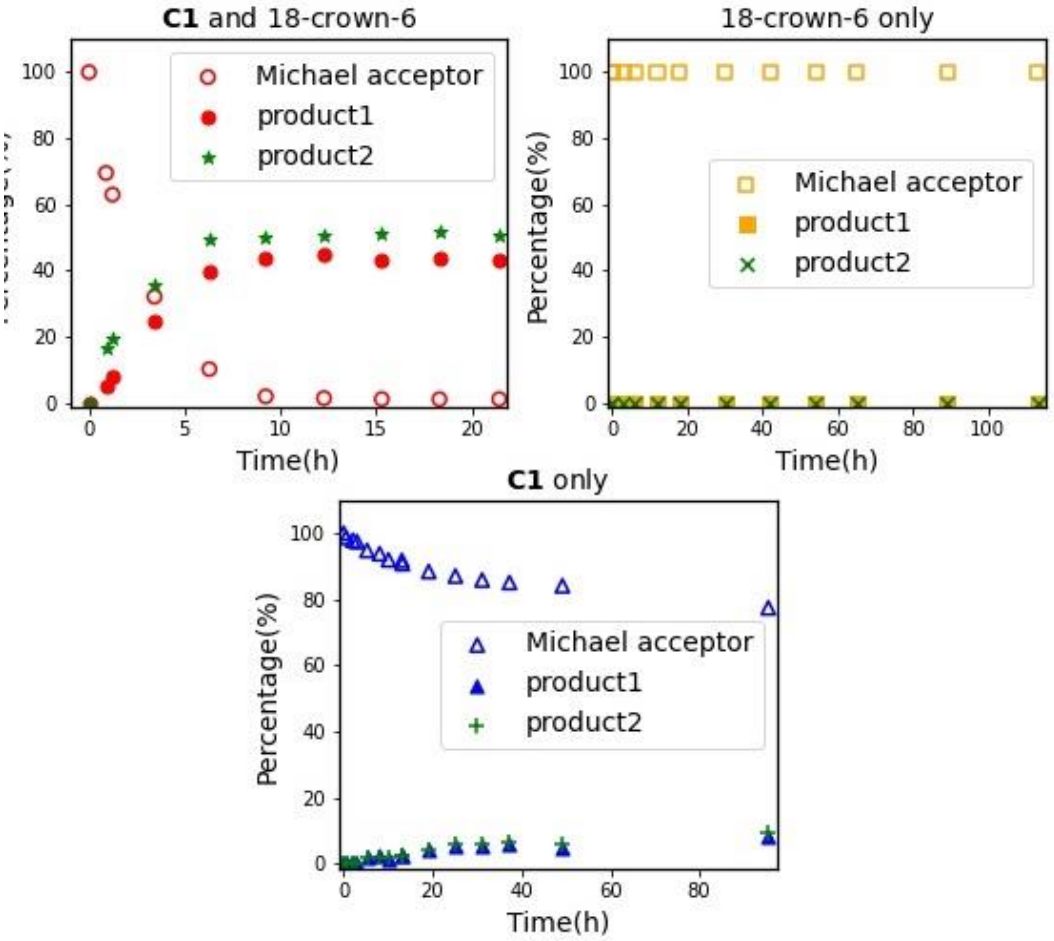

*Figure 2-32. Kinetic profiles of Michael addition between 2.5 mM 1-nitrocyclohexene **E4** and 12.5 mM nitromethylacetate **Nu1**H with 2.5 mM 18-crown-6 and 0.5 mM **C1** (top left), 2.5 mM 18-crown-6 (top right) or 0.5 mM **C1** (bottom).*

2.7.4.11 Michael addition between nitromethane Nu3H and methyl vinyl ketone

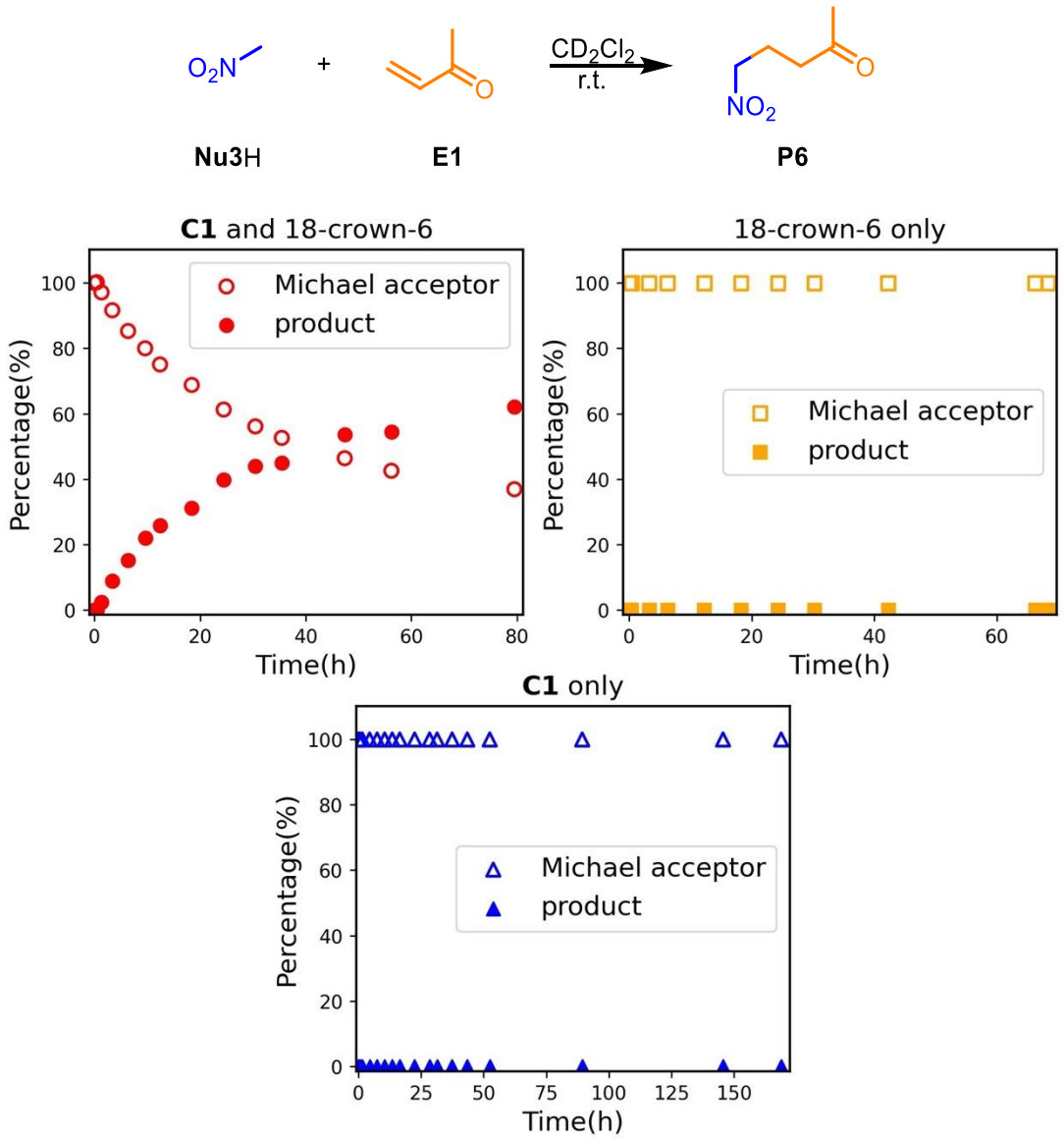

*Figure 2-33. Kinetic profiles of Michael addition between 2.5 mM methyl vinyl ketone **E1** and 12.5 mM nitromethane **Nu3**H with 2.5 mM 18-crown-6 and 0.5 mM **C1** (top left), 2.5 mM 18-crown-6 (top right) or 0.5 mM **C1** (bottom).*

2.7.4.12 Michael addition between malononitrile Nu4H and methyl vinyl ketone

E1

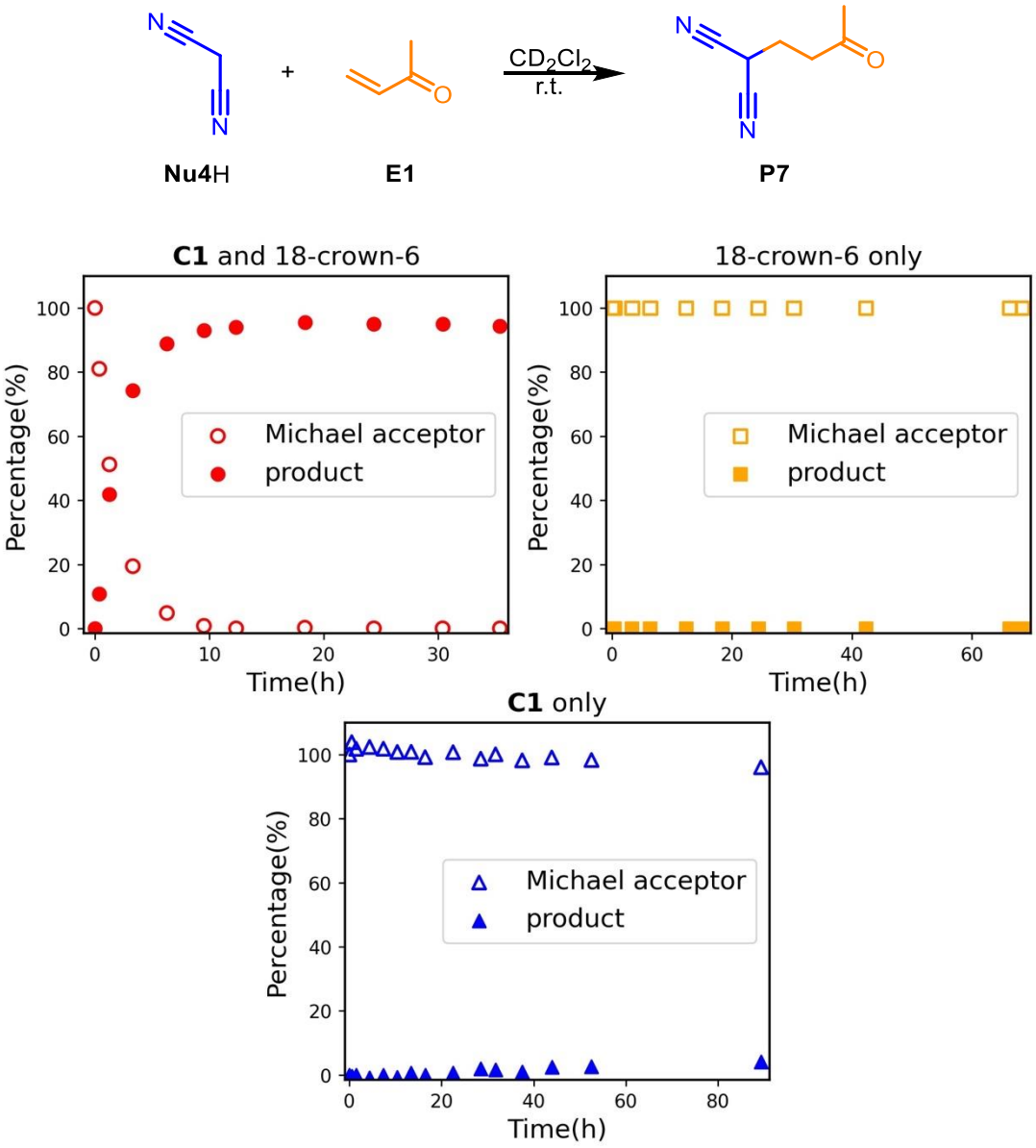

*Figure 2-34. Kinetic profiles of Michael addition between 2.5 mM methyl vinyl ketone **E1** and 12.5 mM malononitrile **Nu4**H with 2.5 mM 18-crown-6 and 0.5 mM **C1** (top left), 2.5 mM 18-crown-6 (top right) or 0.5 mM **C1** (bottom).*

2.7.4.13 Michael addition between benzoylacetontrile Nu5H and methyl vinyl ketone E1

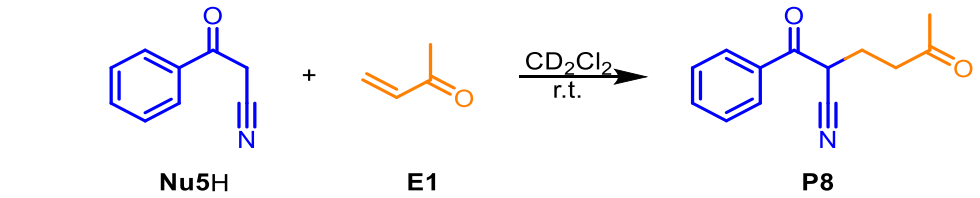

Nu5H **E1** **P8**

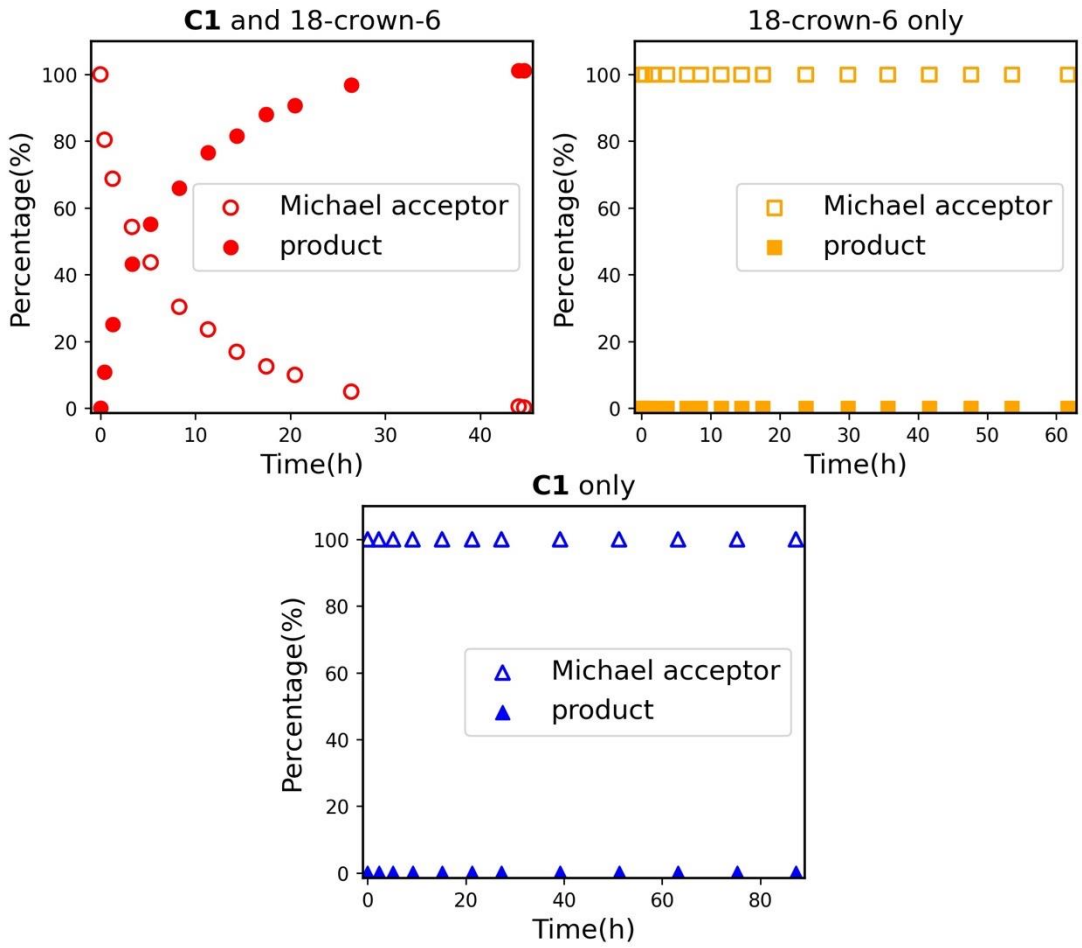

*Figure 2-35. Kinetic profiles of Michael addition between 2.5 mM methyl vinyl ketone **E1** and 12.5 mM benzoylacetonitrile **Nu5**H with 2.5 mM 18-crown-6 and 0.5 mM **C1** (top left), 2.5 mM 18-crown-6 (top right) or 0.5 mM **C1** (bottom).*

2.7.4.14 Introducing P5 into the ongoing Michael addition between nitromethylacetate Nu1H and 1-nitrocyclohexene E4 with C1/18-crown-6

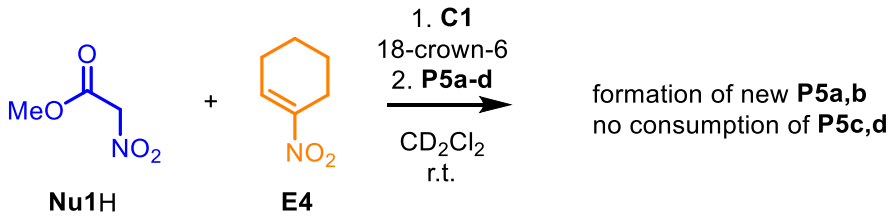

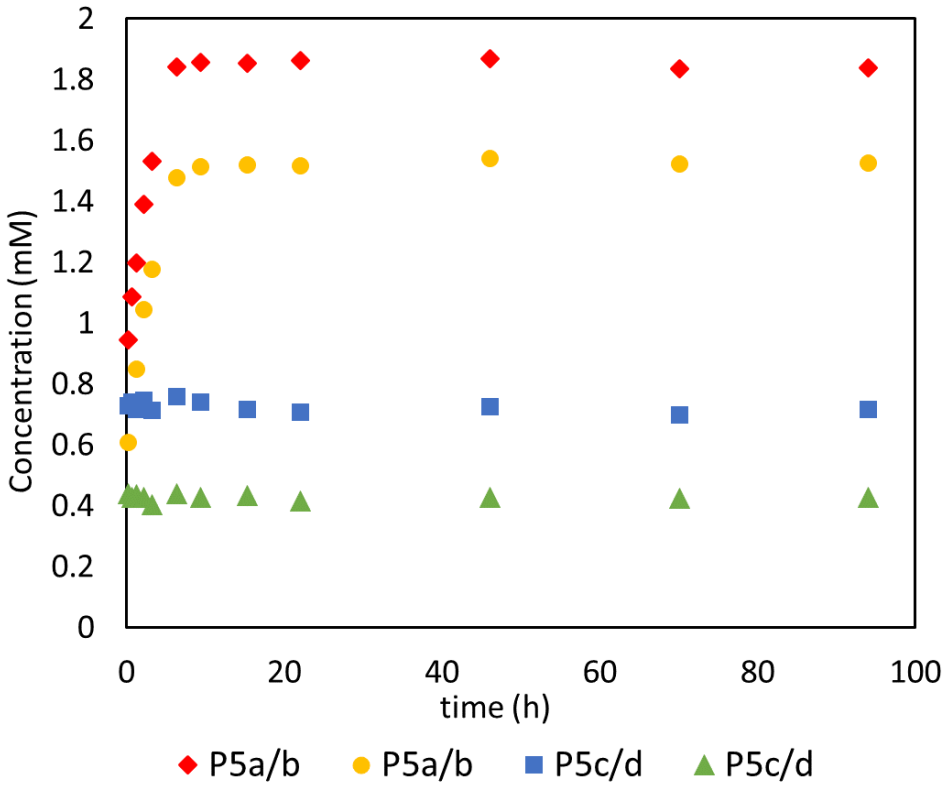

*Figure 2-36. Kinetic profiles of Michael addition between of nitromethylacetate **Nu1**H (12.5 mM) and 1-nitrocyclohexene **E4** (2.5 mM) with **C1** (0.5 mM) and 18-crown-6 (2.5 mM) with A mixture of **P5a-d** (**P5a/b**: 0.6 mM and 0.9 mM, **P5c/d**: 0.7 mM and 0.4 mM) introduced after reaction initiation. Concentration of **P5a/b**: red diamond and yellow circle. Concentration **P5c/d**: blue square and green triangle.*

2.7.5 Binding constant determination via NMR titration

2.7.5.1 General procedure for titrating guests into C1

For each titration, a solution containing **C1** (0.5 mM) and guest (50 mM or 200 mM) was titrated to a 500 µL solution containing **C1** (0.5 mM), maintaining the concentration of **C1** throughout. ^{1}H NMR spectrum was recorded at each titration point. The peak positions of the internal pyridyl hydrogens (shown in blue, Figure 2-37) were plotted against the concentration of guests. The experimental data was fitted to a 1:1 fast exchange binding model (Equation 2-1) using the Levenberg-Marquardt Nonlinear Least-Squares Algorithm built in the R software and the RStudio software interface.

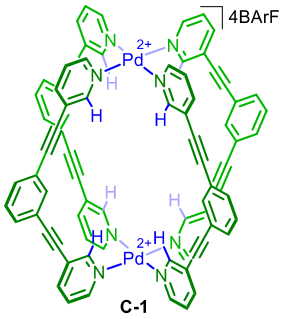

Figure 2-37. Peak positions of the internal pyridyl hydrogens (blue) were monitored during NMR titrations.

$$\delta = \delta_0 + \frac{\Delta\delta_{Max}}{2}\left(\frac{C_{Guest}}{C_{Host}} + \frac{1}{C_{Host}\cdot K_{Ass}} + 1 - \sqrt{\left(\frac{C_{Guest}}{C_{Host}} + \frac{1}{C_{Host}\cdot K_{Ass}} + 1\right)^2 - \frac{4\cdot C_{Guest}}{C_{Host}}}\right)$$

Equation 2-1.

2.7.5.2 Titration of nitromethylacetate Nu1H into C1

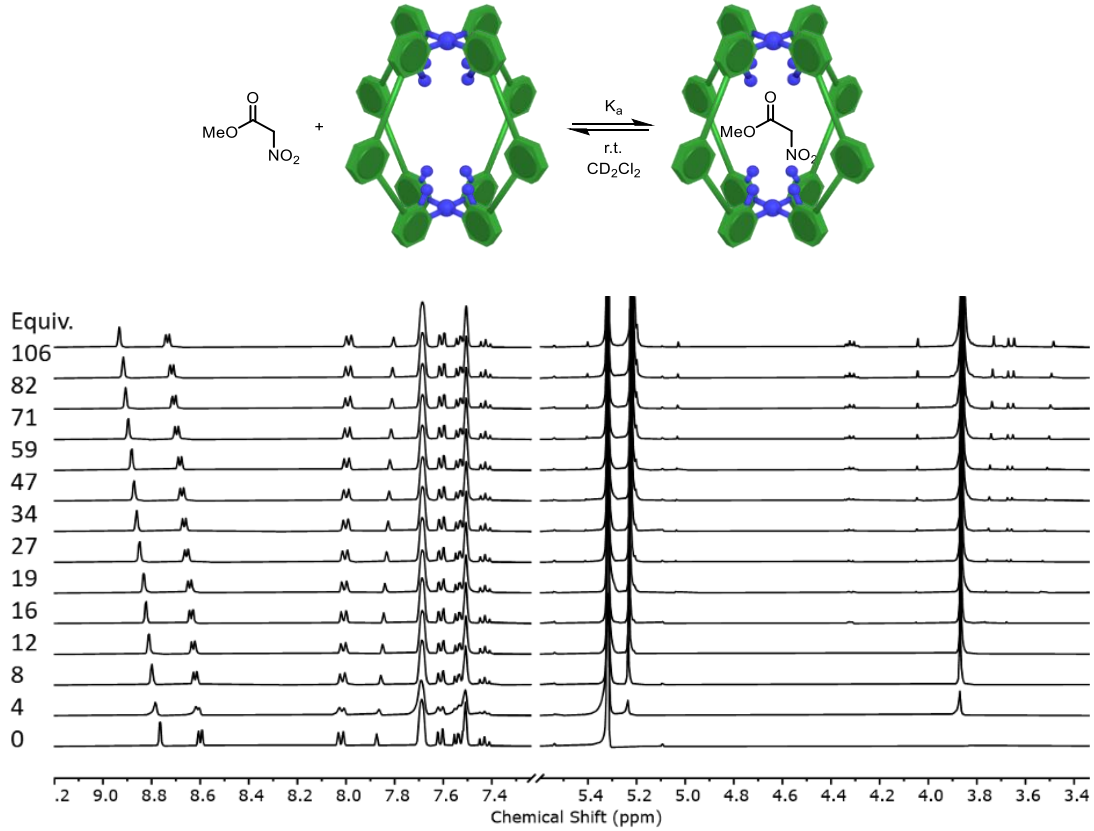

*Figure 2-38. ^{1}H NMR (400 MHz, CD_2Cl_2) spectroscopic data for titration of nitromethylacetate **Nu1H** into **C1**.*

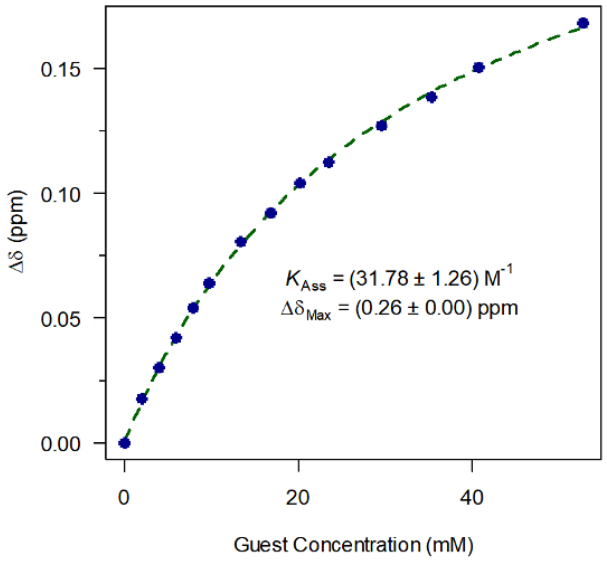

*Figure 2-39. Fitted data for change in peak position with increasing nitromethylacetate **Nu1H** concentration.*

2.7.5.3 Titration of methyl vinyl ketone E1 into C1

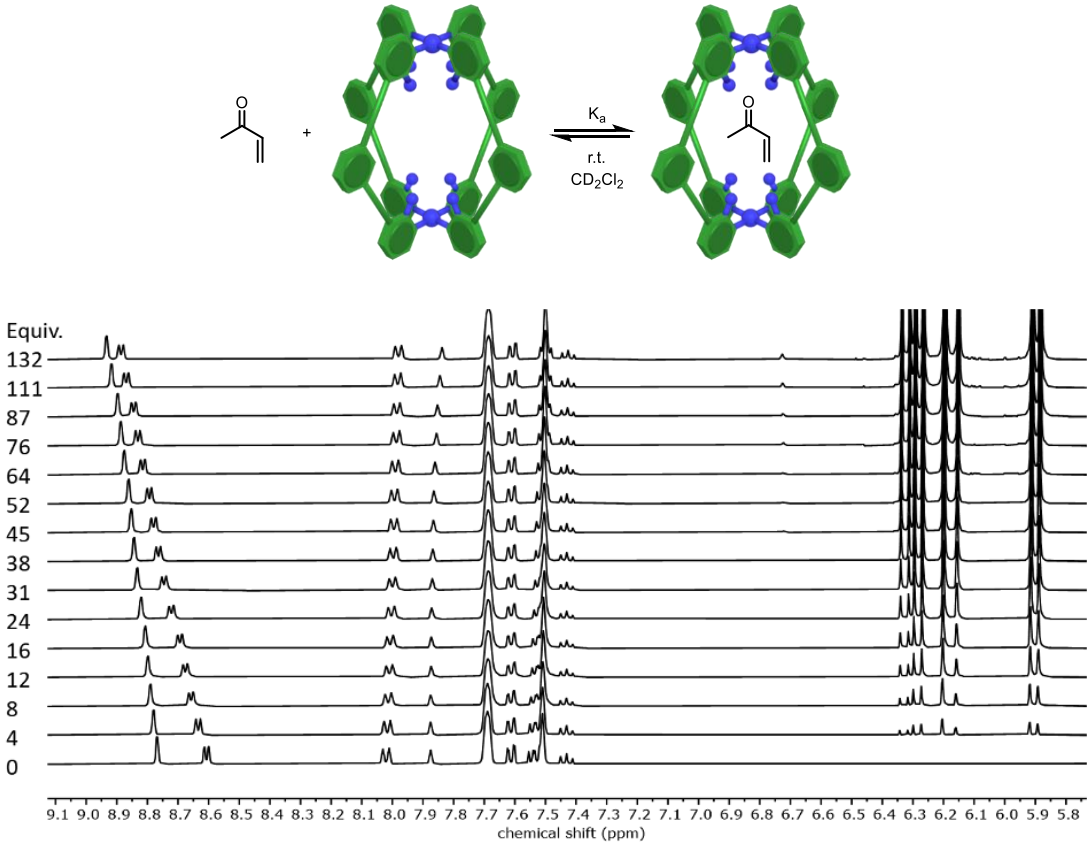

*Figure 2-40. ^1H NMR (400 MHz, CD_2Cl_2) spectroscopic data for titration of methyl vinyl ketone **E1** into **C1**.*

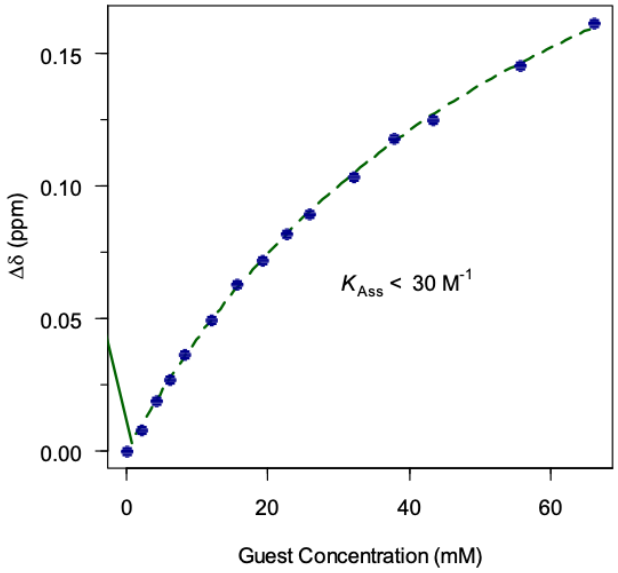

*Figure 2-41. Fitted data for change in peak position with increasing methyl vinyl ketone **E1** concentration.*

2.7.5.4 Titration of dimethylmaleate into C1

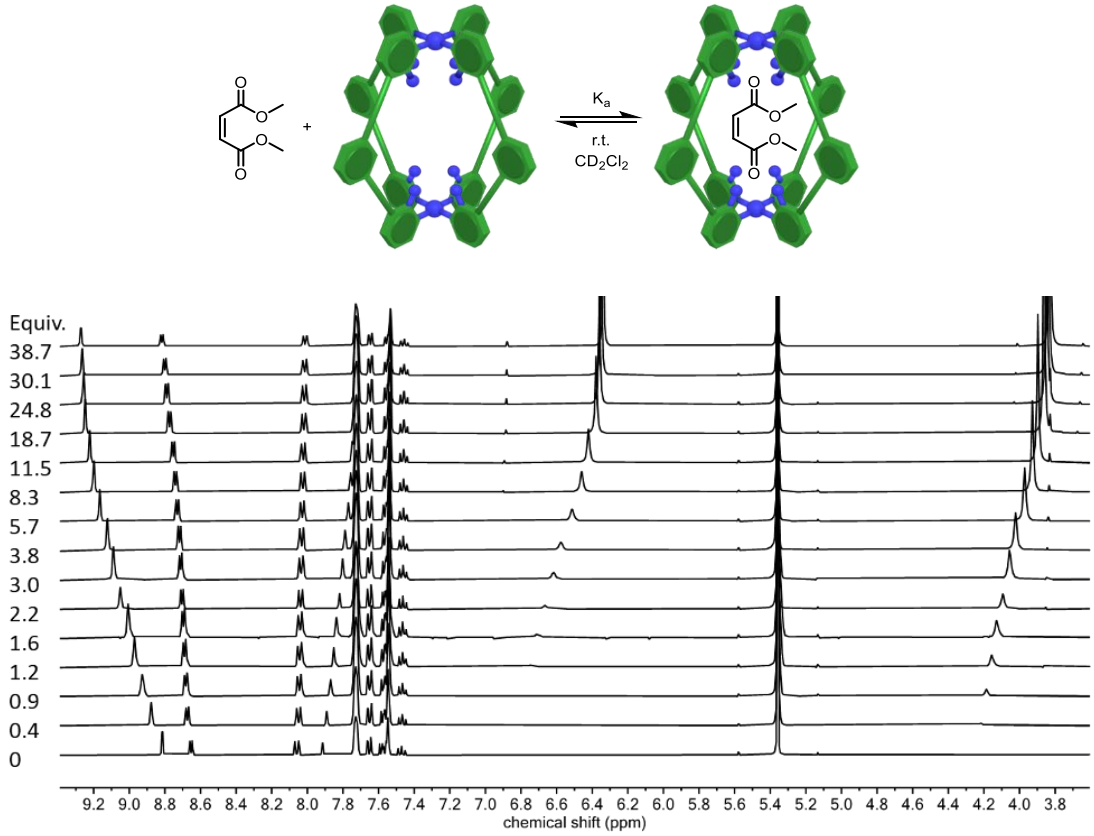

*Figure 2-42. ^{1}H NMR (400 MHz, CD_2Cl_2) spectroscopic data for titration of dimethylmaleate into **C1**.*

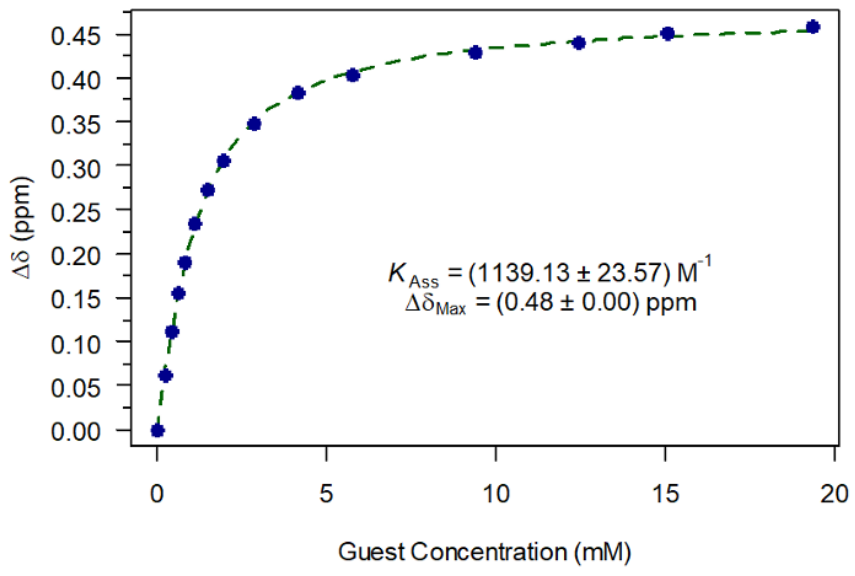

Figure 2-43. Fitted data for change in peak position with increasing dimethylmaleate concentration.

2.7.5.5 Titration of the Michael addition product P1 into C1

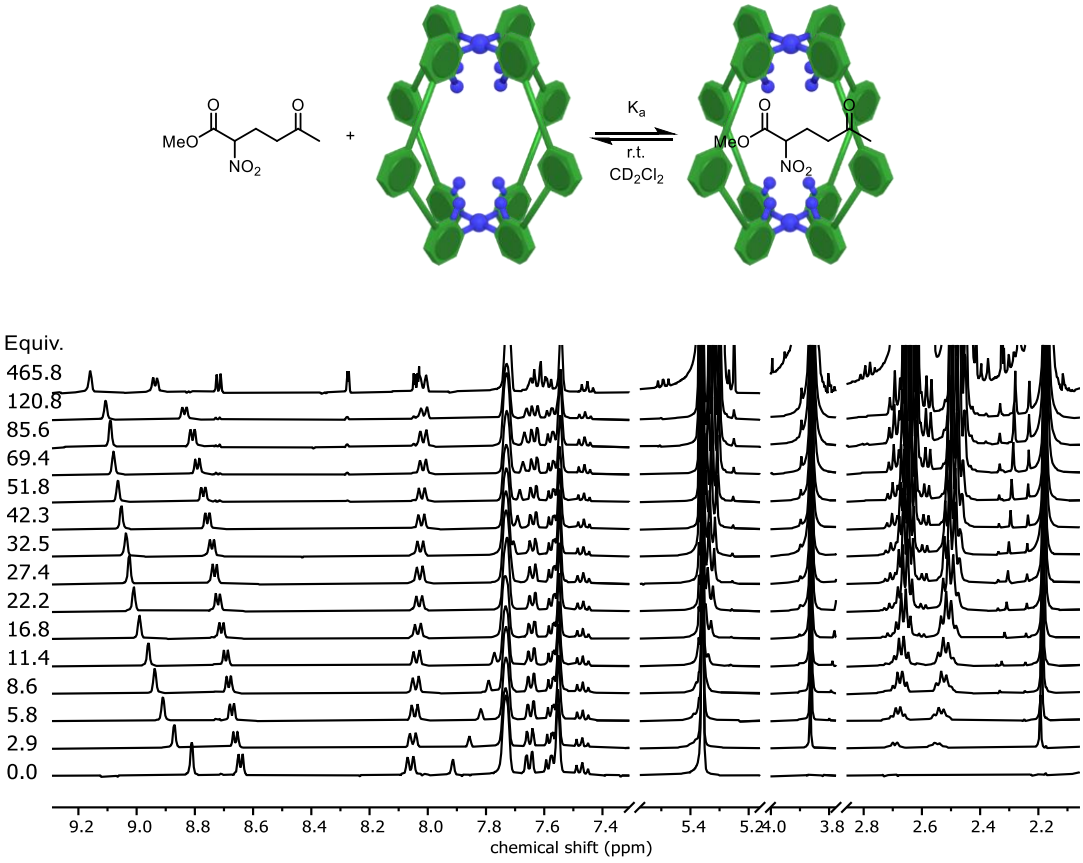

*Figure 2-44. ^{1}H NMR (400 MHz, CD_2Cl_2) spectroscopic data for titration of **P1** into **C1**.*

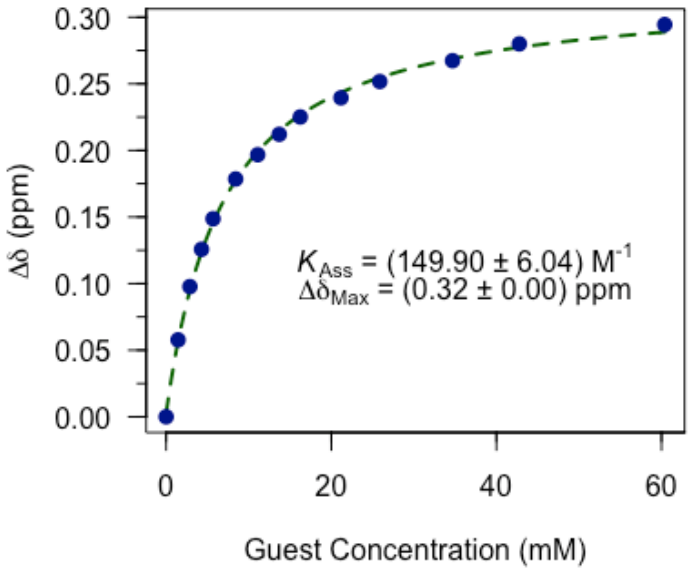

*Figure 2-45. Fitted data for change in peak position with increasing **P1** concentration.*

2.7.5.6 Procedure for titrating C1 into P5 syn- and anti- isomers

P5 isomer mixture was prepared according to the method in section S2.7.6.5. **P5** (7.5 mg) was dissolved in CD_2Cl_2 (400 µL). 10 µL of this **P5** stock solution in combination with internal standard tetrakis(trimethylsilyl)silane (10 µL of a 15.6 mM CD_2Cl_2 stock solution) was further diluted with 480 µL CD_2Cl_2 to make up a 500 µL NMR sample. **C1** (1.3 mg) was added to the **P5** sample as solid and ^{1}H NMR was recorded at each titration point.

2.7.5.7 Pseudo titration of into C1 into P5

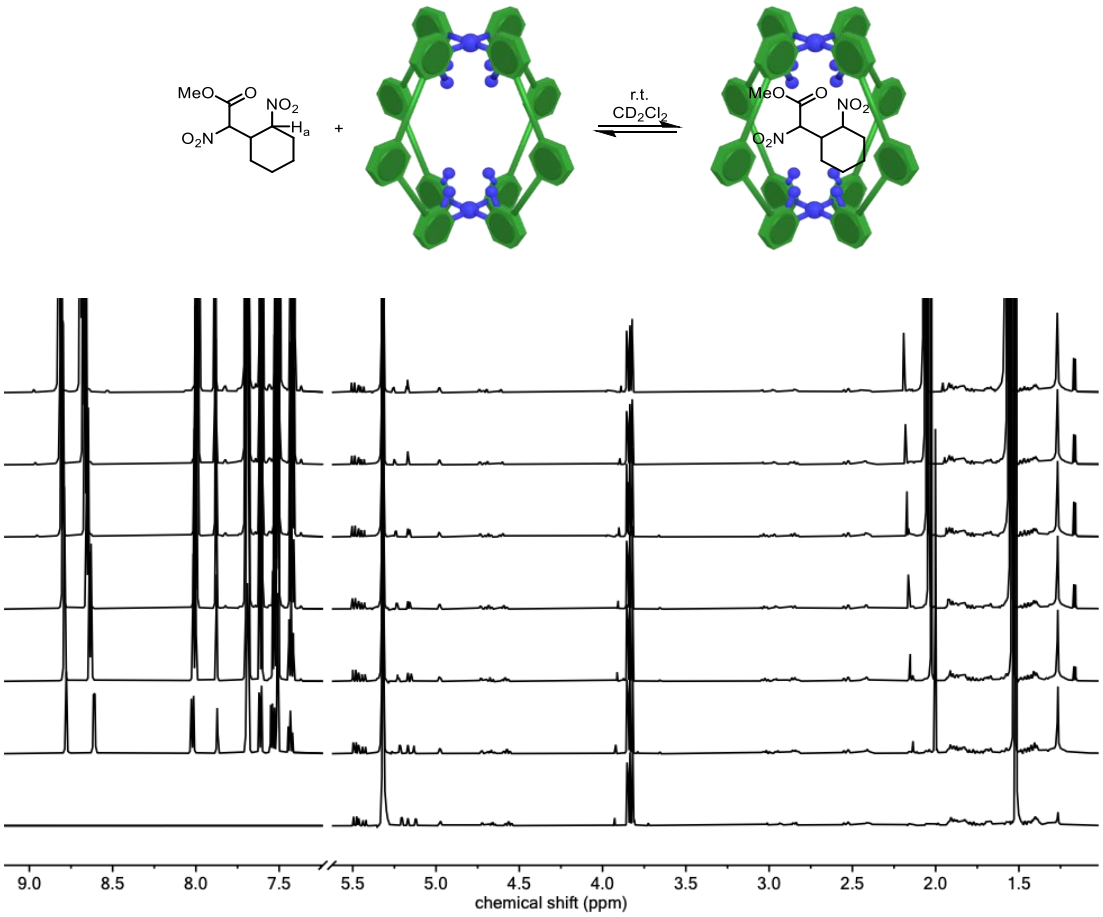

*Figure 2-46. ^{1}H NMR (600 MHz, CD_2Cl_2) spectroscopic data for titration of **C1** into a mixture of **P5** syn- and anti- isomers, **C1** and **P5** region.*

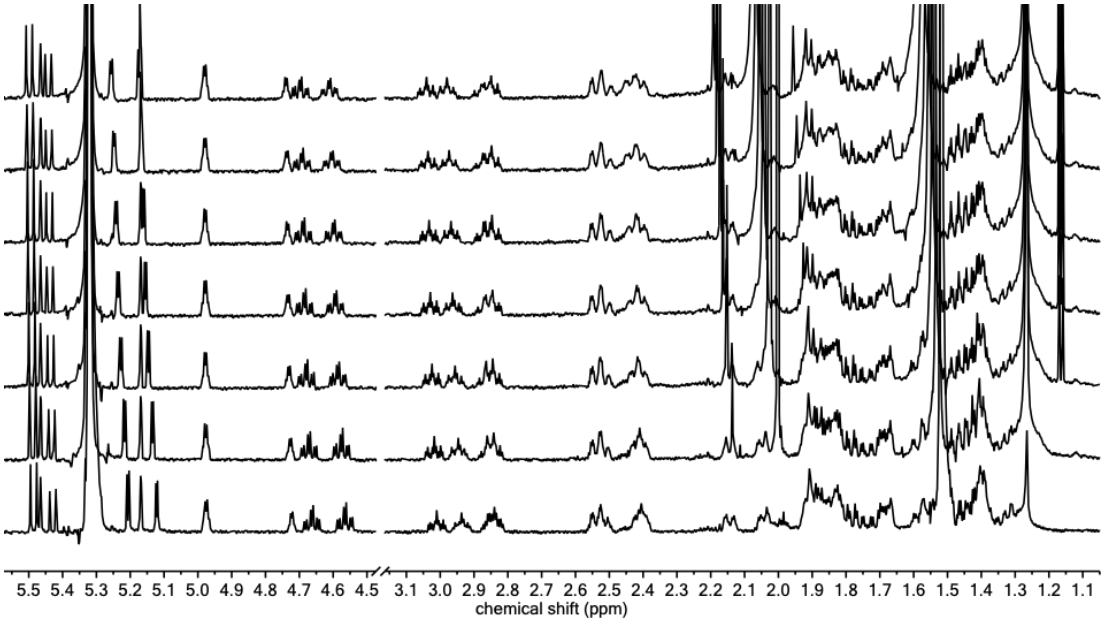

*Figure 2-47. ^{1}H NMR (600 MHz, CD_2Cl_2) spectroscopic data for titration of **C1** into a mixture of **P5** syn- and anti- isomers, zooming in **P5** region.*

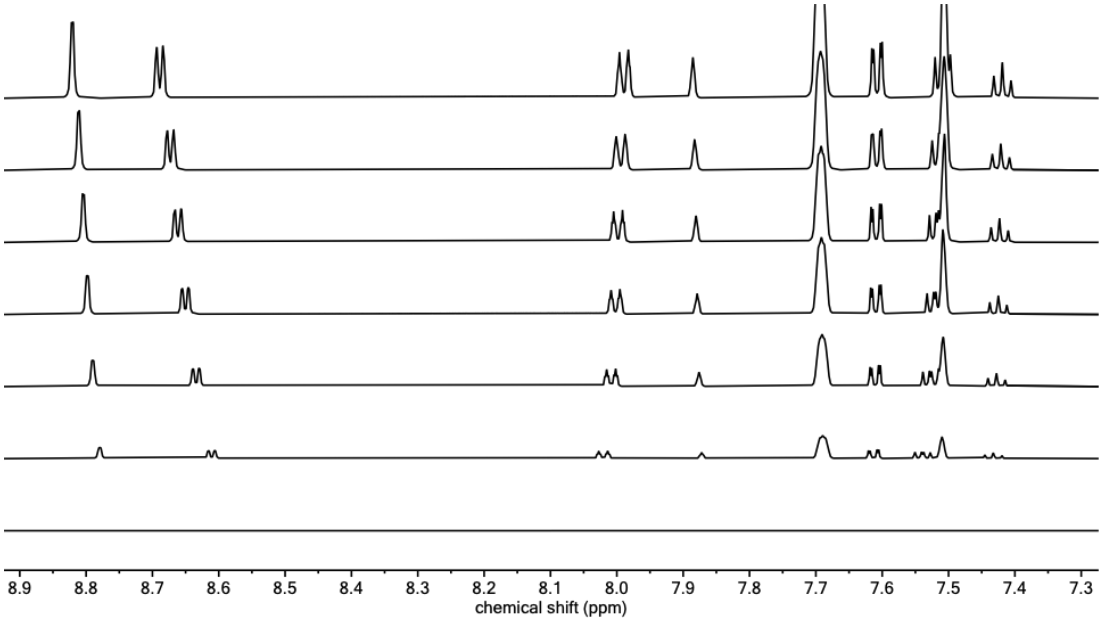

*Figure 2-48. ^{1}H NMR (600 MHz, CD_2Cl_2) spectroscopic data for titration of **C1** into a mixture of **P5** syn- and anti- isomers, zooming in **C1** region.*

2.7.6 Preparation of authentic Michael addition products

2.7.6.1 Michael addition product P1 of nitromethylacetate Nu1H and methyl vinyl ketone E1

Nitromethylacetate (1.5 ml, 16 mmol) and methyl vinyl ketone (0.68 ml, 8.2 mmol) were combined in CH_3CN (30 ml). DBU (0.24 ml, 1.6 mmol) was added to the mixture. The reaction was stirred at room temperature overnight and then quenched with glacial acetic acid (5.0 ml, 87 mmol). The mixture was concentrated *in vacuo*, and the residue was diluted with CH_2Cl_2 (25 ml). The organic layer was washed with H_2O (25 ml) three times before drying over $MgSO_4$. The solvent was removed *in vacuo* and product purified by silica flash column (CH_2Cl_2, R_f = 0.28) to give a light-yellow oil (0.42 g, 27%). ^{1}H NMR (500 MHz, $CDCl_3$) δ 5.22 (dd, J = 8.4, 6.1 Hz, 1H, H_a), 3.79 (s, 3H, H_b), 2.65 – 2.50 (m, 2H, H_c), 2.48 – 2.34 (m, 2H, H_d), 2.12 (s, 3H, H_e) ppm. ^{13}C NMR (126 MHz, $CDCl_3$) δ 206.06, 164.85, 86.63, 53.65, 38.31, 29.91, 24.10 ppm. HRMS (EI): $C_7H_{11}NO_5$ $[M]^{\cdot+}$ found 189.06235, requires 189.06317.

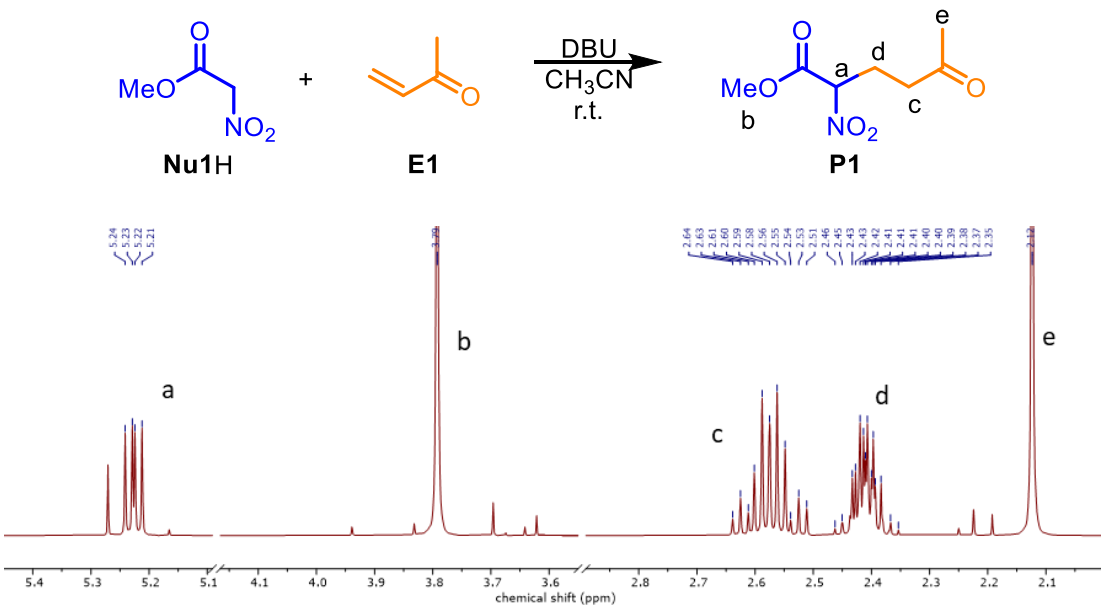

*Figure 2-49. ^{1}H NMR spectrum (500 MHz, $CDCl_3$) of the Michael addition product **P1** of nitromethylacetate **Nu1H** and methyl vinyl ketone **E1**.*

2.7.6.2 Michael addition product P2 of benzoylnitromethane Nu2H and methyl vinyl ketone E1

Benzoylnitromethane (500 mg, 3.03 mmol) and methyl vinyl ketone (0.25 ml, 3.0 mmol) were combined in CH_3CN (20 ml). DBU (88 µl, 0.61 mmol) was added to the mixture. The reaction was stirred at room temperature overnight and then quenched with glacial acetic acid (5.0 ml, 87 mmol). The mixture was concentrated *in vacuo*, and the residue was diluted with CH_2Cl_2 (25 ml). The organic layer was washed with H_2O (25 ml) three times before drying over $MgSO_4$. The solvent was removed *in vacuo* and product purified by silica flash column (CH_2Cl_2, R_f = 0.40) to give a colorless oil (0.18 g, 25%). ^{1}H NMR (500 MHz, $CDCl_3$) δ 8.08 (m, 2H, H_a), 7.65 (m, 1H, H_b), 7.56 – 7.50 (m, 2H, H_c), 6.31 (m, 1H, H_d), 2.74 – 2.60 (m, 2H, H_e), 2.48 – 2.41 (m, 2H, H_f), 2.16 (s, 3H, H_g) ppm. ^{13}C NMR (126 MHz, $CDCl_3$) δ 207.27, 189.48, 134.93, 133.55, 129.29, 129.14, 88.99, 38.64, 30.01, 24.63 ppm. HRMS (EI): $C_{12}H_{13}NO_4$ $[M]^{\cdot+}$ found 235.08348, requires 235.08391.

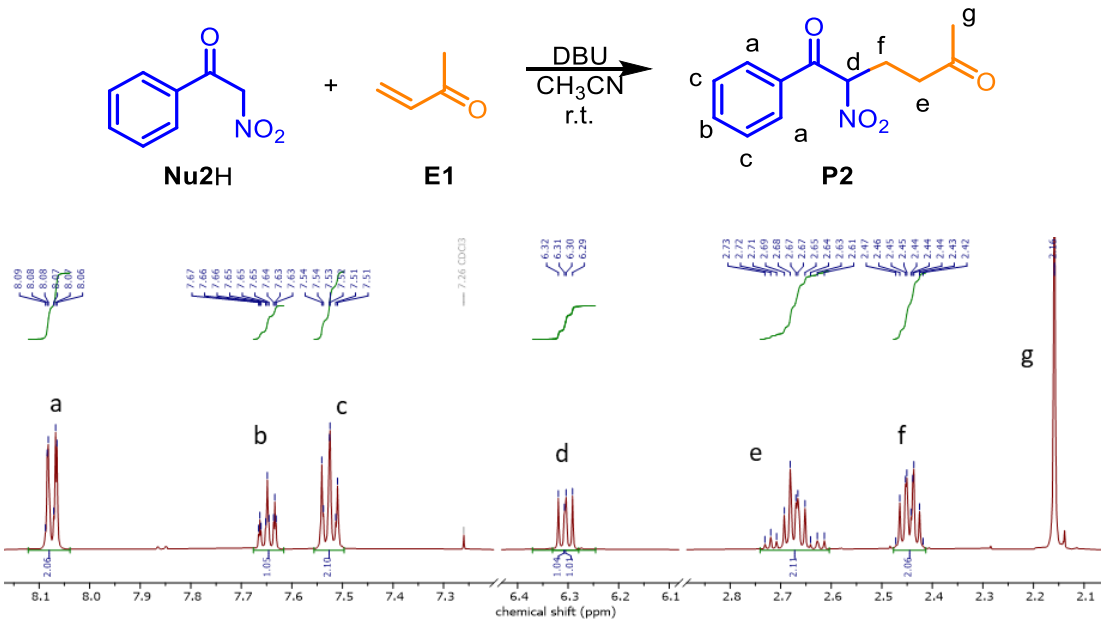

*Figure 2-50. ^{1}H NMR spectrum (500 MHz, $CDCl_3$) of the Michael addition product **P2** of benzoylnitromethane **Nu2H** and methyl vinyl ketone **E1**.*

2.7.6.3 Michael addition product P3 of benzoylnitromethane Nu2H and methyl acrylate E2

Benzoylnitromethane (1.0 g, 6.1 mmol) and methyl acrylate (0.52 ml, 6.1 mmol) were combined in CH_3CN (20 ml). DBU (0.18 ml, 1.2 mmol) was added to the mixture. The reaction was stirred at room temperature for 5 days and then quenched with glacial acetic acid (5.0 ml, 87 mmol). The mixture was concentrated *in vacuo*, and the residue was diluted with CH_2Cl_2 (25 ml). The organic layer was washed with H_2O (25 ml) three times before drying over $MgSO_4$. The solvent was removed *in vacuo* and product purified by silica flash column (CH_2Cl_2, R_f = 0.45) to give a light-yellow oil (0.46 g, 30%). ^{1}H NMR (500 MHz, $CDCl_3$) δ 8.08 (m, 2H, H_a), 7.70 – 7.65(m, 1H, H_b), 7.58 – 7.52 (m, 2H, H_c), 6.42 – 6.36 (m, 1H, H_d), 3.73 (s, 3H, H_e), 2.64 – 2.43 (m, 4H, H_f + H_g) ppm. ^{13}C NMR (126 MHz, $CDCl_3$) δ 189.13, 172.82, 135.03, 133.68, 129.41, 129.24, 88.76, 52.23, 29.52, 25.77 ppm. HRMS (EI): $C_{12}H_{13}NO_5$ $[M]^{\cdot+}$ found 251.07659, requires 251.07882.

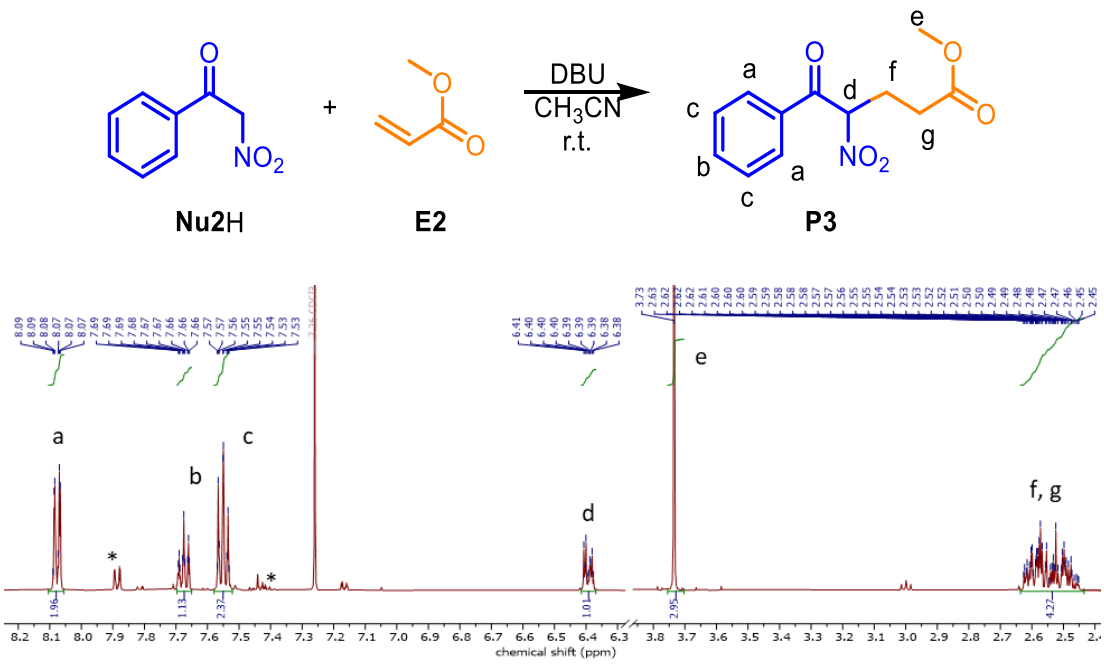

*Figure 2-51. ^{1}H NMR spectrum (500 MHz, $CDCl_3$) of the Michael addition product **P3** of benzoylnitromethane **Nu2H** and methyl acrylate **E2**.*

2.7.6.4 Michael addition product P4 of benzoylnitromethane Nu2H and acrylonitrile E3

This product could not be readily prepared using an uncatalyzed (DBU) method and was prepared using cage catalysis. Benzoylnitromethane (66 mg, 0.40 mmol) and acrylonitrile (5.3 mg, 0.10 mmol) were combined in CH_2Cl_2 (15 ml). **C1** (56 mg, 0.012 mmol) and 18-crown-6 (22.7 mg, 0.0859 mmol) were added to the mixture. The reaction was stirred at room temperature for 140 hours then concentrated *in vacuo*. The residual yellow oil was purified by preparative TLC (CH_2Cl_2, R_f = 0.29), yielding a colorless oil (1.2 mg, 5.5%). ^{1}H NMR (500 MHz, $CDCl_3$) δ 8.05 – 8.00 (m, 2H, H_a), 7.71 – 7.68 (m, 1H, H_b), 7.60 – 7.54 (m, 2H, H_c), 4.75 – 4.62 (m, 3H, H_d + H_f), 2.84 – 2.74 (m, 1H, H_e), 2.64 – 2.56 (m, 1H, $H_{e'}$) ppm. ^{13}C NMR (126 MHz, $CDCl_3$) δ 188.71, 135.36, 133.60, 129.50, 129.17, 115.87, 71.69, 36.37, 26.29 ppm. HRMS (EI): $C_{11}H_{10}N_2O_3$ $[M]^{\cdot+}$ found 218.06822, requires 218.06859.

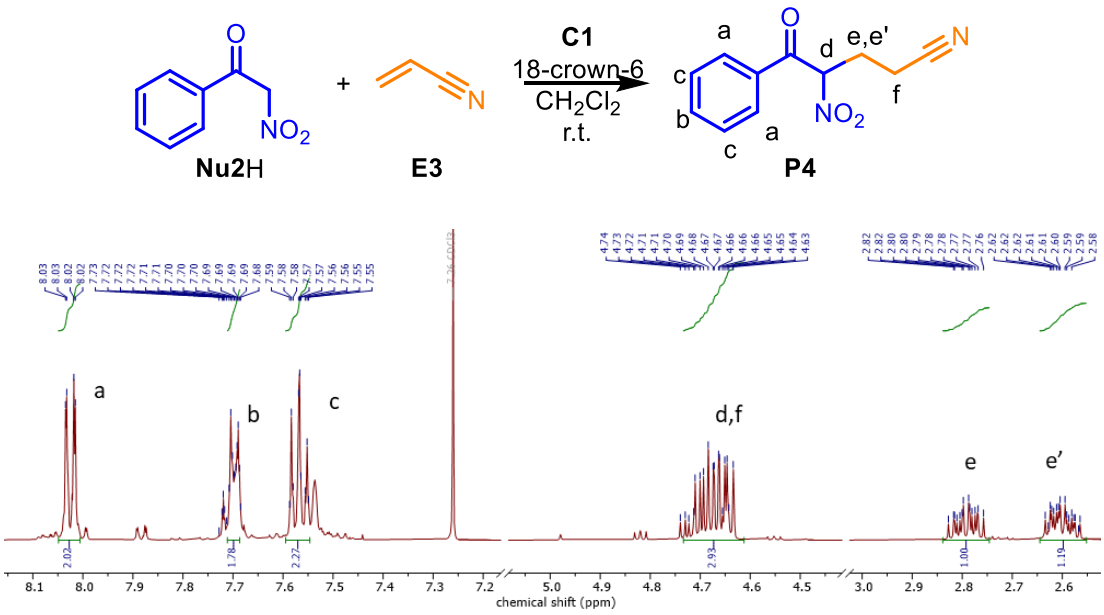

*Figure 2-52. ^{1}H NMR spectrum (500 MHz, $CDCl_3$) of the Michael addition product **P4** of benzoylnitromethane **Nu2H** and acrylonitrile **E3**.*

2.7.6.5 Michael addition product P5 of 1-nitrocyclohexene E4 and nitromethylacetate Nu1H

1-Nitrocyclohexene (80 mg, 0.39 mmol) and nitromethylacetate (234 mg, 1.97 mmol) were combined in CH_2Cl_2 (5 ml). DBU (12 mg, 78 µmol) was added to the mixture. The reaction was stirred at room temperature for five days and then quenched with glacial acetic acid (0.50 ml, 8.7 mmol). The mixture was washed with H_2O (10 ml) three times before drying over $MgSO_4$. Removing the solvent in reduced pressure gave a yellow oil as crude product. This was further purified by preparative TLC (CH_2Cl_2, R_{f1} = 0.47, R_{f2} = 0.55), yielding a colorless oil (11 mg, 13%). The syn- and anti-isomers were assigned according to whether the ^3J coupling constants of proton H_a fall in $^3J_{axial\text{-}axial}$ or $^3J_{axial\text{-}equatorial}$ range. ^1H NMR (500 MHz, $CDCl_3$) δ 5.48 – 5.44 (m, 2H, $H_{b\text{-}\mathbf{P5c}}$ + $H_{b\text{-}\mathbf{P5d}}$), 5.18 (d, J = 3.4 Hz, 1H, $H_{b\text{-}\mathbf{P5a/b}}$), 5.09 (d, J = 3.1 Hz, 1H, $H_{b\text{-}\mathbf{P5a/b}}$), 5.01 (apparent q, J = 3.0 Hz, 1H, $H_{a\text{-}\mathbf{P5c/d}}$), 4.72 (apparent q, J = 3.3 Hz, 1H, $H_{a\text{-}\mathbf{P5c/d}}$), 4.66 (apparent td, J = 11.3, 4.2 Hz, 1H, $H_{a\text{-}\mathbf{P5a/b}}$), 4.57 (apparent td, J = 11.4, 4.2 Hz, 1H, $H_{a\text{-}\mathbf{P5a/b}}$), 3.86 – 3.83 (m, 12H, $H_{c\text{-}\mathbf{P5a}}$ + $H_{c\text{-}\mathbf{P5b}}$ + $H_{c\text{-}\mathbf{P5c}}$ + $H_{c\text{-}\mathbf{P5d}}$), 3.05 – 2.90 (m, 2H, $H_{d\text{-}\mathbf{P5a}}$ + $H_{d\text{-}\mathbf{P5b}}$), 2.87 – 2.80 (m, 2H, $H_{d\text{-}\mathbf{P5c}}$ + $H_{d\text{-}\mathbf{P5d}}$), 2.62 – 2.53 (m, 2H, $H_{e\text{-}\mathbf{P5c}}$+ $H_{e\text{-}\mathbf{P5d}}$), 2.47 – 2.38 (m, 2H, $H_{e\text{-}\mathbf{P5a}}$ + $H_{e\text{-}\mathbf{P5b}}$), 2.16 – 1.31 (m, 28H, $H_{f\text{-}\mathbf{P5a}}$+ $H_{f\text{-}\mathbf{P5b}}$ + $H_{f\text{-}\mathbf{P5c}}$ + $H_{f\text{-}\mathbf{P5d}}$ + $H_{e'\text{-}\mathbf{P5a}}$ + $H_{e'\text{-}\mathbf{P5b}}$ + $H_{e'\text{-}\mathbf{P5c}}$ + $H_{e'\text{-}\mathbf{P5d}}$ + $H_{g\text{-}\mathbf{P5a}}$ + $H_{g\text{-}\mathbf{P5b}}$ + $H_{g\text{-}\mathbf{P5c}}$ + $H_{g\text{-}\mathbf{P5d}}$ + $H_{h\text{-}\mathbf{P5a}}$ + $H_{h\text{-}\mathbf{P5b}}$ + $H_{h\text{-}\mathbf{P5c}}$ + $H_{h\text{-}\mathbf{P5d}}$) ppm. ^{13}C NMR (126 MHz, $CDCl_3$) δ 164.02, 163.75, 163.47, 163.34, 90.35, 88.94, 87.35, 86.68, 85.82, 85.70, 81.69, 81.15, 54.00, 53.98, 53.88, 53.72, 41.71, 41.29, 40.69, 40.60, 32.78, 32.58, 30.16, 30.14, 25.70, 25.44, 24.63, 24.52, 24.45, 24.30, 24.21, 24.15, 24.00, 23.20, 20.20, 20.04 ppm. HRMS (EI): $C_9H_{14}N_2O_6{}^{23}Na$ $[M + Na]^+$ found 269.07290, requires 269.07441.

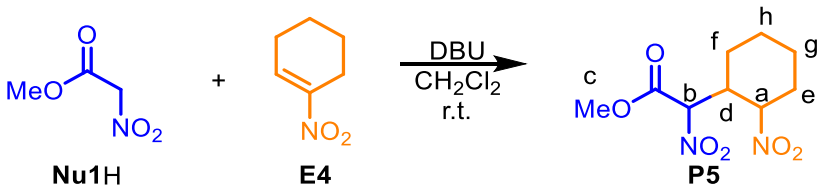

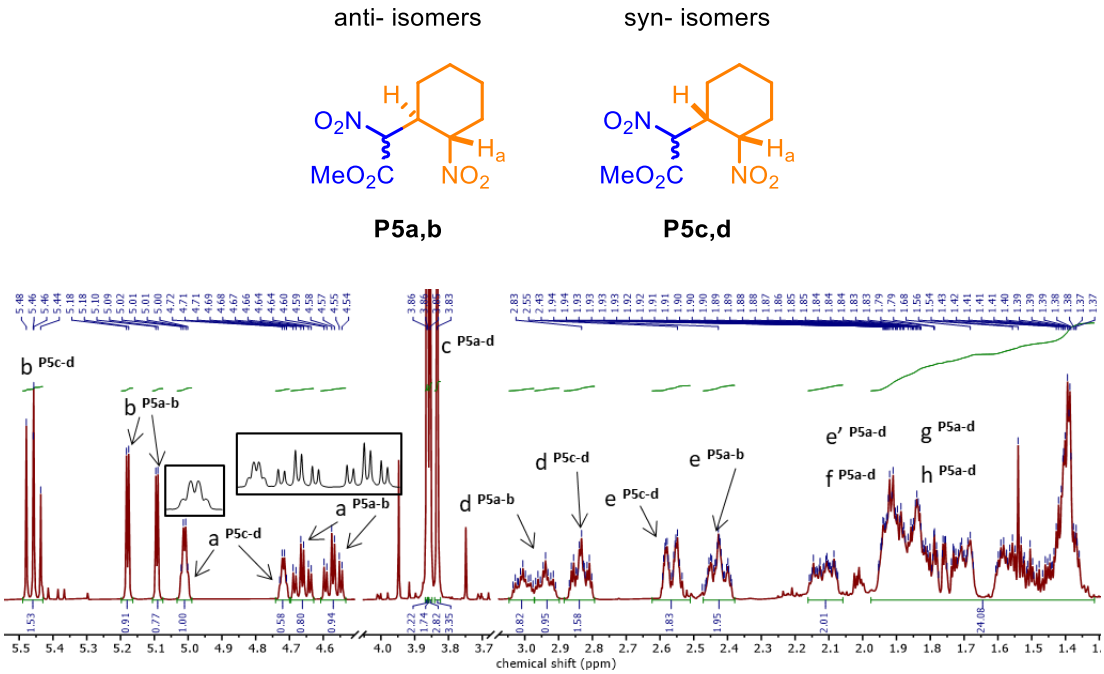

*Figure 2-53. ^{1}H NMR spectrum (500 MHz, $CDCl_3$) of the Michael addition product **P5** of nitromethylacetate **Nu1H** and 1-nitrocyclohexene **E4**.*

2.7.6.6 Michael addition product P7 of malononitrile Nu4H and methyl vinyl ketone E1

Malononitrile (150 mg, 2.27 mmol) and methyl vinyl ketone (84 mg, 1.2 mmol) were combined in CH_2Cl_2 (10 ml). DBU (35 mg, 0.23 mmol) was added to the mixture. The reaction was stirred at room temperature for 35 minutes and then quenched with glacial acetic acid (1.5 ml, 26 mmol). The mixture was concentrated *in vacuo*, and the residue was re-diluted with CH_2Cl_2 (25 ml). The organic layer was washed with H_2O (25 ml) three times before drying over $MgSO_4$. Removing the solvent in reduced pressure gave a yellow oil as crude product (130 mg, 81%). An analytical amount (37 mg) of this oil was purified by preparative TLC (CH_2Cl_2, R_f = 0.33), yielding a colorless oil (5.0 mg, 14%). ^{1}H NMR (500 MHz, $CDCl_3$) δ 4.11 (t, *J* = 7.5 Hz, 1H, H_a), 2.80 (t, *J* = 6.5 Hz, 2H, H_b), 2.29 (td, *J* = 7.5, 6.5 Hz, 2H, H_c), 2.23 (s, 3H, H_d) ppm. ^{13}C NMR (126 MHz, $CDCl_3$) δ 205.83, 112.44, 38.64, 30.11, 25.19, 21.54 ppm. HRMS (EI): $C_7H_8N_2O$ $[M]^{\cdot+}$ found 136.06378, requires 136.06311.

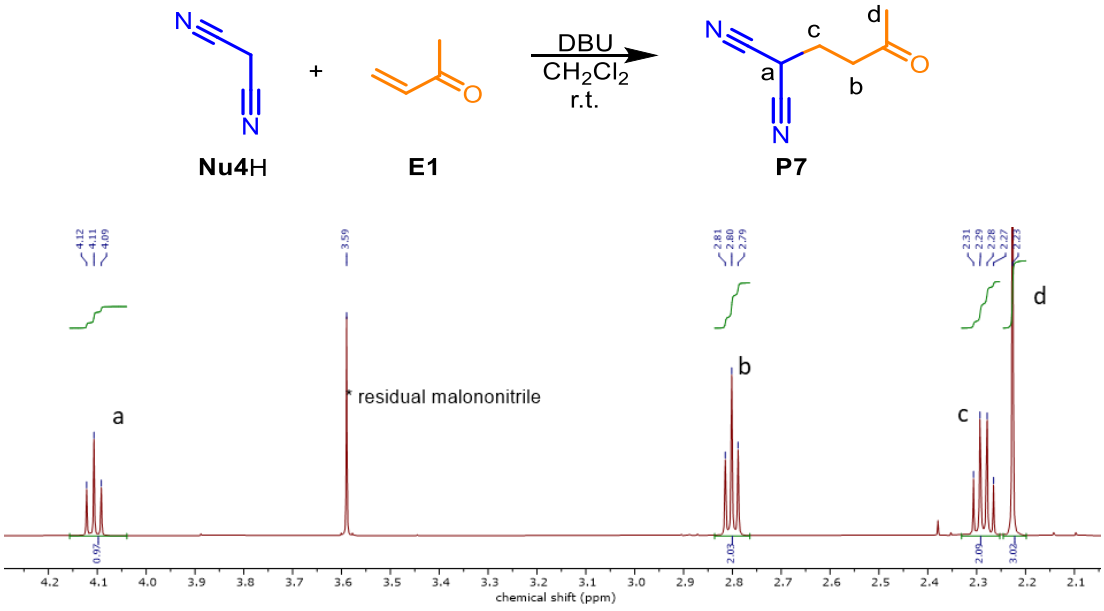

*Figure 2-54. ^{1}H NMR spectrum (500 MHz, $CDCl_3$) of the Michael addition **P7** product of malononitrile **Nu4H** and methyl vinyl ketone **E1**.*

2.7.6.7 Michael addition product P8 of benzoylacetonitrile Nu5H and methyl vinyl ketone E1

Benzoylacetonitrile (880 mg, 6.06 mmol) and methyl vinyl ketone (0.50 ml, 6.1 mmol) were combined in a mixture of CH_3CN (20 ml) and CH_2Cl_2 (15 ml). DBU (0.18 ml, 1.2 mmol) was added to the mixture. The reaction was stirred at room temperature for five days and then quenched with glacial acetic acid (5.0 ml, 87 mmol). The mixture was concentrated *in vacuo*, and the residue diluted with CH_2Cl_2 (25 ml). The organic layer was washed with H_2O (25 ml) three times before drying over $MgSO_4$. Removing the solvent in reduced pressure gave a red oil as crude product (1.1 g, 87%). An analytical amount (25 mg) of this oil was purified by preparative TLC (CH_2Cl_2, R_f = 0.23), yielding a light-yellow oil (6.1 mg, 24%). ^{1}H NMR (500 MHz, $CDCl_3$) δ 8.08 – 8.03 (m, 2H, H_a), 7.68 – 7.64 (m, J = 1H, H_b), 7.57 – 7.51 (m, 2H, H_c), 4.67 (dd, J = 9.5, 5.3 Hz, 1H, H_d), 2.90 – 2.73 (m, 2H, H_e), 2.40 – 2.32 (m, 1H, H_f), 2.21 (s, 3H, H_g), 2.14 – 2.05 (m, 1H, $H_{f'}$) ppm. ^{13}C NMR (126 MHz, $CDCl_3$) δ 207.30, 190.85, 134.77, 133.91, 129.31, 129.10, 117.16, 39.67, 39.06, 30.22, 23.99 ppm. HRMS (EI): $C_{13}H_{13}NO_2$ $[M]^{\cdot+}$ found 215.09299, requires 215.09408.

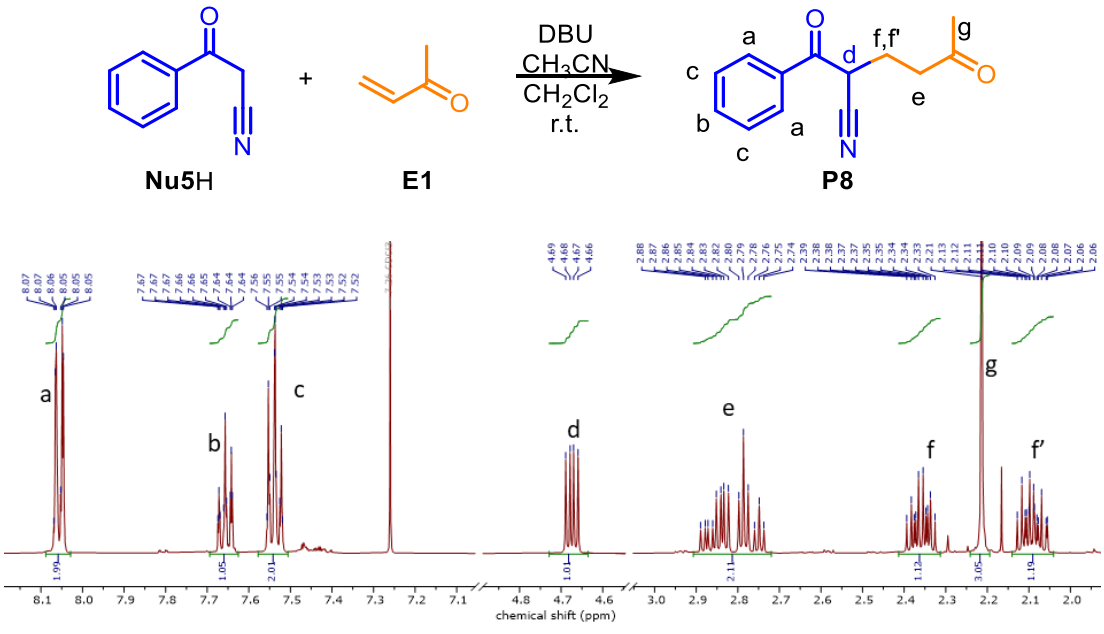

*Figure 2-55. ^{1}H NMR spectrum (500 MHz, $CDCl_3$) of the Michael addition product **P8** of benzoylacetonitrile **Nu5H** and methyl vinyl ketone **E1**.*

2.7.7 Preparative scale Michael addition using C1 as catalyst

Commercial methyl vinyl ketone **E1** was purified via distillation and nitromethylacetate **Nu1H** was purified via silica plug (eluent: CH_2Cl_2) prior to this experiment. Nitromethylacetate **Nu1H** (75 mg, 0.63 mmol) and methyl vinyl ketone **E1** (33 mg, 0.42 mmol) were combined in CH_2Cl_2 (70 ml). **C1** (40 mg, 8.4 µmol, 2.0 mol%) and 18-crown-6 (11 mg, 42 µmol, 10 mol%) were added to the mixture. The reaction was stirred at room temperature for 44 hours then concentrated *in vacuo*. The residual pale-yellow oil was purified by column chromatography (CH_2Cl_2, R_f = 0.28), yielding a colorless oil (72 mg, 91%).

2.7.8 Crystallographic data of P1⊂C1

Experimental: Single colourless block crystals of **P1⊂C1** recrystallised from dichloromethane by slow evaporation. A suitable crystal with dimensions 0.16 × 0.10 × 0.10 mm^3 was selected and mounted on a MITIGEN holder in Paratone oil on a Rigaku Oxford Diffraction SuperNova diffractometer. The crystal was kept at a steady T = 120.01(10) K during data collection. The structure was solved with the 2018/2 version **ShelXT**[70] solution program using dual methods and by using **Olex2**[71] as the graphical interface. The model was refined with the 2018/3 version **ShelXL**[72] using full matrix least squares minimisation on $\boldsymbol{F^2}$.

Crystal data: $C_{219.5}H_{117.5}B_4Cl_{16}F_{96}N_{8.5}O_{2.5}Pd_2$, *Mr* = 5560.95, monoclinic, $P2_1/c$ (No. 14), a = 21.1146(2) Å, b = 39.7901(4) Å, c = 28.2343(3) Å, β = 99.9350(10)°, $\alpha = \gamma$ = 90°, *V* = 23365.4(4) $Å^3$, *T* = 120.01(10) K, *Z* = 4, *Z'* = 1, μ(Cu K_α) = 4.113, 220199 reflections measured, 44585 unique (R_{int} = 0.1030) which were used in all calculations. The final wR_2 was 0.2429 (all data) and R_1 was 0.0835 (I≥2 σ(I)).

Structure:

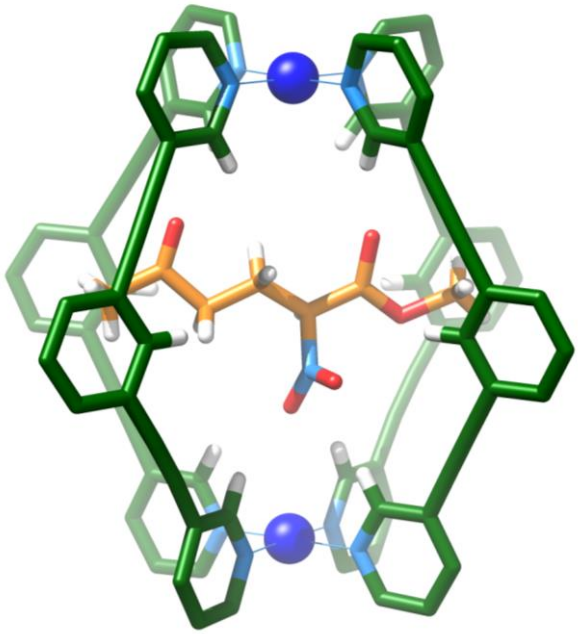

Full crystallographic data of P1⊂C1

Compound	**P1⊂C1**
Formula	$C_{219.5}H_{117.5}B_4Cl_{16}F_{96}N_{8.5}O_{2.5}Pd_2$
$D_{calc.}$/ g cm^{-3}	1.581
μ/mm^{-1}	4.113
Formula Weight	5560.95
Colour	colourless
Shape	block
Size/mm^3	0.16×0.10×0.10
T/K	120.01(10)
Crystal System	monoclinic
Space Group	$P2_1/c$
a/Å	21.1146(2)
b/Å	39.7901(4)
c/Å	28.2343(3)
α/°	90
β/°	99.9350(10)
γ/°	90
V/Å^3	23365.4(4)
Z	4
Z'	1
Wavelength/Å	1.54184
Radiation type	Cu K$_\alpha$
Θ_{min}/°	3.367
Θ_{max}/°	70.745
Measured Refl's.	220199
Indep't Refl's	44585
Refl's I≥2 σ(I)	34511
R_{int}	0.1030
Parameters	3226
Restraints	690
Largest Peak	1.829
Deepest Hole	-1.401
GooF	1.028
wR_2 (all data)	0.2429
wR_2	0.2209
R_1 (all data)	0.1032
R_1	0.0835

2.7.9 Computational methods

All density functional theory calculations were performed in ORCA v. 4.2.1 using a methodology we have found to be accurate for modelling these systems.[33] Geometry optimizations were performed with the hybrid PBE0[73] functional in combination with the def2-SVP[74] basis set and the D3BJ[75],[76] dispersion correction scheme. Palladium was described using default effective core potentials.[77] Using these geometries, energies were calculated using the M06-2X functional,[78] def2-TZVP[74] basis set and SMD[79] implicit solvation model with parameters for dichloromethane. All calculations utilized the resolution of identity with the chain of spheres approximation for the exchange integrals (RIJCOSX) with the default auxiliary basis sets.[80] Initial cage-substrate complexes were generated using cgbind[81] and the conformational space explored manually. Electrostatic potentials (ESP) were constructed using Hirshfeld partial atomic charges obtained at PBE0-D3BJ/def2-SVP level of theory in the *xz* plane and the electric field (***F***) calculated as the gradient (∇ESP(*x*, *z*)).

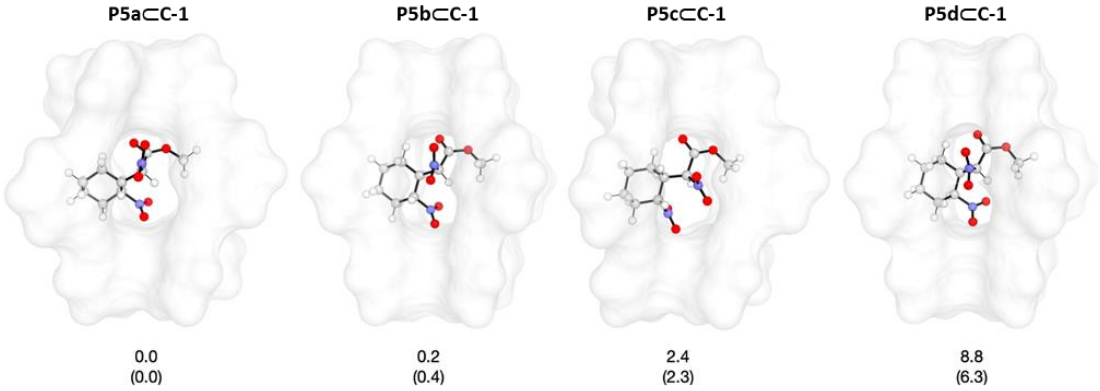

*Figure 2-56. Relative energies in kcal mol-1 and 3D geometries of **P5** diastereomers within **C1** calculated at the SMD(DCM)-M06-2X/def2-TZVP//PBE0-D3BJ/def2-SVP level of theory. Energies for unencapsulated species at the same level of theory are shown in parentheses.*

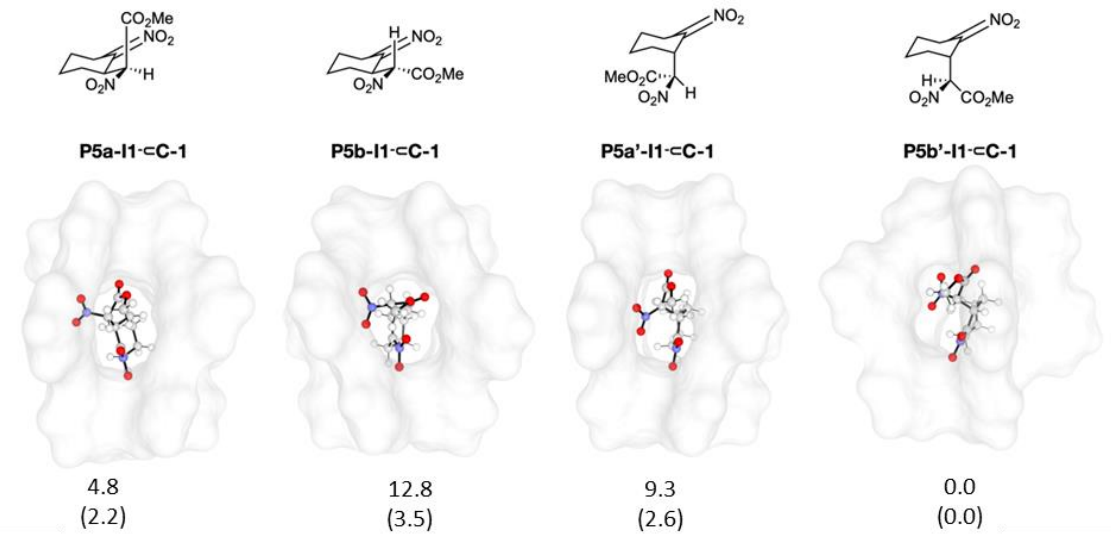

Figure 2-57. Relative energies in kcal mol-1 and 3D geometries of the ***P5-I1$^-$⊂ C1*** *intermediate complexes, calculated at the SMD(DCM)-M06-2X/def2-TZVP//PBE0-D3BJ/def2-SVP level of theory.* ***P5a-I1$^-$*** *and* ***P5a'-I1$^-$*** *are the enantiomeric homochiral intermediates and* ***P5b-I1$^-$*** *are* ***P5b'-I1$^-$*** *and enantiomeric heterochiral intermediates. Each enantiomeric pair have been calculated with nitro-ester methine fragment positioned in either the pseudo-equatorial position (e.g.* ***P5a-I1$^-$*** *and* ***P5b-I1$^-$****) or with the same group in the pseudoaxial position (e.g.* ***P5a'-I1$^-$*** *and* ***P5b'-I1$^-$****).* ***P5b-I1$^-$⊂ C1*** *is highly unstable partially due to a loss of O–H(C) hydrogen bond interaction between the substrate and the cage. Relative energies for the unencapsulated intermediates, at the same level of theory, are shown in parentheses.*

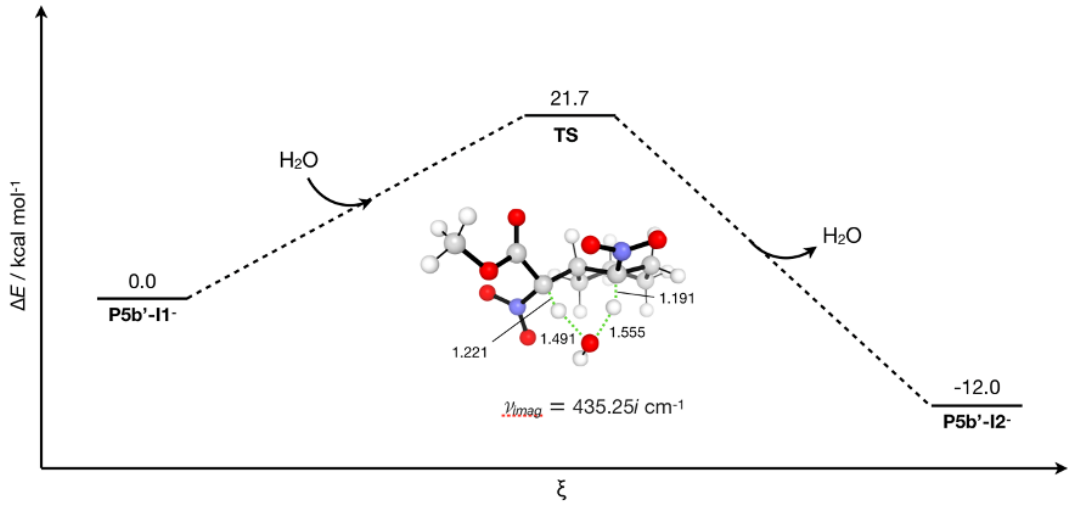

Figure 2-58. Reaction profile for the water-assisted intramolecular proton transfer of ***P5b'-I1$^-$****, calculated at the SMD(DCM)-M06-2X/def2-TZVP//PBE0-D3BJ/def2-SVP level of theory.*

Table 2-3. Calculated absolute (Hartree) and relative (in kcal/mol) energies for species show in Figure 2-56. M1 = PBE0-D3BJ/def2-SVP, M2 = SMD(DCM)-M06-2X/def2-TZVP.

Species	***E*(M1)**	**Δ*E*(M1)**	***E*(M2//M1)**	**Δ*E*(M2//M1)**
P5a	-910.4284014	0.0	-912.0745087	0.0
P5b	-910.4267410	1.0	-912.0738333	0.4
P5c	-910.4223268	3.8	-912.0707644	2.3
P5d	-910.4204814	5.0	-912.0645070	6.3
P5a⊂C1	-4673.8681104	4.0	-4682.1709253	0.0
P5b⊂C1	-4673.8745658	0.0	-4682.1705967	0.2
P5c⊂C1	-4673.8639282	2.6	-4682.1670726	2.4
P5d⊂C1	-4673.8648997	6.1	-4682.1569046	8.8

Table 2-4. Calculated absolute (Hartree) and relative (in kcal/mol) energies for species show in Figure 2-57. M1 = PBE0-D3BJ/def2-SVP, M2 = SMD(DCM)-M06-2X/def2-TZVP.

Species	***E*(M1)**	**Δ*E*(M1)**	***E*(M2//M1)**	**Δ*E*(M2//M1)**
P5a-I1$^-$	-909.8699032	1.5	-911.5809357	2.2
P5b-I1$^-$	-909.8583915	8.7	-911.5789196	3.5
P5a'-I1$^-$	-909.8574333	9.3	-911.5803382	2.6
P5b'-I1$^-$	-909.8722142	0.0	-911.584477	0.0
P5a-I1$^-$⊂C1	-4673.624961	6.0	-4681.727317	4.8
P5b-I1$^-$⊂C1	-4673.607326	17.0	-4681.714503	12.8
P5a'-I1$^-$⊂C1	-4673.621926	7.9	-4681.720167	9.3
P5b'-I1$^-$⊂C1	-4673.634484	0.0	-4681.734958	0.0

Table 2-5. Calculated absolute (Hartree) and relative (in kcal/mol) energies for species show in Figure 2-58. M1 = PBE0-D3BJ/def2-SVP, M2 = SMD(DCM)-M06-2X/def2-TZVP.

Species	***E*(M1)**	**Δ*E*(M1)**	***E*(M2//M1)**	**Δ*E*(M2//M1)**
H_2O	-76.276703	-	-76.43501917	-
P5b'-I1$^-$	-909.8738831	0.0	-911.5853070	0.0
TS	-986.1403275	6.4	-987.9856952	21.7
P5b'-I2$^-$	-909.8945734	-13.0	-911.6044154	-12.0

2.8 References

[1] A. Warshel, P. K. Sharma, M. Kato, Y. Xiang, H. Liu, M. H. M. Olsson, *Chem. Rev.* **2006**, *106*, 3210–3235.
[2] R. R. Knowles, E. N. Jacobsen, *Proc. Natl. Acad. Sci.* **2010**, *107*, 20678–20685.
[3] A. J. Neel, M. J. Hilton, M. S. Sigman, F. D. Toste, *Nature* **2017**, *543*, 637–646.
[4] H. J. Davis, R. J. Phipps, *Chem. Sci.* **2017**, *8*, 864–877.
[5] M. D. Pluth, R. G. Bergman, K. N. Raymond, *Science* **2007**, *316*, 85–88.
[6] S. M. Bierschenk, R. G. Bergman, K. N. Raymond, F. D. Toste, *J. Am. Chem. Soc.* **2020**, *142*, 733–737.
[7] C. J. Hastings, M. D. Pluth, R. G. Bergman, K. N. Raymond, *J. Am. Chem. Soc.* **2010**, *132*, 6938–6940.
[8] D. M. Kaphan, M. D. Levin, R. G. Bergman, K. N. Raymond, F. D. Toste, *Science* **2015**, *350*, 1235–1238.
[9] R. Chakrabarty, P. S. Mukherjee, P. J. Stang, *Chem. Rev.* **2011**, *111*, 6810–6918.
[10] T. R. Cook, P. J. Stang, *Chem. Rev.* **2015**, *115*, 7001–7045.
[11] Y. Sun, C. Chen, J. Liu, P. J. Stang, *Chem. Soc. Rev.* **2020**, *49*, 3889–3919.
[12] G. H. Clever, S. Tashiro, M. Shionoya, *Angew. Chem. Int. Ed.* **2009**, *48*, 7010–7012.
[13] P. Liao, B. W. Langloss, A. M. Johnson, E. R. Knudsen, F. S. Tham, R. R. Julian, R. J. Hooley, *Chem. Commun.* **2010**, *46*, 4932–4934.
[14] J. E. M. Lewis, E. L. Gavey, S. A. Cameron, J. D. Crowley, *Chem. Sci.* **2012**, *3*, 778–784.
[15] W. M. Bloch, J. J. Holstein, W. Hiller, G. H. Clever, *Angew. Chem. Int. Ed.* **2017**, *56*, 8285–8289.
[16] J. E. M. Lewis, A. Tarzia, A. J. P. White, K. E. Jelfs, *Chem. Sci.* **2020**, *11*, 677–683.
[17] T. Murase, Y. Nishijima, M. Fujita, *J. Am. Chem. Soc.* **2012**, *134*, 162–164.
[18] J. L. Bolliger, A. M. Belenguer, J. R. Nitschke, *Angew. Chem. Int. Ed.* **2013**, *52*, 7958–7962.
[19] W. Cullen, M. C. Misuraca, C. A. Hunter, N. H. Williams, M. D. Ward, *Nat. Chem.* **2016**, *8*, 231–236.
[20] C. G. P. Taylor, A. J. Metherell, S. P. Argent, F. M. Ashour, N. H. Williams, M. D. Ward, *Chem. – Eur. J.* **2020**, *26*, 3065–3073.
[21] Y. Zhao, Y. Domoto, E. Orentas, C. Beuchat, D. Emery, J. Mareda, N. Sakai, S. Matile, *Angew. Chem. Int. Ed.* **2013**, *52*, 9940–9943.
[22] Y. Zhao, Y. Cotelle, L. Liu, J. López-Andarias, A.-B. Bornhof, M. Akamatsu, N. Sakai, S. Matile, *Acc. Chem. Res.* **2018**, *51*, 2255–2263.
[23] J. López-Andarias, A. Frontera, S. Matile, *J. Am. Chem. Soc.* **2017**, *139*, 13296–13299.
[24] D. Fiedler, R. G. Bergman, K. N. Raymond, *Angew. Chem. Int. Ed.* **2004**, *43*, 6748–6751.
[25] C. J. Brown, R. G. Bergman, K. N. Raymond, *J. Am. Chem. Soc.* **2009**, *131*, 17530–17531.

[26] M. D. Pluth, R. G. Bergman, K. N. Raymond, *J. Am. Chem. Soc.* **2008**, *130*, 11423–11429.
[27] C. J. Hastings, M. P. Backlund, R. G. Bergman, K. N. Raymond, *Angew. Chem. Int. Ed.* **2011**, *50*, 10570–10573.
[28] W. Cullen, A. J. Metherell, A. B. Wragg, C. G. P. Taylor, N. H. Williams, M. D. Ward, *J. Am. Chem. Soc.* **2018**, *140*, 2821–2828.
[29] Q. Zhang, K. Tiefenbacher, *Nat. Chem.* **2015**, *7*, 197–202.
[30] W. M. Hart-Cooper, K. N. Clary, F. D. Toste, R. G. Bergman, K. N. Raymond, *J. Am. Chem. Soc.* **2012**, *134*, 17873–17876.
[31] T. M. Bräuer, Q. Zhang, K. Tiefenbacher, *J. Am. Chem. Soc.* **2017**, *139*, 17500–17507.
[32] V. Martí-Centelles, A. L. Lawrence, P. J. Lusby, *J. Am. Chem. Soc.* **2018**, *140*, 2862–2868.
[33] T. A. Young, V. Martí-Centelles, J. Wang, P. J. Lusby, F. Duarte, *J. Am. Chem. Soc.* **2020**, *142*, 1300–1310.
[34] R. L. Spicer, A. D. Stergiou, T. A. Young, F. Duarte, M. D. Symes, P. J. Lusby, *J. Am. Chem. Soc.* **2020**, *142*, 2134–2139.
[35] D. C. Rideout, R. Breslow, *J. Am. Chem. Soc.* **1980**, *102*, 7816–7817.
[36] J. Kang, J. Rebek, *Nature* **1997**, *385*, 50–52.
[37] M. Yoshizawa, M. Tamura, M. Fujita, *Science* **2006**, *312*, 251–254.
[38] D. P. August, G. S. Nichol, P. J. Lusby, *Angew. Chem. Int. Ed.* **2016**, *55*, 15022–15026.
[39] L. Guideri, F. De Sarlo, F. Machetti, *Chem. – Eur. J.* **2013**, *19*, 665–677.
[40] F. Ravalico, S. L. James, J. S. Vyle, *Green Chem.* **2011**, *13*, 1778–1783.
[41] R. Srivastava, *J. Mol. Catal. Chem.* **2007**, *264*, 146–152.
[42] D. A. Evans, D. Seidel, *J. Am. Chem. Soc.* **2005**, *127*, 9958–9959.
[43] Y. Hoashi, T. Okino, Y. Takemoto, *Angew. Chem. Int. Ed.* **2005**, *44*, 4032–4035.
[44] P. R. Schreiner, *Chem. Soc. Rev.* **2003**, *32*, 289–296.
[45] T. Okino, Y. Hoashi, Y. Takemoto, *J. Am. Chem. Soc.* **2003**, *125*, 12672–12673.
[46] M. S. Taylor, E. N. Jacobsen, *Angew. Chem. Int. Ed.* **2006**, *45*, 1520–1543.
[47] H. Huang, E. N. Jacobsen, *J. Am. Chem. Soc.* **2006**, *128*, 7170–7171.
[48] K. Wang, X. Cai, W. Yao, D. Tang, R. Kataria, H. S. Ashbaugh, L. D. Byers, B. C. Gibb, *J. Am. Chem. Soc.* **2019**, *141*, 6740–6747.
[49] C. F. Bernasconi, R. L. Montañez, *J. Org. Chem.* **1997**, *62*, 8162–8170.
[50] E. S. Stoyanov, C. A. Reed, *J. Phys. Chem. A* **2004**, *108*, 907–913.
[51] R. B. Sharma, P. Kebarle, *J. Am. Chem. Soc.* **1984**, *106*, 3913–3916.
[52] M. Bühl, G. Wipff, *J. Am. Chem. Soc.* **2002**, *124*, 4473–4480.
[53] L.-D. Syntrivanis, I. Némethová, D. Schmid, S. Levi, A. Prescimone, F. Bissegger, D. T. Major, K. Tiefenbacher, *J. Am. Chem. Soc.* **2020**, *142*, 5894–5900.
[54] N. Nae, J. Jagur-Grodzinski, *J. Am. Chem. Soc.* **1977**, *99*, 489–494.
[55] W. Taleb Bendiab, F. Hamza Reguig, S. Hamad, B. Martínez-Haya, A. M. Krallafa, *J. Incl. Phenom. Macrocycl. Chem.* **2016**, *85*, 83–92.
[56] R. M. Izatt, J. D. Lamb, N. E. Izatt, B. E. Rossiter, J. J. Christensen, B. L. Haymore, *J. Am. Chem. Soc.* **1979**, *101*, 6273–6276.

[57] R. M. Izatt, N. E. Izatt, B. E. Rossiter, J. J. Christensen, B. L. Haymore, *Science* **1978**, *199*, 994–996.
[58] A. Bryson, *J. Am. Chem. Soc.* **1960**, *82*, 4858–4862.
[59] G. Giorgi, P. López-Alvarado, S. Miranda, J. Rodriguez, J. C. Menéndez, *Eur. J. Org. Chem.* **2013**, *2013*, 1327–1336.
[60] J. M. García, M. A. Maestro, M. Oiarbide, J. M. Odriozola, J. Razkin, C. Palomo, *Org. Lett.* **2009**, *11*, 3826–3829.
[61] R. Ballini, D. Fiorini, M. V. Gil, A. Palmieri, *Tetrahedron* **2004**, *60*, 2799–2804.
[62] B. C. Ranu, S. Banerjee, R. Jana, *Tetrahedron* **2007**, *63*, 776–782.
[63] S. Paganelli, A. Sehionato, C. Botteghi, *Tetrahedron Lett.* **1991**, *32*, 2807–2810.
[64] P. B. Kisanga, P. Ilankumaran, B. M. Fetterly, J. G. Verkade, *J. Org. Chem.* **2002**, *67*, 3555–3560.
[65] E. Trogu, F. De Sarlo, F. Machetti, *Chem. – Eur. J.* **2009**, *15*, 7940–7948.
[66] P. R. Schreiner, A. Wittkopp, *Org. Lett.* **2002**, *4*, 217–220.
[67] S. Mecozzi, J. R. Jr, *Chem. – Eur. J.* **1998**, *4*, 1016–1022.
[68] C. A. Hunter, *Angew. Chem. Int. Ed.* **2004**, *43*, 5310–5324.
[69] S. Rezazadeh, V. Devannah, D. A. Watson, *J. Am. Chem. Soc.* **2017**, *139*, 8110–8113.
[70] G. M. Sheldrick, *Acta Crystallogr. Sect. Found. Adv.* **2015**, *71*, 3–8.
[71] O. V. Dolomanov, L. J. Bourhis, R. J. Gildea, J. A. K. Howard, H. Puschmann, *J. Appl. Crystallogr.* **2009**, *42*, 339–341.
[72] G. M. Sheldrick, *Acta Crystallogr. Sect. C Struct. Chem.* **2015**, *71*, 3–8.
[73] C. Adamo, V. Barone, *J. Chem. Phys.* **1999**, *110*, 6158–6170.
[74] F. Weigend, R. Ahlrichs, *Phys. Chem. Chem. Phys.* **2005**, *7*, 3297–3305.
[75] S. Grimme, J. Antony, S. Ehrlich, H. Krieg, *J. Chem. Phys.* **2010**, *132*, 154104.
[76] S. Grimme, S. Ehrlich, L. Goerigk, *J. Comput. Chem.* **2011**, *32*, 1456–1465.
[77] D. Andrae, U. Häußermann, M. Dolg, H. Stoll, H. Preuß, *Theor. Chim. Acta* **1990**, *77*, 123–141.
[78] Y. Zhao, D. G. Truhlar, *Theor. Chem. Acc.* **2008**, *120*, 215–241.
[79] A. V. Marenich, C. J. Cramer, D. G. Truhlar, *J. Phys. Chem. B* **2009**, *113*, 6378–6396.
[80] A. Hellweg, C. Hättig, S. Höfener, W. Klopper, *Theor. Chem. Acc.* **2007**, *117*, 587–597.
[81] T. A. Young, R. Gheorghe, F. Duarte, *J. Chem. Inf. Model.* **2020**, *60*, 3546–3557.

Chapter 3

Non-quinone-based Diels-Alder catalysis of Pd_2L_4 cages

Chapter 3 Non-quinone-based Diels-Alder Catalysis of Pd_2L_4 Cages

*The studies investigating the Diels-Alder reactions of maleimide **3.5** were conducted in collaboration with Dr Vicente Marti-Centelles, a post-doctoral researcher in the Lusby group.*

3.1 Introduction

Traditional supramolecular catalysts often function as an "entropic trap" where reactions are promoted through the high effective molarity of the multiple reaction components that are co-bound in the cavities.[1][2][3] More recent advances in the field have unveiled that reactive intermediates and/or transition state stabilisation by the host molecules can bring about highly efficient, enzyme-like supramolecular catalysis mechanisms.[4][5][6] However, the use of hydrophobic effect still remains the dominant method for substrate encapsulation and cages that are capable of sites specific, directional host-guest interactions are exceedingly rare.[7][8][9][10]

The Lusby group established the methodology of maximising polar host-guest interactions for efficient substrate binding,[11] adapting a Pd_2L_4 cage first reported by Hooley and co-workers.[12] **C1** is equipped with large, non-coordinating $BArF^-$ as charge balancing anions, which leaves the cage cavity "empty" (only occupied by solvent molecules). The inward-facing *ortho*-pyridyl C-H bonds that are highly polarised by the pyridine-Pd^{2+} coordination exhibit excellent hydrogen bond donating properties and can bind complementary quinone guests using electrostatic interactions with the carbonyl oxygen atoms (Figure 3-1). Such binding opens up the scope of supramolecular catalysis using polar, functional group rich substrates, which would not be applicable to systems that employ hydrophobic effect. Moreover, an electrostatic binding model also provides intrinsic electronic "activation" of reactants, meaning that reactivity is no longer dependent on entropic effects.

This ability to modulate the electronic properties of substrates is similar to H-bond donor organocatalysts.[13][14] As such, the homologous Pd_2L_4 structure **C2** has been shown to catalyse the Diels-Alder reactions of the complementary quinone guests with remarkable efficiency (Figure 3-1). The reactivity is ascribed to the ability of **C2** to a) lower the LUMO of the dienophile through binding and b) efficiently stabilise the neutral but polarised Diels-Alder transition state. The Diels-Alder catalysis in **C2** is also among one of the first examples where directional, non-Columbic electrostatic interactions are utilised in supramolecular catalysis. Moreover, as only the quinone molecules required to be bound, this catalytic system does not rely on entropic factors to induce turnover and so product inhibition is minimised. The magnitude of electronic activation by **C1** has been directly assessed by measuring the shift in quinone redox potential.[11][15]

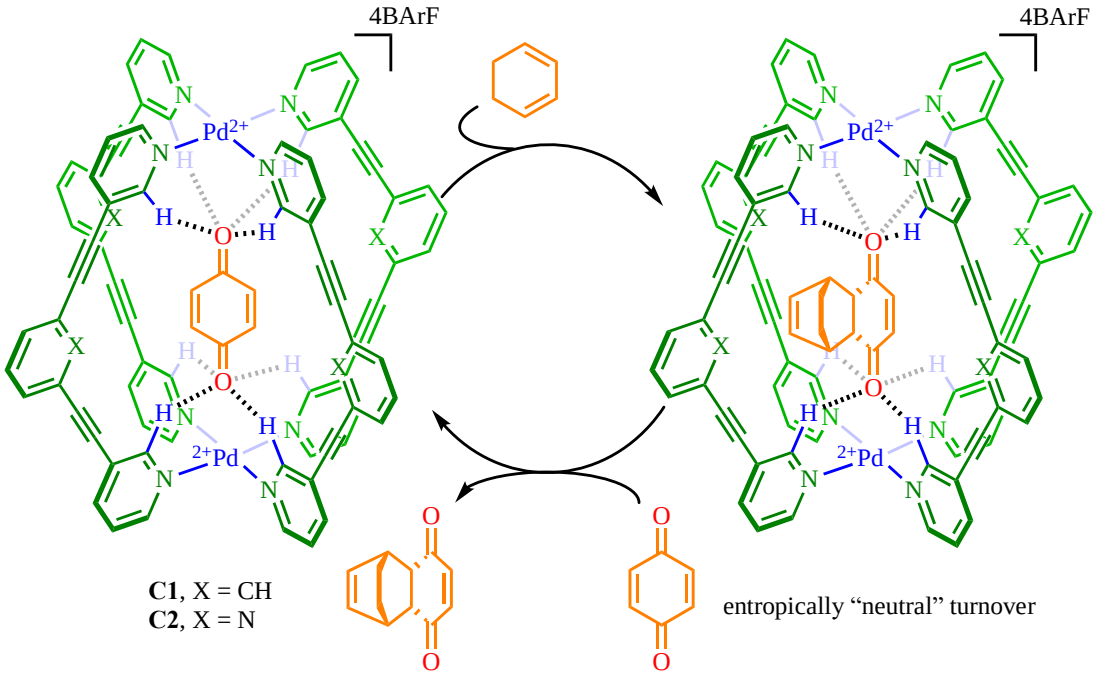

Figure 3-1. The Pd_2L_4 cage catalysed Diels-Alder reaction of the complementary guest, benzoquinone.

3.2 Aims and Objectives

This study aims to expand the scope of the Diels-Alder catalysis in Pd_2L_4 cages and gain a deeper understanding of this process. A range of new, non-quinone-based guest molecules will first be identified and inspected for their binding properties in **C2**. This diverse substrate scope covers functional groups such as esters, ketones and amides.

Branching away from using dienophiles with high complementarity to the cavity, the first part of this work aims to study the catalysis of the weakly binding substrates. Both "doubly" activated guests (the C=C bond is conjugated to two H-bond acceptors that bind to both H-bonding sites of **C2**) and "singly" (the C=C bond is only conjugated to one H-bond acceptor) activated guests are examined. The influence of substrate destabilisation and transition state stabilisation on catalysis will be discussed.

Furthermore, this chapter studies how the microenvironment of the cage cavity may influence the diastereoselective outcomes using non-quinone substrates that form both *endo* and *exo* isomers. Finally, the turnover properties of the **C2** catalysed Diels-Alder reactions will be investigated with different product inhibition scenarios discussed.

3.3 Encapsulation of non-quinone-based dienophiles in C2

Previous studies show that **C2** catalyses Diels-Alder reactions with quinones that bind through simultaneously interacting with both H-bond donor pockets of the cage.[16] Non-quinone-based dienophiles that can interact with **C2** through a similar binding motif were therefore believed to be suitable substrates for expanding the scope of the Diels-Alder catalysis. Dienophiles **3.1**-**3.6** (Figure 3-2). were chosen because they possess two H-bond accepting groups spaced at a similar distance to that in benzoquinone and they are likely to bridge both H-bond sites in **C2**.

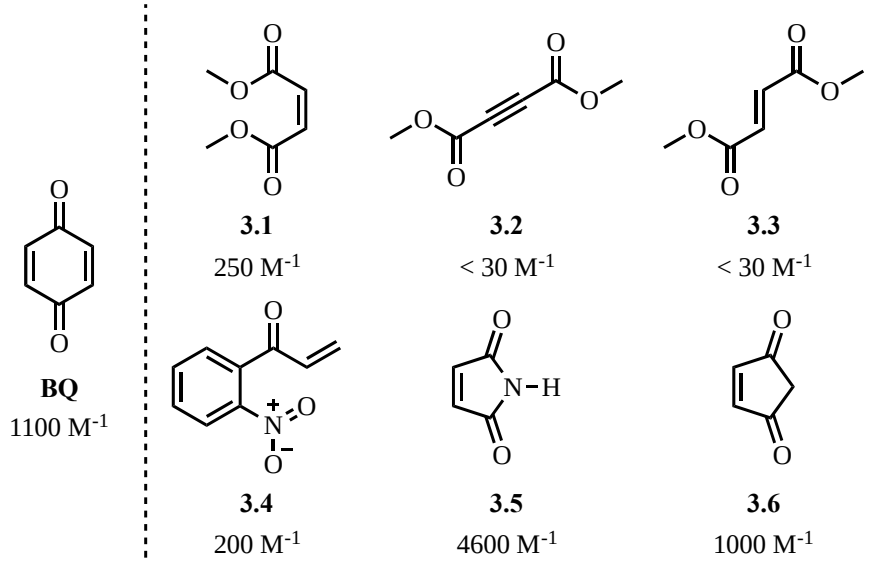

*Figure 3-2. Chemical structures of bridging guests **3.1**-**3.6** and their binding constants in **C2** in comparison to that of benzoquinone.*

3.1-**3.6** exhibit drastically different binding constants with **C2**, ranging from less than 30 M^{-1} up to 4600 M^{-1} (Figure 3-2). For example, **3.1** (K_A = 250 M^{-1}) binds significantly weaker than benzoquinone (K_A = 1100 M^{-1}). Unlike benzoquinone, which adopts a rigid, planar structure, **3.1** has two ester groups that can rotate around the adjacent C-C bonds. Binding **3.1** therefore has a higher entropic barrier as it requires the two C=O bonds to align with each other. It is also likely that the repulsion between the lone pairs on the ester oxygens forces the binding C=O bonds apart, leading to the poorer shape complementarity of **3.1**. Moreover, ester groups are less efficient H-bond

donors than ketones,[17] which causes the lower binding strength of **3.1**. Structurally related ester compounds **3.2** and **3.3** display even weaker binding (< 30 M^{-1}), likely due to the misaligned C=O bonds and also that the carbonyl groups are spaced further apart. Similar to **3.1**, dienophile **3.4** possesses a weak H-bond acceptor, a nitro group,[17] and a free rotating ketone group. This similarly renders **3.4** to be a relatively poor guest, with a binding constant of 200 M^{-1}.

On the other hand, **3.5** (K_A = 4600 M^{-1}) has notably higher binding constants than benzoquinone. The imide groups of **3.5** are better H-bond acceptors than ketones and can lead to stronger interactions.[17] The rigid molecule **3.5** is also pre-organised to bridge both H-bond binding sites of **C2**, reducing the entropic cost for the encapsulation. **3.6** (K_A = 1000 M^{-1}) binds comparably to benzoquinone, owing to their similar rigidity and complementarity with the cage cavity, as well as possessing the same H-bond acceptor groups.

In summary, the variation of guest binding strength reveals that encapsulation in **C2** is determined by multiple factors: complementarity towards the size and shape of the cavity, the inherent H-bond acceptor properties and the pre-organisation that must occur upon association.

3.4 Pd_2L_4 cage catalysed Diels-Alder reactions of non-quinone guests

Many supramolecular catalysis studies focus on exploiting strongly bound substrates. The are many possible reasons for this: it is much easier to investigate the binding of starting materials compared to intermediates or transition states; a tightly binding species will ensure a high concentration of substrate-host complex; and probably because developing high affinity receptors has historically been a defining theme in supramolecular chemistry. In this work, I was interested to explore the Diels-Alder catalysis of the weakly binding guests using **3.1**-**3.5**. Furthermore, **3.1**-**3.3** are thought to be electronically similar to benzoquinone with the carbon-carbon double/triple bond sandwiched between two carbonyl groups. It is also interesting to compare their catalysis with **3.4**, whose C=C bond is only activated by one carbonyl group.

Rate acceleration was observed for the Diels-Alder reaction of **3.1** and **3.7** in the presence of 50 mol% **C2** (orange circles and green triangles, Figure 3-3a) (a relatively high cage loading was used due to the low reactivity). However, adding 3 equivalents of the competitive inhibitor pentacenedione only mildly retarded the reaction but did not reduce the rate of the reaction to the background level. This indicates that the observed catalysis does not solely stem from the substrate being bound and activated within the cage cavity. Firstly, it is feasible that catalysis could occur by interaction with the H-bond donors on the outer face;[18] adding an inhibitor to the Diels-Alder benzoquinone catalysis does not completely halt acceleration either, although the effect is much more pronounced.[16] Another possibility is that the reactivity is partly due to hidden Brønsted acid catalysis.[19] Unpublished research in the Lusby group[20] has shown that these Pd_2L_4 cages are effective at enhancing the acidity of weak acids by binding their anionic conjugate base (although **C1** is much more effective at this form of "exo" catalysis than **C2**). While it could be reasoned that binding the inhibitor in the cavity would prevent the activation of weak acids, anions are known to bind very strongly and could thus act as a competitive binder. Therefore, the commercial sample of **3.1** was washed with $NaHCO_3$ and further purified by a silica plug prior to use and **3.7** was freshly distilled for each experiment in order to remove catalytic

impurities. However, "phantom" catalysis using purified **3.1** and **3.7** persists when the cavity of **C2** is blocked by pentacenedione. It is also feasible that the cage catalyses the hydrolysis of **3.1**,[21][22] and that this generates the corresponding carboxylic acid *in situ*, which is further activated by the cage.

The Diels-Alder reactions using the purified **3.1** and **3.7** samples were also repeated with different batches of **C2**, as prepared by different people in the Lusby group. Disappointingly, these experiments also showed notable inconsistency in the rates of the reactions; at 20 mol% cage loading, the half time of the reactions catalysed by different batches of **C2** compounds varied from 10 hours to 150 hours (Figure 3-3b). Moreover, the reaction of **3.1** and **3.7** was also catalysed using 20 mol% of a mononuclear $Pd(pyridine)_4(BArF)_2$ complex, albeit noticeably slower. This indicates that the Diels-Alder reaction could be catalysed solely through H-bonding to the interior and the exterior of **C2** and that the cavity confinement is not essential. Alternatively, it is also possible that residual impurities in the cage, such as trace amounts of free Pd^{2+}, could contribute to and cause the irreproducible catalytic effects. It should be noted that this inconsistency appears to be confined to the specific reaction of **3.1** as this had not been previously observed using quinone dienophiles.

Despite these problems, it appears that activation of the substrates within **C2** may also contribute to the catalysis of **3.1** and **3.7** as the rate of the reaction declined in the presence of the competitive inhibitor pentacenedione. The geometry of the product **3.8** is analogous to the transition state for this Diels-Alder reaction.[16] **C2** was found to bind the product *endo* **3.8** (K_A = 200 M^{-1}, entry 1, Table 3-1) similarly to the substrate **3.1** (K_A = 250 M^{-1}, entry 1, Table 3-1), which suggests that **C2** is capable of accelerating this reaction. Nevertheless, a definitive conclusion cannot be drawn due to the reaction's sensitivity towards apparent catalytically active impurities.

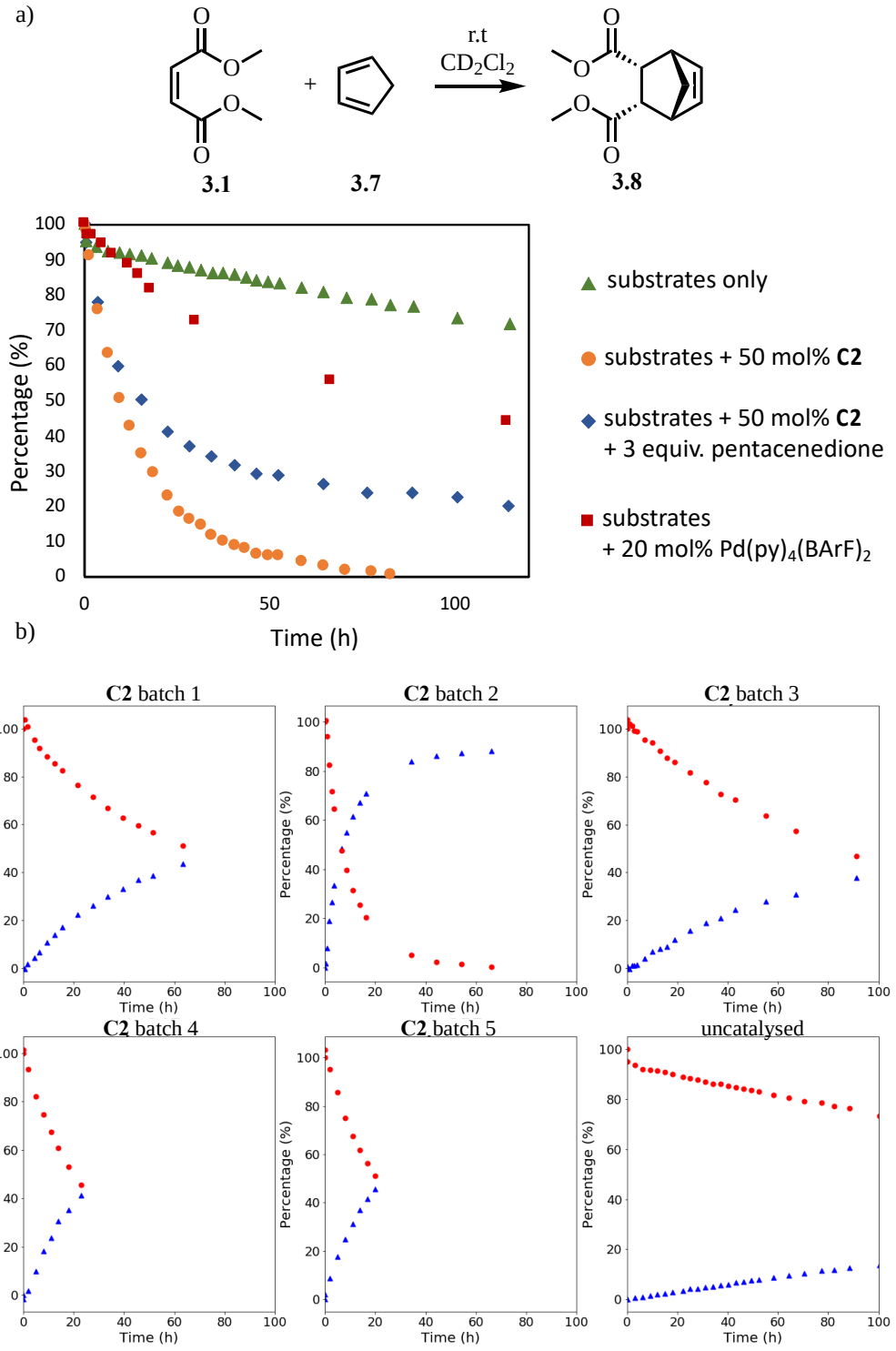

*Figure 3-3. a) While **C2** promotes the reaction Diels-Alder reaction of **3.1** and **3.7**, the catalysis cannot be switched off by competitive inhibitor. Pd(pyridine)$_4$(BArF)$_2$ also shows rate enhancement. b) The kinetic profiles of the reaction of **3.1** and **3.7** in the presence of various batches of **C2** compounds.*

*Table 3-1. Binding constants of dienophiles and Diels-Alder products in **C2**, and the rate enhancements of corrosponding reactions.*

Entry	Dienophile	Diene	$K_{A\text{ - dienophile}}$ (M^{-1})	$K_{A\text{ - product}}$ (M^{-1})	k_{cat} / k_{uncat}
1	**3.1**	**3.7**	250	200[vi]	-
2	**3.2**	**3.7**	< 30	160	135
3	**3.3**	**3.7**	< 30	< 5	0
4	**3.4**	**3.7**	200	~30[vii], ~30[viii]	6.9[ix], 4.9[x]

I then turned my attention to explore the activity of a closely related dienophile, **3.2**. Although **3.2** binds notably weakly in **C2** (K_A < 30 M^{-1}), it is activated by **C2** to undergo Diels-Alder reaction with **3.7**. At 40 mol% **C2** loading (orange circles, Figure 3-4a), a discernible rate enhancement was observed compared to the background rate (blue squares, Figure 3-4a). Fitting the kinetic profile reveals a significant k_{cat}/k_{uncat} of 135 (entry 2, Table 3-1), with k_{cat} and k_{uncat} being the rate constants for the bond forming steps for the bimolecular reactions of **3.7** with **3.2⊂C2** and free **3.2**, respectively. This indicates that the modest acceleration in the observed rate of reaction (k_{obs}) is not because that cage exerts poor "activation" but because the weak substrate association constant gives a low concentration of **3.2⊂C2**. The parameter k_{cat}/k_{uncat} is an important parameter in quantifying cage catalysed Diels-Alder reactions and will be quoted throughout this chapter. The kinetic models and the fitting of k_{cat} and k_{uncat} will be further discussed in section 3.8.6.

Unlike **3.1**, a series of control experiments indicate that the acceleration of **3.2** with **3.7** is directly linked to substrate activation by the cavity. Firstly, in the presence of 5 equivalents of a strongly binding inhibitor, pentacenedione, the catalysis is switched

[vi] K_A value for the *endo* product **3.8**.
[vii] K_A value for the *endo* product **3.11**.
[viii] K_A value for the *exo* product **3.11**.
[ix] k_{cat} / k_{uncat} value for the *endo* reaction of **3.4** and **3.7**.
[x] k_{cat} / k_{uncat} value for the *exo* reaction of **3.4** and **3.7**.

off and the reaction proceeds at the same rate of the background process (red triangles, Figure 3-4a). Secondly, the structurally related analogue **C1** showed no rate acceleration, indicating that the reaction of **3.2** and **3.7** is only promoted in the specific cavity of **C2**, further suggesting that free Lewis acidic Pd^{2+} ions or interactions with the cage periphery are not responsible for catalysis.

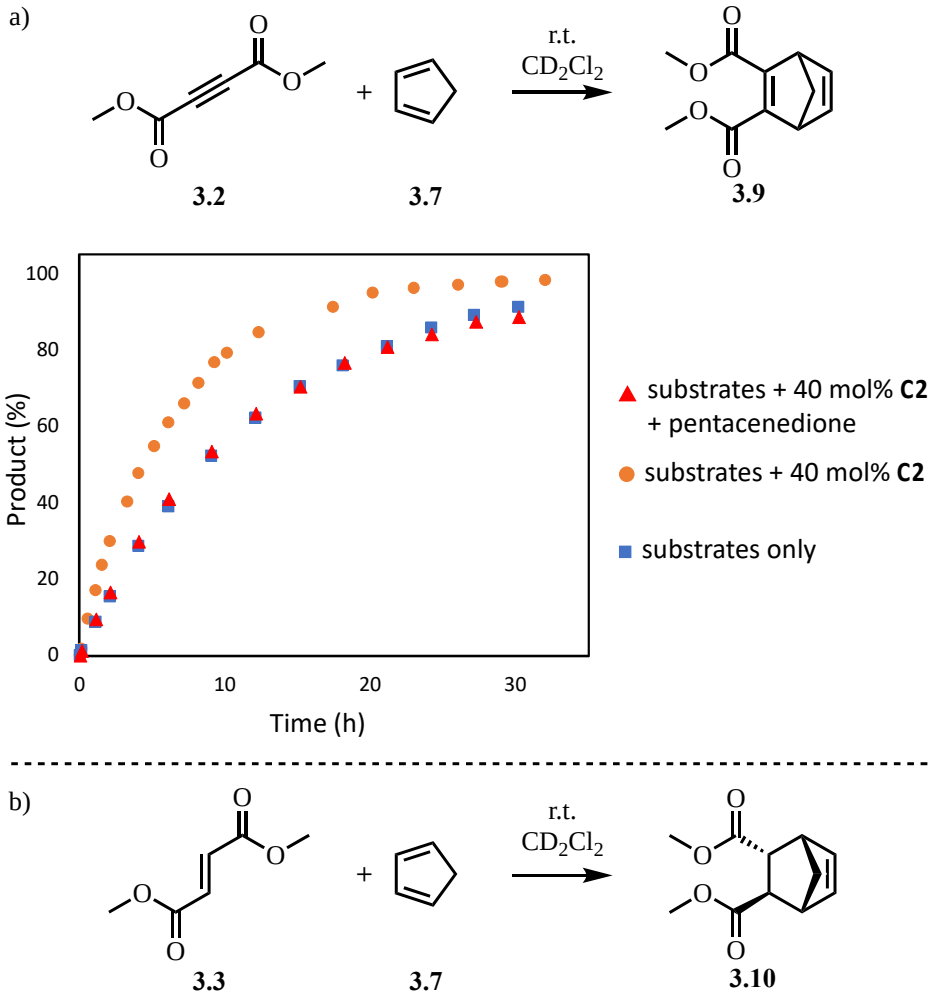

*Figure 3-4. a) Scheme and kinetic profile of the Diels-Alder reaction of **3.2** and **3.7**. b) The Diels-Alder reaction of **3.3** and **3.7**.*

Interestingly, the reaction of the similarly weakly binding ester dienophile **3.3** and **3.7** is not promoted by **C2**. In order to further inspect the significant difference in the catalytic properties of the two apparently similar substrates **3.2** and **3.3**, the binding of the corresponding products **3.9** and **3.10** in **C2** was examined. The structures of these products resemble the transition state geometries of their respective Diels-Alder

reactions and so the binding studies give an indication of whether the cage can accommodate the increased steric bulk of the TS to the bound substrate. In spite of the weak encapsulation of **3.2** (K_A < 30 M^{-1}), the product **3.9** binds reasonably strongly (K_A = 160 M^{-1}) (entry 2, Table 3-1), indicating **C2** favours to stabilise the transition state over the substrates. The product **3.10**, on the other hand, does not appear to be a guest (K_A < 5M^{-1}) (entry 3, Table 3-1). It is highly likely that this weak binding occurs because the two ester groups of the transition state adopt a *trans* conformation preventing simultaneous interactions with both binding sites of **C2**, which has D_{4h} symmetry. These results highlight that the complementarity between the cavity and the TS, rather than the cavity and the substrate, plays the essential role in cage catalysis.

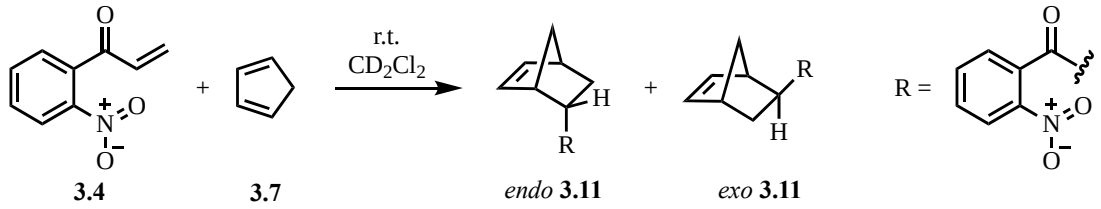

3.4 **3.7** *endo* **3.11** *exo* **3.11**

*Scheme 3-1. The Diels-Alder reaction of **3.4** and **3.7**.*

The Diels-Alder catalysis of **C2** was further expanded to the dienophile **3.4**. This substrate is distinct from the quinones or any of the diester compounds described so far because, while it binds through the simultaneous interactions of two H-bond acceptor group with the "top" and "bottom" of the cage, its dienophilic C=C bond is only conjugated to one of the electron withdrawing groups, which correspondingly can only be activated by single H-bond door pocket. At 60 mol% **C2** loading, a mild rate enhancement was observed for the reaction of **3.4** with **3.7** (Scheme 3-1**)**. The addition of the inhibitor pentacenedione to **C2** suppresses all catalysis, while analogous cage **C1** showed no reactivity, again indicating a true cavity-based effect.

Both *endo* and *exo* products **3.11** bind weakly in **C2**, indicating a modest transition state stabilisation. This is consistent with the relatively inferior rate acceleration: k_{cat} / k_{uncat} = 6.9 for *endo* **3.11** and k_{cat} / k_{uncat} = 4.9 for *exo* **3.11** (entry 4, Table 3-1). No significant change in the product distribution was observed, as the formations of both diastereoisomers were catalysed at a similar rate. Unsurprisingly, both *endo* **3.11**

and *exo* **3.11** exhibit similar binding strength (entry 4, Table 3-1), which corresponds to the non-stereoselective transition state recognition.

It is interesting to compare the reaction of **3.2** to that of **3.4**. Although **3.2** is the weaker binding substrate, the catalysis of **3.2** is more efficient due to the more favoured transition state binding. While most of the previous cage catalysis research has focused on using "good guests" as substrates, the studies described in this section further highlight the hidden potential that these systems have to catalyse reactions of weakly binding reactants, opening up the possibility of applying them to a wider scope of reactions.

3.5 Diastereoselectivity in Pd_2L_4 catalysed Diels-Alder reactions

It could be anticipated that the significant acceleration observed for benzoquinone dienophiles would translate to maleimide substrates, such as **3.5**. Like benzoquinones, they are strong guests (K_A = 7400 M^{-1} in **C1** and K_A = 4600 M^{-1} in **C2**, entry 1, Table 3-3) and their eneone moiety is doubly activated by both H-bond donor pockets. However, both **C1** and **C2** only provide very weak overall acceleration for the Diels-Alder reactions of maleimide (Figure 3-5). The strong binding of the substrate indicates that this is not due to a low concentration of the host-guest complex.

While the acceleration using maleimide is modest, what is more interesting is the effect the cage has on diastereoselectivity. The reaction of maleimide, **3.5**, with furan, **3.12** (Figure 3-4a), is a useful reaction to study because the uncatalysed reaction (a) can produce significant quantities of both *exo* and *endo* diastereomers and (b) the *endo* product is a kinetic product, which can then undergo the retro-Diels-Alder reaction before generating the more thermodynamically stable *exo* product. As such, there is the possibility that a cage catalyst could influence any of the three elementary steps – the two forward Diels-Alder processes, $k_{endo\text{-}f}$ and $k_{exo\text{-}f}$, and the retro-reaction, $k_{endo\text{-}b}$.

A comparison of the kinetic profiles for the uncatalysed reaction of maleimide, **3.5**, with furan, **3.12**, against the reactions mediated by **C1** and **C2** indicate that both cages influence the cycloaddition / retro-cycloaddition, and in different ways (Figure 3-5a-c). With **C2**, the shape of the kinetic profile appears similar to the uncatalysed reaction, just the rate of overall conversion and the subsequent conversion from kinetic *endo* to *exo*-products is quicker (Figure 3-5c). In contrast, in the presence of **C1**, the shape of the kinetic profile is distinct from the uncatalysed reaction, with the most obvious feature being that the *exo* product is both kinetically and thermodynamically preferred (Figure 3-5d). To further understand these differences, the effect of each cage on the retro-reaction was also investigated (Figure 3-6). As can be seen, the rate of the uncatalysed reaction is the same as in the presence of **C1**, showing this cage does not catalyse the retro reaction, whereas in the presence of **C2**, the reaction is notably

quicker. Analysis of the kinetic data indicates that **C2** speeds up the retro reaction by a factor of about 7 ($k_{cat\text{-}endo\text{-}b}/k_{uncat\text{-}endo\text{-}b}$ = 7.37).

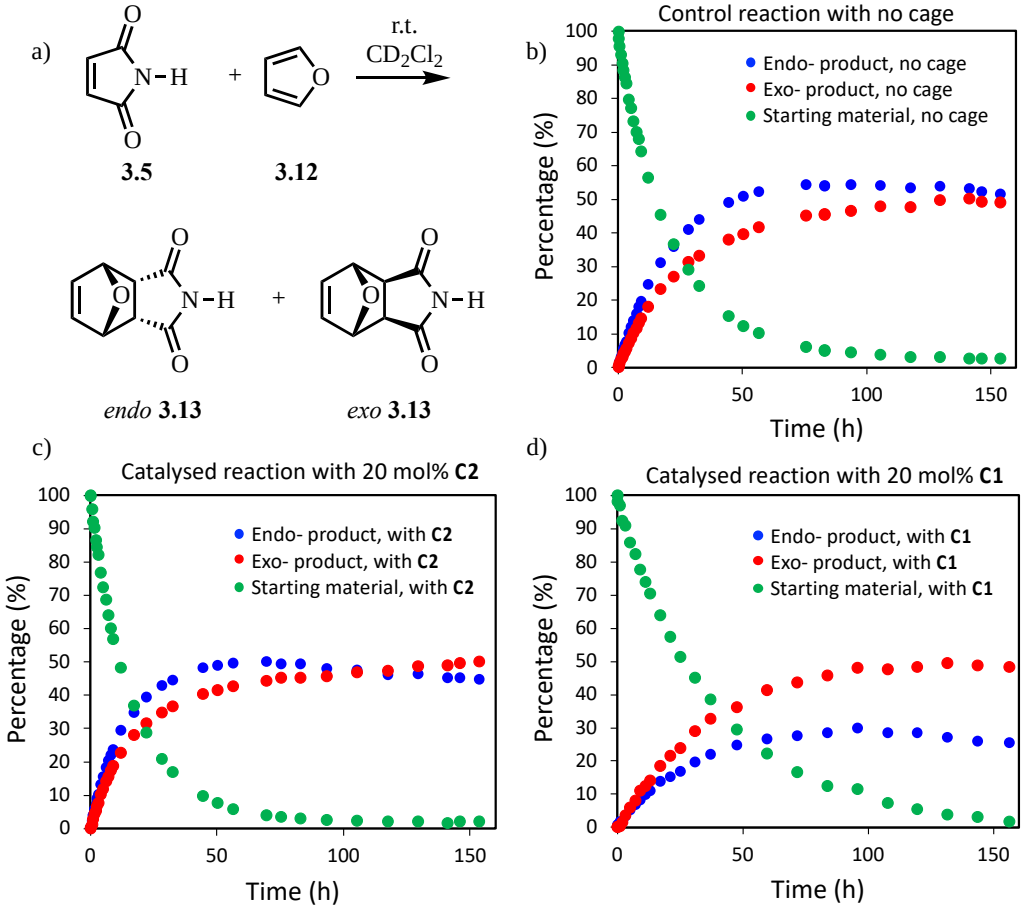

*Figure 3-5. a) The Diels-Alder reaction between **3.5** and **3.12**. b) The kinetic profile for the reaction with no cage present as a catalyst. c) The kinetic profile for the reaction with 20 mol% **C2** as the catalyst. d) The kinetic profile for the reaction with 20 mol% **C1** as the catalyst.*[xi]

[xi] *exo* **3.13** forms a strongly binding complex with **C1** and gradually precipitated as crystals. Red data points in figure (d) represent the concentration of *exo* **3.13** remaining in solution.

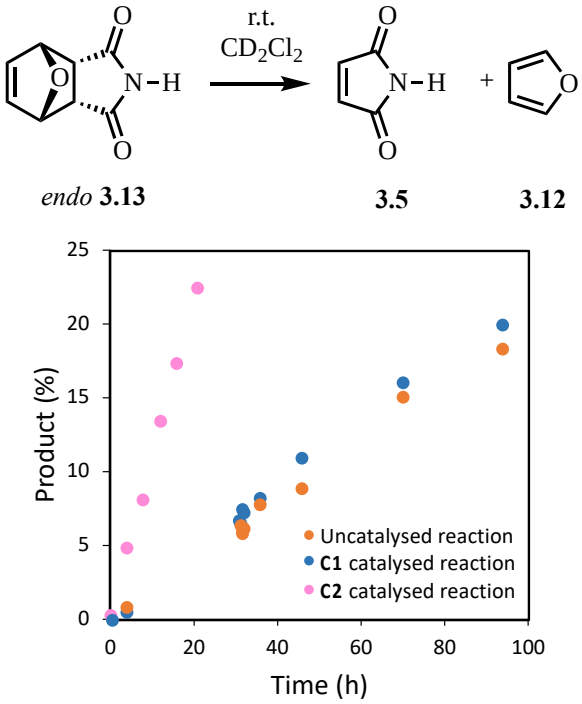

*Figure 3-6. Retro-Diels-Alder reaction of endo **3.13**.*

Kinetic modelling of the cage-mediated forward reactions show that **C2** catalyses all three elementary steps, while **C1** only accelerates the formation of the *exo* adduct (Table 3-2). While the difference in the uncatalysed and catalysed rate constants are modest, this nonetheless highlights how subtle structural changes in the cage can have an impact on similar reactions. This result is also supported with the host-guest binding studies of the *endo* and *exo* products, which serve as TS mimics. Adding a mixture of *endo* and *exo* **3.13** to **C1** results in a selective shift in the ^{1}H NMR signals of the *exo* compound, while the *endo* resonances are unaffected (Figure 3-7). An NMR titration of purified *exo* **3.13** with **C1** reveals a K_A of 5300 M^{-1} (Table 3-3). When the mixture of *exo* and *endo* **3.13** was added to **C2**, the ^{1}H NMR signals of both diastereomers shift, showing that both compounds are guests, which is consistent with **C2** affecting all three elementary processes (Figure 3-8). The binding constants for these compounds are shown in Table 3-3.

*Table 3-2. The kinetic parameters fitted for the Diels-Alder reaction of **3.5** and **3.12**.*

Entry	Fitted parameter	**C1** catalysed reaction	**C2** catalysed reaction	Uncatalysed reaction
1	$k_{uncat\text{-}endo\text{-}f}$	0.0217 ($M^{-1}h^{-1}$)	0.0217 ($M^{-1}h^{-1}$)	0.0217 ($M^{-1}h^{-1}$)
2	$k_{uncat\text{-}endo\text{-}b}$	0.0019 (h^{-1})	0.0019 (h^{-1})	0.0019 (h^{-1})
3	$k_{uncat\text{-}exo\text{-}f}$	0.0162 ($M^{-1}h^{-1}$)	0.0162 ($M^{-1}h^{-1}$)	0.0162 ($M^{-1}h^{-1}$)
4	$k_{uncat\text{-}exo\text{-}b}$	0	0	0
5	$k_{cat\text{-}endo\text{-}f}$	0	0.058 ($M^{-1}h^{-1}$)	-
6	$k_{cat\text{-}endo\text{-}b}$	0	0.014 (h^{-1})	-
7	$k_{cat\text{-}exo\text{-}f}$	0.045 ($M^{-1}h^{-1}$)	0.043 ($M^{-1}h^{-1}$)	-
8	$k_{cat\text{-}exo\text{-}b}$	0	0	-

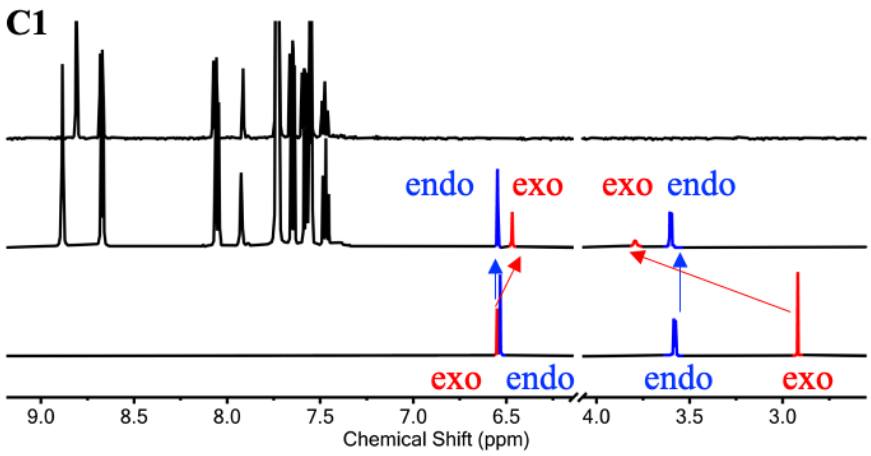

*Figure 3-7. Chemical shift of endo/exo **3.13** upon addition of **C1**.[1]H NMR spectra (500 MHz, CD_2Cl_2) of (bottom) endo/exo **3.13**, (middle) 1 equivalent of **C1** and 1 equivalent of **3.13** (endo/exo ratio ca. 2:1) and (top) **C1**.*

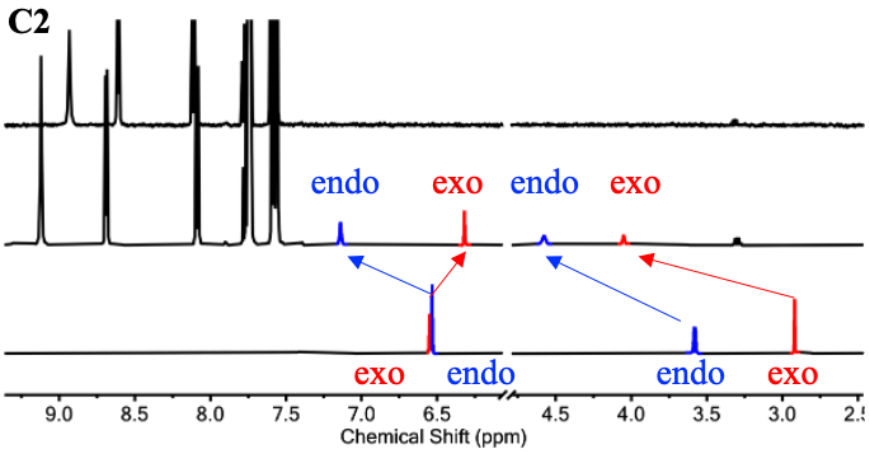

*Figure 3-8. Chemical shift of endo/exo **3.13** upon addition of **C2**.[1]H NMR spectra (500 MHz, CD_2Cl_2) of (bottom) endo/exo **3.13**, (middle) 1 equivalent of **C2** and 1 equivalent of **3.13** (endo/exo ratio ca. 2:1) and (top) **C2**.*

*Table 3-3. Binding constants of **3.5**, endo/exo **3.13** in **C1** and **C2**.*

Entry	Guest	K_A in **C1** (M^{-1})	K_A in **C2** (M^{-1})
1	**3.5**	7400	4600
2	*endo* **3.13**	< 5	3900
3	*exo* **3.13**	5300	8500

3.6 Discussion on product inhibition with Pd_2L_4 Diels-Alder catalysis and overall catalytic performance

The co-encapsulation method has been the dominant strategy for promoting bimolecular fusion reactions using supramolecular catalysts.[23] This strategy requires the supramolecular host to bind two guests at the same time, catalysing the reaction by increasing the effective molarity. Nevertheless, the use of this method is often faced with severe product inhibition, mainly due to the high entropic penalty associated with the turnover step where two molecules of substrates are required to displace one molecule of product. Conversely, the Diels-Alder catalysis with **C2** adopts a single species turnover strategy (Figure 3-1) and the product only needs to be replaced by the dienophile. Additionally, the dominant interaction between the dienophile and **C2** and the product and **C2** are approximately the same (i.e. 8 CH···O interactions). The combination of these factors means that the turnover step is often energetically neutral, both in terms of enthalpy and entropy.

Despite these considerations, the Diels-Alder catalysis of **C2** can still be prone to product inhibition. This is best exemplified by the reaction of dienophile **3.5** with diene **3.14**, where a sharp inflection point was observed for the kinetic profile of the catalysed reaction (Figure 3-10a). While the initial rate of product formation / substrate consumption in the presence of **C2** is faster compared to the background reaction (k_{cat}/k_{uncat} = 56), the catalysed rate drops to a level similar to the uncatalysed process at approximately 20% conversion. As the cage equivalents in this reaction is also 20 mol%, the kinetic data would suggest that the turnover number for **C2** is not much higher than one. This product inhibition was corroborated by separately measuring the affinity of the product **3.15**. This is a remarkably strong guest, where the binding constant exceeds the limit of using NMR titrations for fast exchange guests,[24] with the lower bound estimated to be $K_A = 10^5$ M^{-1} (see simulation in section 3.8.5.17), which is at least 20 times higher than the dienophile **3.5**. The product inhibition therefore reflects the diminishing concentration of the substrate-cage complex, **3.5**⊂**C2**, as more of the tighter binding product is generated. In contrast, the reaction

of **3.5** and **3.16** shows no obvious signs of product inhibition (Figure 3-10b), which is consistent with the product, **3.17**, only showing three times the affinity (K_A = 13000 M^{-1}) of the substrate. These differences are explained by considering the conformational similarities and differences between the TS and the product. For the cage to be a catalyst, it must interact with the TS stronger than the substrate. For a cyclic diene, which produces a conformationally locked, bicyclic product, this means that catalysis and product inhibition are intrinsically linked; the cage must bind the product reasonably well to be a catalyst, because this is structurally reminiscent of the TS, which semi-empirical calculations show (Figure 3-9). This strong binding of the product then hinders turnover. In the case of the acyclic diene, the product is not conformationally locked, meaning that the TS and product are structurally distinct, so that the cage can be a good catalyst without being hindered by poor turnover.

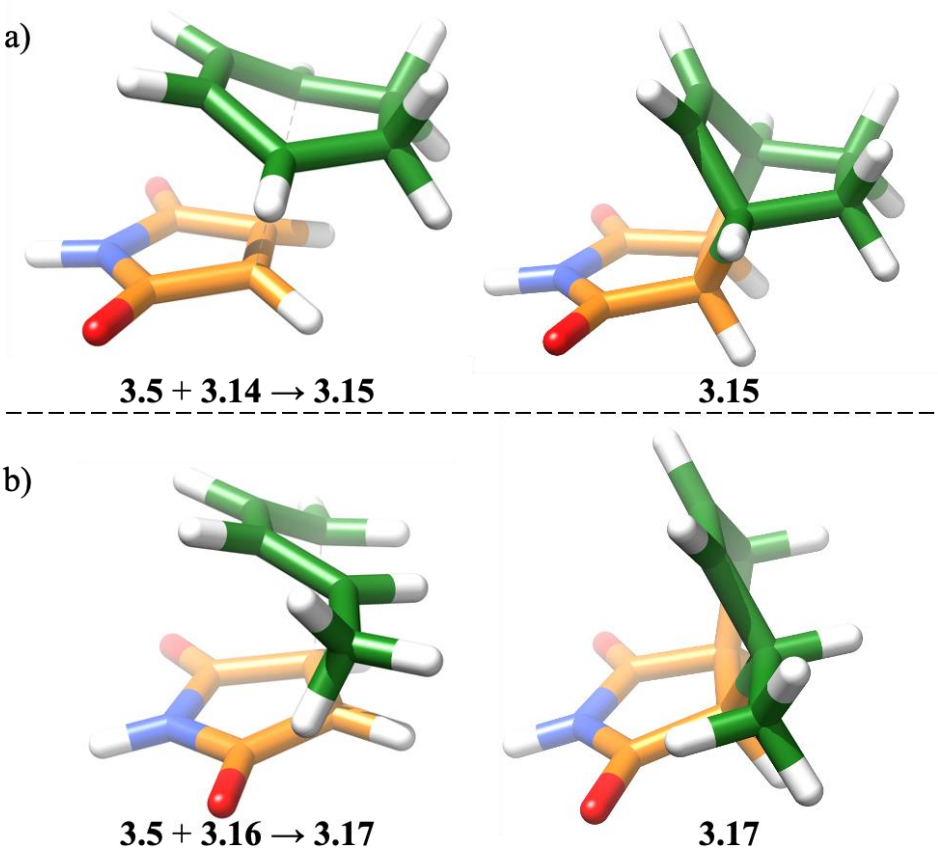

Figure 3-9. The geometries of the transition states and products were optimised with the semi-empirical PM6 method using Spartan 10.

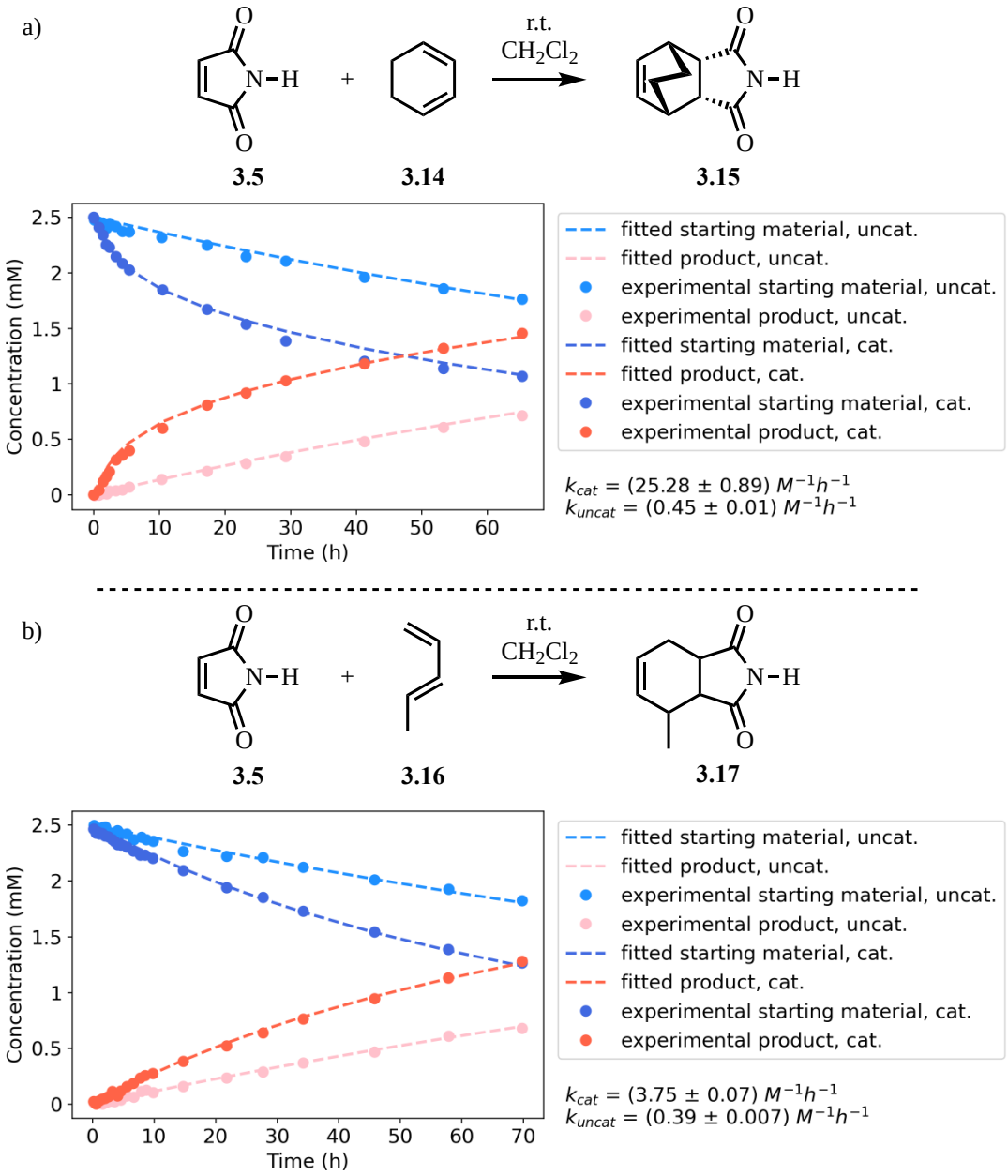

*Figure 3-10. a) the **C2** catalysed (20 mol%) and uncatalyed Diels-Alder reaction of **3.5** and **3.14**. b) the **C2** catalysed (20 mol%) and uncatalysed Diels-Alder reaction of **3.5** and **3.16**.*

Another scenario of product inhibition involves the product being spontaneously converted into a stronger binder, as is the case for the **C2** catalysed reaction between **3.6** and **3.7**. Interestingly, the kinetic profile shows no profound inflection point that

indicates severe product inhibition (Figure 3-11).[xii] Rather the poor turnover is revealed by adding an additional 5 equivalents of **3.18** before the cage catalysed reaction was initiated, and no rate enhancement is observed compared to the background reaction. Although in CD_2Cl_2 **3.6** predominantly exists as the keto form, the product **3.18** significantly favours the enolized form.[25] Tetracationic **C2** also facilitates the deprotonation of the enol **3.18** by binding the anionic conjugate base. The resulting enolate **3.18**$^-$ tightly occupies **C2** preventing further catalysis. The anion binding is supported by the lack of guest displacement upon addition of the very strong guest, pentacenedione ($K_A = 8 \times 10^8\ M^{-1}$). It is noteworthy that the ^{1}H NMR signals of **3.18** notably broaden in the presence of **C2**, possibly as a result of that enolate **3.18**$^-$ exchanges with **C2** at an intermediate rate in comparison to the NMR timescale.

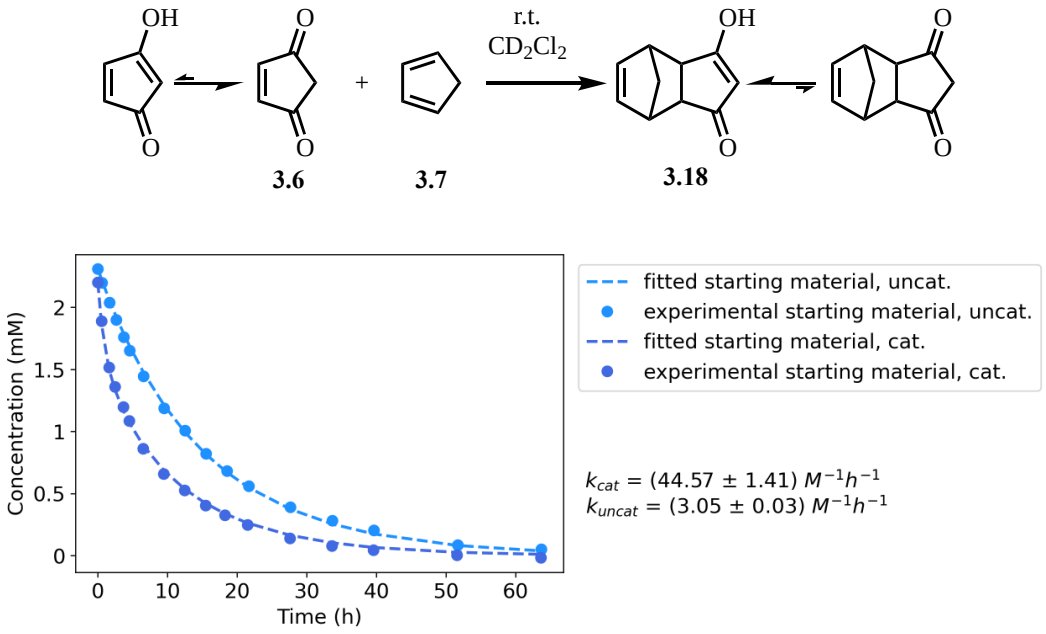

*Figure 3-11. The **C2** catalysed (20 mol%) and uncatalyed Diels-Alder reaction of **3.6** and **3.7**. Product concentration not obtained due to broadened spectra in the presence of **C2**.*

[xii] An inflection point on the kinetic profile usually indicates severe product inhibition. However, the inflection could be weak and difficult to identify to the naked eyes. Factors such as the relative binding constants of the dienophile and the product and the relative rate of the catalysed and uncatalysed reactions can affect the curvature of the inflection. See the supporting information for simulation on product inhibition with varying binding constants and rate constants.

Finally, it is worth considering the relative acceleration that Pd_2L_4 cages provide towards different dienophile substrates. For example, **3.5** is an excellent guest for both **C1** and **C2** (K_A = 7400 M^{-1} and 4600 M^{-1} respectively), similar in magnitude to benzoquinone (K_A = 8000 M^{-1} and 1100 M^{-1} respectively),[16] yet the acceleration in the Diels-Alder reactions are drastically different, with benzoquinones displaying k_{cat}/k_{uncat} of up to 1400,[16] whereas **3.5** only shows a maximum k_{cat}/k_{uncat} of just 50. This re-emphasises that the strength of substrate binding is a poor indicator of catalytic performance. In order for a cage to be an effective Diels-Alder catalyst, the cage must be able to lower the energy of the TS with respect to the bound substrate. With maleimide, benzoquinone and indeed any other enone substrate, H-bonding interactions stabilise the increased electron density on the carbonyl oxygen atoms as electrons flow from the diene towards the LUMO of the dienophile.[26] This electrostatic mechanism is universal to all H-bond catalysts, supramolecular cages and small molecule systems alike. In cage catalysis, a second component – the global 3D recognition of the entire TS – can either add to or detract from the electrostatic stabilisation. For example, if the shape of the TS is matched to the cavity (or it forms other favourable interactions) then this will bring down the TS energy, whereas unfavourable interactions or steric clashes will increase the TS energy. Using this analysis, it is interesting to compare the catalysis towards benzoquinone and maleimide substrates. Both of these substrates bind to the cage with similar affinities, and their relative recognition of TS mimics are also similar, yet the rate enhancement of benzoquinone Diels-Alder reactions is an order of magnitude greater than maleimide substrates. This would indicate that the difference stems from electronic effects, wherein partial charge separation at the TS is affected differently between these two classes of what are apparently similar substrates.

3.7 Conclusions

A range of non-quinone-based neutral guests were identified for **C2** and their encapsulation properties were discussed. The higher rigidity of the substrates and the better complementarity to the cavity contribute to strong host-guest binding. Guests bearing good hydrogen bond acceptor groups also display higher association constants.

The Diels-Alder reactions of the newly identified guests were studied in the presence of **C1**/**C2**. No correlation has been found between the substrate binding constants and the catalytic efficiency. Weakly binding substrates can be efficiently activated, and strong guests do not necessarily grant high rate acceleration. Rather, the transition state stabilisation by the cages' cavity was found to be essential for the rate and diastereoselectivity enhancement.

The Diels-Alder catalysis in **C2** requires only the binding of the dienophile. Catalytic turnover in such systems entails the entropically "neutral" displacement of the product with the dienophile. The relative binding strength of the substrate and the product therefore dictates the efficiency of the turnover. For the reactions involving cyclic dienes, product inhibition and transition state stabilisation can be two sides of the same coin, as constrained bicyclic Diels-Alder adducts often highly resemble the transition state geometries. While the reactions engaging an acyclic diene can still be efficiently accelerated in **C2**, the resulting products can allow weakly binding conformations that facilitate product release.

3.8 Experimental

3.8.1 General information

Unless otherwise stated, all reagents and solvents were purchased from Alfa Aesar, VWR, Fluorochem or Sigma Aldrich and used without further purification. Column chromatography was carried out using Geduran Si60 (40-63 μm) as the stationary phase and TLC was performed on precoated Kieselgel 60 plates (0.20 mm thick, 60F254. Merck, Germany) and observed under UV light at 254 nm. All reactions were carried out under air and at room temperature, unless otherwise stated.

All ^{1}H and ^{13}C NMR spectra were recorded on either a 500 MHz Bruker AV III equipped with a DCH cryo-probe (Ava500), a 400MHZ Bruker AV III equipped with BBFO+ probe (Ava400), a 500 MHz Bruker AV IIIHD equipped with a Prodigy cryo-probe (Pro500) or a 600 MHz Bruker AV IIIHD equipped with a TCI cryo-probe (Ava600) at a constant temperature of 300 K. Chemical shifts are reported in parts per million. Coupling constants (*J*) are reported in hertz (Hz). Standard abbreviations indicating multiplicity were used as follows: m = multiplet, q = quartet, t = triplet, d = doublet, s = singlet. All analysis was performed with MestReNova, Version 14.0.0. All assignments were confirmed using a combination of COSY, NOESY, HMBC and HSQC NMR spectra.

3.8.2 Synthesis for catalysis experiments and NMR titrations

Cages **C1**[11] and **C2**,[16] **3.4**,[27] *exo* **3.8**,[28] **3.9**,[29] **3.10**,[30] *exo* **3.13**,[31] *endo* **3.13**,[31] **3.15**,[32] **3.18**,[33]were prepared according to literature procedures.

3.8.3 General procedure for NMR scale catalysis experiments

Prior to NMR scale reactions the commercial starting materials were purified as follows. Dimethyl acetylenedicarboxylate **3.2** and 4-cyclopentene-1,3-dione **3.6** were purified by silica plug (eluent: CH_2Cl_2). Dimethyl maleate **3.1** was washed with $NaHCO_3$ before purification by silica plug (eluent: CH_2Cl_2). Dimethyl fumarate **3.3** and maleimide **3.5** were recrystallised from ^{i}PrOH. Cyclopentadiene **3.7** was freshly distilled before use each time.

For catalysed Diels-Alder reactions: To an NMR tube was introduced a solution containing 450 µL CD_2Cl_2, the cage compound (0.25 µmol or 0.5 µmol as a solid), the diene (20 µL of a 312.5 mM or 625 mM CD_2Cl_2 stock solution), the dienophile (20 µL of a 62.5 mM CD_2Cl_2 stock solution), and the internal standard tetrakis(trimethylsilyl)silane (10 µL of a 15.6 mM CD_2Cl_2 stock solution).

For background Diels-Alder reactions: To an NMR tube was introduced a solution containing 450 µL CD_2Cl_2, the diene (20 µL of a 312.5 mM or 625 mM CD_2Cl_2 stock solution), the dienophile (20 µL of a 62.5 mM CD_2Cl_2 stock solution), and the internal standard tetrakis(trimethylsilyl)silane (10 µL of a 15.6 mM CD_2Cl_2 stock solution).

For Diels-Alder reactions with cage and competitive inhibitors: To an NMR tube was introduced a solution containing 450 µL CD_2Cl_2, the cage compound (0.25 µmol as a solid) and pentacenedione (0.75 µmol as a solid) or anthraquinone (25 µmol as a solid). The diene (20 µL of a 312.5 mM or 625 mM CD_2Cl_2 stock solution), the dienophile (20 µL of a 62.5 mM CD_2Cl_2 stock solution), and the internal standard tetrakis(trimethylsilyl)silane (10 µL of a 15.6 mM CD_2Cl_2 stock solution) were then added to the NMR tube.

3.8.4 Catalysis experiment product characterisation

The products of each NMR scale reaction were identified by comparing the spectra to either previously reported ^{1}H NMR spectroscopic data or to the data obtained from authentically synthesised products.

3.8.4.1 Literature reported product identification

The literature data for **3.8**, **3.9**, **3.10**, **3.13** and **3.15** are found in the following sources:[34][35][32][36][37][38]

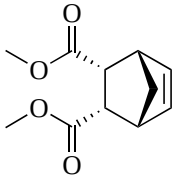

endo **3.8**

Kinet. Catal., **2013**, *54*, 469–474.

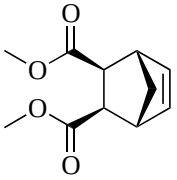

exo **3.8**

Kinet. Catal., **2013**, *54*, 469–474.

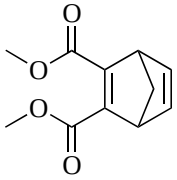

3.9

J. Org. Chem., **2013**, *78*, 2012–2025.

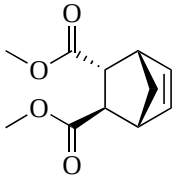

3.10

Kinet. Catal., **2013**, *54*, 469–474.

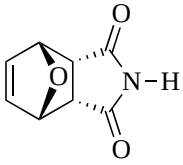

endo **3.13**

J. Am. Chem. Soc., **2018**, *140*, 5009–5013.

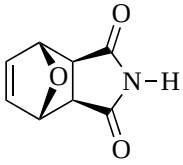

exo **3.13**

J. Am. Chem. Soc., **2018**, *140*, 5682–5685.

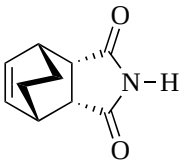

3.15

Synth. Commun., **2011**, *41*, 2769–2793.

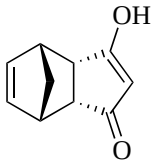

3.18

J. Org. Chem., **1982**, *47*, 4491–4498.

3.8.4.2 Preparation of authentic Diels-Alder product 3.11

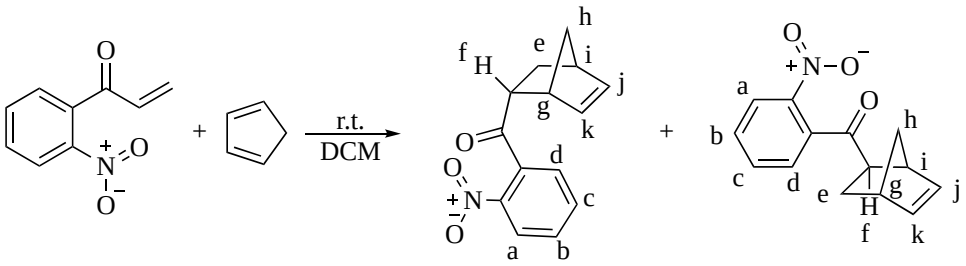

3.4 **3.7** *endo* **3.11** *exo* **3.11**

1-(2-Nitrophenyl)propen-1-one, **3.4**, (0.20 mL, 1.7 mmol) and cyclopentadiene, **3.7**, (0.14 mL, 1.9 mmol) were combined in CH_2Cl_2 (0.4 mL). The reaction mixture was stirred at room temperature overnight and was concentrated *in vacuo*. The separation of the *endo* and *exo* products proved to be non-trivial. Hence a small amount of pure *endo* and *exo* products were obtained by preparative scale TLC (CH_2Cl_2), both as light-yellow oils (yield *endo*: 4 mg, 0.02 mmol, 1%, yield *exo*: 3 mg, 0.01 mmol, 1%). *endo* and *exo* products are identified using NOESY spectra where the cross peak between the bridgehead proton $H_{h'}$ and the proton H_f is only observed for the *endo* conformation.

endo **3.11**: ^{1}H NMR (500 MHz, $CDCl_3$) δ 8.12 (dd, J = 8.3, 1.2 Hz, 1H, H_a), 7.76 – 7.69 (m, 1H, H_c), 7.62 – 7.57 (m, 1H, H_b), 7.32 (dd, J = 7.6, 1.4 Hz, 1H, H_d), 6.29 (dd, J = 5.7, 3.1 Hz, 1H, H_j), 5.92 (dd, J = 5.7, 2.8 Hz, 1H, H_k), 3.48 (ddd, J = 9.0, 4.6, 3.4 Hz, 1H, H_f), 3.15 – 3.04 (m, 1H, H_g), 2.99 – 2.92 (m, 1H, H_i), 1.92 (ddd, J = 11.8, 9.0, 3.8 Hz, 1H, H_e), 1.61 (dddd, J = 11.8, 4.6, 2.7, 0.5 Hz, 1H, $H_{e'}$), 1.52 – 1.43 (m, 1H, H_h), 1.37 – 1.30 (m, 1H, $H_{h'}$) ppm.

endo **3.11**: ^{13}C NMR (126 MHz, $CDCl_3$) δ 203.63, 146.05, 138.68, 138.59, 134.31, 131.33, 130.38, 128.05, 124.51, 51.32, 50.36, 46.65, 43.11, 29.25 ppm.

exo **3.11**: ^{1}H NMR (500 MHz, $CDCl_3$) δ 8.12 (dd, J = 8.2, 1.1 Hz, 1H, H_a), 7.75 – 7.68 (m, 1H, H_c), 7.63 – 7.57 (m, 1H, H_b), 7.44 (dd, J = 7.6, 1.4 Hz, 1H, H_d), 6.19 (dd, J = 5.7, 3.0 Hz, 1H, H_k), 6.08 (dd, J = 5.7, 3.1 Hz, 1H, H_j), 3.12 – 3.04 (m, 1H, H_i), 3.03 – 2.98 (m, 1H, H_g), 2.71 (ddd, J = 8.7, 4.7, 1.4 Hz, 1H, H_f), 2.21 – 2.13 (m, 1H, H_e), 1.75 – 1.65 (m, 1H, H_h), 1.45 – 1.31 (m, 2H, $H_{h'}$+$H_{e'}$) ppm.

exo **3.11**: ^{13}C NMR (126 MHz, $CDCl_3$) δ 205.06, 146.26, 138.90, 138.77, 135.90, 134.23, 130.55, 128.13, 124.64, 51.29, 46.70, 46.04, 42.17, 30.57 ppm.

HRMS (EI): $C_{14}H_{13}O_3N_1$ $[M]^{\cdot+}$ found 243.08847, requires 243.08900.

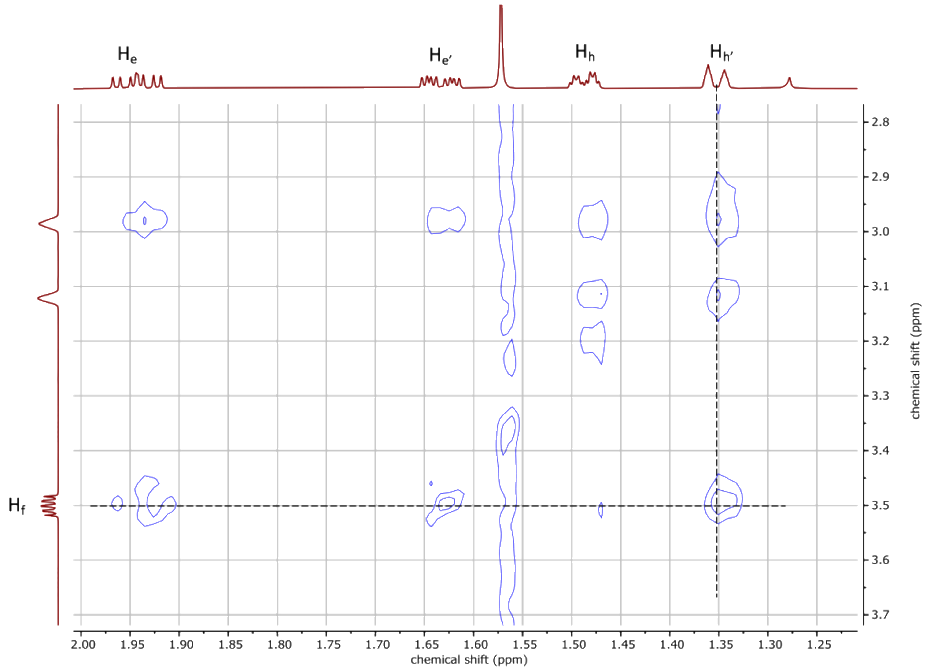

*Figure 3-12. Partial NOESY spetrum for endo **3.11**.*

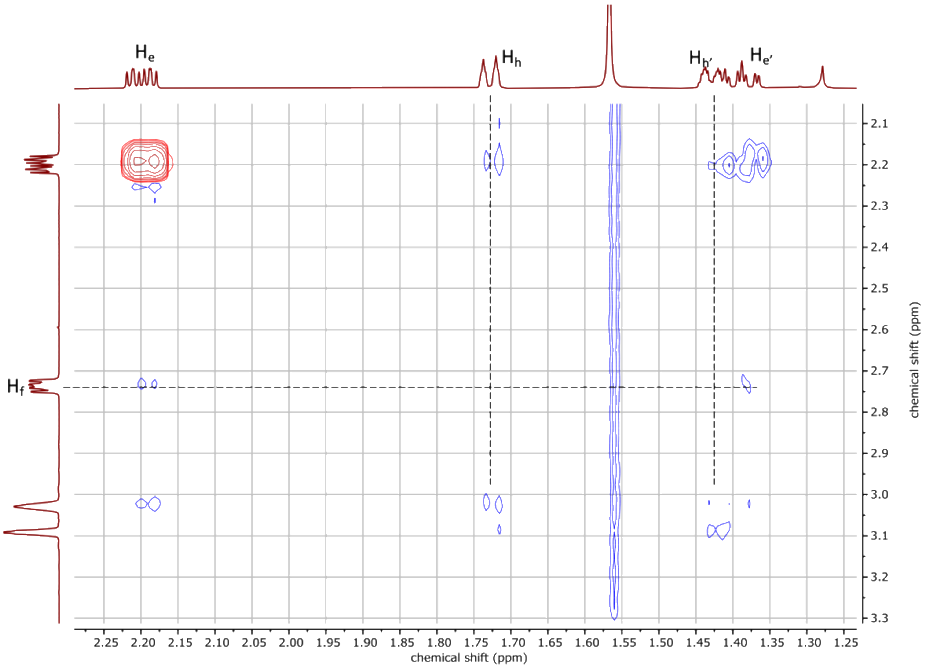

*Figure 3-13. Partial NOESY spetrum for exo **3.11**.*

3.8.4.3 Preparation of authentic Diels-Alder product 3.17

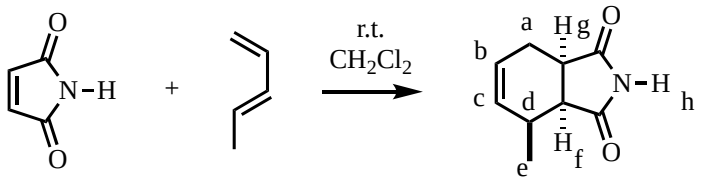

3.5 **3.16** **3.17**

Maleimide, **3.5**, (50 mg, 0.52 mmol) and 1,5-pentadiene, **3.16**, (42 mg, 0.62 mmol) were combined in CH_2Cl_2 (6 mL) and the reaction mixture was stirred at room temperature for 11 days. The solvent and excess 1,5-pentadiene were removed under reduced pressure. The resulting solid was recrystallised in toluene, giving an off-white solid as the pure product (yield: 41 mg, 45%).

^{1}H NMR (500 MHz, $CDCl_3$) δ 8.05 (bs, 1H, H_h), 5.94 – 5.86 (m, 1H, H_b), 5.80 (m, 1H, H_c), 3.17 (m, 1H, H_g), 3.06 (dd, *J* = 9.0, 6.7 Hz, 1H, H_f), 2.67 (ddd, *J* = 15.6, 6.5, 2.5 Hz, 1H, H_a), 2.54 – 2.42 (m, 1H, H_d), 2.22 – 2.11 (m, 1H, $H_{a'}$), 1.37 (d, *J* = 7.4 Hz, 3H, H_e) ppm. The *endo* conformation was confirmed by the ^3J coupling constant of H_f which falls into the *cis* coupling constant range.

^{13}C NMR (126 MHz, $CDCl_3$) δ 180.07, 178.22, 134.99, 127.10, 45.64, 41.75, 30.42, 23.72, 16.76 ppm.

HRMS (EI): $C_9H_{12}O_2N_1$ $[M]^{\cdot+}$ found 166.08730, requires 166.08626.

3.8.5 Determination of binding constants via ^{1}H NMR titration

3.8.5.1 General procedure of ^{1}H NMR titrations

For each titration, a solution containing cage (0.5 mM) and guest of a suitable concentration (typical concentrations are 10 mM, 25 m, 50 mM and 200 mM) was titrated into a 500 µL solution containing only cage (0.5 mM), maintaining the concentration of the cage species throughout. A ^{1}H NMR spectrum was recorded at each titration point. Unless specified, the peak positions of the internal pyridyl hydrogens were plotted against the concentration of guests, as exemplified with **C1** in Figure 3-14. The experimental data was fitted to a 1:1 fast exchange binding model (Equation 3-1) using the Levenberg-Marquardt Nonlinear Least-Squares Algorithm built in the R software and the RStudio software interface.

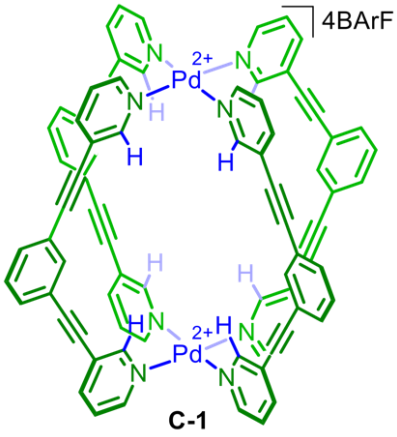

*Figure 3-14. Peak positions of the internal pyridyl hydrogens (blue) were monitored during NMR titrations, exemplified with **C1**.*

$$\delta = \delta_0 + \frac{\Delta\delta_{Max}}{2}\left(\frac{C_{Guest}}{C_{Host}} + \frac{1}{C_{Host}\cdot K_{Ass}} + 1 - \sqrt{\left(\frac{C_{Guest}}{C_{Host}} + \frac{1}{C_{Host}\cdot K_{Ass}} + 1\right)^2 - \frac{4\cdot C_{Guest}}{C_{Host}}}\right)$$

Equation 3-1

3.8.5.2 ^{1}H NMR titration data of 3.2 into C2

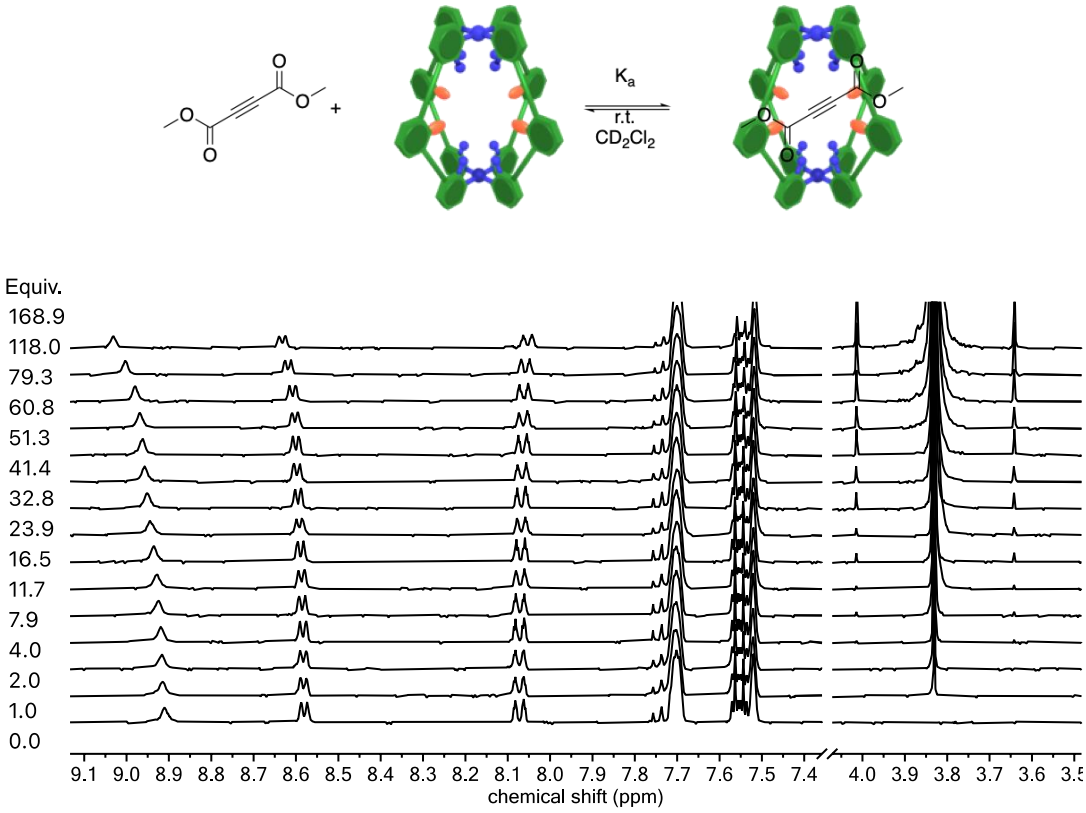

*Figure 3-15. ^{1}H NMR (400 MHz, CD_2Cl_2) spectroscopic data for titration of **3.2** into **C2**.*

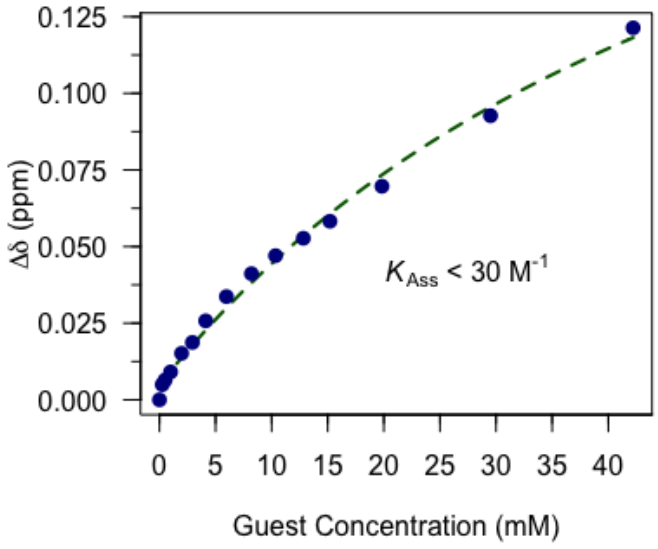

*Figure 3-16. Fitted data for change in peak position with increasing **3.2** concentration.*

3.8.5.3 ^{1}H NMR titration data of 3.3 into C2

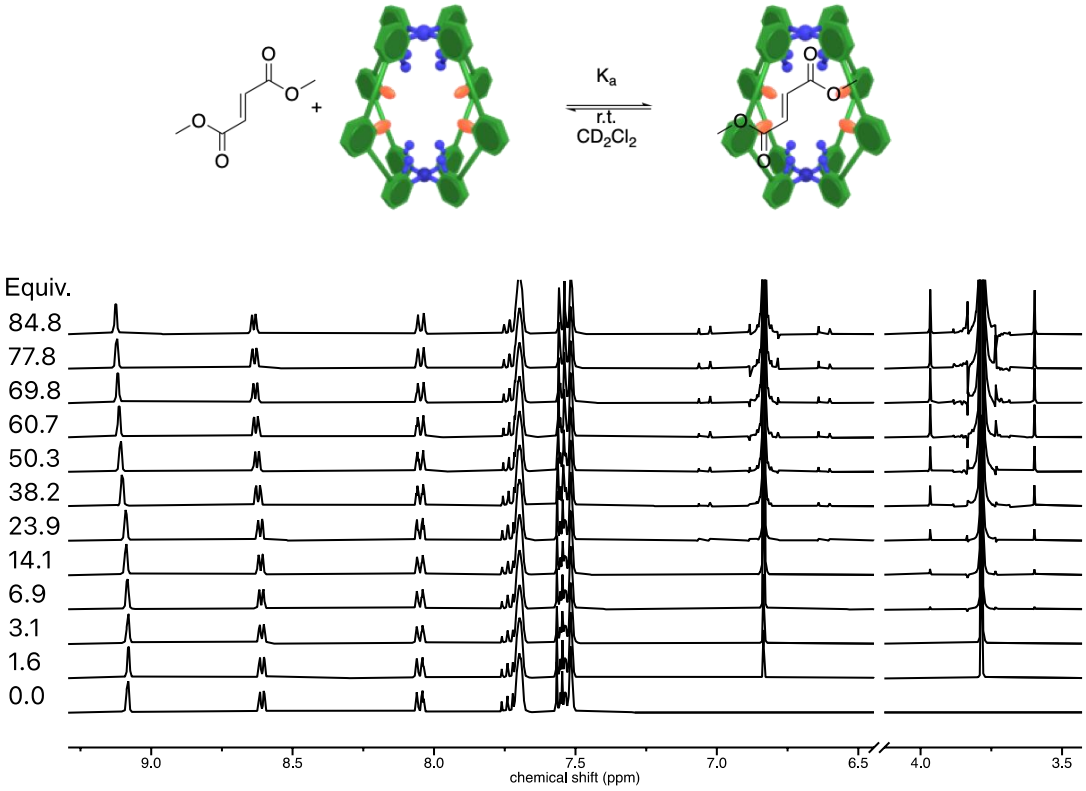

*Figure 3-17. 1H NMR (400 MHz, CD2Cl2) spectroscopic data for titration of **3.3** into **C2**.*

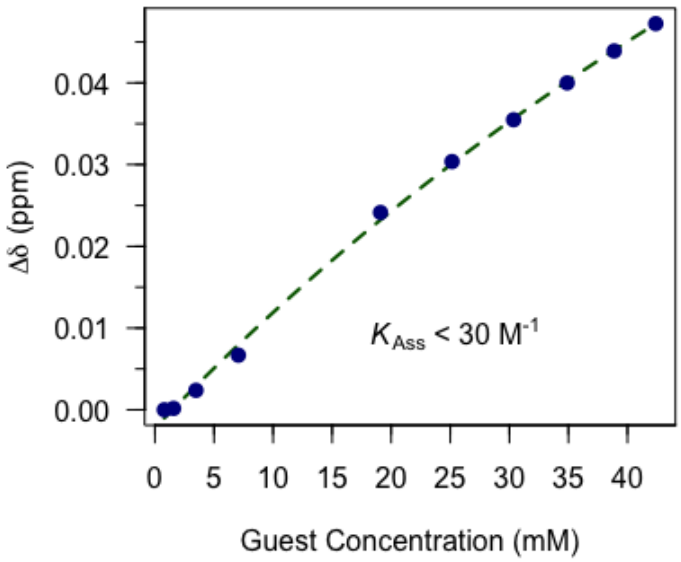

*Figure 3-18. Fitted data for change in peak position with increasing **3.3** concentration.*

3.8.5.4 ^{1}H NMR titration data of 3.4 into C2

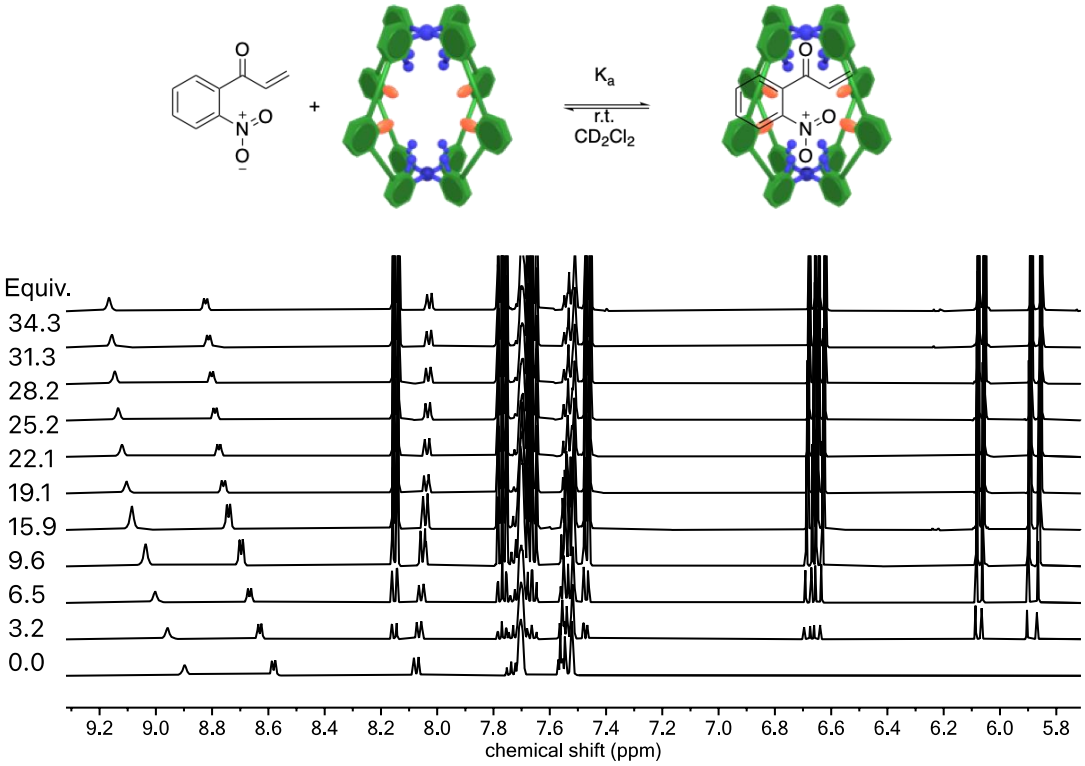

*Figure 3-19. ^{1}H NMR (400 MHz, CD_2Cl_2) spectroscopic data for titration of **3.4** into **C2**.*

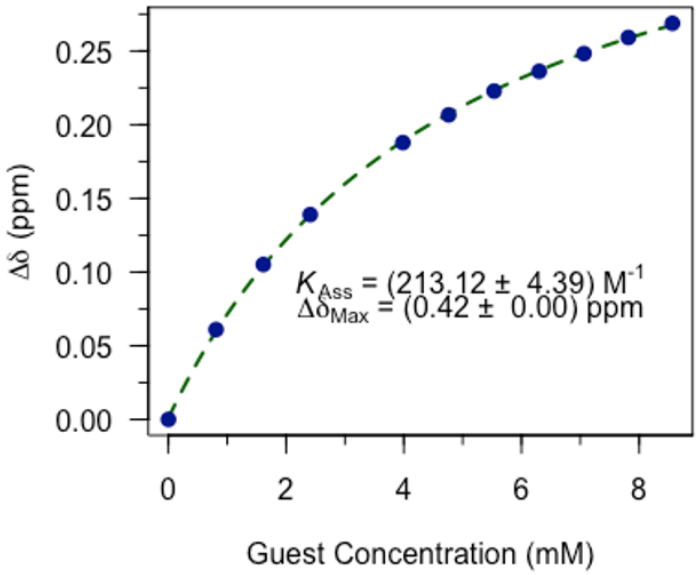

*Figure 3-20. Fitted data for change in peak position with increasing **3.4** concentration.*

3.8.5.5 ^{1}H NMR titration data of 3.5 into C1

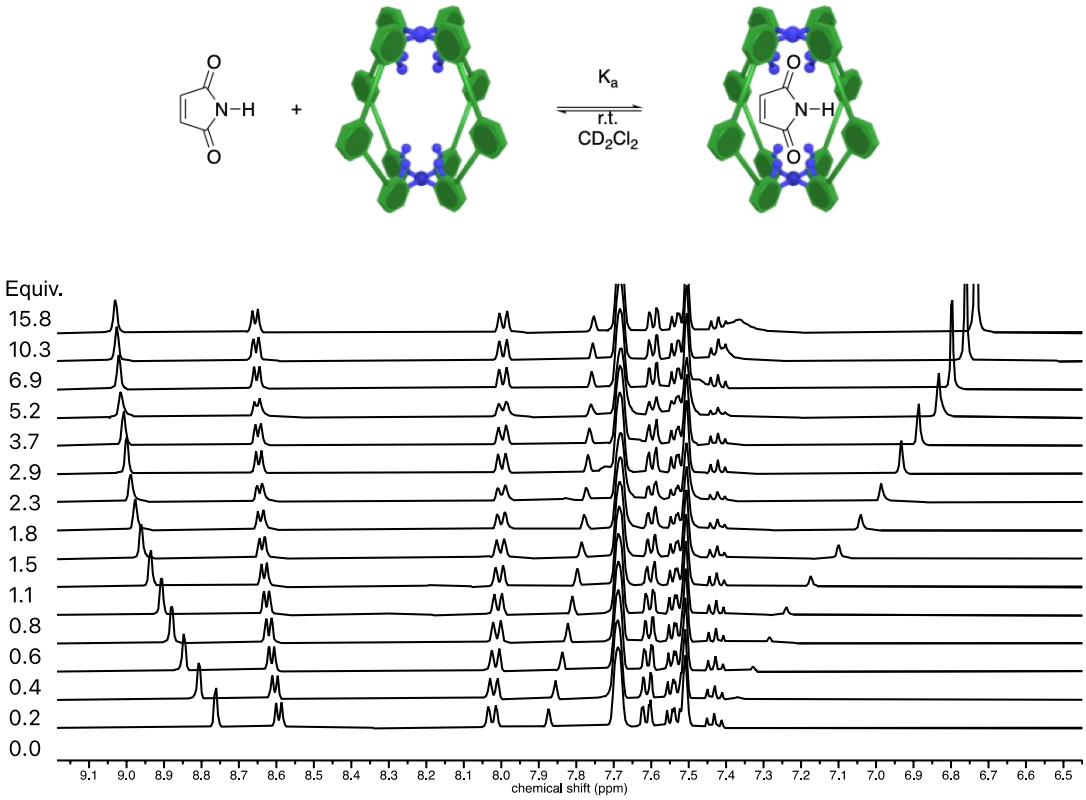

*Figure 3-21. ^{1}H NMR (400 MHz, CD_2Cl_2) spectroscopic data for titration of **3.5** into **C1**.*

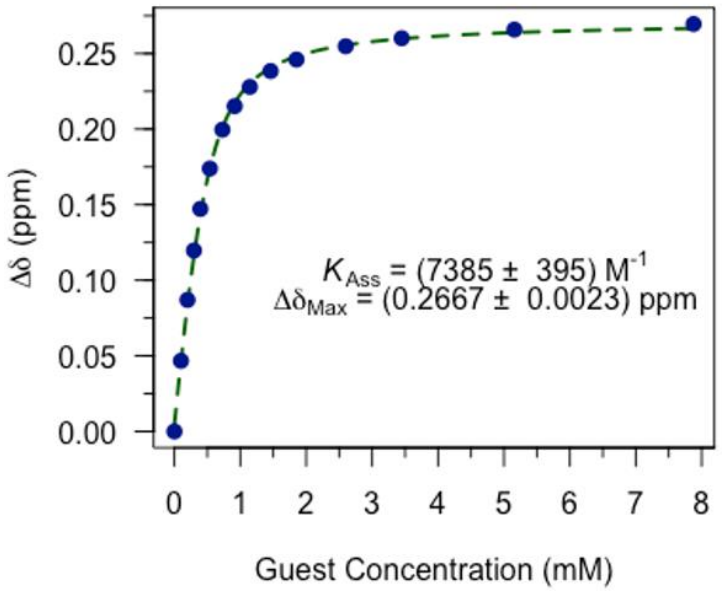

*Figure 3-22. Fitted data for change in peak position with increasing **3.5** concentration.*

3.8.5.6 ^{1}H NMR titration data of 3.5 into C2

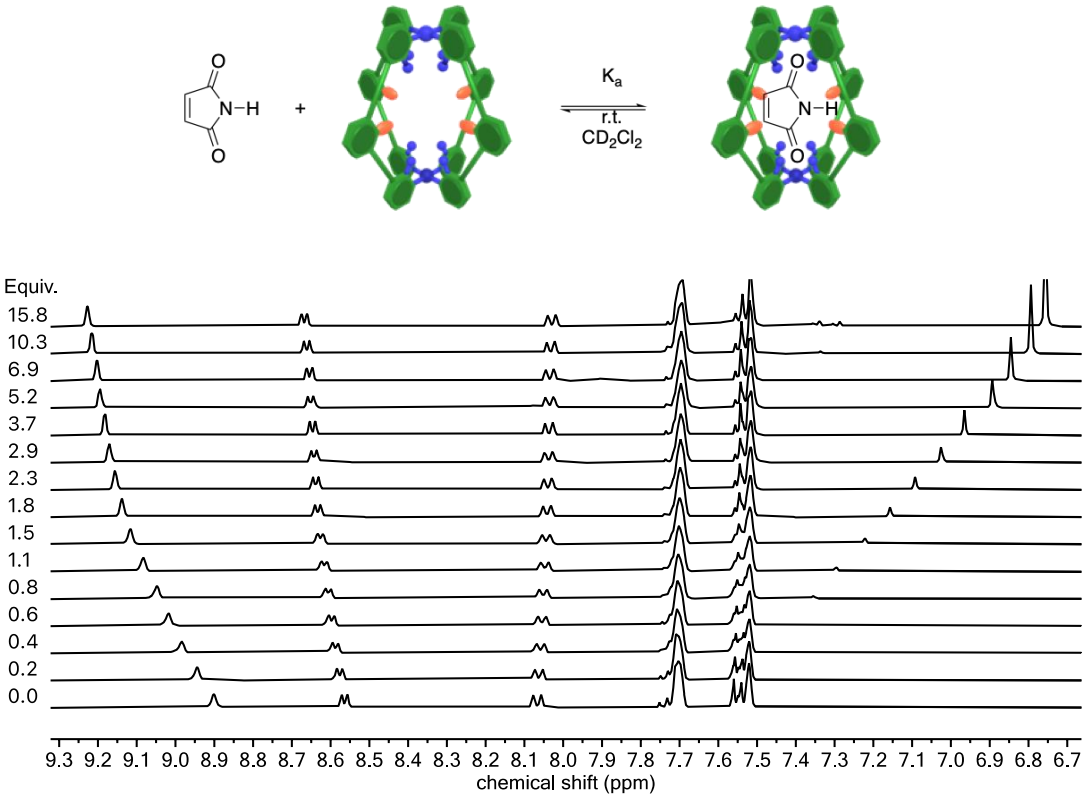

*Figure 3-23. ^{1}H NMR (400 MHz, CD_2Cl_2) spectroscopic data for titration of **3.5** into **C2**.*

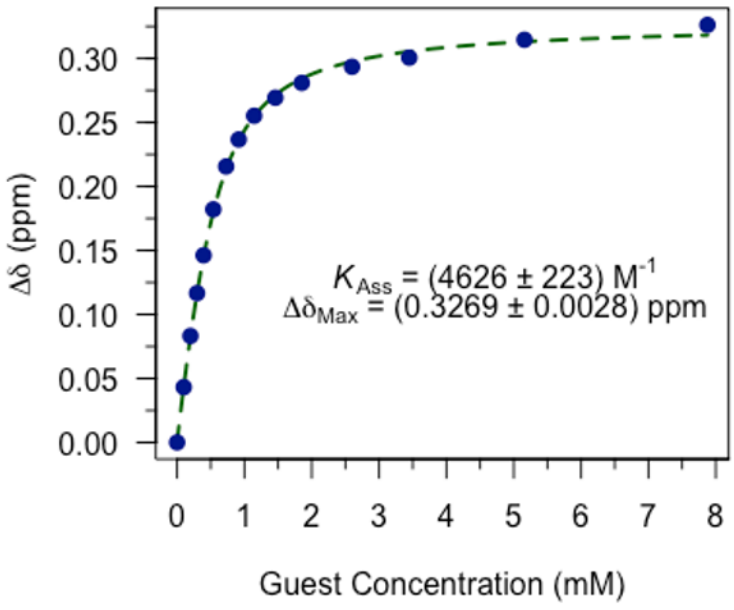

*Figure 3-24. Fitted data for change in peak position with increasing **3.5** concentration.*

3.8.5.7 ^{1}H NMR titration data of 3.9 into C2

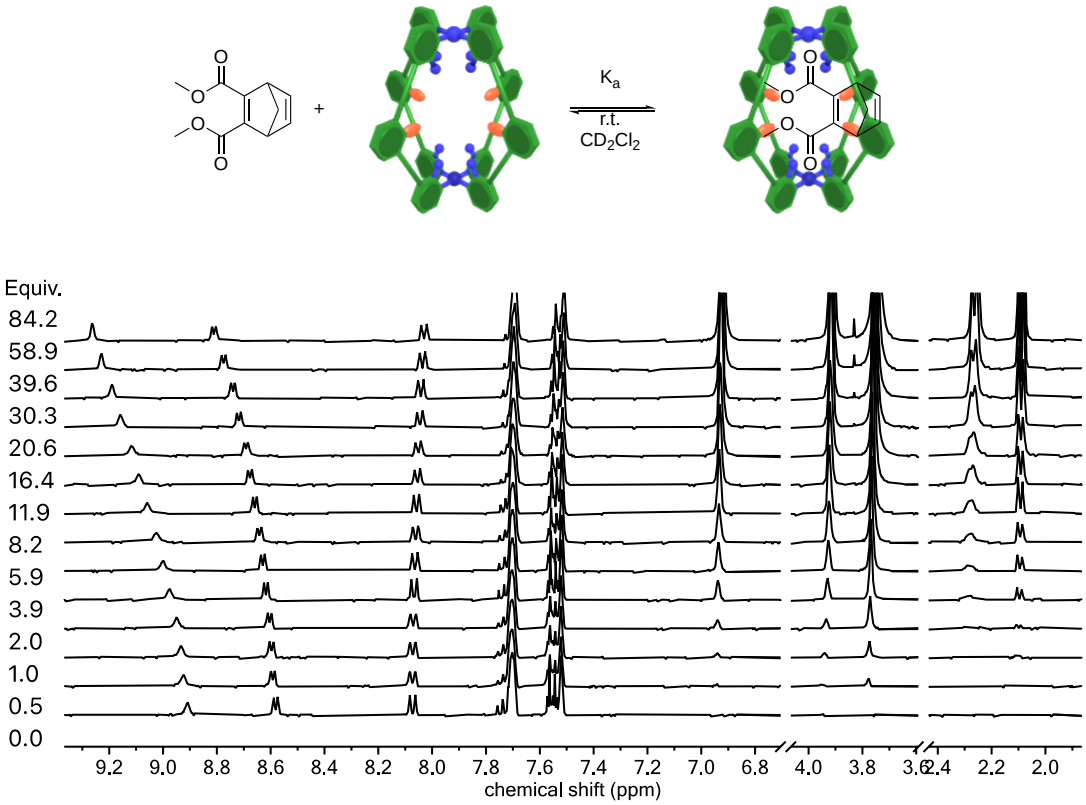

*Figure 3-25. ^{1}H NMR (400 MHz, CD_2Cl_2) spectroscopic data for titration of **3.9** into **C2**.*

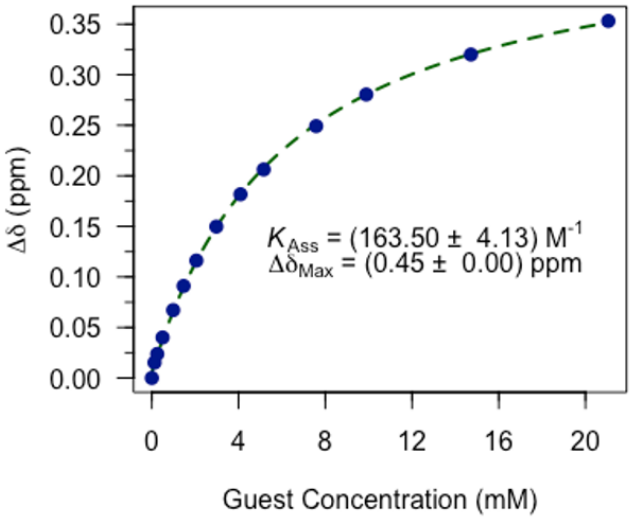

*Figure 3-26. Fitted data for change in peak position with increasing **3.9** concentration.*

3.8.5.8 ^{1}H NMR titration data of 3.10 into C2

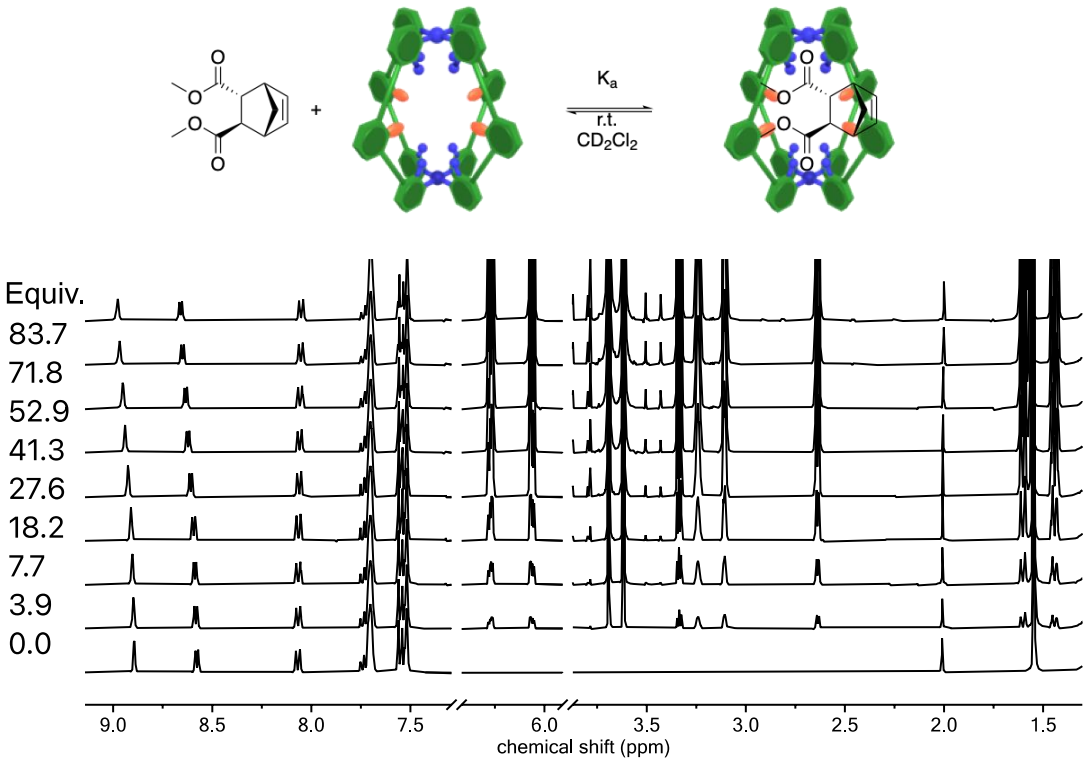

*Figure 3-27. ^{1}H NMR (400 MHz, CD_2Cl_2) spectroscopic data for titration of **3.10** into **C2**.*

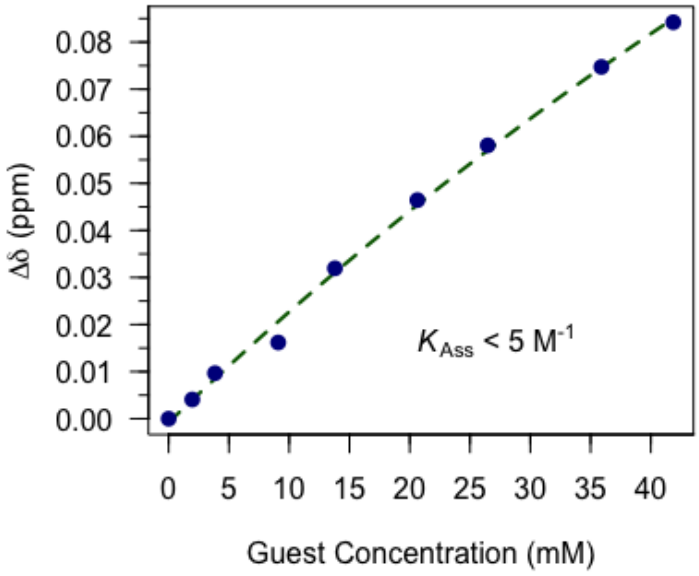

*Figure 3-28. Fitted data for change in peak position with increasing **3.10** concentration.*

3.8.5.9 ^{1}H NMR pseudo titration data of *endo* 3.11 into C2

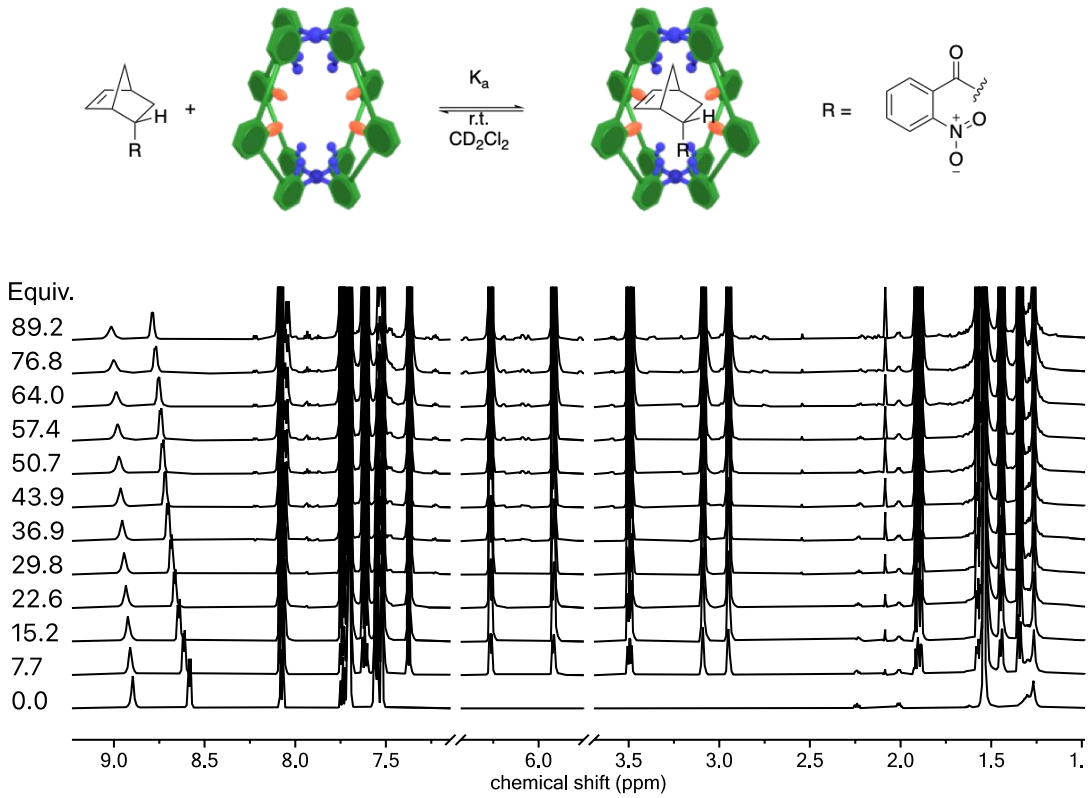

*Figure 3-29. ^{1}H NMR (600 MHz, CD_2Cl_2) spectroscopic data for titration of endo **3.11** into **C2**.*

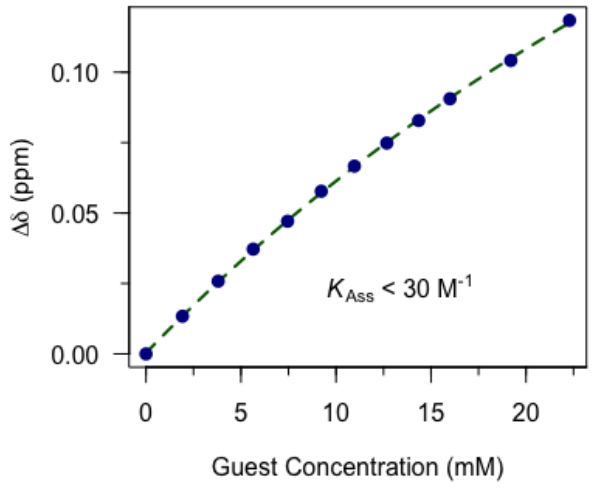

*Figure 3-30. Fitted data for change in peak position with increasing endo **3.11** concentration.*

3.8.5.10 ^{1}H NMR pseudo titration data of *exo* 3.11 into C2

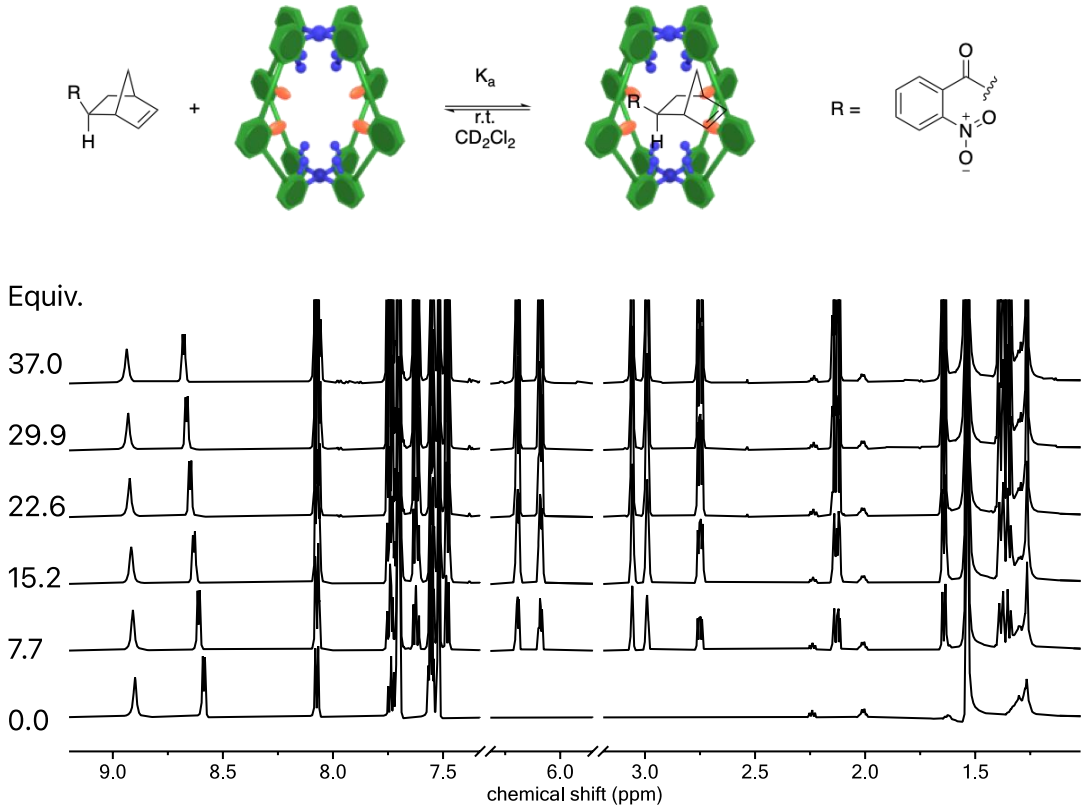

*Figure 3-31. ^{1}H NMR (600 MHz, CD_2Cl_2) spectroscopic data for titration of exo **3.11** into **C2**.*

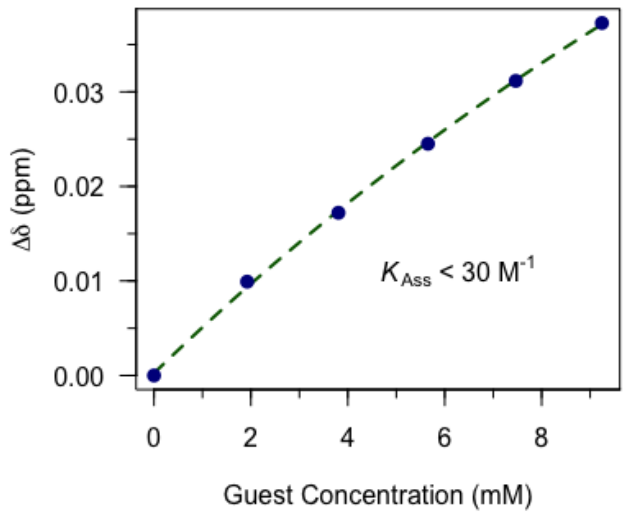

*Figure 3-32. Fitted data for change in peak position with increasing exo **3.11** concentration.*

3.8.5.11 ^{1}H NMR titration data of *endo* 3.13 into C1

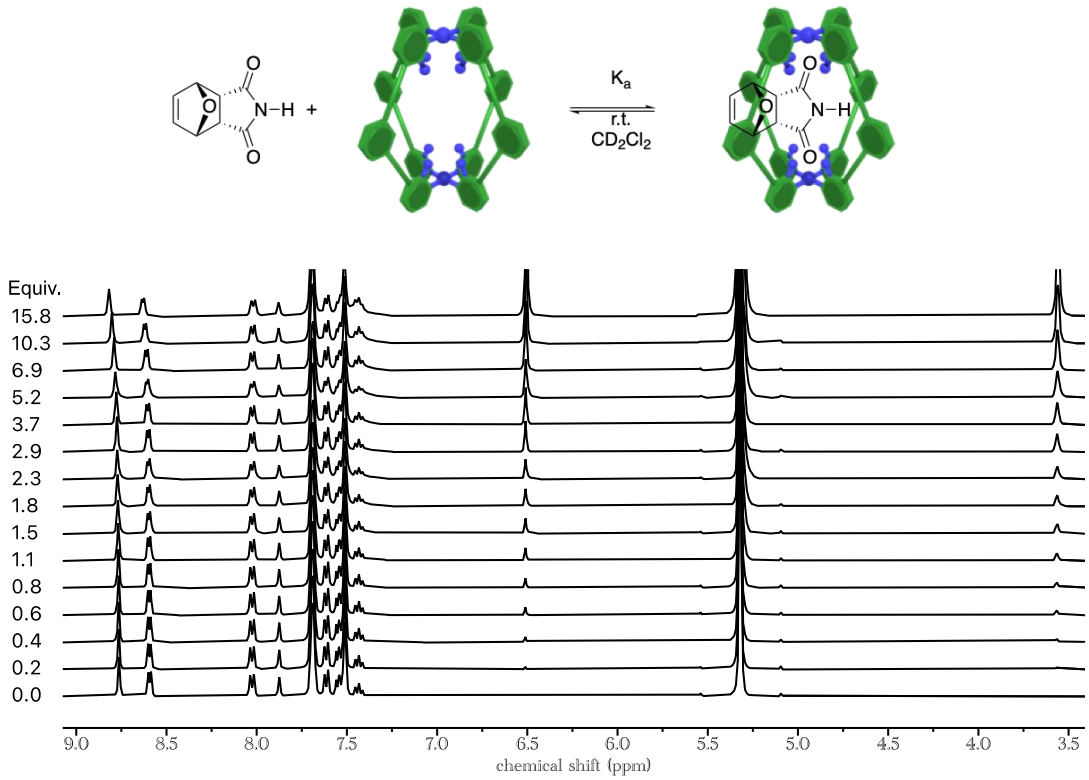

*Figure 3-33. ^{1}H NMR (400 MHz, CD_2Cl_2) spectroscopic data for titration of endo **3.13** into **C1**.*

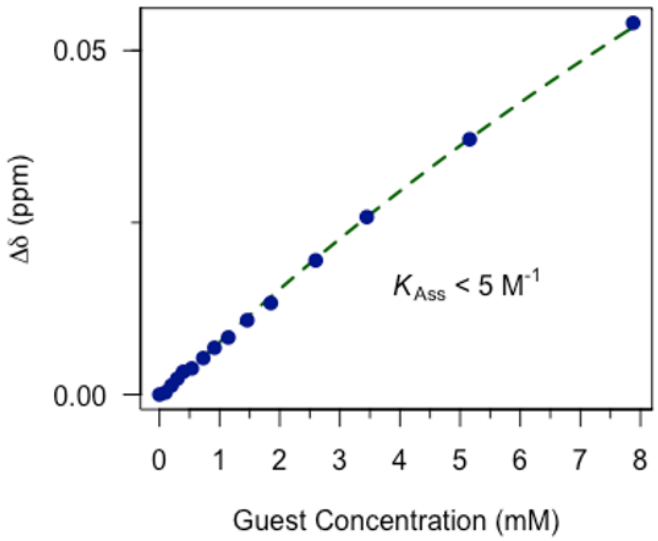

*Figure 3-34. Fitted data for change in peak position with increasing endo **3.13** concentration.*

3.8.5.12 ^{1}H NMR titration data of *exo* 3.13 into C1

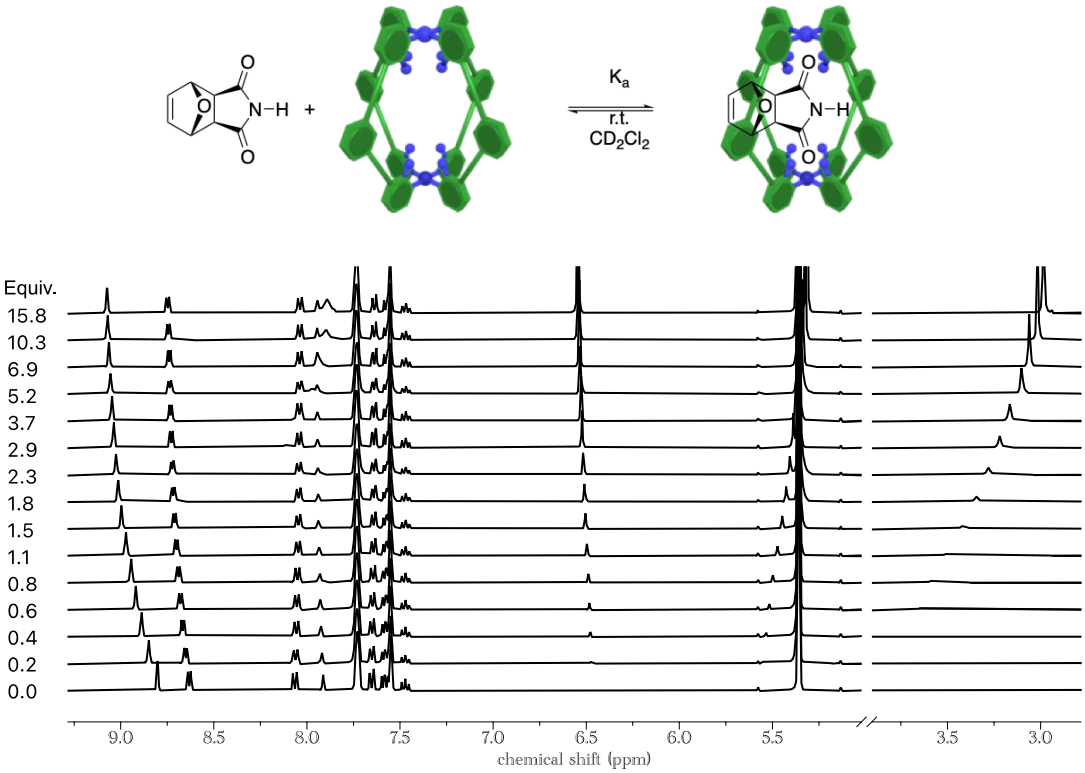

*Figure 3-35. ^{1}H NMR (400 MHz, CD_2Cl_2) spectroscopic data for titration of exo **3.13** into **C1**.*

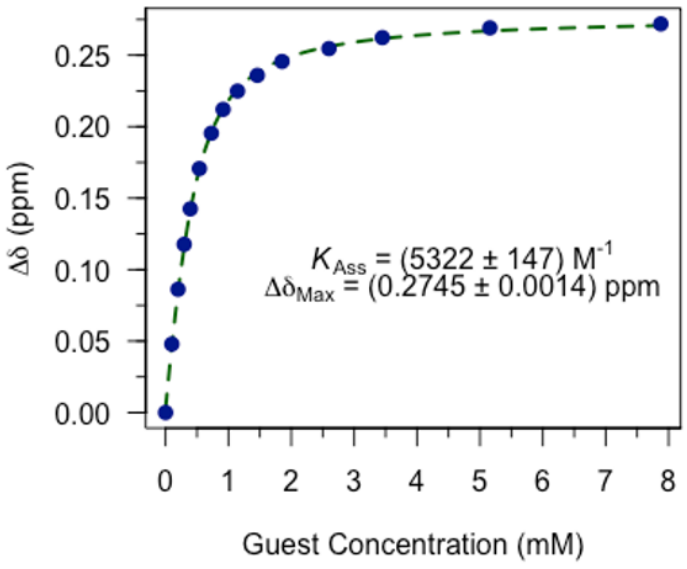

*Figure 3-36. Fitted data for change in peak position with increasing exo **3.13** concentration.*

3.8.5.13 ^{1}H NMR titration data of *endo* 3.13 into C2

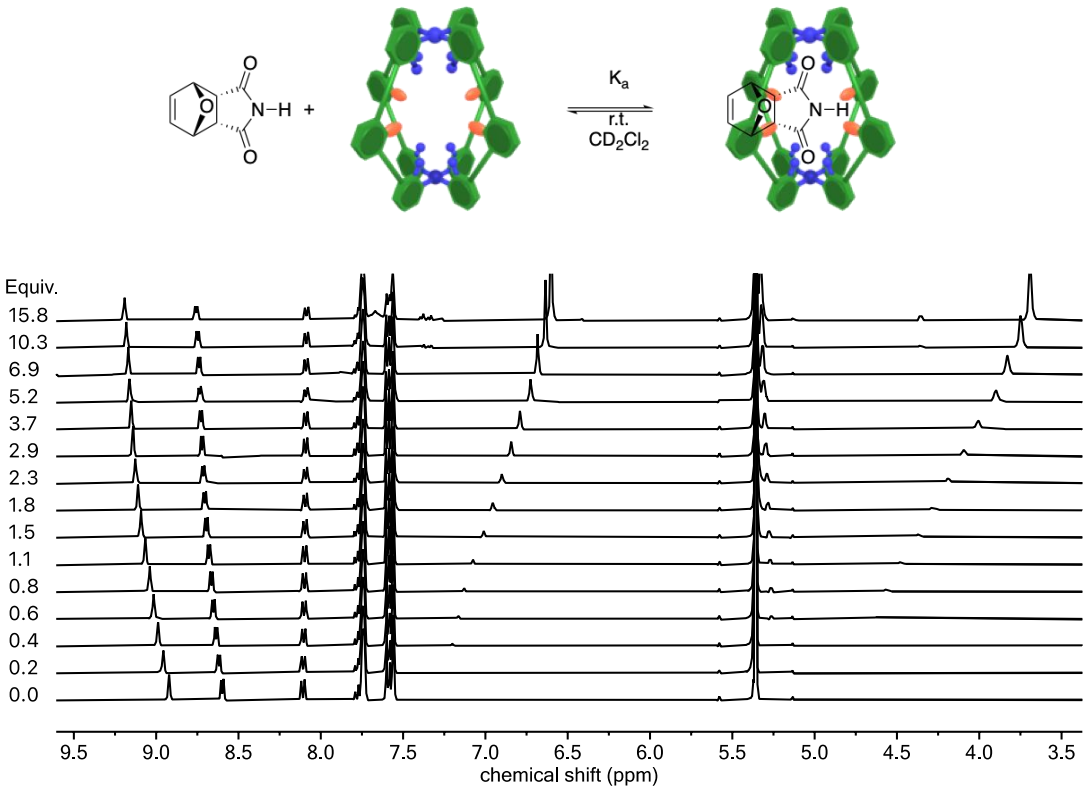

*Figure 3-37. ^{1}H NMR (400 MHz, CD_2Cl_2) spectroscopic data for titration of endo **3.13** into **C2**.*

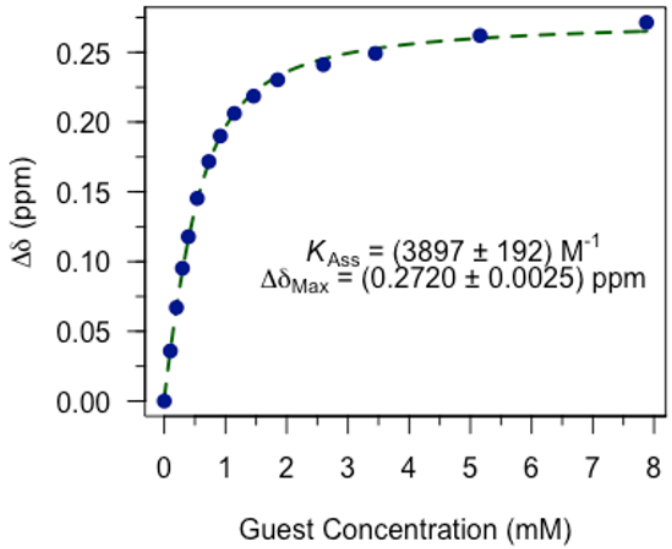

*Figure 3-38. Fitted data for change in peak position with increasing endo **3.13** concentration.*

3.8.5.14 ^{1}H NMR titration data of *exo* 3.13 into C2

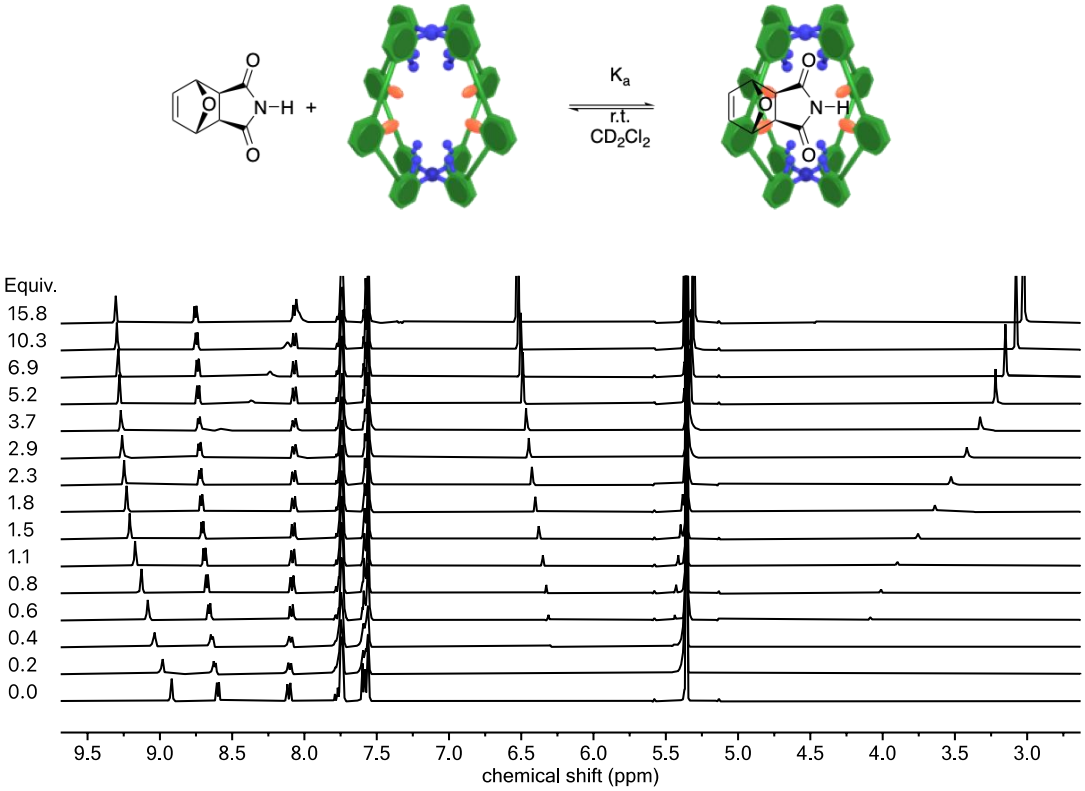

*Figure 3-39. ^{1}H NMR (400 MHz, CD_2Cl_2) spectroscopic data for titration of exo **3.13** into **C2**.*

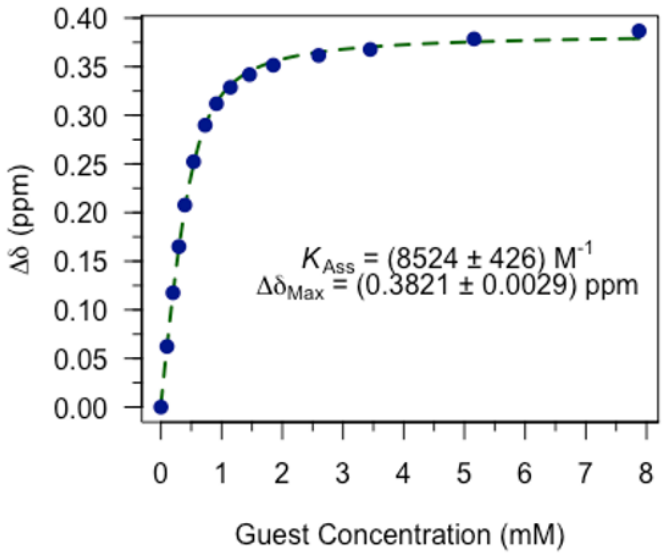

*Figure 3-40. Fitted data for change in peak position with increasing exo **3.13** concentration.*

3.8.5.15 ^{1}H NMR titration data of 3.6 into C2

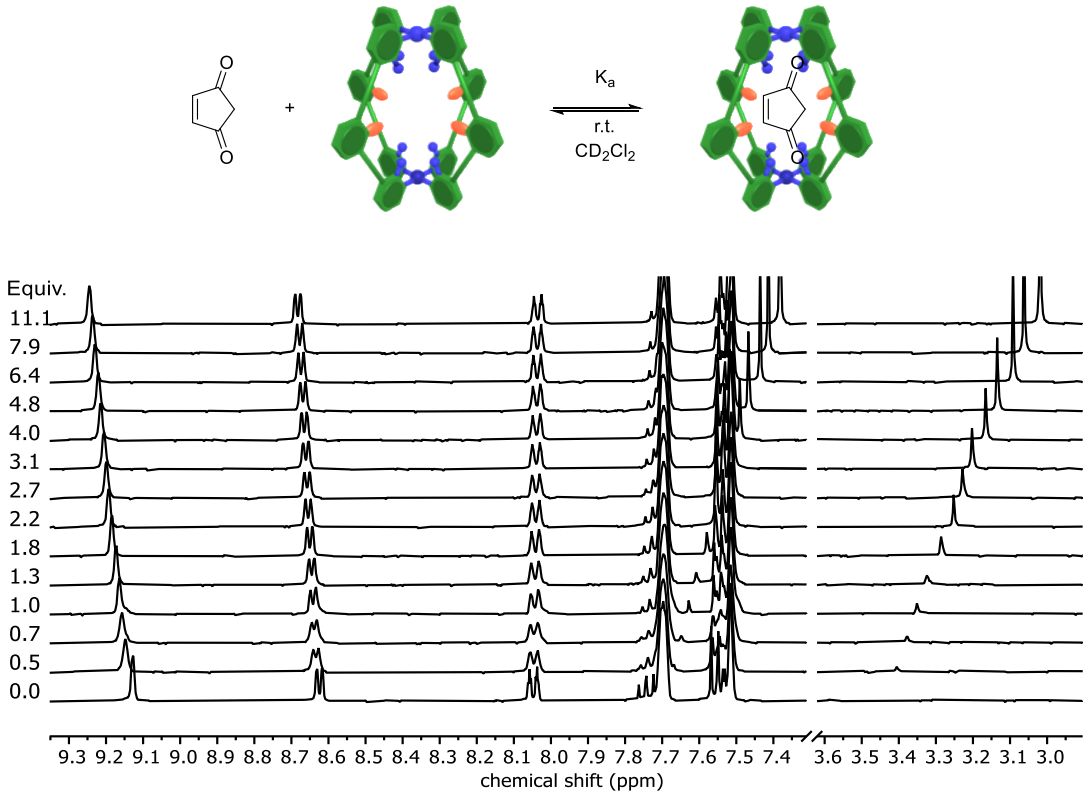

*Figure 3-41. ^{1}H NMR (400 MHz, CD_2Cl_2) spectroscopic data for titration of **3.6** into **C2**.*

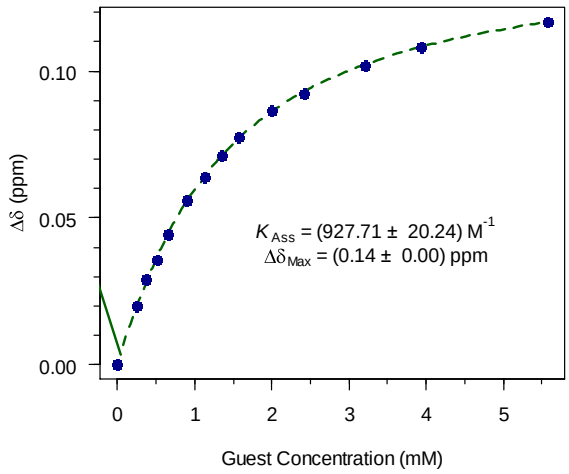

*Figure 3-42. Fitted data for change in peak position with increasing **3.6** concentration.*

3.8.5.16 ^{1}H NMR titration data of 3.17 into C2

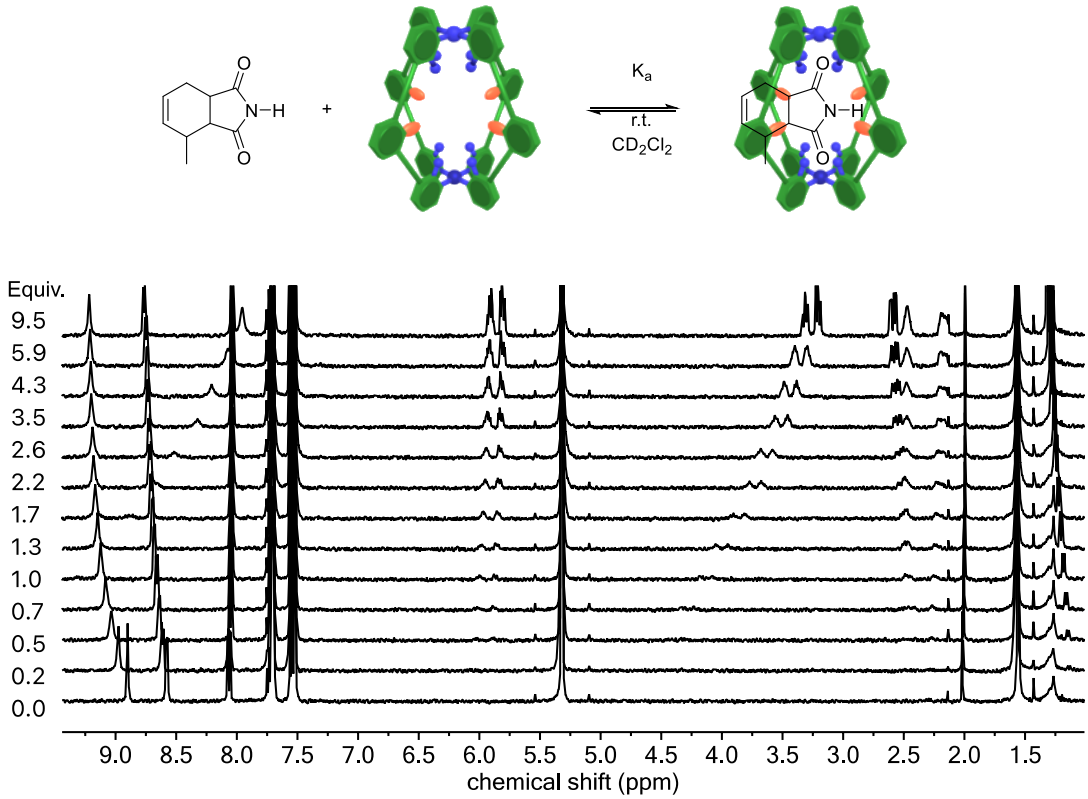

*Figure 3-43. ^{1}H NMR (400 MHz, CD_2Cl_2) spectroscopic data for titration of **3.17** into **C2**.*

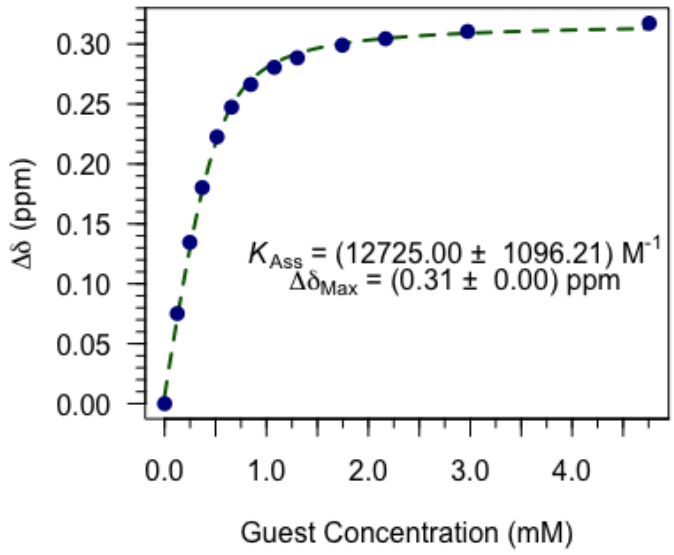

*Figure 3-44. Fitted data for change in peak position with increasing **3.17** concentration.*

3.8.5.17 ^{1}H NMR titration data of 3.15 product into C2

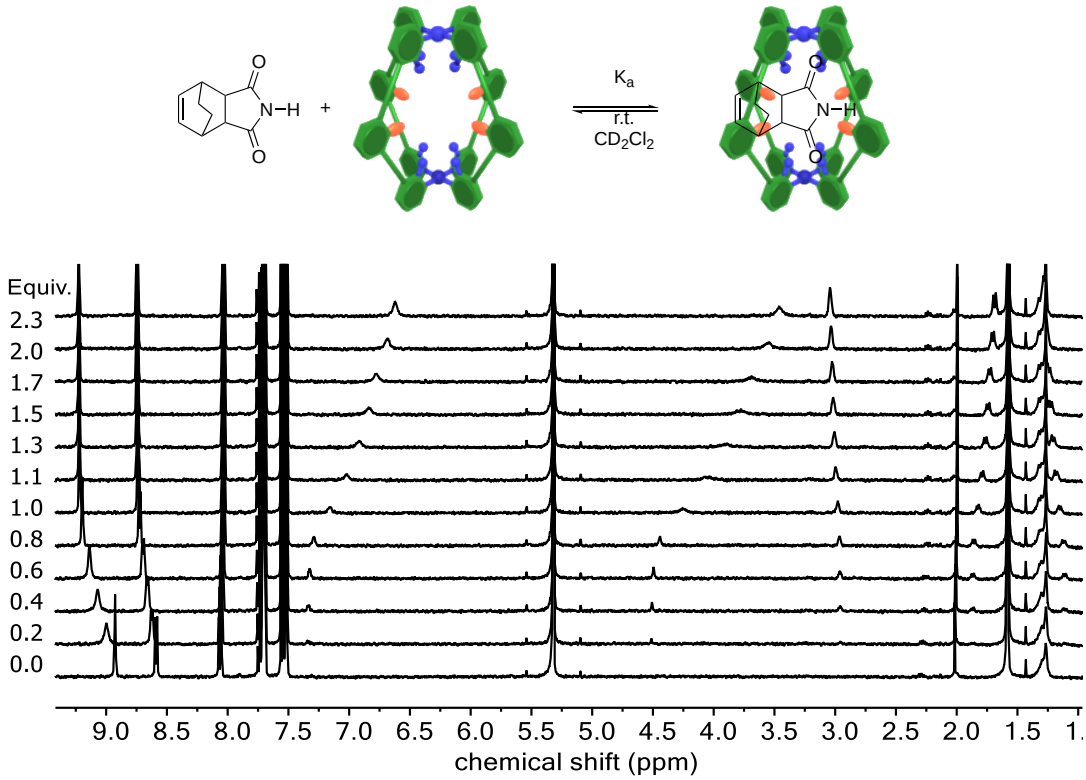

*Figure 3-45. ^{1}H NMR (400 MHz, CD_2Cl_2) spectroscopic data for titration of **3.15** into **C2**.*

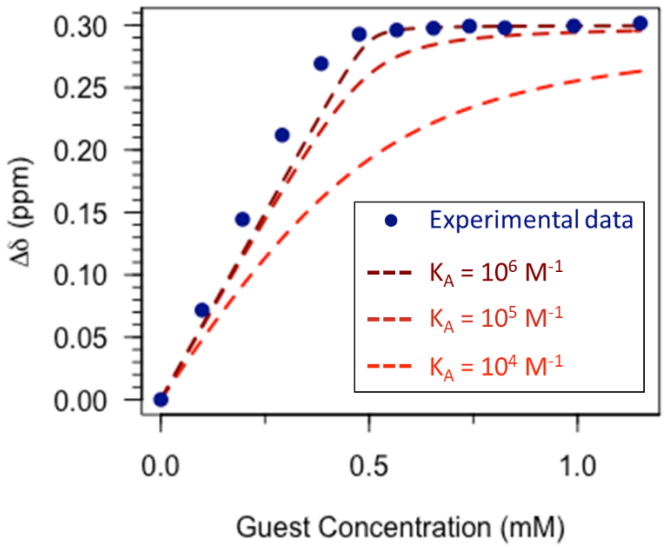

*Figure 3-46. Blue dots: peak position change with increasing **3.15** concentration. Red dashed lines: simulated 1:1 binding isotherms with varying association constants. The non-linear part of the experimental data is restricted to a small region. The binding of **3.15** exceeds the limit of NMR titration, and the lower limit is estimated to be 10^5 M^{-1}.*

3.8.6 Kinetic parameter fitting for Diels-Alder reactions

3.8.6.1 Procedure and kinetic model

The kinetic parameters of the uncatalysed and cage catalysed Diels-Alder reactions (k_{uncat} and k_{cat}) were obtained by fitting the experimental data to appropriate kinetic models, as shown below, using the Levenberg-Marquardt algorithm with Python 3.7.4.

The Diels-Alder reactions generating only one product (i.e. the formation of **3.9**, **3.10**, **3.15**, **3.18** and **3.17**) were fitted to the uncatalysed and catalysed kinetic models described in the previous publication from the Lusby group.[16] The Diels-Alder reaction of **3.4** and **3.7** is irreversible and forms both the *endo* and the *exo* products. The kinetic models hence incorporate parameters such as $k_{cat\text{-}endo}$, $k_{uncat\text{-}endo}$, $k_{cat\text{-}exo}$ and $k_{uncat\text{-}exo}$.

The Diels-Alder reaction of **3.5** and **3.12** forms both the *endo* and the *exo* products. *endo* **3.13** undergoes retro-Diels-Alder reaction and regenerates **3.5** and **3.12**. The fitting of the kinetic parameters for the reactions involving **3.5** and **3.12** is described in detail as a representative example.

The uncatalysed kinetic model is shown in Figure 3-47. The contribution of the forward and the backward background reactions are considered for both *endo* and *exo* product (step 1 and 2). Experimental evidence suggests that *exo* **3.13** does not undergoes retro-Diels-Alder reaction and $k_{uncat\text{-}exo\text{-}b}$ is set to be 0 h^{-1} in the fitting.

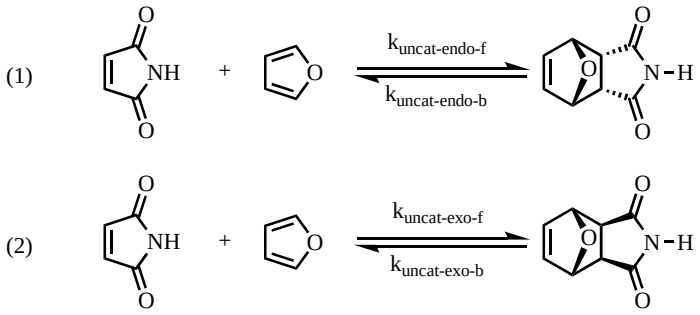

*Figure 3-47. The kinetic model for the uncatalysed Diels-Alder reaction of **3.5** and **3.12**.*

The uncatalysed kinetic model is shown in Figure 3-48. The contribution of the forward and the backward background reactions are considered for both *endo* and *exo* product (step 1 and 2). Prior to the catalysed bond formation steps, **C1**/**C2** binds **3.5** to

form the active species (step 3). Steps 4 and 5 depict the forward and reverse Diels-Alder reactions within the cavity, and steps 6 and 7 show the release of *endo* and *exo* **3.13**. The complete model of the **C2** catalysed reaction is composed of step 1 through 7. When using **C1** as the catalyst, the *exo* **3.13**⊂**C1** complex was observed to precipitate over the course of the reaction. Therefore, step 8 was introduced to account for this event.

For the purpose of fitting, disassociation rates of host-guest complexes ($k_{SM\text{-}D}$, $k_{P\text{-}endo\text{-}D}$ and $k_{P\text{-}exo\text{-}D}$) are set to be 10^3 h^{-1}, assuming that the guest binding steps (steps 3, 6 and 7) are sufficiently faster than the catalysed and uncatalysed reaction steps (steps 1, 2, 4 and 5). Note that this assumption is based on the fast cage/guest exchange rate as observed in the NMR spectra. Association rates are then calculated using the binding constants and the relation: $K_A = k_A / k_D$. *exo* **3.13** is the stable thermodynamic product and does not undergo the reverse reaction, hence its catalysed rate constant $k_{cat\text{-}exo\text{-}b}$ is set to be 0 h^{-1} (the same for $k_{uncat\text{-}exo\text{-}b}$).

The kinetic parameters of the background reaction were obtained by fitting the control experiment data to the uncatalysed kinetic model (entries 1-3, Table 3-4). Given the kinetic parameters of the background reactions and the encapsulation/disassociation processes ($k_{uncat\text{-}endo\text{-}f}$, $k_{uncat\text{-}endo\text{-}b}$, $k_{uncat\text{-}exo\text{-}f}$, $k_{uncat\text{-}exo\text{-}b}$, $k_{SM\text{-}A}$, $k_{SM\text{-}D}$, $k_{P\text{-}endo\text{-}A}$, $k_{P\text{-}exo\text{-}A}$), the fitting of the **C1** and **C2** catalysed reaction data gives the catalysed rate constants as shown in entries 4-8, Table 3-4.

The experimental observations support the fitted kinetic parameters. $k_{cat\text{-}endo\text{-}b}$ was found to be 0 h^{-1} for **C1** catalysed reaction and 0.014 h^{-1} in **C2**, indicating the retro-Diels-Alder reaction of *endo* **3.13** is exclusively catalysed by **C2**. This was cross-validated with the control reactions where *endo* **3.13** was charged with 150 mol% **C1**, **C2** or no catalyst. While no discernible rate acceleration was observed for the **C1** catalysed reaction, **C2** was found to catalyse the retro-Diels-Alder reaction of *endo* **3.13**. Furthermore, the fitted rate constant of the uncatalysed backward (retro-Diels-Alder) reaction, $k_{uncat\text{-}endo\text{-}b}$ = 0.0019 h^{-1}, is in good consistency with that calculated by measuring the initial rate of the decomposition of 0.4 mM *endo* **3.13**, $k_{uncat\text{-}endo\text{-}b}$ = 0.002 h^{-1}.

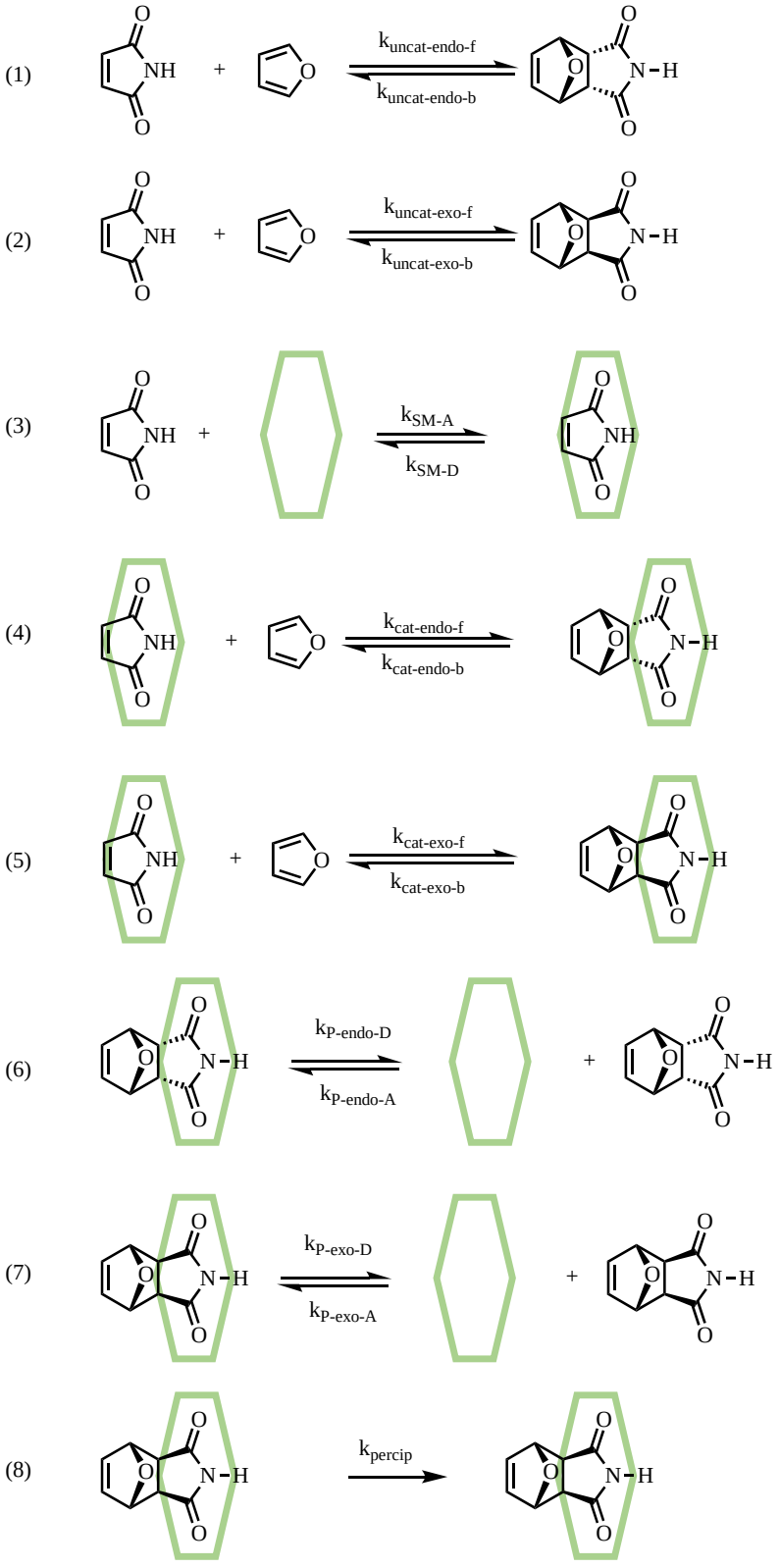

*Figure 3-48. Kinetic models of cage catalysed Diels-Alder reaction of **3.5** and **3.12**.*

*Table 3-4. The kinetic parameters fitted for the Diels-Alder reaction of **3.5** and **3.12**.*

Entry	Fitted parameter	**C1** catalysed reaction	**C2** catalysed reaction	Uncatalysed reaction
1	$k_{uncat\text{-}endo\text{-}f}$	0.0217 ($M^{-1}h^{-1}$)	0.0217 ($M^{-1}h^{-1}$)	0.0217 ($M^{-1}h^{-1}$)
2	$k_{uncat\text{-}endo\text{-}b}$	0.0019 (h^{-1})	0.0019 (h^{-1})	0.0019 (h^{-1})
3	$k_{uncat\text{-}exo\text{-}f}$	0.0162 ($M^{-1}h^{-1}$)	0.0162 ($M^{-1}h^{-1}$)	0.0162 ($M^{-1}h^{-1}$)
4	$k_{uncat\text{-}exo\text{-}b}$	0	0	0
5	$k_{cat\text{-}endo\text{-}f}$	0	0.058 ($M^{-1}h^{-1}$)	-
6	$k_{cat\text{-}endo\text{-}b}$	0	0.014 (h^{-1})	-
7	$k_{cat\text{-}exo\text{-}f}$	0.045 ($M^{-1}h^{-1}$)	0.043 ($M^{-1}h^{-1}$)	-
8	$k_{cat\text{-}exo\text{-}b}$	0	0	-

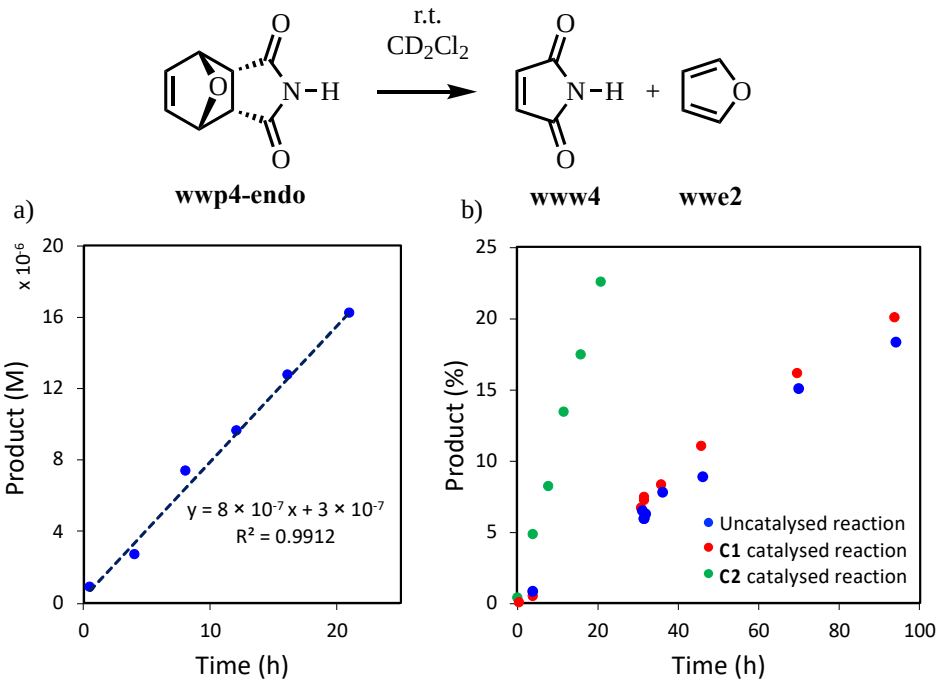

*Figure 3-49. a) The intitial rate V_{init} measured for the uncatalysed retro-Diels-Alder reaction of 0.4 mM endo-**3.13** is 8×10^{-7} M h^{-1}, giving the rate constant $k_{uncat\text{-}endo\text{-}b}$ of 0.002 h^{-1}. b) The retro-Diels-Alder reaction of endo-**3.13** is catalysed by **C2** and not affected by **C1**. The*

3.8.6.2 Simulation of product inhibition

The turnover step of the Diels-Alder reactions in **C2** is influenced by the binding equilibria of the bound starting material (the dienophile) and the product. Herein, kinetic profiles of the cage catalysed reactions are simulated by varying the binding constants of the starting material and the product, providing a visualisation of this turnover model. The simulations were carried out using the appropriate kinetic models discussed in section 3.8.6.1.

Figure 3-50 presents the simulated kinetic profiles of reactions that form products with varying binding constants. The following catalytic condition is maintained for all the simulation sets: initial concentration of dienenophile = 2.5 mM, initial concentration of diene = 6.25 mM, concentration of cage = 0.5 mM, binding constant of dienenophile ($K_{A\text{-}SM}$) = 2000 M^{-1}, k_{uncat} = 0.5 $M^{-1}h^{-1}$ and k_{cat} = 50 $M^{-1}h^{-1}$. The binding affinities of the products are represented as multiples of the binding constants of the dienophile ($K_{A\text{-}P}/K_{A\text{-}SM}$). One can envisage such two extreme boundary scenarios: a) when the product does not bind in the cage, i.e., $K_{A\text{-}P}$ = 0 M^{-1} (shown as grey squares), and b) when the system is uncatalysed (shown as black circles). As the product becomes an increasingly better guest than the starting material ($K_{A\text{-}P}$/ $K_{A\text{-}SM}$ increases), the convex kinetic curve exhibits more pronounced inflection. In the case of $K_{A\text{-}P}/K_{A\text{-}SM}$ = 150, the inflection point converges around when the amount of product equals to the amount of cage. This suggests that all cage species are only able to perform catalysis once and do not turnover.

Although the abrupt change in reaction rate is characteristic of severe product inhibition, it can be difficult to observe with the naked eye, especially when the background reaction is fast and the rate enhancement is poor. Figure 3-51 showcases such a scenario. The kinetic profile simulations were repeated with the background rate raised up to k_{uncat} = 5 $M^{-1}h^{-1}$ and the other conditions remained the same as in Figure 3-50.

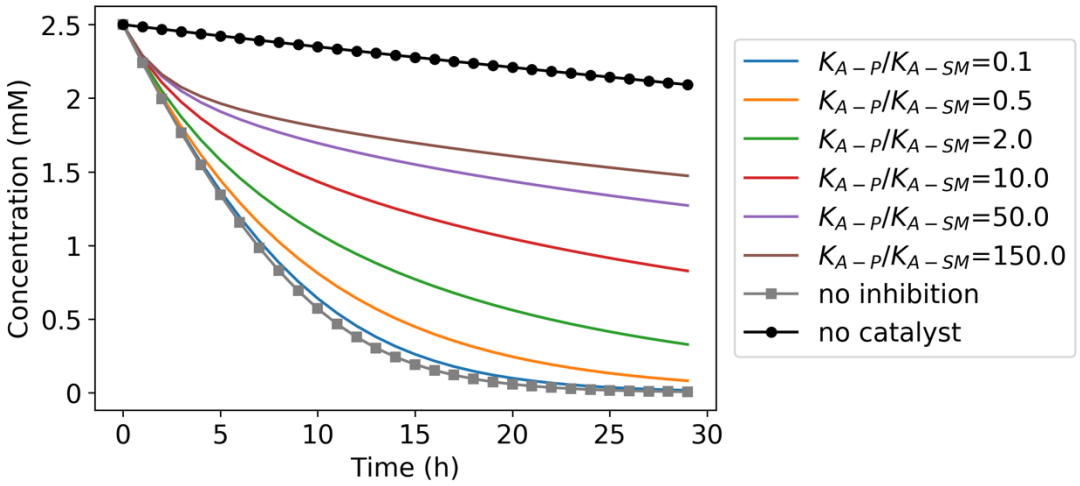

Figure 3-50. Simulated kinetic profiles with varying binding constants of the product. Simulation was carried out with the conditions: initial concentration of dienenophile = 2.5 mM, initial concentration of diene = 6.25 mM, concentration of cage = 0.5 mM, binding constant of dienenophile ($K_{A\text{-}SM}$) = 2000 M^{-1}, k_{uncat} = 0.5 $M^{-1}h^{-1}$ and k_{cat} = 50 $M^{-1}h^{-1}$.

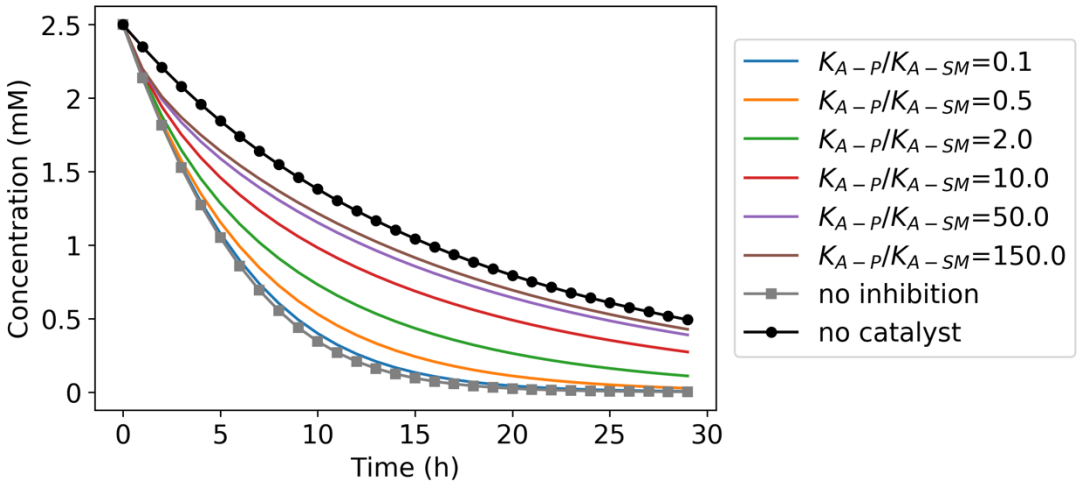

Figure 3-51. Simulated kinetic profiles with varying binding constants of the product. Simulation was carried out with the conditions: initial concentration of dienenophile = 2.5 mM, initial concentration of diene = 6.25 mM, concentration of cage = 0.5 mM, binding constant of dienenophile ($K_{A\text{-}SM}$) = 2000 M^{-1}, k_{uncat} = 5 $M^{-1}h^{-1}$ and k_{cat} = 50 $M^{-1}h^{-1}$.

3.8.6.3 The Diels-Alder reaction between 3.2 and 3.7

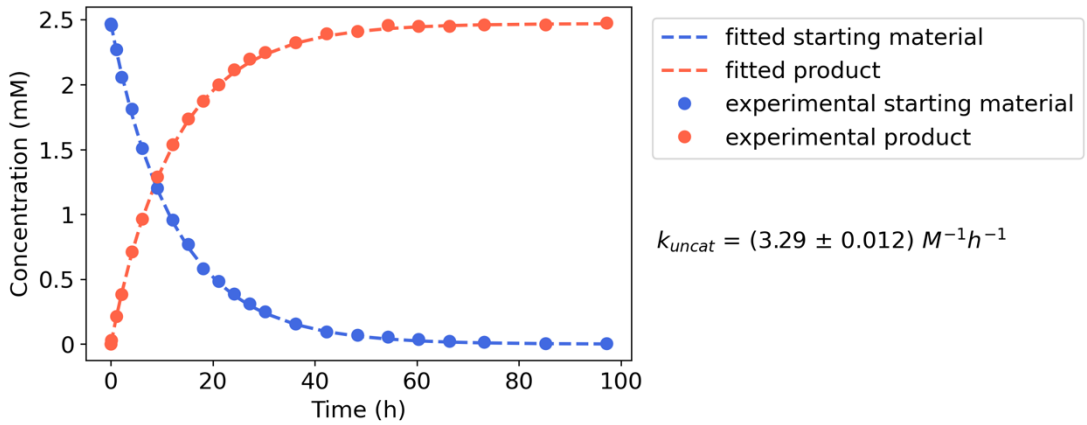

*Figure 3-52. Kinetic fitting for the uncatalysed Diels-Alder reaction between **3.2** (2.5 mM) and **3.7** (25 mM).*

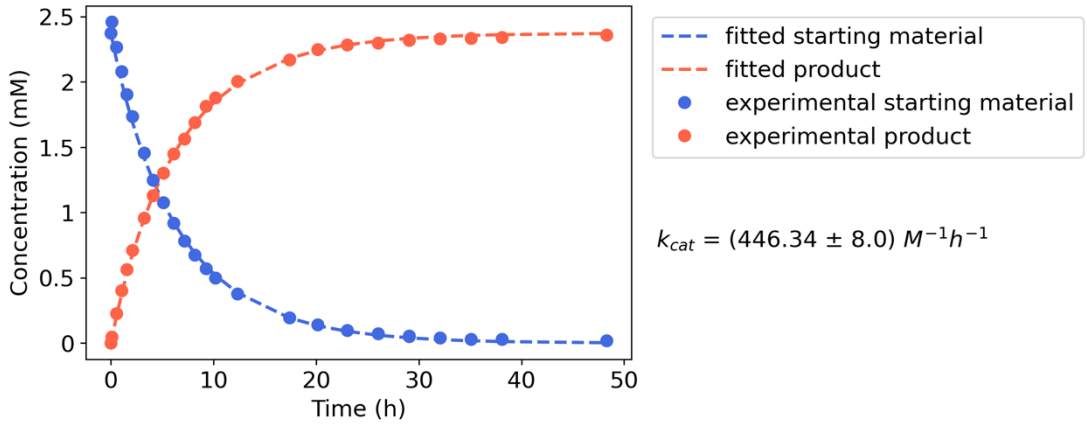

*Figure 3-53. Kinetic fitting for the catalysed Diels-Alder reaction between **3.2** (2.5 mM) and **3.7** (25 mM) with **C2** (0.5 mM).*

3.8.6.4 The Diels-Alder reaction between 3.3 and 3.7

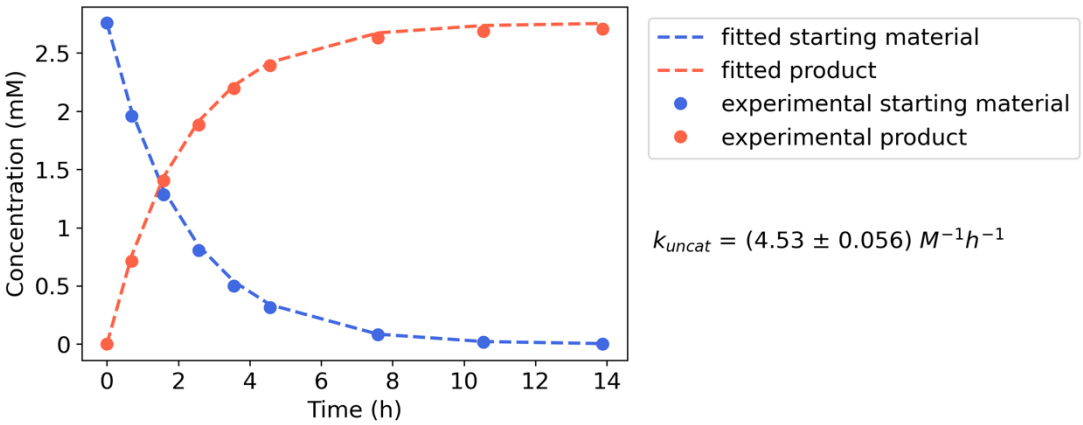

*Figure 3-54. Kinetic fitting for the uncatalysed Diels-Alder reaction between **3.3** (2.5 mM) and **3.7** (12.5 mM).*

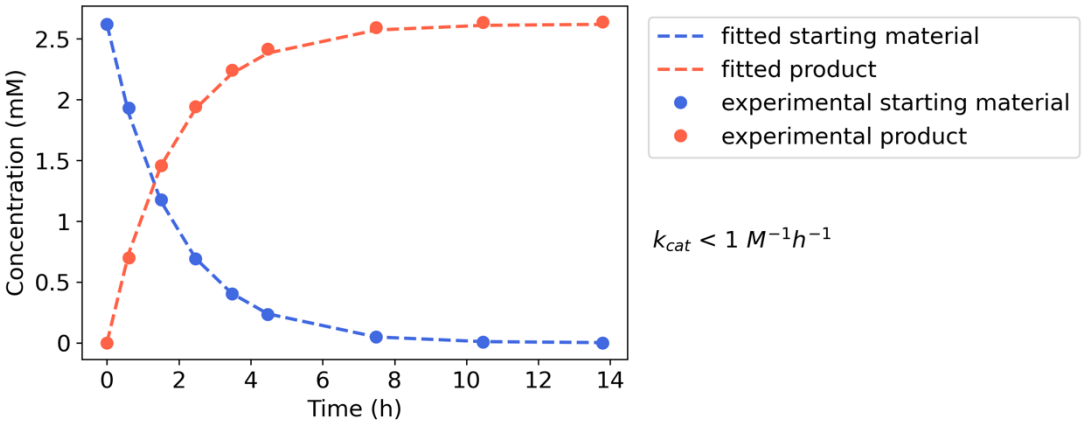

*Figure 3-55. Kinetic fitting for the catalysed Diels-Alder reaction between **3.3** (2.5 mM) and **3.7** (12.5 mM) with **C2** (1 mM).*

3.8.6.5 The Diels-Alder reaction between 3.4 and 3.7

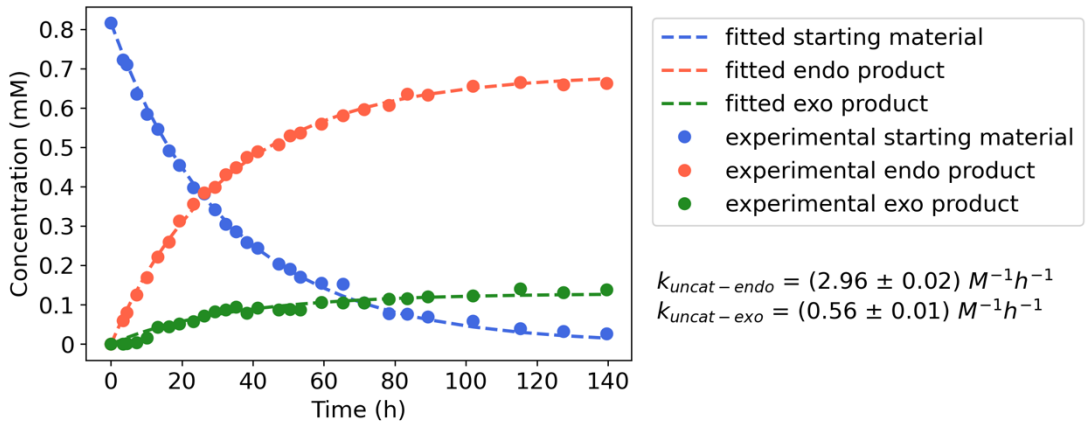

*Figure 3-56. Kinetic fitting for the uncatalysed Diels-Alder reaction between **3.4** (0.8 mM) and **3.7** (8 mM).*

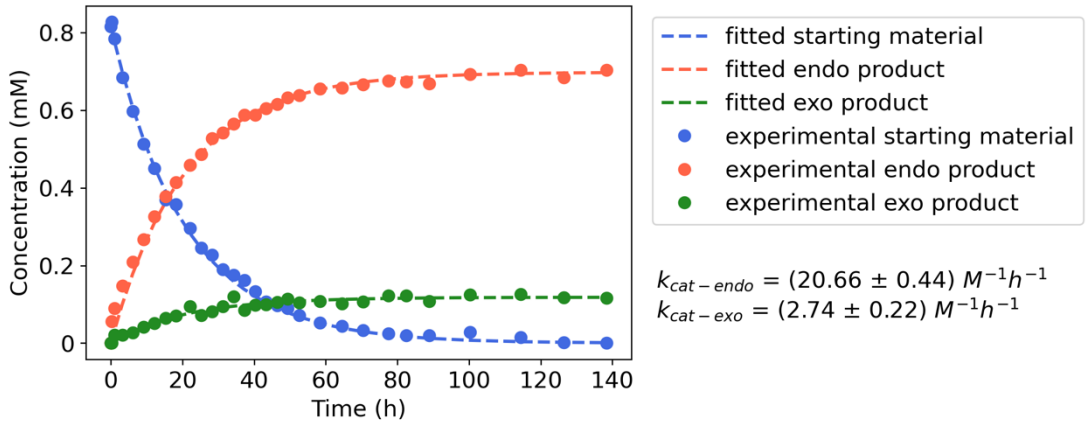

*Figure 3-57. Kinetic fitting for the catalysed Diels-Alder reaction between **3.4** (0.8 mM) and **3.7** (8 mM) with **C2** (0.5 mM).*

3.8.6.6 The Diels-Alder reaction between 3.5 and 3.12

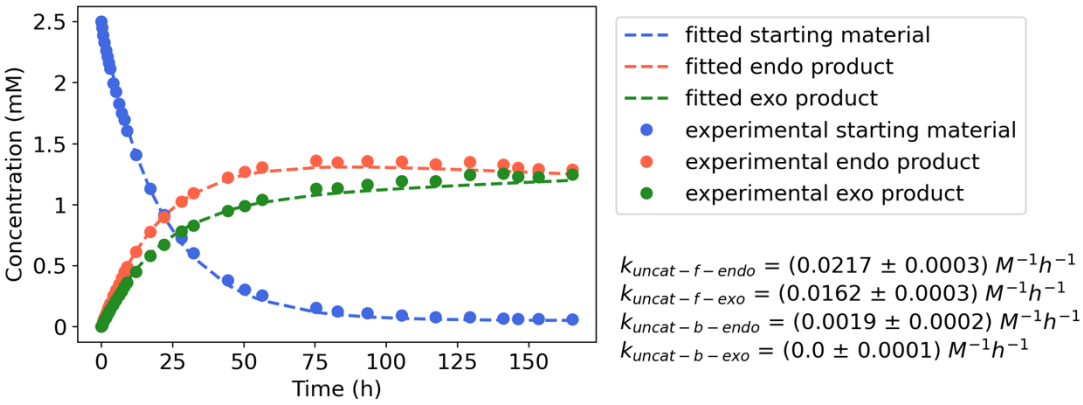

*Figure 3-58. Kinetic fitting for the uncatalysed Diels-Alder reaction between **3.5** (2.5 mM) and **3.12-d₄** (1.25 M).*

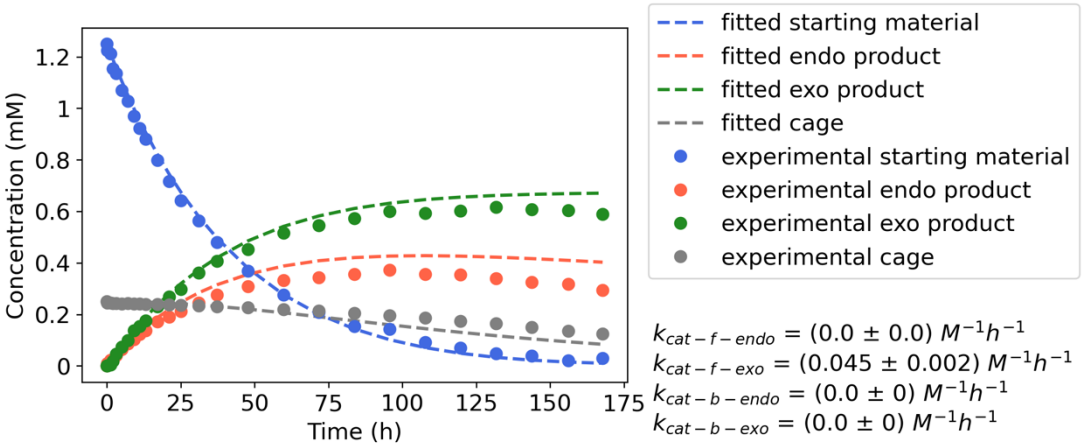

*Figure 3-59. Kinetic fitting for the catalysed Diels-Alder reaction between **3.5** (1.25 mM) and **3.12-d₄** (0.625 M) with **C1** (0.5 mM). The product exo **3.13** and **C1** form a complex which percipitates over the course of the reaction (grey circles). This was taken into account while fitting for kinetic parameters (grey dashed line), and the rate of percipitation was found to be 0.012 $M^{-1}h^{-1}$. Reduced concentration was used for the **C1** catalysed reacion in comparision to the background reaction and the **C2** catalysed reaction due to the fast percipitation at high concentration.*

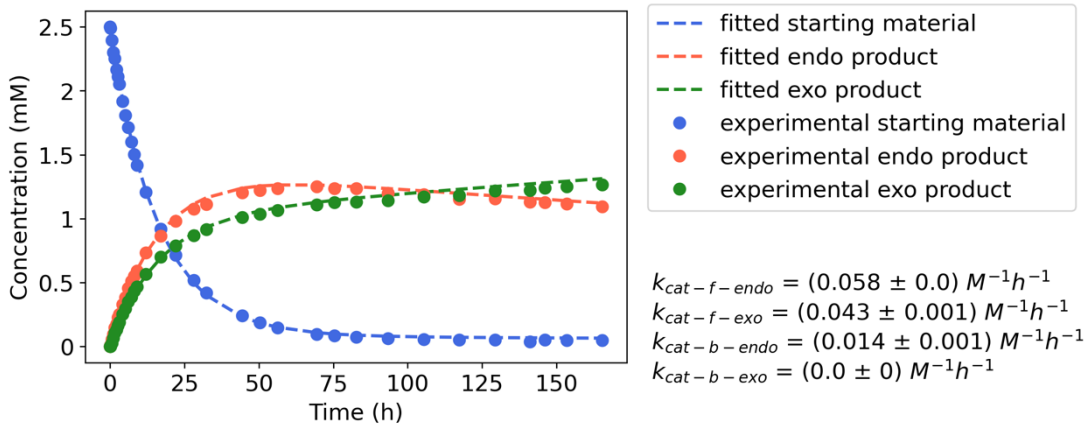

*Figure 3-60. Kinetic fitting for the catalysed Diels-Alder reaction between **3.5** (2.5 mM) and **3.12-d$_4$** (1.25 M) with **C2** (0.5 mM).*

3.8.6.7 The Diels-Alder reaction between 3.5 and 3.14

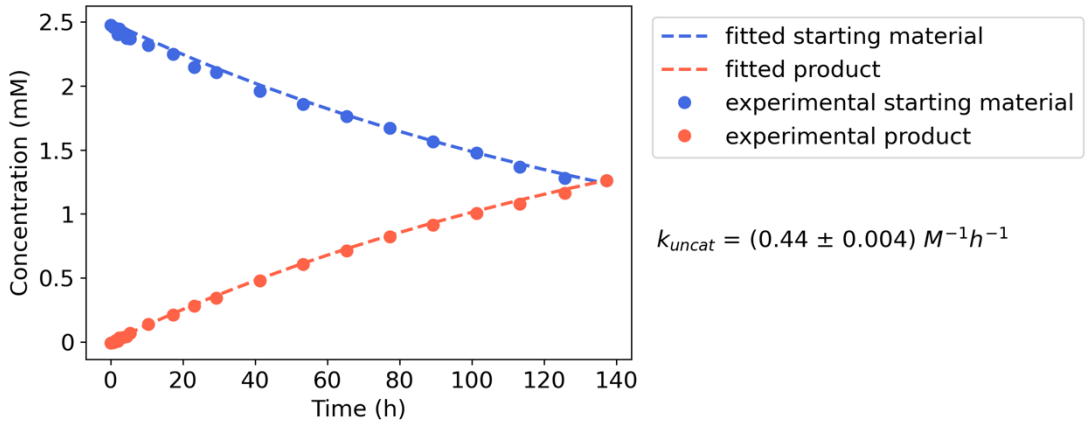

*Figure 3-61. Kinetic fitting for the uncatalysed Diels-Alder reaction between **3.5** (2.5 mM) and **3.14** (12.5 mM).*

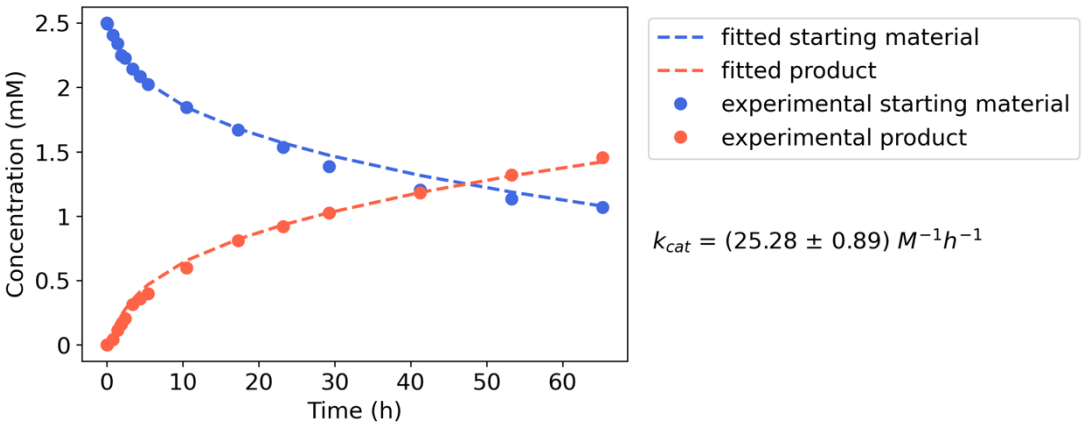

*Figure 3-62. Kinetic fitting for the catalysed Diels-Alder reaction between **3.5** (2.5 mM) and **3.14** (12.5 mM) with C2 (0.5 mM).*

3.8.6.8 The Diels-Alder reaction between 3.5 and 3.16

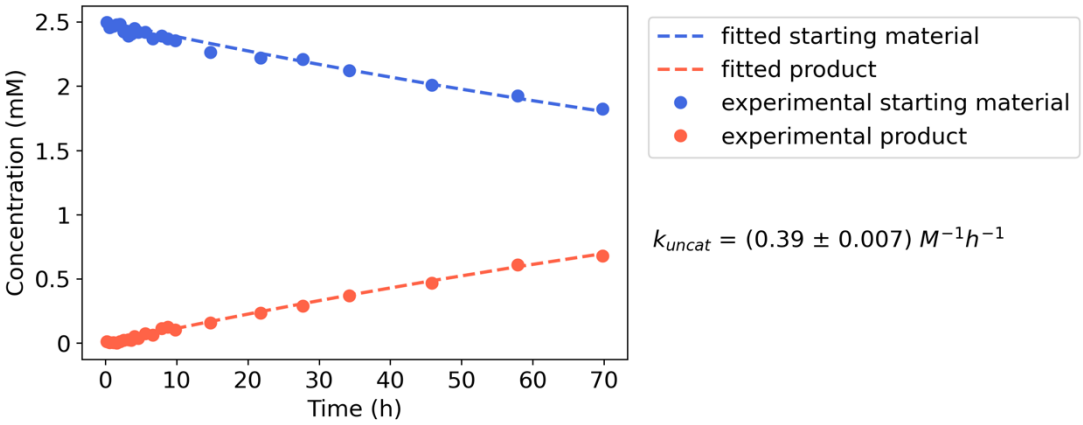

*Figure 3-63. Kinetic fitting for the uncatalysed Diels-Alder reaction between **3.5** (2.5 mM) and **3.16** (12.5 mM).*

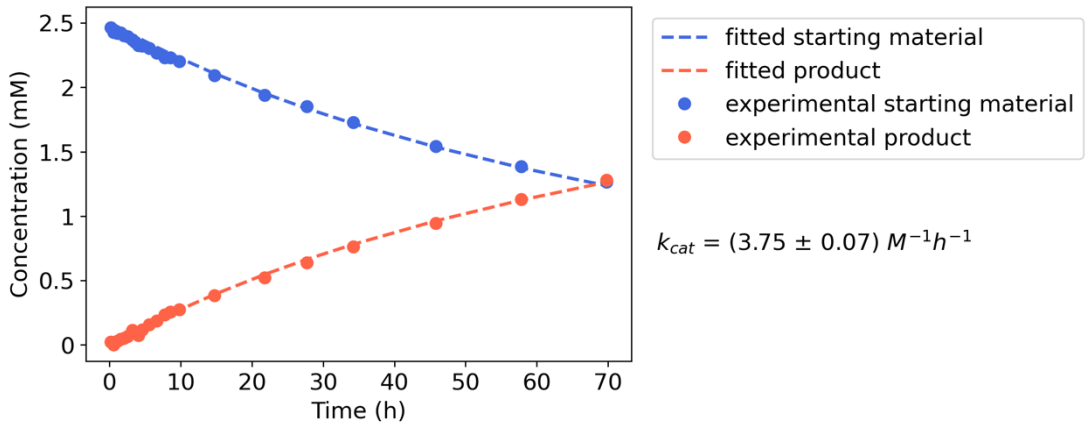

*Figure 3-64. Kinetic fitting for the catalysed Diels-Alder reaction between **3.5** (2.5 mM) and **3.16** (12.5 mM) with **C2** (0.5 mM).*

3.8.6.9 The Diels-Alder reaction between 3.6 and 3.7

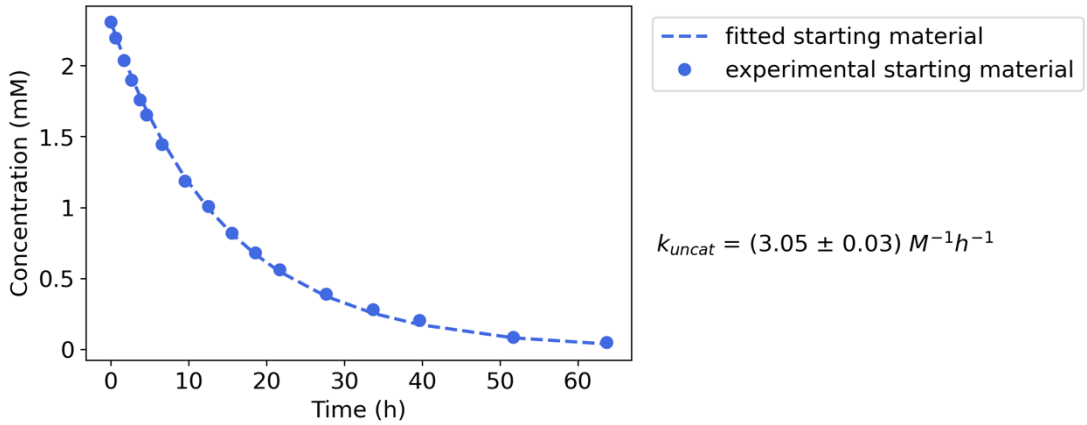

*Figure 3-65. Kinetic fitting for the uncatalysed Diels-Alder reaction between **3.6** (2.5 mM) and **3.7** (25 mM).*

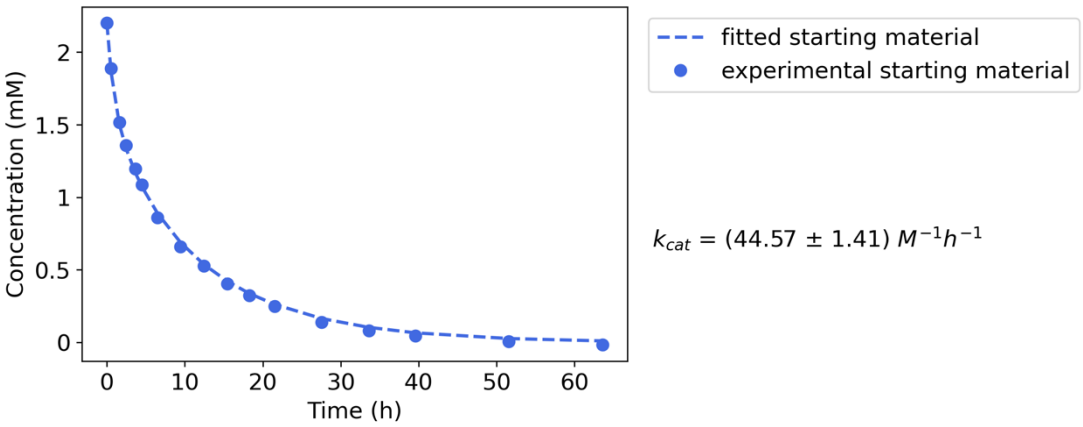

*Figure 3-66. Kinetic fitting for the catalysed Diels-Alder reaction between **3.6** (2.5 mM) and **3.7** (25 mM) with **C2** (0.5 mM). The binding constant of the product was estimated to be 240000 $M^{-1}$for the purpose of fitting.*

3.9 References

[1] M. Yoshizawa, M. Tamura, M. Fujita, *Science* **2006**, *312*, 251–254.
[2] J. Kang, J. Rebek, *Nature* **1996**, *382*, 239–241.
[3] C. J. Walter, H. L. Anderson, J. K. M. Sanders, *J. Chem. Soc. Chem. Commun.* **1993**, 458–460.
[4] C. J. Hastings, M. D. Pluth, R. G. Bergman, K. N. Raymond, *J. Am. Chem. Soc.* **2010**, *132*, 6938–6940.
[5] M. D. Pluth, R. G. Bergman, K. N. Raymond, *Science* **2007**, *316*, 85–88.
[6] W. M. Hart-Cooper, K. N. Clary, F. D. Toste, R. G. Bergman, K. N. Raymond, *J. Am. Chem. Soc.* **2012**, *134*, 17873–17876.
[7] W. Cullen, M. C. Misuraca, C. A. Hunter, N. H. Williams, M. D. Ward, *Nat. Chem.* **2016**, *8*, 231–236.
[8] D. Fiedler, R. G. Bergman, K. N. Raymond, *Angew. Chem. Int. Ed.* **2004**, *43*, 6748–6751.
[9] H. Takezawa, T. Kanda, H. Nanjo, M. Fujita, *J. Am. Chem. Soc.* **2019**, *141*, 5112–5115.
[10] D. Masseroni, S. Mosca, M. P. Mower, D. G. Blackmond, J. Rebek, *Angew. Chem. Int. Ed.* **2016**, *55*, 8290–8293.
[11] D. P. August, G. S. Nichol, P. J. Lusby, *Angew. Chem. Int. Ed.* **2016**, *55*, 15022–15026.
[12] P. Liao, B. W. Langloss, A. M. Johnson, E. R. Knudsen, F. S. Tham, R. R. Julian, R. J. Hooley, *Chem. Commun.* **2010**, *46*, 4932–4934.
[13] A. Wittkopp, P. R. Schreiner, *Chem. – Eur. J.* **2003**, *9*, 407–414.
[14] P. R. Schreiner, A. Wittkopp, *Org. Lett.* **2002**, *4*, 217–220.
[15] R. L. Spicer, A. D. Stergiou, T. A. Young, F. Duarte, M. D. Symes, P. J. Lusby, *J. Am. Chem. Soc.* **2020**, *142*, 2134–2139.
[16] V. Martí-Centelles, A. L. Lawrence, P. J. Lusby, *J. Am. Chem. Soc.* **2018**, *140*, 2862–2868.
[17] C. A. Hunter, *Angew. Chem. Int. Ed.* **2004**, *43*, 5310–5324.
[18] V. Martí-Centelles, R. L. Spicer, P. J. Lusby, *Chem. Sci.* **2020**, *11*, 3236–3240.
[19] E. B. Mubofu, J. B. F. N. Engberts, *J. Phys. Org. Chem.* **2004**, *17*, 180–186.
[20] R. L. Spicer, *Turning Capsule Catalysis Inside-out* **2020**, the University of Edinburgh.
[21] J. L. Bolliger, A. M. Belenguer, J. R. Nitschke, *Angew. Chem. Int. Ed.* **2013**, *52*, 7958–7962.
[22] C. G. P. Taylor, A. J. Metherell, S. P. Argent, F. M. Ashour, N. H. Williams, M. D. Ward, *Chem. – Eur. J.* **2020**, *26*, 3065–3073.
[23] M. Yoshizawa, J. K. Klosterman, M. Fujita, *Angew. Chem. Int. Ed.* **2009**, *48*, 3418–3438.
[24] P. Thordarson, *Chem. Soc. Rev.* **2011**, *40*, 1305–1323.
[25] N. G. Ramesh, F. J. A. D. Bakkeren, D. de Groot, U. Passamonti, A. J. H. Klunder, B. Zwanenburg, *Tetrahedron* **2001**, *57*, 9877–9887.
[26] P. R. Schreiner, *Chem. Soc. Rev.* **2003**, *32*, 289–296.
[27] W. Li, J.-D. Long, Y.-Y. Qian, Y. Long, X.-J. Xu, Y.-J. Wang, Q. Shen, Z.-N. Wang, X.-C. Yang, L. Xiao, H.-P. Sun, Y.-L. Xu, Y.-Y. Chen, Q. Xie, Y.-H.

Wang, L.-M. Shao, J.-G. Liu, Z.-B. Qiu, W. Fu, *ACS Chem. Neurosci.* **2017**, *8*, 766–776.
[28] M. S. Morgan, R. S. Tipson, A. Lowy, W. E. Baldwin, **1944**, 4.
[29] I. Michieletto, F. Fabris, O. De Lucchi, *Tetrahedron Asymmetry* **2000**, *11*, 2835–2841.
[30] S. Niwayama, H. Cho, M. Zabet-Moghaddam, B. R. Whittlesey, *J. Org. Chem.* **2010**, *75*, 3775–3780.
[31] H. Kwart, I. Burchuk, *J. Am. Chem. Soc.* **1952**, *74*, 3094–3097.
[32] M. R. Johnson, J. F. Gauuan, C. Guo, P. R. Guzzo, V.-D. Le, R. A. Shenoy, J. Hamby, H. Roark, M. Stier, J. E. Mangette, *Synth. Commun.* **2011**, *41*, 2769–2793.
[33] H. Clavier, L. Giordano, A. Tenaglia, *Angew. Chem. Int. Ed.* **2012**, *51*, 8648–8651.
[34] R. A. Valiulin, T. M. Arisco, A. G. Kutateladze, *J. Org. Chem.* **2013**, *78*, 2012–2025.
[35] R. V. Ashirov, D. I. Zemlyakov, A. A. Lyapkov, S. A. Kiselev, *Kinet. Catal.* **2013**, *54*, 469–474.
[36] R. Subramanyam, P. D. Bartlett, G. Y. M. Iglesias, W. H. Watson, J. Galloy, *J. Org. Chem.* **1982**, *47*, 4491–4498.
[37] E. H. Discekici, A. H. St. Amant, S. N. Nguyen, I.-H. Lee, C. J. Hawker, J. Read de Alaniz, *J. Am. Chem. Soc.* **2018**, *140*, 5009–5013.
[38] B. Graham, A. E. R. Fayter, J. E. Houston, R. C. Evans, M. I. Gibson, *J. Am. Chem. Soc.* **2018**, *140*, 5682–5685.

Chapter 4

Development and Catalysis of Novel Pd_2L_4 Systems

Chapter 4 Development and Catalysis of Novel Pd_2L_4 Systems

Computations experiments in this chapter were carried out by Tom A. Young, a PhD student at the Chemistry Research Laboratory, University of Oxford, Mansfield Road, Oxford, OX1 3TA, UK. ***C5*** *was synthesised by Dr Helen O'Connor, a post-doctoral researcher in the Lusby group.*

4.1 Introduction

A vast number of coordination cage structures have been made accessible by the rational design methods that encode the structural information of the self-assemblies into the geometries of the building blocks, namely the metal centres and the organic ligands.[1][2] In comparison, coordination cages that have shown catalytic properties are surprisingly scarce. While research groups such as those of Fujita, Raymond, Toste, Bergman and Ward have demonstrated impressive supramolecular catalysis including the Diels-Alder[3][4] and Knoevenagel[5] reactions, the aza-Cope[6] and Prins[7] rearrangements, the Nazarov[8] cyclisation, the Kemp elimination[9] and a broad range of hydrolysis reactions[10][11][12], the investigations primarily use the same archetypical $Pd_6L_4^{12+}$, $Ga_4L_6^{12-}$ and $Co_8L_{12}^{16+}$ cages. Most of the researches focus on expanding the catalytic reaction scopes of a known cage, and the studies on how the structural modification of the cage can impact catalysis are relatively rare.[13][14][15]

In order to develop new and better catalysts, a clear understanding of existing systems is essential. The Lusby group's first study on Diels-Alder catalysis of benzoquinone **4.1** and cyclopentadiene **4.2** had already generated several interesting questions, the most obvious being why do two almost identical cages show very different catalytic properties (Figure 4-1a,b)? The experimental data pointed to two key factors that explain why **C2** is a very good catalyst and that **C1** is completely inactive. Firstly, **C2** is much more effective at stabilising the TS, which was inferred by binding studies with the TS analogue, **4.3**; **C2** binds this compound much more strongly than **C1** (Figure 4-1c). Additionally, the lone pairs of **C2** destabilise quinone binding (Figure

4-1c). Both of these factors combine to give a smaller energy barrier between the bound quinone and the TS.

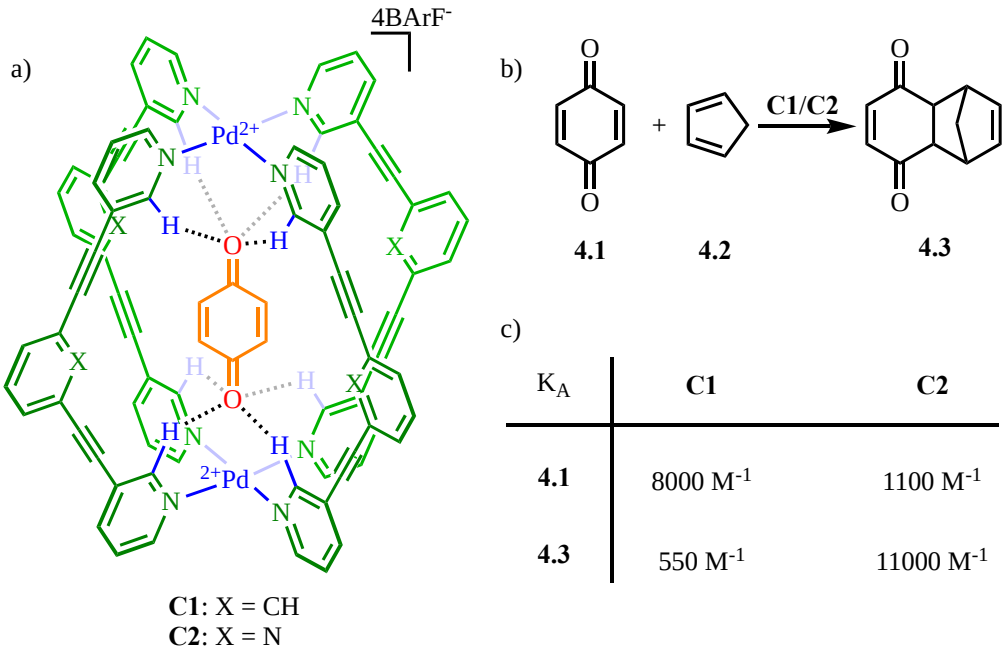

*Figure 4-1. a) Chemical structure of **C1** and **C2**. Benzoquinone is bound through H-bonding. b) A representative Diels-Alder reaction catalysed by **C2**. c) The binding constants of benzoquinone **4.1** and TS state analouge **4.3** in **C1** and **C2**.*

To shed more light on the origins of the catalysis and the subtleties that are often involved, the Lusby group have been collaborating with Duarte and co-workers since 2017, who have used various computational tools to add further insight. These calculations can provide an estimate of the electronic and steric contributions to the reaction energies in the **C1** and **C2** mediated processes. The enhanced reactivity of the bound quinones stem from hydrogen bonding between the oxygen atoms of these substrates and eight inwards facing ortho-pyridyl C-H bonds. These C-H groups are rendered H-bond acidic by proximity to the Pd^{2+} ions. Calculations reveal that this polarisation gives **4.1** a slight positive charge by removing its electron density;[16] **4.1** is therefore activated as a dienophile and has a LUMO energy reduction of 1.5 eV in **C1** and 1.6 eV in **C2**[17]. The similar magnitude of the electronic substrate activation in both cages suggests there is a counterproductive factor that makes the **C1** structure incapable of catalysis.

The calculated transition states of **4.1** and isoprene in **C1** and **C2** are shown in Figure 4-2. Non-covalent interaction plots of these TS structures reveal steric clashes between the diene and the central C-H moiety of **C1**. Conversely, the pyridine group in **C2** forms favourable hydrogen bonds to stabilise the TS. These results give rise to the first question that will be explored in this chapter: are Pd_2L_4 cages with less crowded cavities superior at catalysing quinone-based Diels-Alder reactions?

Furthermore, the optimised transition state geometries require the incoming diene to interact with the bound **4.1** through one cage window, suggesting a large distortion energy cost to reach the TS (Figure 4-2). Distortion/interaction analysis is used to unpick the specifics of the steric effect during the cycloaddition. This analysis breaks down the activation energy ($\Delta E^{\ddagger}$) into: a) distortion components ($\Delta E^{\ddagger}_{d}$) which represent the energy required to distort reactants from the ground state to the transition state conformations, and b) interaction components ($\Delta E^{\ddagger}_{int}$) representing the energy gained by the interaction between these distorted fragments. For the **C1**/**C2** catalysed Diels-Alder reactions, the distortion components were divided into the distortion penalty of isoprene, **4.1** (benzoquinone), **C1**/**C2** and of complex **4.1⊂C1**/**C2** (Table 4-1). It was shown that both isoprene and **4.1⊂C1** suffer a higher distortion penalty to reach the TS compared to **C2** ($\Delta\Delta E_{\mathbf{C2\text{-}C1}} = -1.3$ kcal mol^{-1} for the diene and $\Delta\Delta E_{\mathbf{C2\text{-}C1}} = -3.2$ kcal mol^{-1} for **4.1⊂CX**). It is noteworthy that the interaction energy ($\Delta E^{\ddagger}_{int}$) is significantly lower in both **C1** and **C2** in comparison to the uncatalysed reaction, supporting the generic LUMO stabilisation. These computational insights identified the flexibility of the Pd_2L_4 cages as a key factor for modification in order to optimise quinone-based Diels-Alder reactions. The development of new cages that aim to explore these steric and flexibility factors will be described in this chapter.

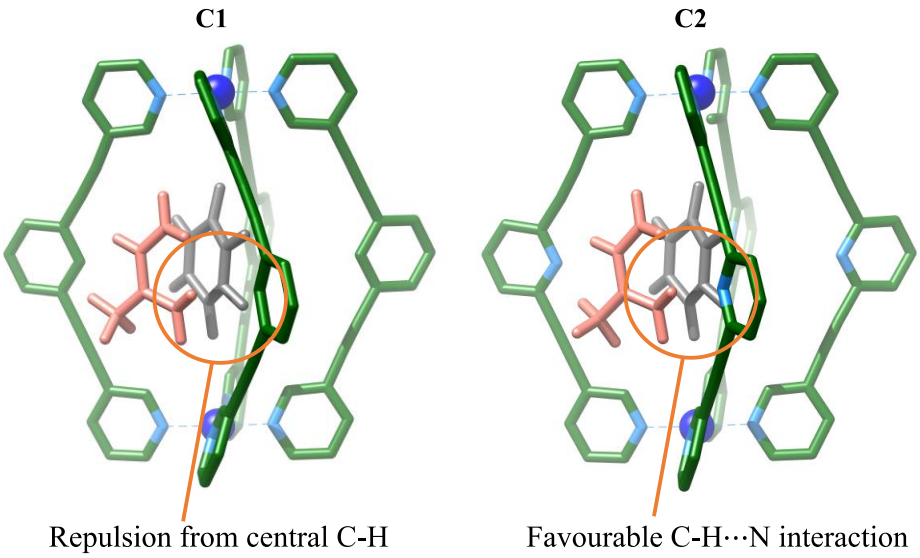

*Figure 4-2. Calculated transition state of reaction of **4.1** and isoprene in **C1** and **C2**.*

*Table 4-1. Distortion/interaction analysis for the Diels-Alder reaction between **4.1** and **isoprene** calculated at the SMD(DCM)-M2 level of theory*[xiii]

	Distortion energy components				Total distortion energy[xiv]	Interaction energy[xv]	Activation energy
	$\Delta E^{\ddagger}_{d}$ [**CX**]	$\Delta E^{\ddagger}_{d}$ [diene]	$\Delta E^{\ddagger}_{d[\mathbf{4.1}]}$	$\Delta E^{\ddagger}_{d[\mathbf{bq\subset CX}]}$	$\Delta E^{\ddagger}_{d[\mathbf{bq\subset CX}+diene]}$	$\Delta E^{\ddagger}_{int}$	$\Delta E^{\ddagger}$
uncat.	-	15.8	7.1	-	22.9	-13.0	9.9
C1	5.2	16.2	8.8	13.2	29.4	-19.2	10.2
C2	5.1	14.9	9.3	10.0	24.9	-20.4	4.5
$\Delta\Delta E_{\mathbf{C2-C1}}$[xvi]	-0.1	-1.3	0.5	-3.2	-4.5	-1.2	-5.7

[xiii] Distortion energy of the cage ($\Delta E^{\ddagger}_{d[\mathbf{CX}]}$) , diene ($\Delta E^{\ddagger}_{d[diene]}$), dienophile ($\Delta E^{\ddagger}_{d[\mathbf{bq}]}$), and **4.1⊂CX** complexes ($\Delta E^{\ddagger}_{d[\mathbf{bq\subset CX}]}$). All energies are given in kcal mol^{-1}.
[xiv] Sum of diene and quinone distortion.
[xv] The interaction energy is defined as $\Delta E^{\ddagger}_{int} = \Delta E^{\ddagger} - \Delta E^{\ddagger}_{d}$, where $\Delta E^{\ddagger}$ is the activation energy and total $\Delta E^{\ddagger}_{d} = \Delta E^{\ddagger}_{d[\mathbf{bq\subset CX}]} + \Delta E^{\ddagger}_{d[diene]}$.
[xvi] Relative energy with **C2** compared to with **C1**, negative values show the process is more favourable in **C2** than **C1**.

4.2 Aims and Objectives

In light of the computational insights, two novel Pd_2L_4 cages were identified to inspect the influence of cage structure on catalysis. Namely, the new designs attempt to reduce the steric clashes between the cage and the reacting molecules and possibly to introduce greater flexibility to the cages. First, the impact of the structural modification on the cages' host-guest chemistry with quinone-type guests will be discussed. Next, a description of their catalytic properties, using the Diels-Alder and Michael model reactions, will be presented.

4.3 Development of novel Pd_2L_4 catalysts

4.3.1 Design of ligands L3 and L4

The modularity of Pd_2L_4 systems offers an easy means of structural modification. The prerequisite for forming Pd_2L_4 architectures is the use of a concave "banana" shaped ditopic ligand with their coordination vectors being co-linear.[18] Coordination vectors describe the interactions between the ligands and the metal components,[1] and for ditopic nitrogen-coordination-based ligands often used in Pd_2L_4 cages, the coordination vectors are along the N-Pd bonds. Therefore, 5-isoquinoline and 5-imidazole groups were selected as alternate coordinating groups that would help the ligands retain parallel coordination vectors with a suitable linking motif (Figure 4-3).

The new ligands I identified, **L3** and **L4**, were designed so that the two nitrogen atoms would be spaced similarly to **L1 / L2** (Figure 4-3), which in turn would produce cages with a Pd-Pd distance that roughly matched the parent Pd_2L_4 cage systems, **C1** and **C2** that are built from **L1** and **L2**. This would then allow a direct comparison using similar sized substrates. One of the crucial differences, however, is that the cages of **L3** and **L4** would possess larger lateral space around the reactants and in theory result in less steric clash. Furthermore, the two phenyl groups linked by a carbon-carbon single bond in **L4** can introduce greater flexibility into the corresponding Pd_2L_4 cage. This ligand design also presents an opportunity to introduce axial chirality into the structure, by using sterically crowded biphenyl groups.

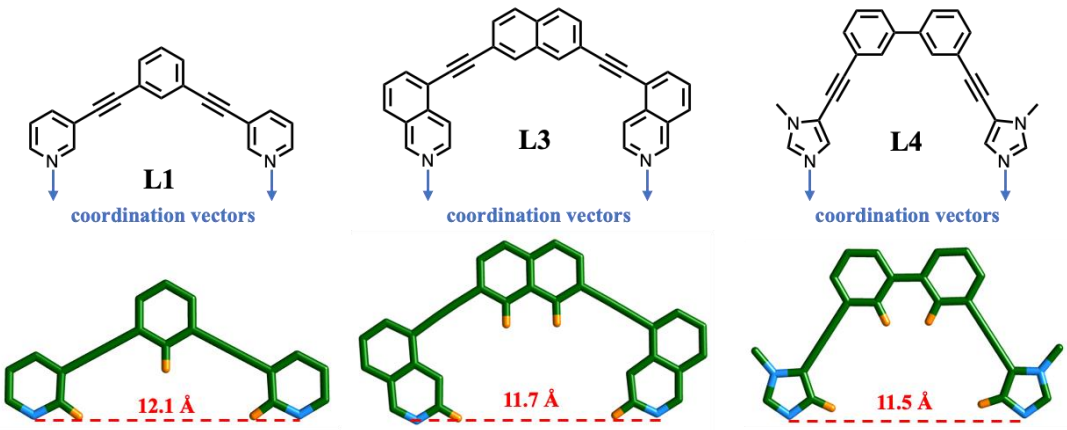

*Figure 4-3. Chemical structures (top) and Spartan models (bottom) of ligand **L1**, **L3** and **L4**.*

4.3.2 Synthesis of C3

The ligand **L3** was readily obtained in 70% yield using the Sonogashira coupling of 2,7-diethylnylnaphthalene and commercially available 5-bromoisoquinoline. 2,7-diethylnylnaphthalene was prepared by the Sonogashira coupling between 2,7-dibromonaphthalene and trimethylsilyl (TMS) acetylene followed by the deprotection of the TMS group according to the literature procedures.[19][20][21] The cage **C3** was synthesised in an analogous manner[22][23] to the parent cages, **C1** and **C2**, where initially the triflate cage, $Pd_2\mathbf{L3}_4{\cdot}4OTf$ was obtained through the self-assembly reaction of **L3** and $Pd(CH_3CN)_4(OTf)_2$ in a 2:1 ratio. The coordinating solvent CH_3CN is usually the ideal candidate for the synthesis of Pd_2L_4 triflate cages. However, due to the poor solubility of **L3** in CH_3CN, a solvent mixture of DCM and CH_3CN (1:1) was required. The $Pd_2\mathbf{L3}_4{\cdot}4OTf$ product precipitated over the course of the reaction and was isolated by adding Et_2O to the concentrated reaction mixture. A full characterisation of the intermediate species $Pd_2\mathbf{L3}_4{\cdot}4OTf$ was problematic on account of its poor solubility towards a range of solvents including DCM, CH_3CN and DMSO. Anion metathesis of the $Pd_2\mathbf{L3}_4{\cdot}4OTf$ species yielded the final BArF cage, **C3**, in 86% yield, which was soluble in DCM. ^{1}H NMR characterisation revealed that the product was a single, high symmetry species, which showed shifts compared to the free ligand consistent with cage formation i.e., deshielding of H_a-H_c that are next to the coordinating N atom (Figure 4-4). The ratio of $Pd_2\mathbf{L3}_4$ to BArF signals also indicated stoichiometric anion exchange.

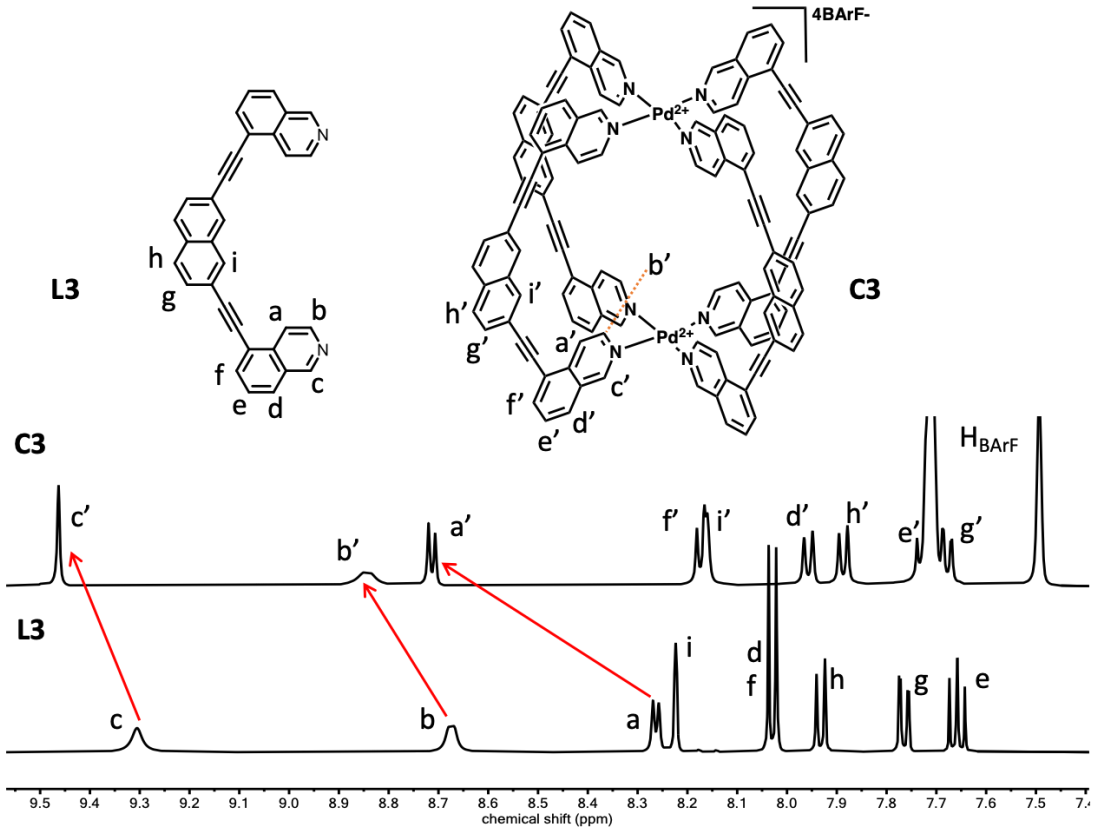

*Figure 4-4. ^1H NMR (500 MHz, CD_2Cl_2) spectra and assignment of **L3** and **C3**.*

The diffusion NMR technique (DOSY) is used to estimate the size of molecules by monitoring their diffusion in solution, with the relationship between hydrodynamic radius and diffusion coefficient defined by Equation 4-1. It is noteworthy that the Stokes-Einstein equation assumes a spherical particle, and the calculated hydrodynamic radii of cages are approximations rather than precise measurements. Nevertheless, ^{1}H DOSY NMR experiments offer a reasonable method to distinguish the size difference between a free ligand and the cage it forms. These experiments showed that the free ligand has a hydrodynamic radius of 4.7 Å while the complex is notably larger with a hydrodynamic radius of 13.8 Å. In fact, the hydrodynamic radius of **C3** is just slightly larger than the parent cage, **C2** (12.1 Å), as would be predicted.[23] ESI-MS analysis also confirms the Pd_2L_4 stoichiometry (Figure 4-18 through Figure 4-21), exhibiting 2+, 3+ and 4+ charged states.

$$D = \frac{kT}{6\pi\eta R}$$

Equation 4-1. Stokes-Einstein equation. D: diffusion coefficient, η: solvent viscosity, k: Boltzman constant, T: temperature and R: solute hydrodynamic radius.

X-ray crystallography is a powerful technique for comparing the structures of different cages. Interestingly, the structure of the "empty" (only occupied by solvent molecules) parent cage **C1** had not been previously obtained, only those that contained either a triflate anion or some bound guest.[24][22] Consequently, it was found that single crystals of "empty" **C1** could be yielded by slow evaporation from a DCM solution. In the case of **C3**, single crystals were obtained by layering a DCM solution of the cage with toluene. Both X-ray crystal structures (Figure 4-5a,b and Figure 4-5c,d) confirm Pd_2L_4 connectivity, and as was expected, the Pd-Pd distance in **C3** (12.6 Å) is similar to that in **C1** (11.7 Å). Also, both structures show that the Pd^{2+} ions adopt close to ideal square planar geometry, with the adjacent N-Pd bond angles in **C3** measuring between 89º and 91º, and the opposing pyridine N-Pd-N angle measuring approximately 177º. For comparison, the adjacent N-Pd bond angles in **C1** are in the range of 89º - 91º and the opposing N-Pd-N angles are between 177º and 179º.

While the above parameters are similar for both cages, there are significant differences in the global structures. As expected, the concaved shape of **L3** leads to a larger lateral cavity volume; the distance between the inward facing naphthalene carbons (the 1-position) of the two opposing ligands in **C3** is 14.8 Å, increasing from the 10.8 Å in **C1** between the inward facing central benzene carbons (distances shown in grey dashed line in Figure 4-5a,c). Also, the overall symmetries of the two cages are quite different, with **C1** adopting a near perfect D_{4h} symmetry, with minimal amounts of twisting; the largest dihedral angle between the central benzene in **C1** and the complexed pyridine rings is *ca*. 25º. On the other hand, **L3**, which interestingly possesses the same number of free rotors, shows much greater distortion, with the naphthalene moiety rotating approximately 60º out of plane with respect to the isoquinoline ring. Although these differences may be due to crystal packing effects, these structures would seem to suggest that **C3** possesses significantly more flexibility than **C1**.

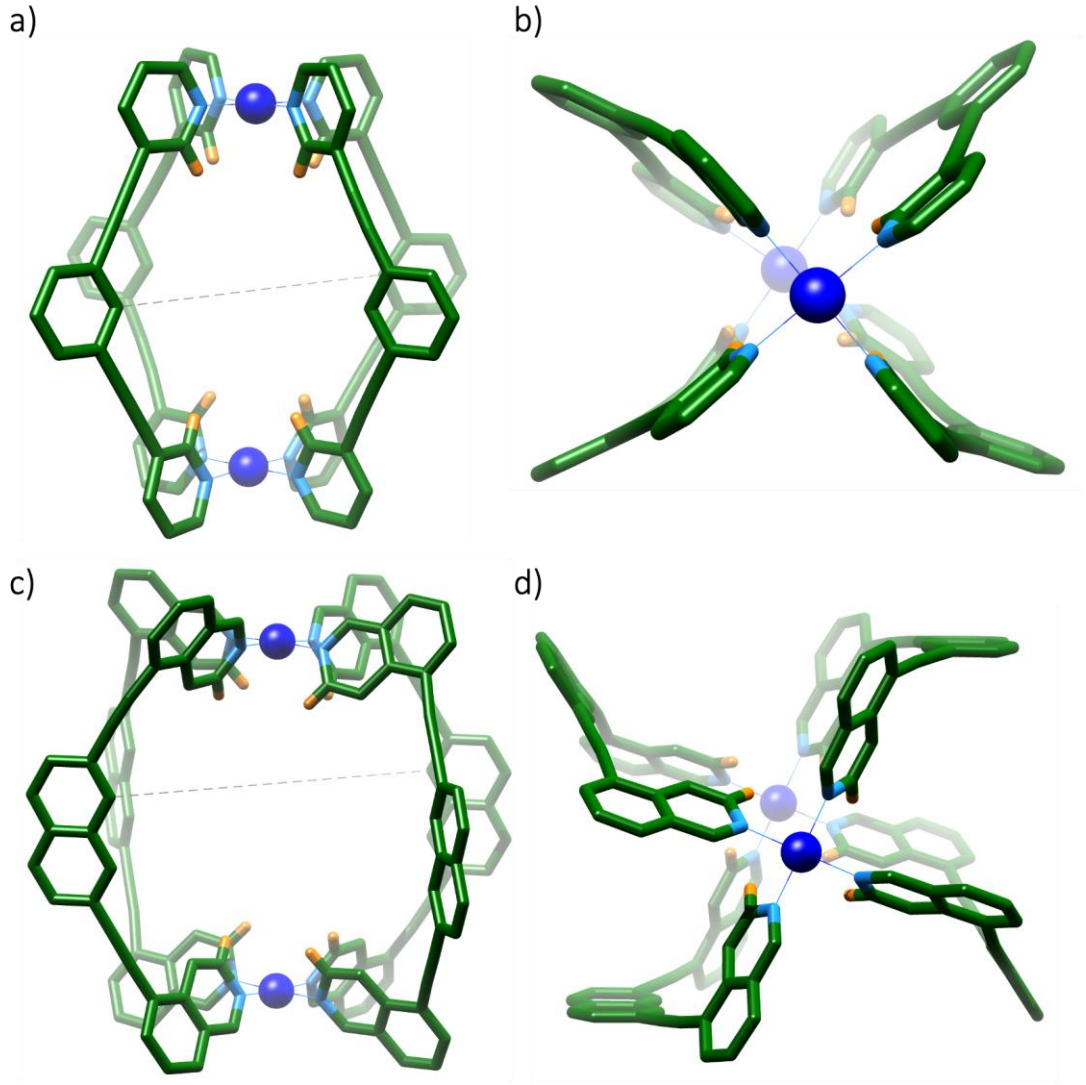

*Figure 4-5. X-ray crystal structures of **C1** with sideview (a) and topview (b). X-ray crystal structures of **C3** with sideview (c) and topview (d). Solvents, counteranions and non-binding protons are omitted for clarity. Colour code: C: green, N: light blue, Pd: blue, H: orange.*

It is also interesting to note that in the crystal structures, all four charge balancing BArF anions are found to associate with the exterior of **C1** and **C3**, leaving the cavities to be occupied by only solvent molecules. This supports our supposition that the use of BArF plays a major role in enhancing the cage's host-guest properties towards organic guests, which do not have to compete for the cavity with associated counteranions, as is the case with small non-coordinating anions such as BF_4^-, PF_6^- and OTf^- that are commonly employed in coordination assembly structures.[25][22][26]

4.3.3 Synthesis of C4

The imidazole containing ligand, **L4**, was prepared in 53% yield using a simple one-step Sonogoshira coupling reaction between commercially available 3,3'-dibromo-1,1'-biphenyl and 5-ethylnyl-1-methyl-imidazole. The synthesis of **C4** followed a similar procedure to **C1**, **C2** and **C3**; combining 2 equivalents of **L4** and 1 equivalent of $Pd(CH_3CN)_4(OTf)_2$ in a solvent mixture of CH_3CN and DCM (7:3) led to the formation of $Pd_2\mathbf{L4}_4 \cdot 4OTf$, which was isolated by precipitation using Et_2O. The BArF cage, **C4**, was prepared by anion exchange between $Pd_2\mathbf{L4}_4.4OTf$ and NaBArF in DCM in 51% yield.

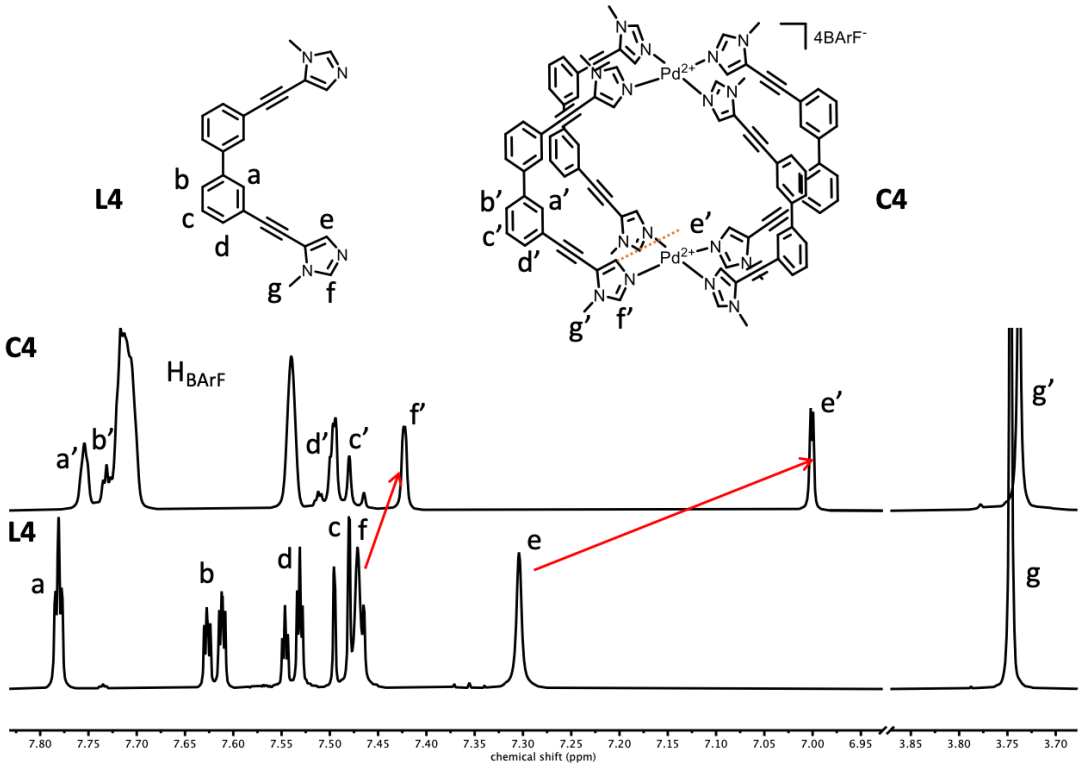

*Figure 4-6. ^1H NMR (500 MHz, CD_2Cl_2) assignment of **L4** and **C4**.*

The ^1H NMR spectrum of **C4** indicates that it is a single, high symmetry species (Figure 4-6), however, there are some unusual features. Most Pd_2L_4 supramolecular cages display deshielded ^1H NMR signals due to the electron withdrawing nature of Pd^{2+},[27] yet an upfield shift was observed for the majority of **C4** protons compared to free ligand **L4** (Figure 4-6). One possible explanation for the deshielding effects, particularly for the imidazole signals which are most affected, is that a propeller twist

within the tetra(imidazole)Pd motif (see single XRD structure in Figure 4-7) brings the H-atoms of one heterocycle closer the π-surface of the adjacent heterocycle. This twisting is likely to be a dynamic process, which when acting in concert with the rest of the rotatable bonds, allow the overall structure to flex and "breathe". This type of motion could be the likely cause for the broadening observed throughout the NMR spectrum Figure 4-6.[28]

C4 shows a significantly larger hydrodynamic radius (obtained from ^{1}H DOSY NMR) of 12.9 Å compared with the ligand **L4** (4.6 Å). This increase in size supports the formation of a supramolecular structure. **C4** also has a slightly larger hydrodynamic radius than **C1** (12.1 Å), although Spartan modelling suggests **L4** to be a "shorter" ligand (Figure 4-3). This observation is explained by the higher convex nature of **L4**, which leads to a larger lateral cage dimension, which in turn gives a larger hydrodynamic radius when approximated as a sphere. The Pd_2L_4 composition was further confirmed by ESI-MS analysis, where the 2+, 3+ and 4+ charged states were observed.

Single crystals of **C4** that were of sufficient quality for X-ray crystallographic analysis were isolated following layering a DCM solution of the cage with toluene. The structure that was obtained confirms **C4** was the expected Pd_2L_4 topology (Figure 4-7). The Pd-Pd distance in **C4** (10.8 Å) is slightly shorter than the 11.7 Å distance in **C1**, and again the Pd ions adopt close to ideal square planar geometry, with all the N-Pd-N bond angles in the range of 89º - 91º. The distance measured between the inward facing biphenyl carbons on the opposing ligand is 15.2 Å (distance shown in grey dashed line in Figure 4-7a), meaning that **C4** is even "wider" than **C3**. The distortion away from ideal D_{4h} symmetry is even more pronounced than **C3**, which, when considered alongside the broadened NMR spectrum, suggests that **C4** is highly dynamic. Such observations are counter to the widely held view that coordination cage assemblies are highly rigid entities. It is also interesting to note the relative orientation of the imidazole units with respect to each other, which may cause the shielding effects in the ^{1}H NMR spectrum. In many Pd_2L_4 structures, the coordinating ring sits perpendicular to the plane created by the N_4Pd primary coordination sphere. In

contrast, **C4** shows that the imidazole groups are significantly rotated away from this 90° torsional angle. This twisting also means that the polarised CH bonds from the 5-position of the imadazole ring (H atoms in Figure 4-7 shown in orange) do not point directly into the cavity in an analogous fashion to the *ortho*-pyridyl "binding" protons in the structures of **C1** and **C2**. This observation hints that the host-guest properties of **C4** could be quite different.

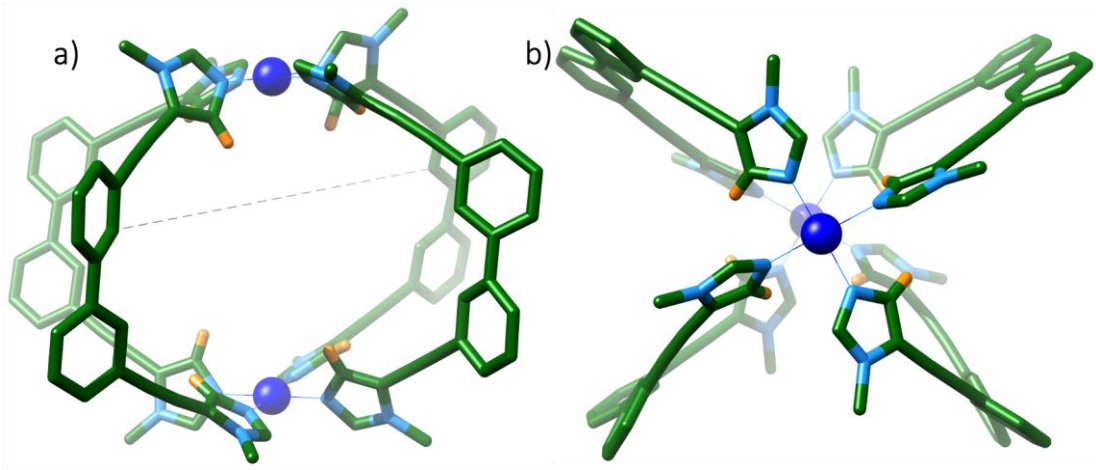

*Figure 4-7. X-ray crystal structure of **C4** with sideview (a) and topview (b). Solvent, counteranions and non-binding protons are omitted for clarity. Colour code: C: green, N: light blue, Pd: blue, H: orange.*

4.4 Host-guest chemistry of novel Pd_2L_4 cages

The host-guest chemistry of **C3** and **C4** with quinone-type guests was investigated. In general, **C3** showed lower affinity for quinones than either **C1**/**C2**, and **C4** showed even weaker binding towards all of the guests that were tried (Figure 4-8, Table 4-2. Binding constants of quinone guests in cage **C1**-**C4**.). The encapsulation of **4.1**, **4.4** and **4.6** in **C3** is up to 4 orders of magnitude weaker than in **C1** and roughly 10% of that in **C2**. The downfield shift of the inward facing proton *ortho*- to the Pd-N bond in the presence of quinones (Figure 4-9) strongly suggests that **C3** binds guests using the same H-bond interactions as seen in **C1**/**C2**. Furthermore, the rate of exchange between encapsulated and unbound guest increases for **C3** compared with **C1**/**C2**. For instance, the binding of **4.6** in **C1/C2** is slow on the NMR timescale while the in-out exchange of **4.6** in **C3** is intermediate on the NMR timescale. The increased guest exchange rate is also consistent with the observed decrease in the binding constant of **4.6** in **C3**, as slow guest exchange often requires tight binding and fast guest exchange indicates weaker encapsulation, although these factors are not strictly correlated.[29][30]

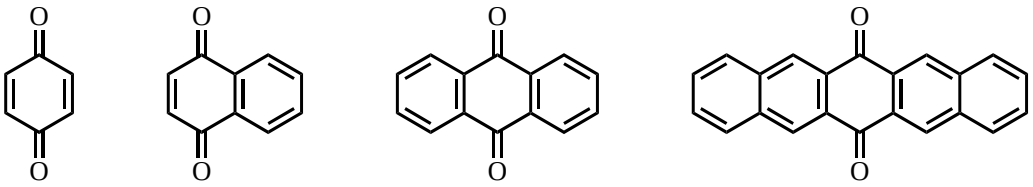

4.1 **4.4** **4.5** **4.6**

*Figure 4-8. Chemical structures of guests **4.1**-**4.5**.*

*Table 4-2. Binding constants of quinone guests in cage **C1-C4** measured in CD_2Cl_2.*

Host / Guest	**C1**[22]	**C2**[23][17]	**C3**	**C4**
4.1	8×10^3 M^{-1}	1.1×10^3 M^{-1}	82 M^{-1}	weak
4.4	3.16×10^5 M^{-1}	2.7×10^3 M^{-1}	227 M^{-1}	-
4.5	4.89×10^7 M^{-1}	8.5×10^3 M^{-1}	-	weak
4.6	7.94×10^8 M^{-1}	8.88×10^5 M^{-1}	3.5×10^4 M^{-1}	weak
Guest exchange rate of **4.6**	slow	slow	intermediate	fast

In spite of the general weakened host-guest interactions, **C3** retains the same quinone binding trend as **C1**/**C2**; the binding constants are positively correlated to the number of aromatic rings. Such an effect could stem from π··· π interactions imposed by the naphthalene moiety in the centre of **L3**, as evidenced by the upfield shift of $H_{h'}$ and $H_{g'}$ (shown in blue in Figure 4-9). Unsurprisingly, the shielding of the ligand protons is more pronounced with guests containing a larger aromatic surface, hence a greater shift was observed for **4.6** than for **4.1** or **4.4**. CH··· π interactions between the naphthyl protons ($H_{i'}$) and the extended quinones may also contribute to the stronger binding of **4.6,** however, due to the intermediate exchange rate and signal overlap, $H_{i'}$ could not be identified through the course of the titrations. Although such edge-to-face interactions previously seen in **C1**[22] may be weakened in **C3** due to the extra lateral space, they still appear to be important as evidenced by the better binding of **4.6**.

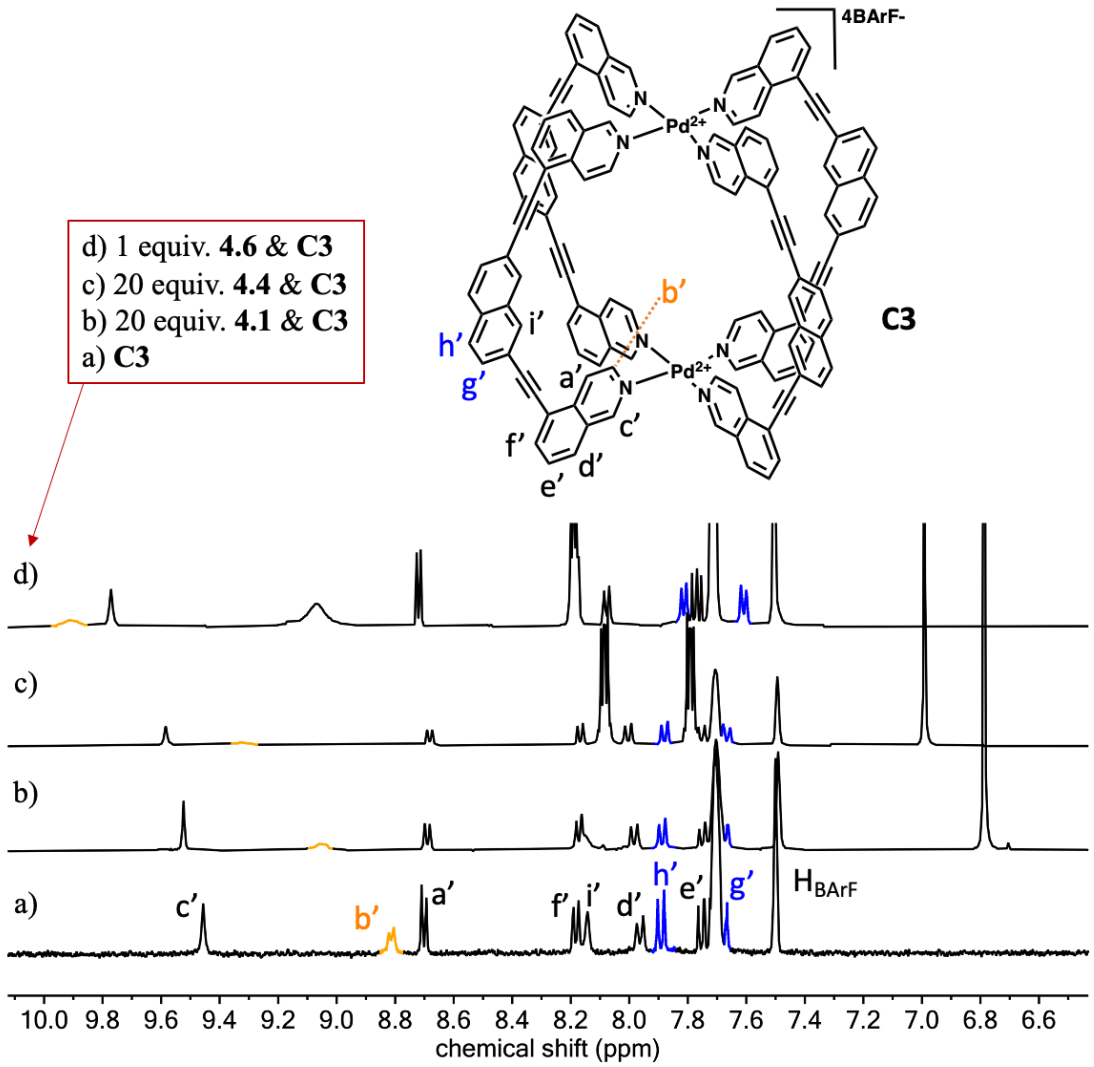

*Figure 4-9. ^{1}H NMR (500 MHz, CD_2Cl_2) spectra for binding of **4.1**, **4.4**, and **4.6** in **C3**.*

The interactions between quinones and **C4** are significantly weaker than in **C1**/**C2**/**C3** and accurate association constants could not be obtained because under the ^{1}H NMR titration conditions, the host-guest binding does not reach saturation even when the maximum amount of quinones allowed by their solubility is used. Instead, the host-guest chemistry of **C4** was qualitatively visualised by pseudo titrations (Figure 4-10). The inner cavity binds quinones through the polarised C-H bonds (the 5-position on the imidazole ring), as evidenced by the consistent deshielding of the $H_{e'}$ protons, akin to the same binding mode in **C1**/**C2**/**C3**. Weak binding is indicated by a modest shift of these protons even in the presence of 100 equivalents of **4.1** and the lack of saturation at a high loading (50 equivalents) of a traditionally strong binder, **4.5**.

Moreover, the fast guest exchange kinetics of **4.6** in **C4** suggests poor binding, as strong binding of **4.6** often leads to slow or intermediate exchange rates on the NMR time scale (Table 4-2).[29][30] Interestingly, the interaction with quinone guests results in a small shift of the outer peaks $H_{f'}$. This indicates that quinones may also bind on the exterior of the cage that has previously been observed with **C1**/**C2** and PPh_3O.[31]

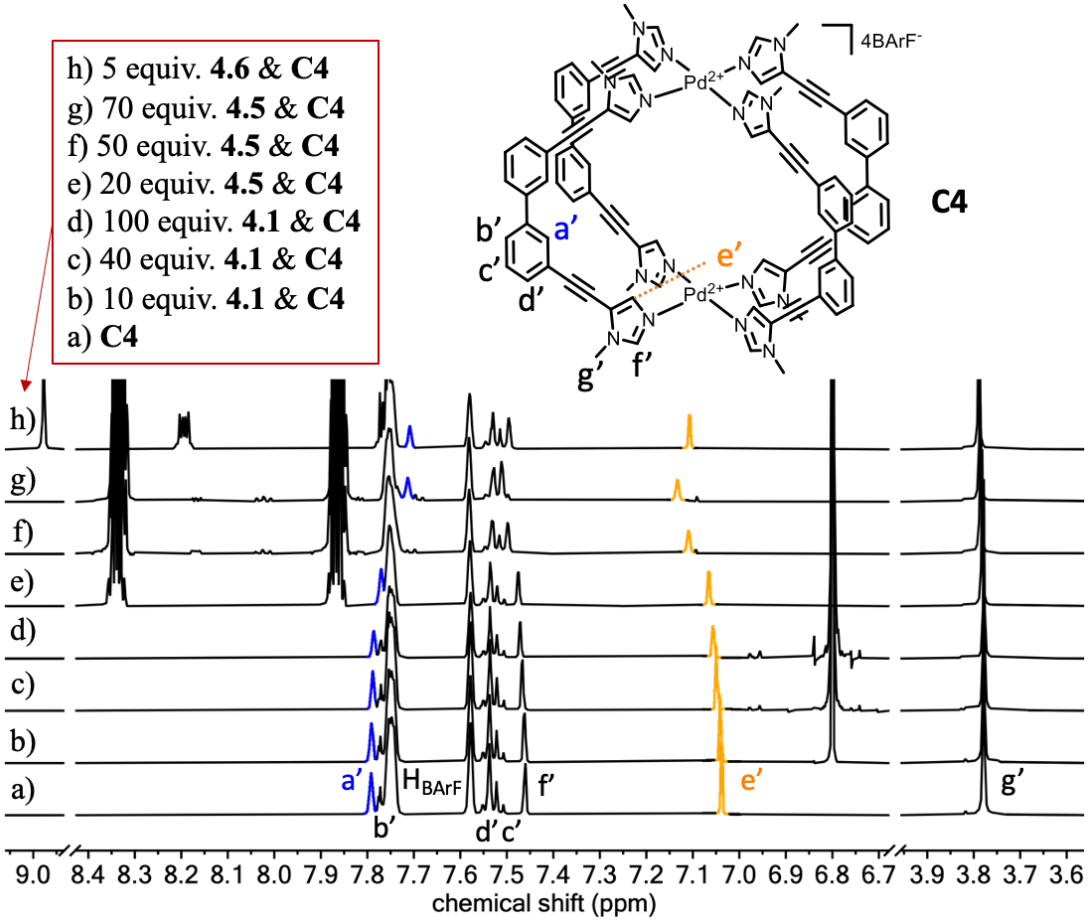

*Figure 4-10. ^1H NMR (500 MHz, CD_2Cl_2) data for binding of **4.1**, **4.5**, and **4.6** in **C4**.*

Due to low solubility of **4.6**, a pseudo titration of **4.6** was not performed and the NMR spectrum was recorded with 5 equivalents of **4.6**. The trend remains for **C4** that more aromatic rings correlates to stronger quinone binding. Despite the lack of accurate binding constants, stronger encapsulation can be implied by a more significant change in the chemical shift of $H_{e'}$ at a lower guest loading (Figure 4-10). For example, 5 equivalents of **4.6** leads to a larger shift than 20 equivalents of **4.5**, which shifts $H_{e'}$ more than 100 equivalents of **4.1**, indicating the binding strength in **C4**: **4.6**>**4.5**>**4.1**.

The shielding of $H_{a'}$ with the larger guests supports this affinity order and is likely to be caused by the CH···π interaction with the extended aromatic rings of the larger quinones (shown in blue in Figure 4-10). Again, the central phenyl motifs of **L4** recognise **4.6** the most effectively. The large π surface of **4.6** projects into the **C4** windows and is in close proximity with the central biphenyl C-H bonds. Additionally, π···π stacking may contribute to the stabilisation of larger quinones as demonstrated by the upfield shift of $H_{d'}$ and $H_{c'}$.

Several possible explanations can be used to account for the weakened quinone binding in both **C3** and **C4**, and these are not mutually exclusive. Firstly, the "height" of the new cage cavity is slightly different from that in **C1**, in spite of the careful ligand design. The Pd-Pd distances measured for **C3** and **C4** are 12.6 Å and 10.8 Å, respectively. The slight deviation from the 11.7 Å distance in **C1** may make the cavity less than optimal such that the cages may need to distort to accommodate the guest.

Secondly, due to the directionality of hydrogen bonding, the best guest inclusion occurs when the Pd_2L_4 cage adopts a D_{4h} symmetry, which allows all 8 C-H bonds to interact with the carbonyl groups effectively (Figure 4-5a). However, **C3** and **C4** both possess an inherent twist in the structure, which rotates the hydrogen bond donors away from pointing into the cavity (Figure 4-5c and Figure 4-7a). Furthermore, **C3** and **C4** appear to be more flexible compared to **C1**, which creates an energetic (entropic) penalty upon binding associated with the restriction of these dynamic processes; in short, **C3** and **C4** are less pre-organised to bind quinones.

One other factor is the intrinsic electronic properties of the different coordinating heterocycles. Isoquinoline and pyridine are both electron deficient heterocycles, meaning that the hydrogen atoms of these ring systems possess more δ+ character (which is readily observable by ^{1}H NMR), making them more suitable as H-bond donors. In contrast, imidazole is an electron-rich heterocycle, and the equivalent H-atom are much less electron deficient and thus inferior H-bond donors.

4.5 Diels-Alder catalysis of novel Pd_2L_4 systems

The model reactions of **4.1** with several dienes were used to test the Diels-Alder catalytic abilities of the novel cages (Scheme 4-1). Experimental data was fit to the kinetic model described in Chapter 3 to obtain the rate constants of the C-C bond forming steps for both the cage catalysed (k_{cat}) and the background (k_{uncat}) reactions. When reacting **4.1** with **4.2** in the presence of 20 mol% **C3**, a 78-fold rate acceleration (k_{cat}/k_{uncat}) was observed (entry 3, Table 4-3). When **4.7** was used as the diene, 20 mol% **C3** accelerated the reaction of **4.1** by 44-fold (entry 5, Table 4-3).

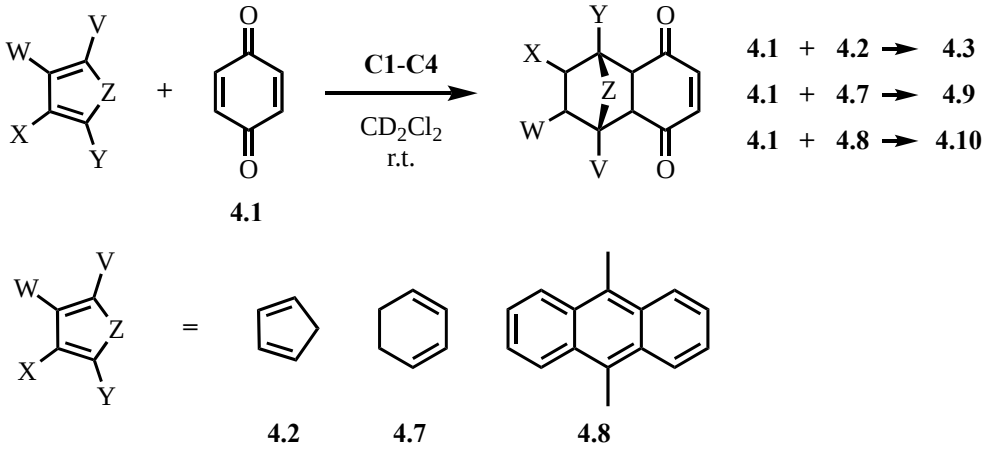

*Scheme 4-1. The cage catalysed Diels-Alder reactions of **4.1***

*Table 4-3. Catalytic effects of **C1-C4** on the Diels-Alder reaction of **4.1**.*

Entry	Dienophile	Diene	Cage	$K_{A\text{ - dienophile}}$ (M^{-1})	k_{cat} / k_{uncat}
1	**4.1**	**4.2**	**C1**	8000	< 1[23]
2	**4.1**	**4.2**	**C2**	1100	430[23]
3	**4.1**	**4.2**	**C3**	80	78
4	**4.1**	**4.2**	**C4**	< 30	< 1
5	**4.1**	**4.7**	**C3**	80	44
6	**4.1**	**4.8**	**C2**	1100	< 1[23]
7	**4.1**	**4.8**	**C3**	80	< 1

These results are encouraging because they demonstrate that the Pd_2L_4 Diels-Alder catalysis approach can be modulated by varying cage structure and that the activity of **C2** is not a serendipitous, sole example. As discussed in section 4.4 **C3** retains the guest binding features of **C1**/**C2** where quinone-type molecules H-bond to the cage binding pockets. It is therefore postulated that **C3** catalyses the Diels-Alder reaction of quinones in the same manner as **C2**, namely by lowering the dienophile LUMO. However, calculations have shown that this is clearly not the only factor; **C1** is just as effective at lowering the LUMO as **C2** but shows no activity (Table 4-3, entry 1 and entry 2).[17] An alternative way to consider and rationalise this different catalytic activity is by considering transition state stabilisation; lowering the TS energy *relative* to the substrate energy generates a lower energy barrier and so acceleration occurs. This TS stabilisation can be manifested in different ways. In normal-electron demand Diels-Alder reactions, electrons flow from the electron-rich diene to the electron poor dienophile, which results in a localised increase in the electron density on the electron withdrawing functional group (such as a carbonyl) which is typically found in the dienophile. With a H-bond donor catalyst, this makes the interaction between the TS and the catalyst stronger than the interaction between the catalyst and the substrate, which gives greater stabilisation to the TS energy relative to the substrate, causing the reaction to go quicker. This type of electronic TS recognition plays a key role in the cage catalysis described but again it does not describe why **C1** is an ineffective catalyst. The second way that TS stabilisation manifests itself, is structural recognition. Does the catalyst recognise the structure (i.e. general shape and relative functional group disposition) of the TS? This type of recognition is less relevant to small molecule systems as all the catalyst recognises is a single functional group, which is present in both the substrate and the TS. However, in cage catalysis, as in enzymology, this factor is important and is what explains the difference between the activities of the two parent cages: **C1** has relatively poor structural complementarity to the TS, which is not the case with **C2**. The evidence for this type of structural TS complementarity comes from binding experiments with a TS mimic, the Diels-Alder adduct (**4.3**) of benzoquinone **4.1** and cyclopentadiene **4.2** (Table 4-4, Figure 4-11). Not only does **C2** bind **4.3** nearly 20 times more strongly than **C1**, it also binds this compound more strongly than the

substrate. Crucially, **C2** exhibits selective structural recognition of the TS by 1.4 kJ mol^{-1}. Conversely, **C1** actually binds the substrate much better than the TS mimic (by 1.6 kJ mol^{-1}) so could be considered an "anti-catalyst"!

*Table 4-4. The stabilisation of **4.1** and **4.3** when bound in cage **C1-3**. The Gibbs free energies were calculated using the binding constansts.*

Cage	$\Delta G_{binding}$ **4.1**	$\Delta G_{binding}$ **4.3**	$\Delta\Delta G_{binding}$ (**4.4-4.1**)
C1	− 5.3 kcal mol^{-1}	− 3.7 kcal mol^{-1}	1.6 kcal mol^{-1}
C2	− 4.1 kcal mol^{-1}	− 5.5 kcal mol^{-1}	− 1.4 kcal mol^{-1}
C3	− 2.6 kcal mol^{-1}	− 4.0 kcal mol^{-1}	− 1.4 kcal mol^{-1}

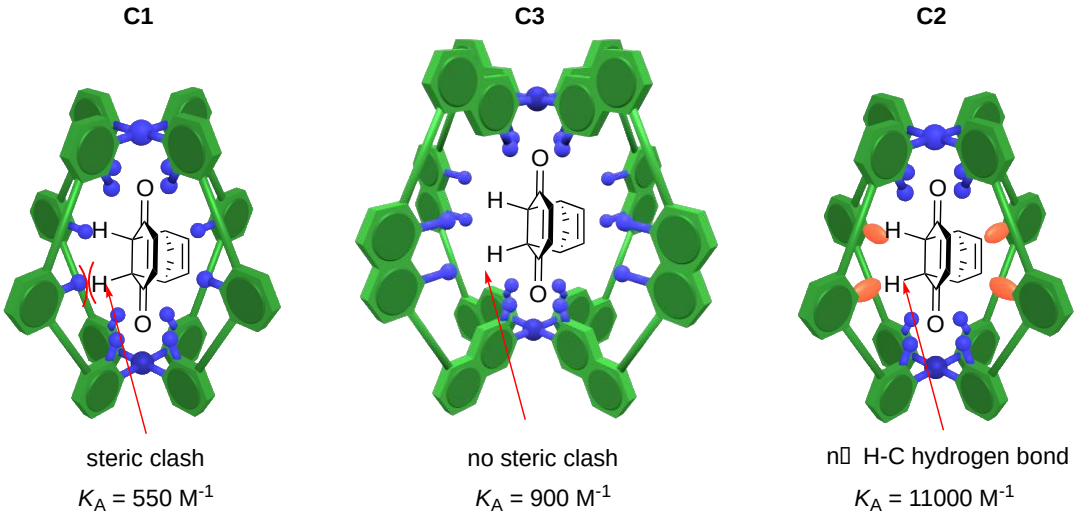

*Figure 4-11. Interactions imposed by the central moietied of **C1-C3** affect the binding of **4.3**.*

In the case of **C3**, it could be anticipated that the increased lateral space around the equator of the cavity reduces the cage's ability to structurally differentiate the substrate and the TS. Interestingly, however, this doesn't appear to be the case. **C3** binds the TS mimic (900 M^{-1}) better than the substrate (80 M^{-1}) by nearly an order of magnitude, which corresponds to 1.4 kJ mol^{-1}, and is roughly the same selectivity that is observed by **C2** (Table 4-4). While the selective recognition of the TS mimic by **C2** was attributed to favourable interactions between the equatorial lone pair (Figure 4-11) and the more electron deficient H-bond atoms of the TS mimic, it is less clear what the origin of the selective binding is in the case of **C3**. Nevertheless, when compared with

C1 whose poor TS mimic binding is caused by the steric clash between **4.3** and the cage's central benzene C-H bonds (Figure 4-11), **C3** has more lateral cavity space and therefore less steric hinderance for TS recognition. These results would also suggest that if the selectivity of the structural recognition between **C2** and **C3** is comparable, i.e. $\Delta\Delta G_{binding}$(substrate-TS mimic) are similar (Table 4-4), then the difference in the acceleration must be an electronic effect. This could possibly be due to the general distortion in the cage structures, which results in the H-bond donor atoms of the cage being less pre-disposed to form strong interactions more generally.

The TS between **4.1** and **4.2** is still relatively compact and so it was anticipated that a more noticeable, and a more favourable difference could be observed using **C3** to promote the Diels-Alder reaction with a bulkier diene. As such, the Diels-Alder reaction of dimethylanthracene, **4.8**, which is not accelerated by **C2**, was also investigated. Unfortunately, when **4.8** was reacted **4.1** in the presence of 20 mol% **C3**, no rate acceleration was found (entry 7, Table 4-3). While the portals and lateral space around the bound quinone are bigger in the case of **C3**, the lack of reactivity could be due to steric clash at the "top" and "bottom" of the cage. The orbital overlap that is required would have the dimethyl substituents pointed towards the Pd coordination spheres, and so perhaps the lack of reactivity is due to restricted space in the part of the cage where **C2** and **C3** are more similar.

When Diels-Alder catalysis was attempted with **C4**, using **4.1** and **4.2** as model substrates, unfortunately no rate enhancement was observed (entry 4, Table 4-3). This is likely due to its very weak interaction with the substrate and by extension the TS, as a result of the distortion of the cage that causes the inward facing imidazole CH groups to be poorly aligned for interactions within the cavity and/or the poor H-bond donor properties of the more electron rich imidazole rings.

4.6 Michael addition catalysis of novel Pd_2L_4 systems

C3 and **C4** were also tested for their Michael addition activities using the reaction of **4.12** and **4.11** (Figure 4-12a). As discussed extensively in Chapter 2, **C1** enhances the acidity of the pro-nucleophile **4.11**, by stabilising its conjugate base through electrostatic attraction. With no Brønsted basic functionalities present in the reaction mixture, H_2O acts as a proton elicitor forming the hydronium ion. The addition of 18-crown-6 further facilitates the deprotonation of **4.11** by binding and lowering the energy of hydronium ions in the apolar solvent DCM (Figure 4-12b). Control experiments described in Chapter 2 showed that the catalytic addition of **4.12** and **4.11** arises from the cavity of **C1**, rather than free Pd^{2+} ions or the exterior of the cage.

In addition to **C3** and **C4**, the "naphthyl-cage" **C5**, which was developed by Dr Helen O'Connor in the Lusby group, was also tested in the screening (Figure 4-12c). All three new cages **C3-C5** demonstrated an ability to promote the model reaction of **4.12** and **4.11** with the assistance of 18-crown-6 (Table 4-5, entry 3-5). Quantitative measures such as k_{cat}/k_{uncat} are much more difficult to derive for the Michael addition reaction. Therefore, the performance has been judged by comparing yields at different times points, with the ranking: **C1 > C2 > C3 > C5 > C4** (Table 4-5). Within that ranking, **C3** could be considered a good catalyst, with activity comparable to **C2**, however, **C5** and in particular, **C4** are noticeably worse. With the affinity of 18-crown-6 to H_3O^+ remaining constant, the varied degrees of reaction promotion are therefore linked to the structural differences between the Pd_2L_4 cages.

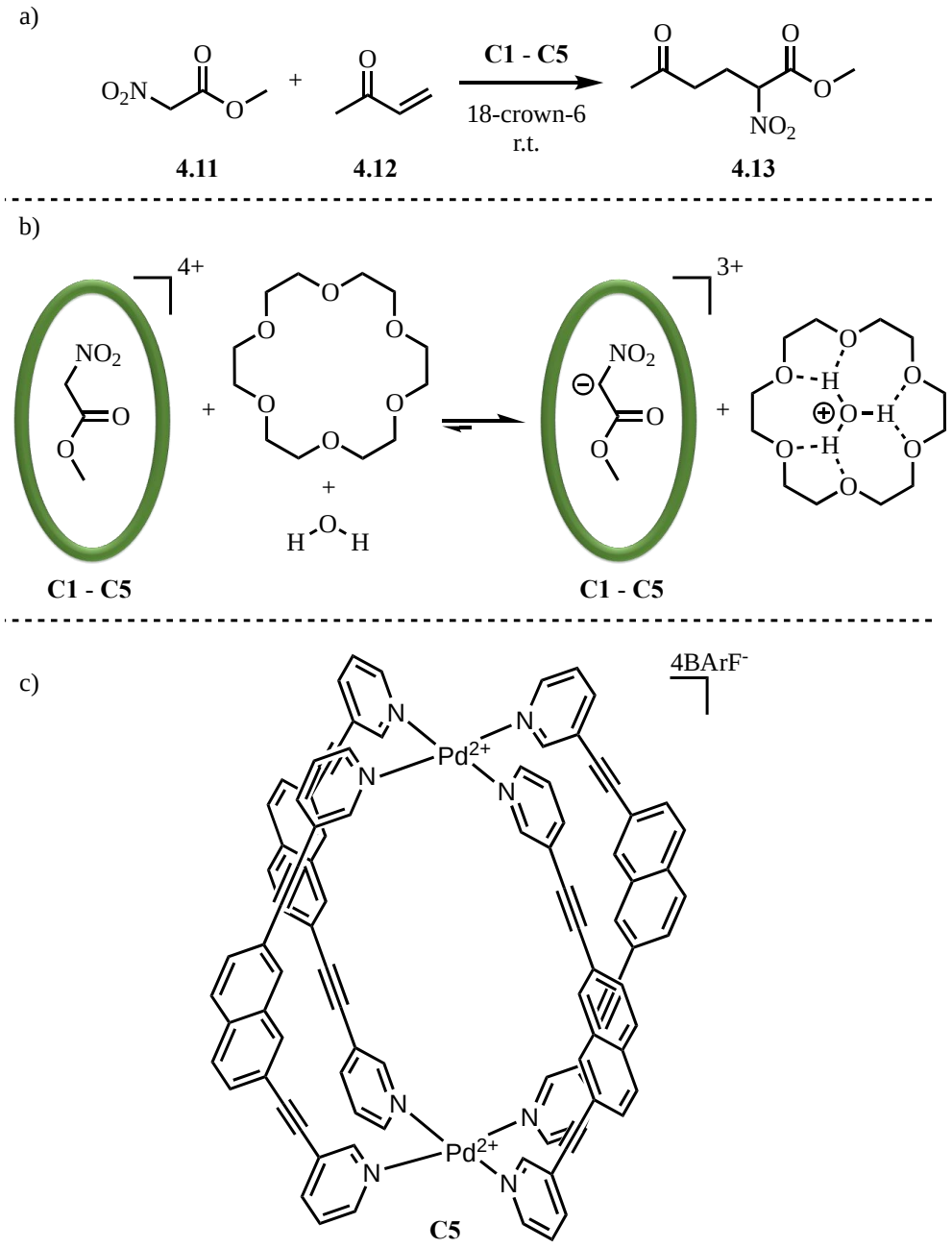

*Figure 4-12. a) The Michael addition between **4.12** and **4.11**. b) Synergistic pro-nucleophile activation using a Pd_2L_4 cage and 18-crown-6. c) Chemical structure of **C5**.*

*Table 4-5. Comparison across catalysts **C1-C5** for the Michael addition of **4.12** and **4.11**.*

Entry	Cage	NMR yield at				
		t = 1h	t = 3h	t =12 h	t = 30 h	t = 120 h
1	**C1**	≥ 98%	≥ 98%	≥ 98%	≥ 98%	≥ 98%
2	**C2**	15%	-	72%	90%	≥ 98%
3	**C3**	1%	16%	34%	93%	≥ 98%
4	**C4**	0	0	1%	3%	8%
5	**C5**	-	2%	-	36%	≥ 98%

C1 and **C2** are highly analogous with similar cavity lengths and rigidity of the ligands. The disparity in their activity, as discussed in Chapter 2, is attributed to the better anion stabilisation in **C1** than in **C2**, which is a consequence of more pronounced electrostatic potential (ESP) field effects in **C1** (Figure 4-13). ESP analysis also suggest that **C3** and **C5** would both bind anions less strongly than **C1** (Figure 4-13), which supports the less efficient catalysis by **C3** and **C5**. It is worth noting that unlike **C1** and **C2** that have D_{4h} symmetry, **C3** and **C5** both show significant twisting in the calculated structure. While the ESP slices of **C1**/**C2** along the XZ plane contain two opposing ligands, a plane passing through both Pd^{2+} centres does not exist for **C3** or **C5** due to the lack of reflection symmetry of the cages. Therefore, the ESP slices of **C3**/**C5** on the XZ plane are a rough guide of their electrostatic properties, and direct comparison across **C2**/**C3**/**C5** is problematic. Nevertheless, the fact that **C1** displays more efficient catalysis than **C2**/**C3**/**C5** can be explained by its significantly higher ESP effect.

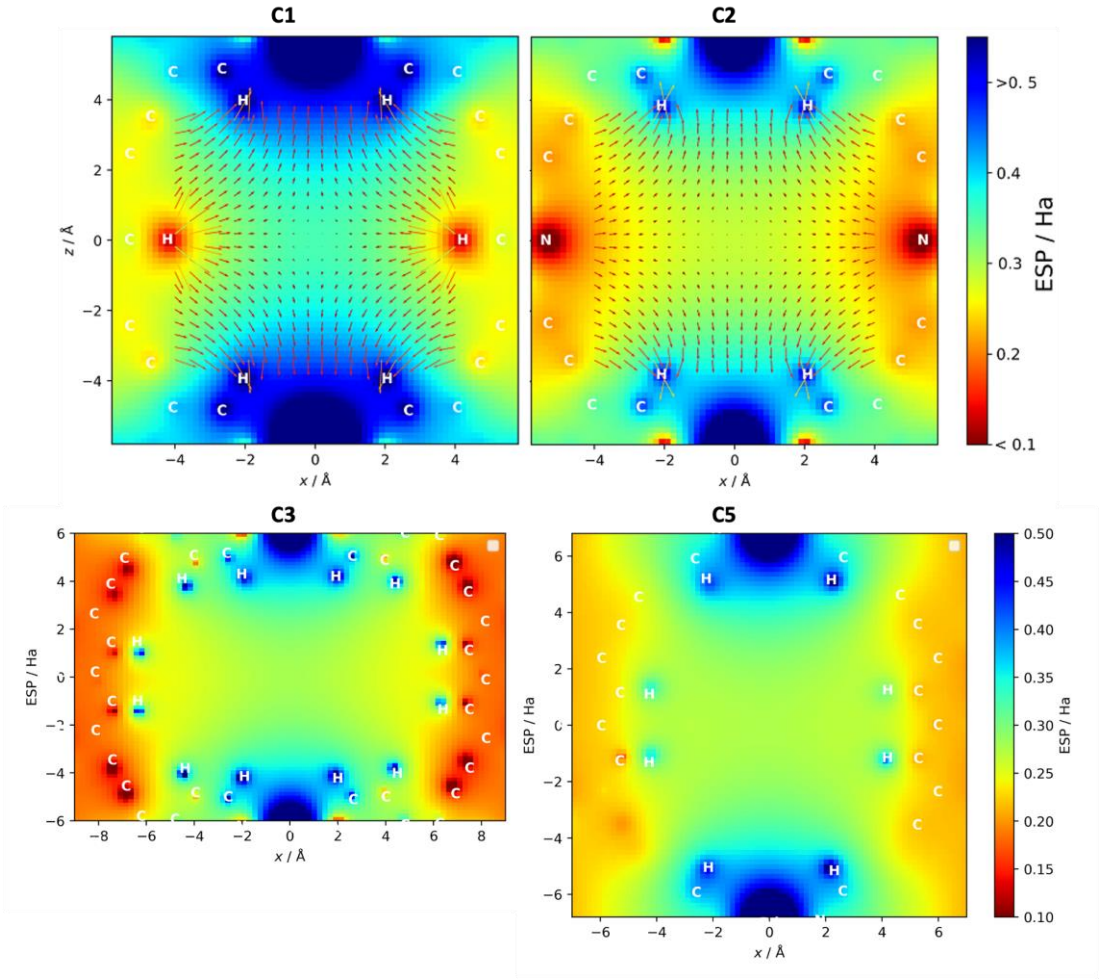

*Figure 4-13. Electrostatic potential (ESP) slices of cage **C1**, **C2**, **C3** and **C5** on the XZ plane.*

It is also interesting to consider the higher catalytic activity of **C3** compared with **C5**; the reaction promoted by **C3** and **C5** yielded 93% and 36% product at 30 hours, respectively (Table 4-5, entry 3 and entry 5). As discussed in Chapter 2, the catalysis of **4.12** and **4.11** likely involves the encapsulation of both substrates simultaneously, with a single H-bond pocket binding **4.12** and the other interacting with **4.11** (Figure 4-14). In other words, there may exist an ideal distance where the nucleophilic carbon atom of **4.12** is in an optimal position to attack the 1,4-position of **4.11**. As a corollary of that, the intermediate oxyanion that results from nucleophilic attack will be best stabilised if it can simultaneously interact with both Pd sites. It is interesting to note that the Pd-Pd distance in **C3** (12.6 Å) is close to that in **C1** (11.7 Å), such that a similar separation of the substrates is likely (and/or that the subsequent intermediate can

bridge both sites similarly well). Conversely, the cavity of **C5** is notably longer, with a Pd-Pd distance of 13.7 Å. The poorer activity of **C5** compared to **C3** would therefore suggest that the *ca.* 12 Å separation is much closer to ideal than the *ca.* 14 Å in **C5**.

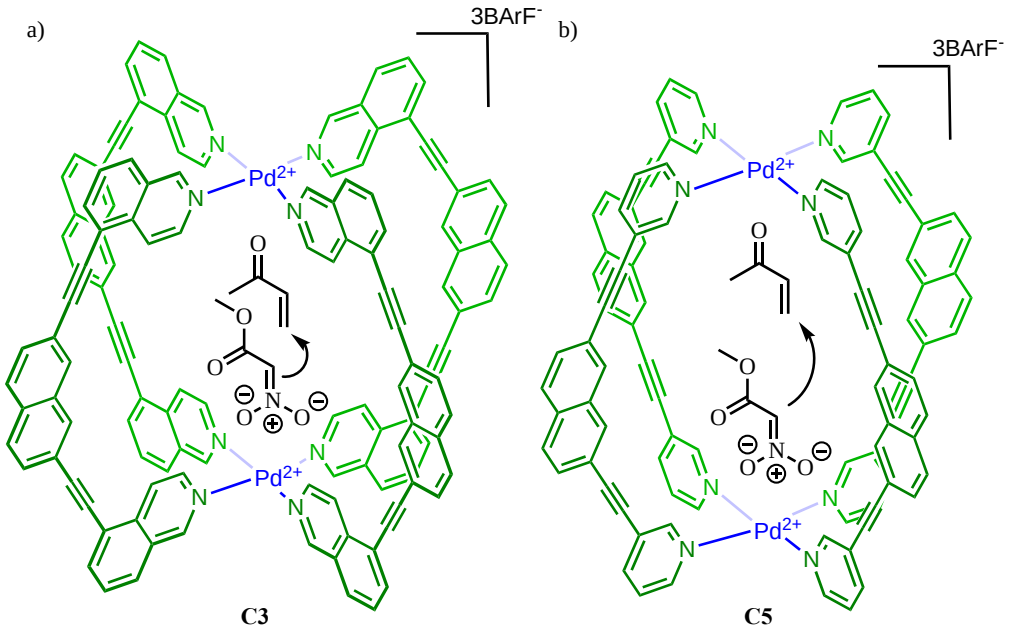

*Figure 4-14. Co-binding of Michael substrates **4.12** and **4.11** in a) **C3** and b) **C5**.*

C4 shows the lowest Michael catalytic ability, yielding only 8% product at 120 hours (Table 4-5, entry 4). For context, the same reactions catalysed by **C1**-**C3** or **C5** all proceeded to completion in the same time. This may be because **C4** has the lowest ESP among **C1**-**C5**. However, a direct comparison of the ESP of **C4** is nontrivial as the energy minimised structure of **C4** displays significant twisting. However, as discussed in section 4.4 the highly dynamic nature of **C4** results in poor pre-organisation for neutral quinone guest binding. It could be inferred that the stabilisation of anionic species is also compromised by the lack of binding site pre-organisation which then leads to poor Michael catalysis. That **C4** displays some latent catalytic activity towards Michael addition but none in the case of Diels-Alder catalysis might be explained by coulombic effects: the cationic cage is able to provide some stabilisation of the anionic intermediates in the case of carbanion addition but it does not influence the cycloaddition between neutral substrates.

The best catalyst among the new cages, **C3**, was also tested for its diastereoselectivity (Figure 4-15a). As demonstrated in Chapter 2, the reaction of **4.11** and **4.14** yields an almost equal amount of all four diastereoisomers **4.15a-d** with an organic base, DBU, as the catalyst, while only the anti-isomers are formed in the presence of **C1** and 18-crown-6. This selectivity towards **4.15a,b** is retained when **C3** is the catalyst (Figure 4-15d). The retention of the stereoselectivity indicates that the nitronate intermediate **4.15-I1**$^-$ is likely to adopt the same conformation in **C3** as in **C1**. The subsequent proton transfer is stereoselective and only delivery of the H^+ to the same face of the nitronate group as the nitro-methine group leads to exclusive anti-isomers (Figure 4-15c). The lack of influence of the cavity lateral space suggests that the conformation of the intermediate is dictated by the distal binding pockets. Interestingly, the addition of **4.11** to **4.14** proceeds slightly faster with **C3** than **C1** (Figure 4-15b). This may be explained by the higher flexibility of **C3** and the larger cavity volume reducing the steric crowding at the TS.

While the Diels-Alder reaction catalysis has been largely confined to **C2** and **C3**, the enhancement of Michael additions displays a larger Pd_2L_4 catalyst scope (**C1-5**). This is likely because Diels-Alder reactions demand strict orbital overlap.[32][33] Such specific substrate orientation is more likely to be disrupted by steric clashes within the cages. The binding of the neutral transition state also requires highly directional H-bonding. In other words, all four ortho-pyridyl C-H bonds in each binding pocket need to point to the carbonyl group in the TS. On the other hand, the catalysis of Michael additions primarily relies on using coulombic interactions to increase the effective molarity of the nucleophile. As **C1-C5** all display a 4+ charge, they may all increase the pro-nucleophilicity of **4.11**, although their ability to do so can be influenced by their guest binding properties and their inherent electrostatic fields.

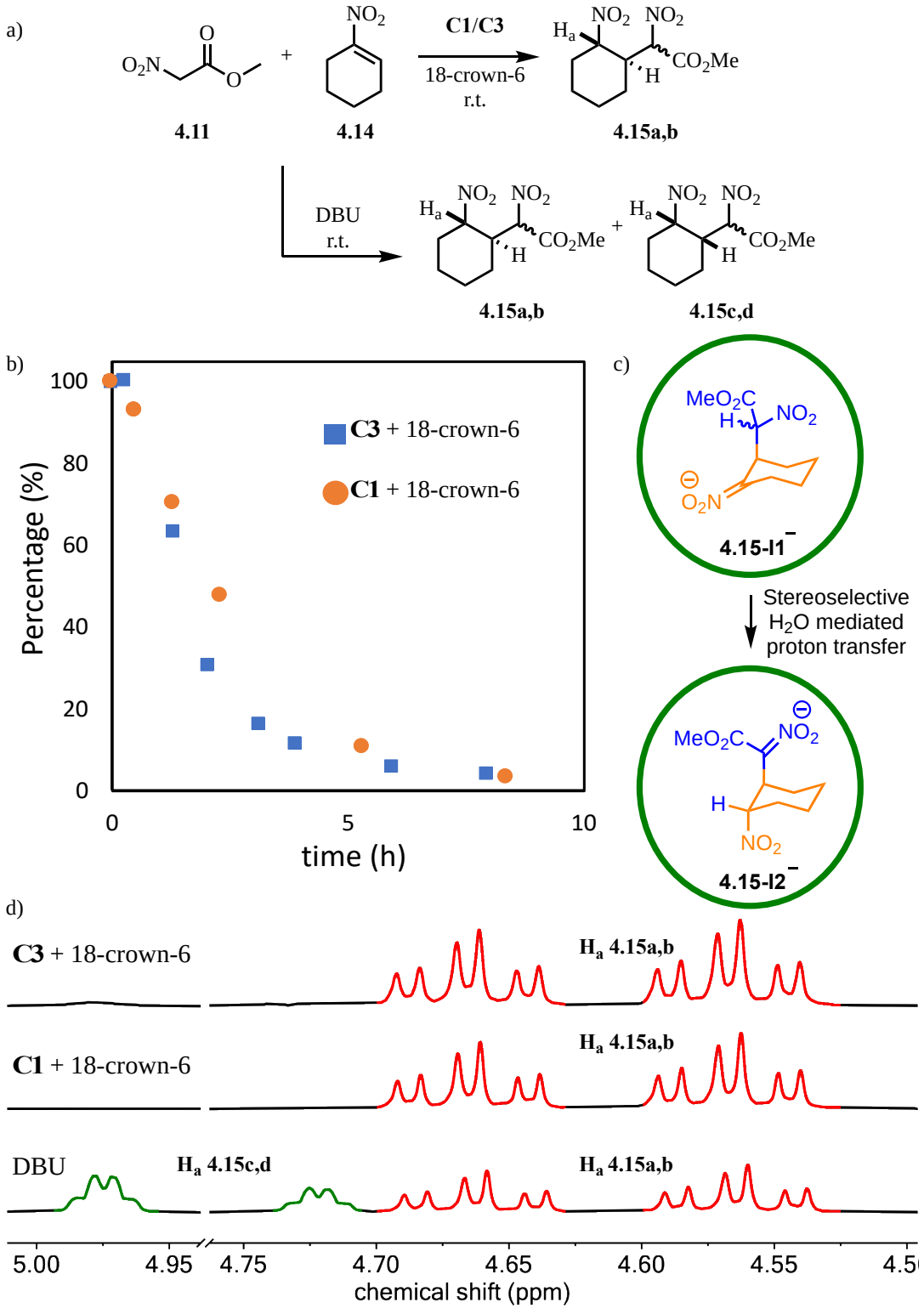

*Figure 4-15. a) The Michael addition of **4.11** and **4.14** under cage or DBU catalysed conditions. b) Kinetic profile of **C1**/**C3** and 18-crown-6 promoted reaction of **4.11** and **4.14**. c) Cage cavity stabilises intermediate **4.15-I1**$^-$ which undergoes highly stereoselective H_2O mediated proton transfer. d) Stereoselective cage catalysis.*

4.7 Conclusion

Two novel Pd_2L_4 cages were successfully synthesised, facilitated by the modularity of the Pd_2L_4 systems. This allows rational designs that attempt to retain the general guest binding and catalytic properties of the parent systems widely studied in the Lusby group (**C1** and **C2**). However, it has become clear that making changes to probe a single aspect of cage catalysis has significant knock-on effects. To be more specific, **L3** and **L4** were conceived to assess the effect of increasing the lateral dimension of the cage cavities compared to **C1**/**C2**. This has not only led to more flexible cages but also differences in their ability to provide electrostatic interactions, either via hydrogen bonding or coulombic effects. Even though both cages revealed inferior catalytic properties compared to the original systems, the results presented here provide further understanding of the key factors that influence enclosed reactivity.

Pre-organisation of the cage binding sites has proved to be essential for strong encapsulation of quinones, especially when other factors such as the cavity length remain relatively constant. This is probably a reflection that quinones are an ideal guest for the parent cage systems used by the Lusby group. A certain level of cage flexibility and reasonable cavity space proved to be essential for promoting Diels-Alder reactions. However, excessive degrees of rotational freedom of the ligands (e.g. **L4**) impairs Diels-Alder catalysis by reducing effective substrate or TS binding. While the more flexible cages may promote Michael additions to a lesser extent due to their weak substrate/TS binding, the Michael catalysis is complicated by the inherent differences of the electrostatic field in **C1**-**C5**. These results demonstrate that multiple factors need to be carefully balanced while developing supramolecular receptors and catalysts, not least the trade-off between pre-organisation and flexibility.

4.8 Experimental

4.8.1 General information

Unless otherwise stated, all reagents and solvents were purchased from Alfa Aesar, VWR, Fluorochem or Sigma Aldrich and used without further purification. Column chromatography was carried out using Geduran Si60 (40-63 μm) as the stationary phase and TLC was performed on precoated Kieselgel 60 plates (0.20 mm thick, 60F254. Merck, Germany) and observed under UV light at 254 nm. All reactions were carried out under air and at room temperature, unless otherwise stated.

All ^{1}H and ^{13}C NMR spectra were recorded on either a 500 MHz Bruker AV III equipped with a DCH cryo-probe (Ava500), a 400MHZ Bruker AV III equipped with BBFO+ probe (Ava400), a 500 MHz Bruker AV IIIHD equipped with a Prodigy cryo-probe (Pro500) or a 600 MHz Bruker AV IIIHD equipped with a TCI cryo-probe (Ava600) at a constant temperature of 300 K. Chemical shifts are reported in parts per million. Coupling constants (J) are reported in hertz (Hz). Standard abbreviations indicating multiplicity were used as follows: m = multiplet, q = quartet, t = triplet, d = doublet, s = singlet. All analysis was performed with MestReNova, Version 14.0.0. All assignments were confirmed using a combination of COSY, NOESY, HMBC and HSQC NMR spectra.

4.8.2 General procedure for NMR scale catalysis experiments

Prior to NMR scale reactions the commercial starting materials were purified as follows. Benzoquinone **4.1** was recrystalised from 1:5 DCM:petroleum ether (60 C°-80 C°). Methyl vinyl ketone **4.12** and 1-nitrocyclohexene **4.14** were purified by distillation. Methylnitroacetate **4.11**, was purified by silica plug (eluent: CH_2Cl_2). Cyclopentadiene **4.2** was freshly distilled before use each time. Other commercial materials were used without domestic purification.

For catalysed Diels-Alder reactions: To an NMR tube was introduced a solution containing 450 μL CD_2Cl_2, the cage compound (0.25 μmol or 0.5 μmol as solid), the diene (20 μL of a 312.5 mM or 625 mM CD_2Cl_2 stock solution), the dienophile (20

µL of a 62.5 mM CD_2Cl_2 stock solution), and the internal standard tetrakis(trimethylsilyl)silane (10 µL of a 15.6 mM CD_2Cl_2 stock solution).

For background Diels-Alder reactions: To an NMR tube was introduced a solution containing 450 µL CD_2Cl_2, the diene (20 µL of a 312.5 mM or 625 mM CD_2Cl_2 stock solution), the dienophile (20 µL of a 62.5 mM CD_2Cl_2 stock solution), and the internal standard tetrakis(trimethylsilyl)silane (10 µL of a 15.6 mM CD_2Cl_2 stock solution).

For catalysed Michael addition reactions: To an NMR tube was introduced a solution containing 450 µL CD_2Cl_2, the cage compound (0.25 µmol as solid), the Michael donor (20 µL of a 312.5 mM CD_2Cl_2 stock solution), the Michael acceptor (10 µL of a 125 mM CD_2Cl_2 stock solution), and the internal standard tetrakis(trimethylsilyl)silane (10 µL of a 15.6 mM CD_2Cl_2 stock solution). The Michael addition was started by the addition of 18-crown-6 (10 µL of a 125 mM CD_2Cl_2 stock solution).

4.8.3 Catalysis experiment product identification

The products of each NMR scale reaction were identified by comparing the spectra to previously reported ^{1}H NMR spectroscopic data.

The literature data for **4.3-10** are found in the following sources[34][35][36]:

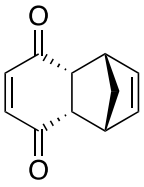

4.3

Bioorg. Med. Chem. Lett. 2012, 22, 6053–6058.

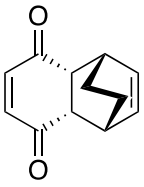

4.9

Angew. Chem. Int. Ed. 2009, 48, 5958–5961.

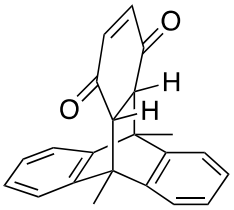

4.10

J. Am. Chem. Soc. 1993, 115, 11600–11601.

See Chapter 2 for the ^{1}H NMR spectroscopic data for the Michael addition products **4.13** and **4.15**.

4.8.4 Synthesis of novel Pd_2L_4 cages

4.8.4.1 Preparation of 2,7-bis(trimethylsilylethynyl)naphthalene

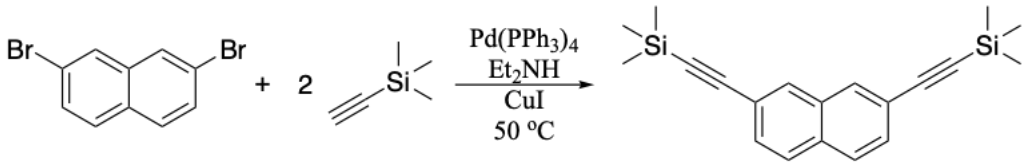

2,7-Bis(trimethylsilylethynyl)naphthalene was prepared using an adapted literature procedure.[19] 2,7-Dibromonaphthalene (3.500 g, 12.24 mmol), trimethylsilylacetylene (2.890 g, 29.37 mmol), $Pd(PPh_3)_4$ (707 mg, 0.610 mmol) and CuI (117 mg, 0.610 mmol) were combined in anhydrous Et_2NH (100 mL) under N_2 atmosphere. The reaction mixture was heated at 50 °C for 50 hours. White precipitate was filtered under suction and washed with Et_2NH (40 mL). The solvent was removed under reduced pressure. The crude mixture was purified by column chromatography (4% EtOAc in hexane, R_f = 0.15) to give an off-white solid as product (3.0 g, 76%). The NMR data matched literature values.[20]

^{1}H NMR (500 MHz, $CDCl_3$): δ 7.88 (d, J = 1.4 Hz, 2H), 7.68 (d, J = 8.5 Hz, 2H), 7.46 (dd, J = 8.4, 1.5 Hz, 2H), 0.25 (s, 18H) ppm.

4.8.4.2 Preparation of 2,7-diethynylnaphthalene

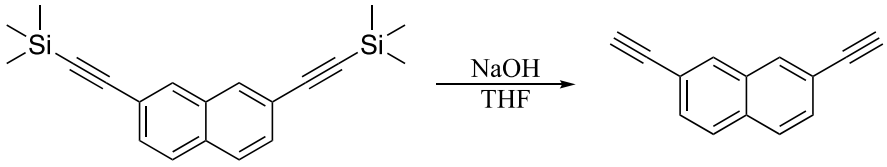

2,7-diethylnylnaphthalene was prepared according to literature procedure and NMR data matched literature values.[21]

^{1}H NMR (400 MHz, $CDCl_3$): δ 7.97 (s, 2H), 7.76 (d, J = 8.8 Hz, 2H), 7.54 (dd, J = 8.4, 1.6 Hz, 2H), 3.17 (s, 2H) ppm.

4.8.4.3 Preparation of 2,7-bis(isoquinoline-7-ylethylnyl)naphthalene (L3)

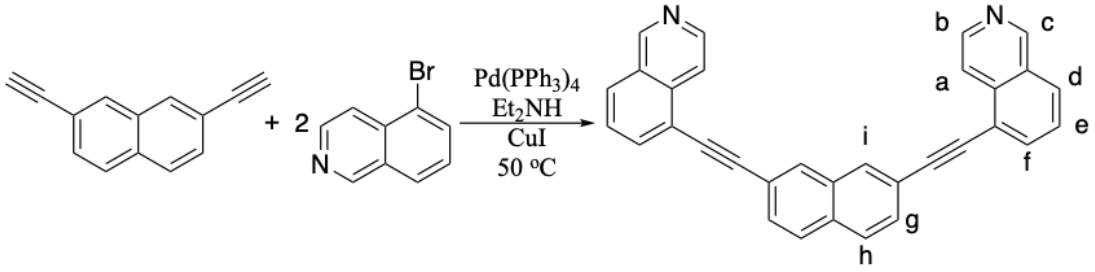

2,7-Diethylnylnaphthalene (590 mg, 3.35 mmol), 5-bromoisoquinoline (1.67 g, 8.04 mmol), $Pd(PPh_3)_4$ (194 mg, 0.170 mmol) and CuI (32 mg, 0.17 mmol) were combined in anhydrous Et_2NH (40 mL) under a N_2 atmosphere. The mixture was heated at 50 °C for 48 hours. The solvent was removed *in vacuo* and the residue recrystallised from CH_3CN. The resulting solid was partially dissolved in boiling acetone (300 mL) and the solution filtered over celite, with the residue further eluted with acetone (100 mL). The combined acetone solution was concentrated under reduced pressure to give a pale yellow solid (1.0 g, 70%).

^{1}H NMR (500 MHz, CD_2Cl_2) δ 9.31 (s, 2H, H_c), 8.67 (d, J = 5.5 Hz, 2H, H_b), 8.26 (d, J = 5.5 Hz, 2H, H_a), 8.22 (m, 2H, H_i), 8.05 – 7.99 (m, 4H, H_d + H_f), 7.93 (d, J = 8.6 Hz, 2H, H_h), 7.76 (dd, J = 8.6, 1.5 Hz, 2H, H_g), 7.64 (m, 2H, H_e) ppm.

^{13}C NMR (126 MHz, CD_2Cl_2) δ 153.27, 144.56, 136.38, 134.64, 133.16, 133.00, 131.85, 129.78, 128.92, 128.71, 128.63, 127.27, 121.65, 120.42, 119.06, 95.73, 87.25 ppm.

^{1}H DOSY NMR (500 MHz, CD_2Cl_2) 1.14×10^{-9} m^2/s, hydrodynamic radius: 4.6 Å.

HRMS (ESI): $C_{32}H_{19}N_2$ $[M+H]^+$ found 431.15480, requires 431.15428.

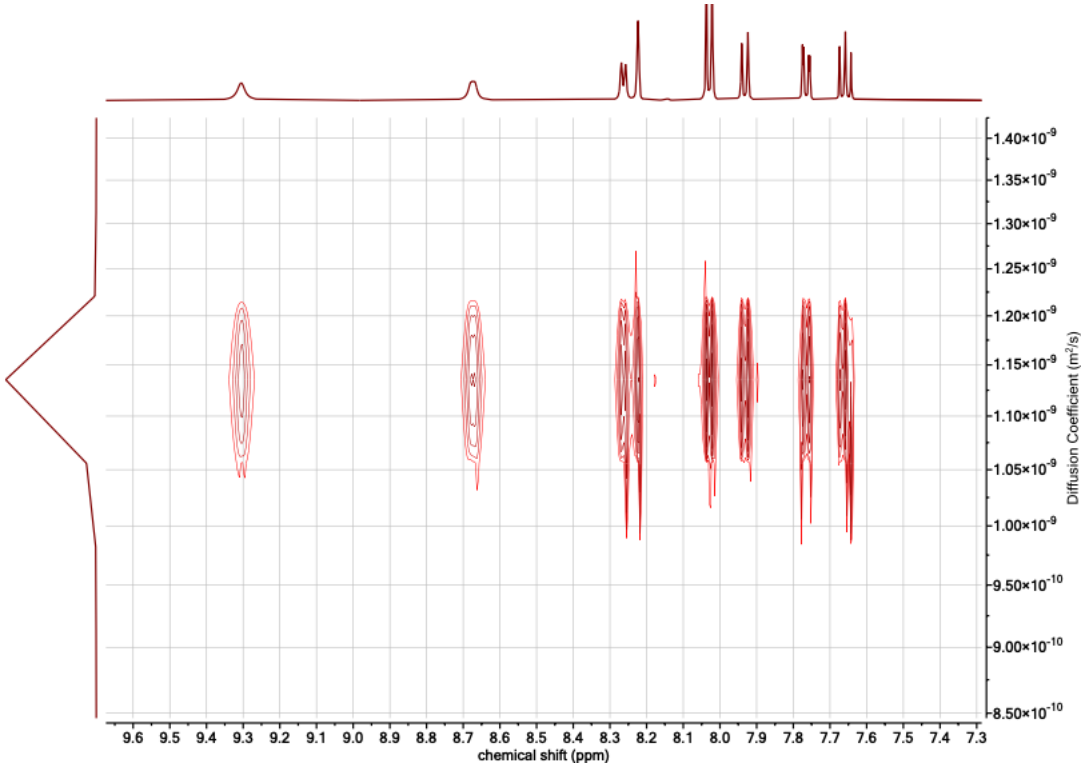

*Figure 4-16. ^1H DOSY NMR (500 MHz CD_2Cl_2) spectrum of **L3**.*

4.8.4.4 Preparation of $Pd_2L3_4{\cdot}4OTf$ cage

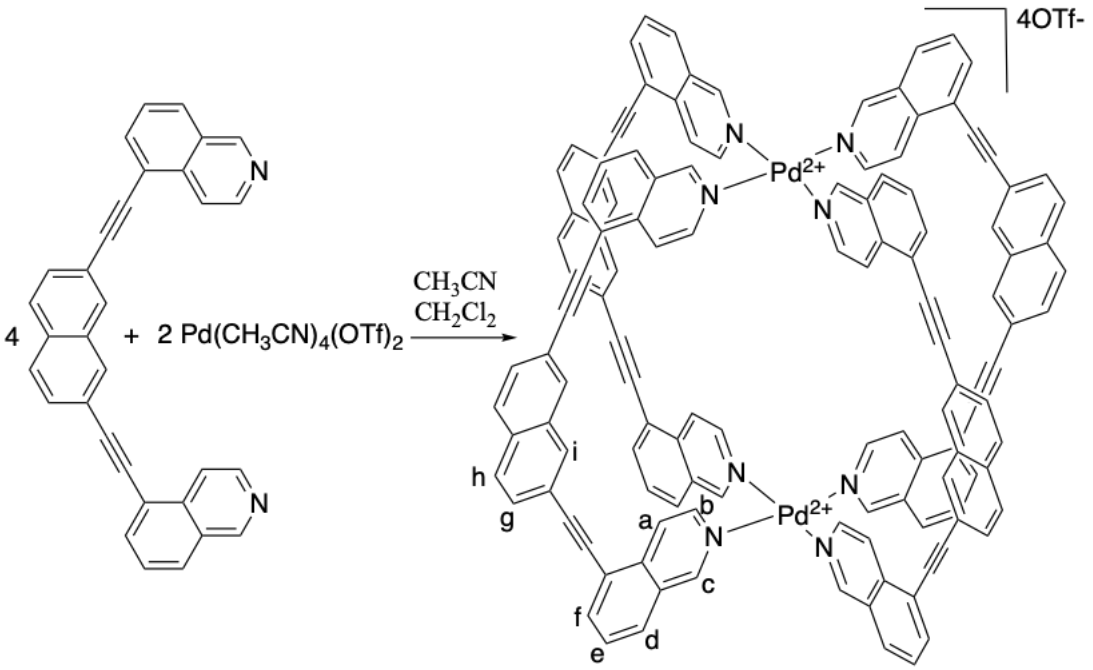

2,7-Bis(isoquinoline-7-ylethylnyl)naphthalene (200 mg, 0.470 mmol) was dissolved in CH_2Cl_2 (40 mL). $Pd(CH_3CN)_4(OTf)_2$ (132 mg, 0.232 mmol, 1.57 mL of a 0.148 mM stock solution) was diluted with CH_3CN to give a 40 mL solution. The $Pd(CH_3CN)_4(OTf)_2$ solution was added to the 2,7-bis(isoquinoline-7-ylethylnyl)naphthalene solution dropwise. The reaction mixture was stirred at room temperature overnight. The solvent was removed *via* rotary evaporation and the resulting solid was suspended and sonicated in CH_2Cl_2 (25 mL) for 20 minutes. A yellow powder product was collected by filtration (0.26 g, 86%). The product was used for anion metathesis without further purification.

NMR spectroscopic data was not recorded due to the poor solubility of the product.

4.8.4.5 Preparation of C3

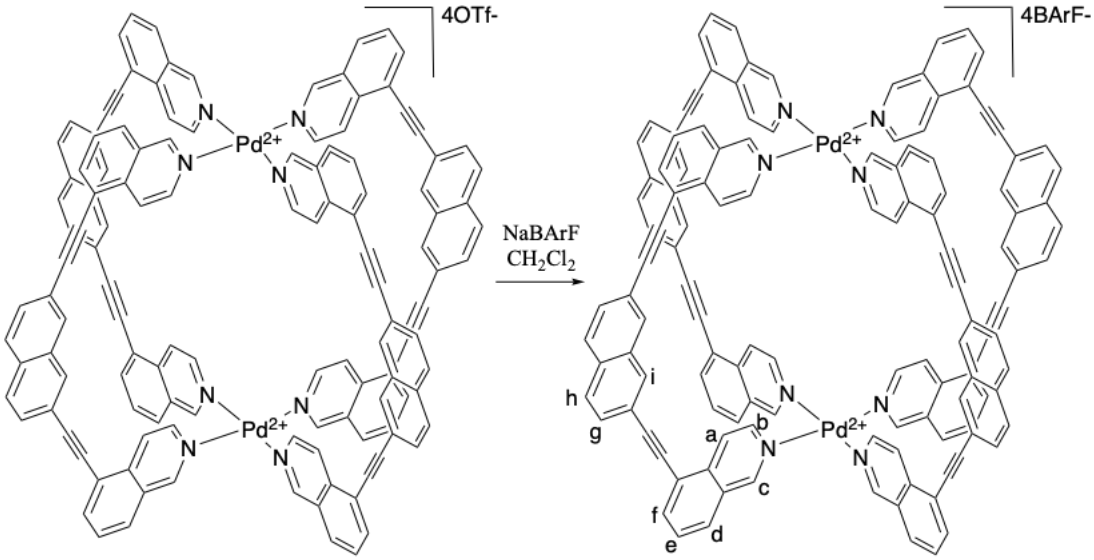

Pd_2**L3**$_4$·4OTf (50 mg, 20 μmol) was sonicated in CH_2Cl_2 (20 mL) for 5 minutes. NaBArF (70 mg, 79 μmol) was added and the mixture was further sonicated for 10 minutes. The reaction mixture was filtered and the residue washed with CH_2Cl_2 (5 mL) three times. The filtrated was concentrated *in vacuo*, yielding yellow crystalline solids as the product (92 mg, 86%).

^{1}H NMR (500 MHz, CD_2Cl_2) δ 9.45 (s, 8H, H_c), 8.81 (bs, 8H, H_b), 8.70 (d, J = 5.9 Hz, 8H, H_a), 8.18 (dd, J = 7.3, 1.1 Hz, 8H, H_f), 8.15 (s, 8H, H_i), 7.96 (d, J = 8.6 Hz, 8H, H_d), 7.89 (d, J = 8.5 Hz, 8H, H_h), 7.74 (dd, J = 8.6, 7.3 Hz, 8H, H_e), 7.72 – 7.69 (m, 32H, H_{BArF}), 7.68 (dd, J = 8.5, 1.5 Hz, 8H, H_g), 7.49 (s, 16H, H_{BArF}) ppm.

^{13}C NMR (126 MHz, CD_2Cl_2) δ 162.17 (q, $J_{C\text{-}B}$ = 50.0 Hz, C_{BArF}), 155.40, 140.47, 139.19, 137.42, 135.21 (m, C_{BArF}), 133.79, 132.66, 131.91, 131.77, 130.11, 129.92, 129.69 – 128.83 (m, C_{BArF}), 128.41, 125.77, 121.83, 120.69, 117.99 – 117.78 (m, C_{BArF}), 98.66, 84.57 ppm. One quaternary peak is missing.

^{19}F NMR (471 MHz, CD_2Cl_2) δ -62.73 ppm.

^{1}H DOSY NMR (500 MHz, CD_2Cl_2) 3.82×10^{-10} m^2/s, hydrodynamic radius: 13.8 Å.

ESI TOF HRMS m/z: Found 1830.3810 $[M–2BArF]^{2+}$, calculated for $[C_{192}H_{96}B_2F_{48}N_8Pd_2]^{2+}$ 1830.26. Found 931.8414 $[M–3BArF]^{3+}$, calculated for

$[C_{160}H_{84}BF_{24}N_8Pd_2]^{3+}$ 932.49. Found 483.619 $[M–4BArF]^{4+}$, calculated for $[C_{128}H_{72}N_8Pd_2]^{4+}$483.60.

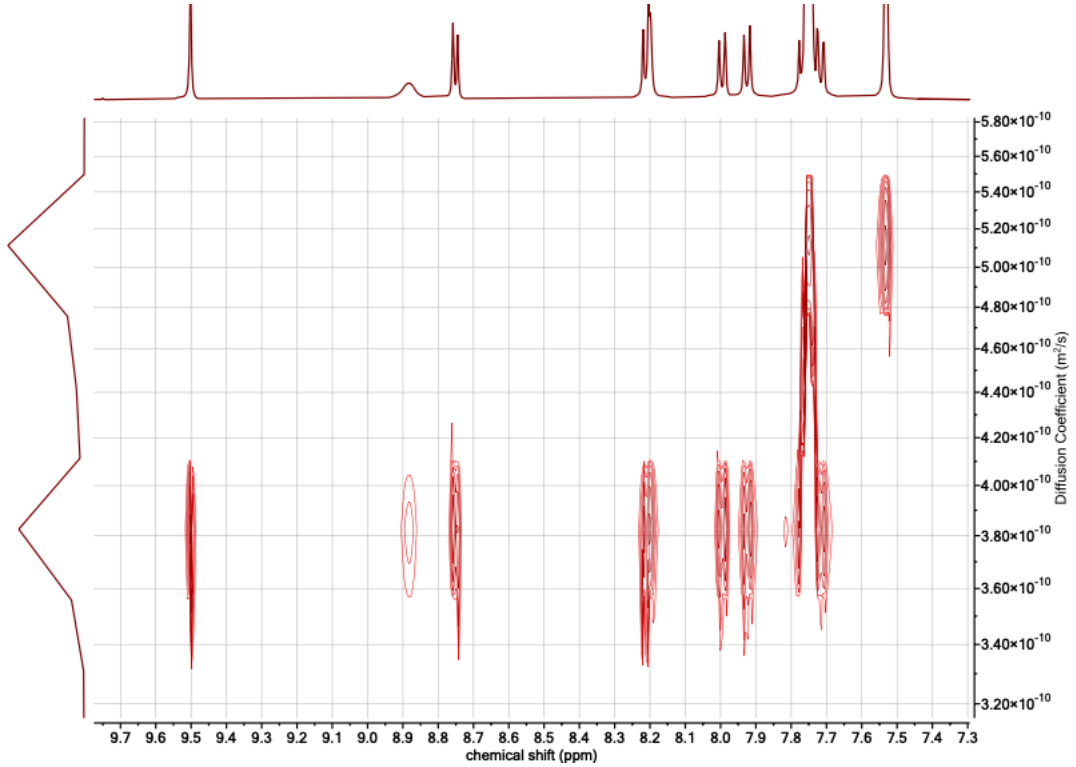

*Figure 4-17. ^1H DOSY NMR (500 MHz CD_2Cl_2) spectrum of **C3**.*

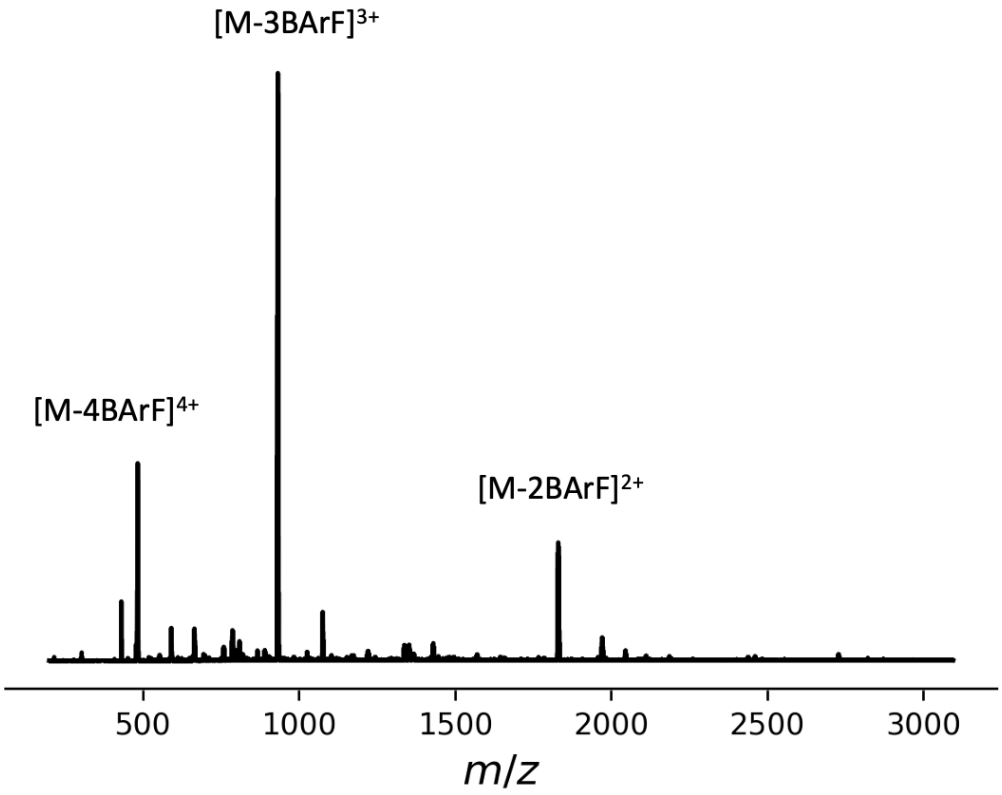

*Figure 4-18. ESI TOF HRMS of **C3**.*

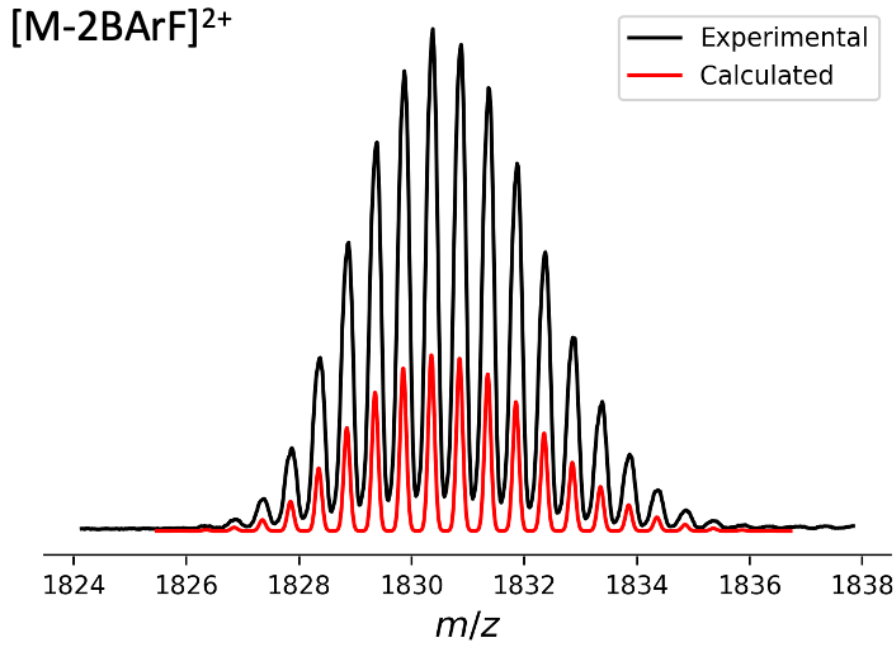

*Figure 4-19. ESI TOF HRMS of **C3** [M-2BArF]$^{2+}$.*

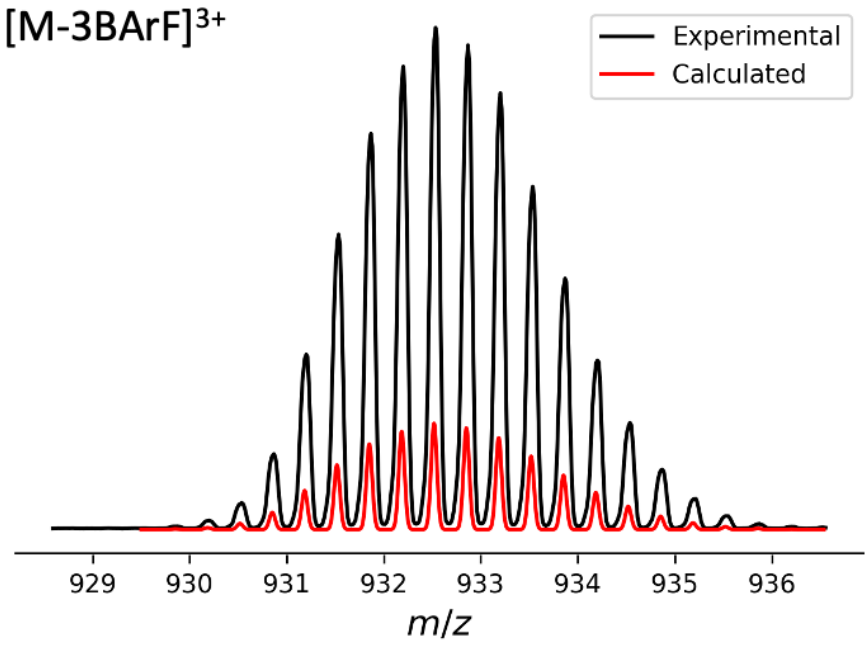

*Figure 4-20. ESI TOF HRMS of **C3** [M-3BArF]$^{3+}$.*

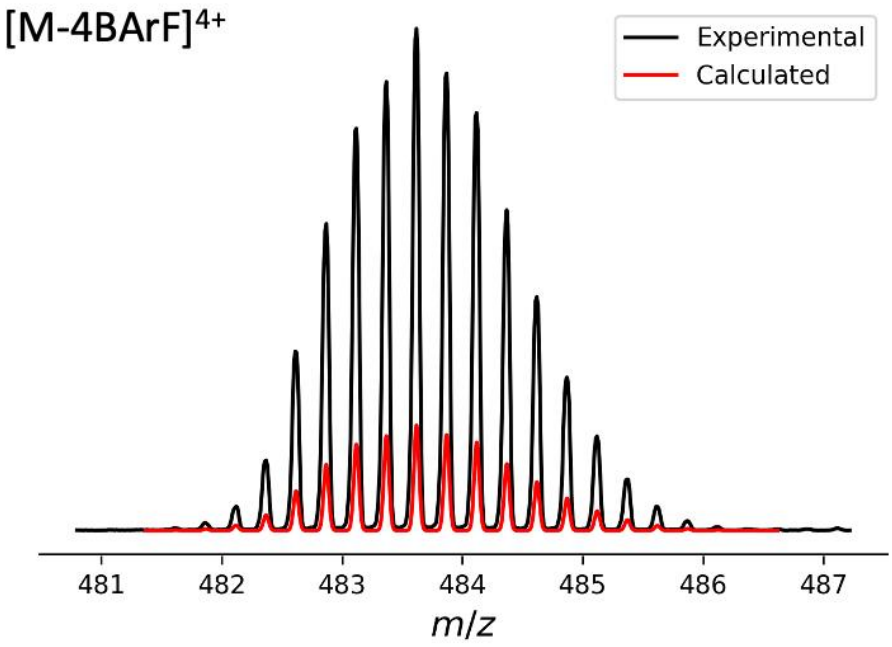

*Figure 4-21. ESI TOF HRMS of **C3** [M-4BArF]$^{4+}$.*

4.8.4.6 Preparation of 3,3'-bis(1-methylimidazole-5-ylethylnyl)-1,1'-biphenyl (L4)

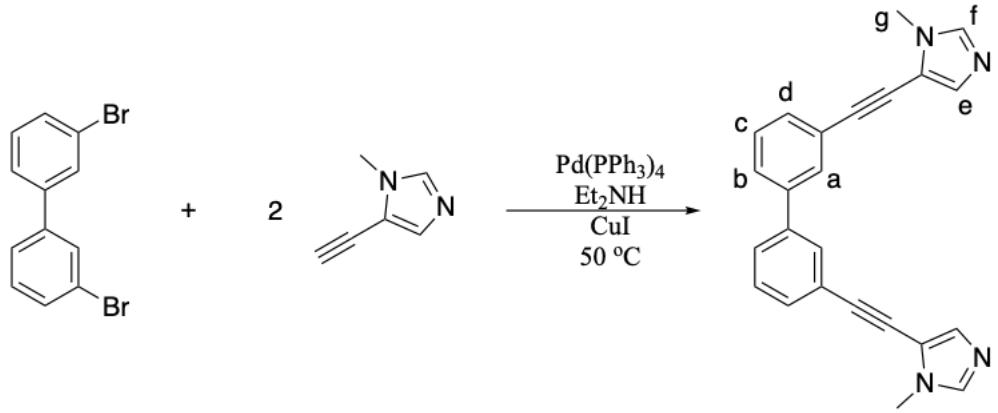

3,3'-Dibromo-1,1'-biphenyl (1.22 g, 3.91 mmol), 5-ethylnyl-1-methyl-imidazole (0.96 mL, 9.4 mmol), CuI (60 mg, 0.31 mmol) and $Pd(PPh_3)_4$ (0.66 g, 0.57 mmol) were combined in anhydrous Et_2NH (100 mL) under N_2 atmosphere. The reaction mixture was heated at 50 ºC for 60 hours. The solvent was removed *in vacuo*. The crude product was recrystallised in CH_3CN, yielding a pale yellow solid (0.75 g, 53%).

^{1}H NMR (500 MHz, $CDCl_3$) δ 7.76 – 7.72 (m, 2H, H_a), 7.60 – 7.57 (m, 2H, H_b), 7.53 – 7.50 (m, 2H, H_d), 7.49 (s, 2H , H_f), 7.48 – 7.43 (m, 2H, H_c), 7.36 (d, J = 1.0 Hz, 2H, H_e), 3.76 (s, 6H, H_g) ppm.

^{13}C NMR (126 MHz, $CDCl_3$) δ 140.73, 138.62, 134.86, 130.64, 130.10, 129.21, 127.56, 123.34, 116.25, 96.19, 77.6, 32.24 ppm.

HRMS (ESI): $C_{24}H_{19}N_4$ $[M+H]^+$ found 363.16280, requires 363.16042.

^{1}H DOSY NMR (500 MHz, CD_2Cl_2) 1.14×10^{-9} m^2/s, hydrodynamic radius: 4.6 Å.

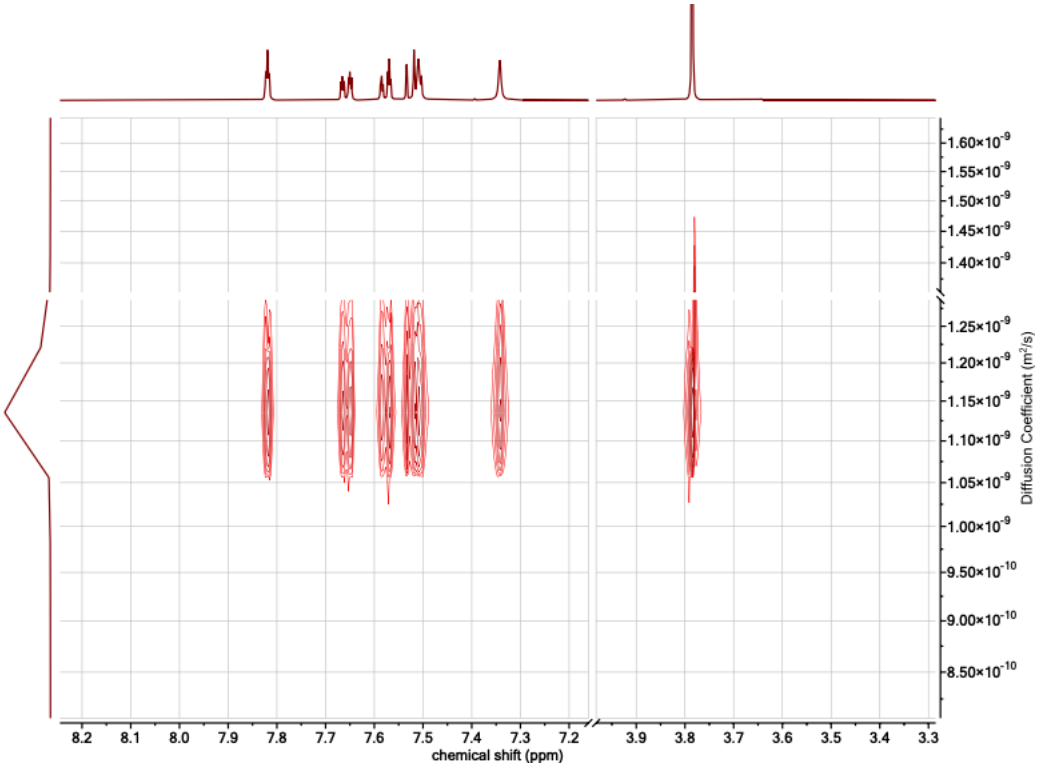

*Figure 4-22. ^1H DOSY NMR (500 MHz CD_2Cl_2) spectrum of **L4**.*

4.8.4.7 Preparation of Pd_2L4_4·4OTf

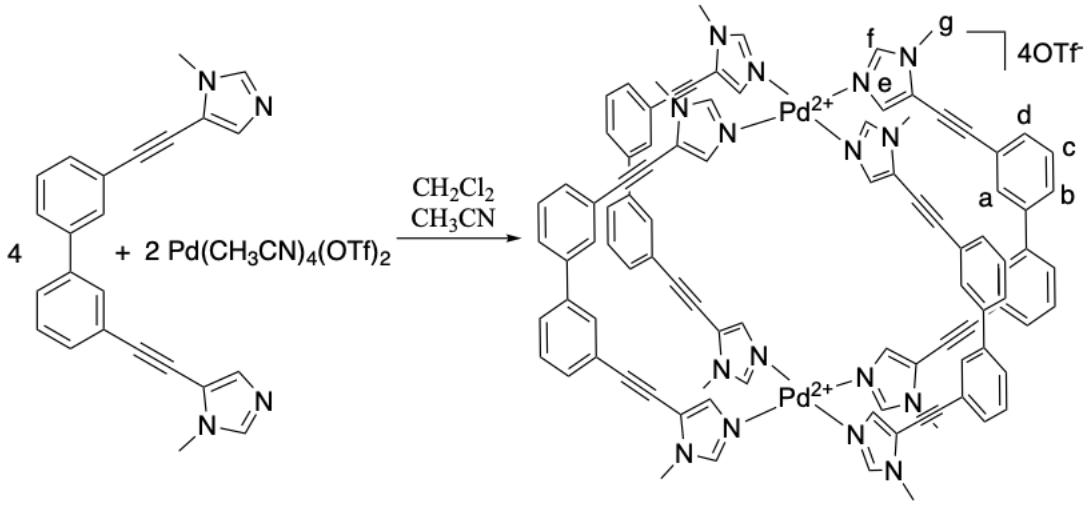

3,3'-Bis(1-methylimidazole-5-ylethylnyl)-1,1'-biphenyl (200 mg, 0.55 mmol) was dissolved in a mixture of CH_3CN (28 mL) and CH_2Cl_2 (12 mL). $Pd(CH_3CN)_4(OTf)_2$ (157 mg, 0.276 mmol, 2.06 mL of a 0.135 mM stock solution) was added to the 3,3'-bis(1-methylimidazole-5-ylethylnyl)-1,1'-biphenyl solution dropwise. The reaction mixture was stirred at room temperature for 48 hours before the solvent was partially removed *via* rotary evaporation. Et_2O (40 mL) was added to crash out a solid which was collected *via* filtration. The solid was washed with Et_2O (20 mL) three times to give a dark green product (210 mg, 70 %).

^{1}H NMR (500 MHz, CD_3CN) δ 7.92 (s, 8H, H_f), 7.91 – 7.88 (m, 8H, H_a), 7.80 – 7.75 (m, 8H, H_b), 7.61 – 7.55 (m, 8H, H_d), 7.55 – 7.50 (m, 8H, H_c), 7.41 (d, J = 1.3 Hz, 8H, H_e), 3.78 (s, 24H, H_g) ppm.

^{13}C NMR (126 MHz, CD_3CN) δ 141.17, 140.53, 133.05, 131.36, 130.78, 130.68, 128.68, 123.08, 118.99, 97.09, 74.76, 34.31 ppm.

4.8.4.8 Preparation of C4

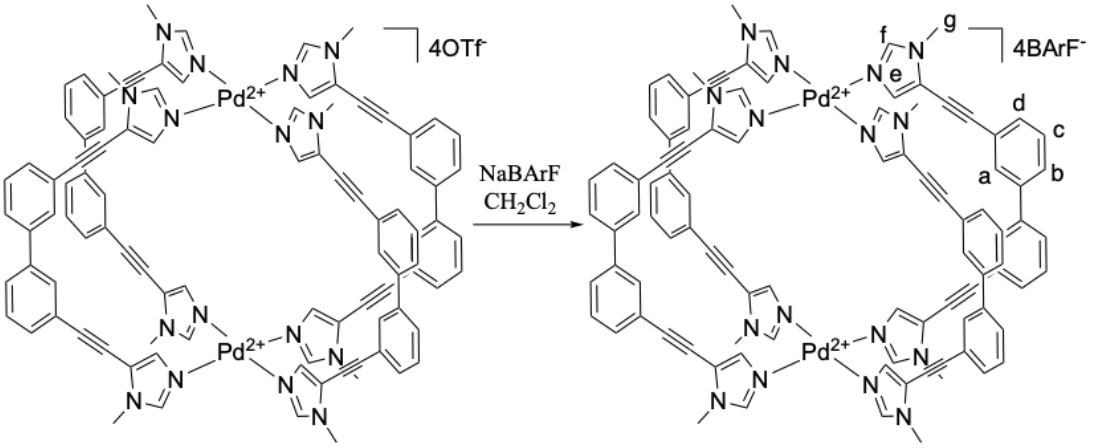

Pd_2**L4**$_4$·4OTf (65 mg, 29 µmol) was sonicated in CH_2Cl_2 (4 mL) for 10 minutes. The solid collected by filtration (46 mg, 20 µmol) was re-suspended in CH_2Cl_2 (20 mL) and sonicated for 10 minutes. NaBArF (72 mg, 82 µmol) was added and the mixture was further sonicated for 15 minutes. The resulting precipitant was removed by gravity filtration. The filtrate was concentrated *in vacuo*, giving a white solid as product (53 mg, 51%).

Due to the heavy overlap of **C4** cage and $BArF^-$ ^{1}H NMR signals in CD_2Cl_2, ^{1}H and ^{13}C NMR data of **C4** cage are provided in CD_3CN as well as CD_2Cl_2.

^{1}H NMR (500 MHz, CD_3CN) δ 7.88 – 7.87 (m, 8H, H_a), 7.81 – 7.75 (m, 16H, H_f + H_b), 7.71 – 7.68 (m, 32H, H_{BArF}), 7.66 (s, 16H, H_{BArF}), 7.61 – 7.55 (m, 8H, H_d), 7.53 – 7.49 (m, 8H, H_c), 7.34 (d, J = 1.3 Hz, 8H, H_e), 3.77 (s, 24H, H_g) ppm.

^{1}H NMR (500 MHz, CD_2Cl_2) δ 7.76 – 7.75 (m, 8H, H_a), 7.74 – 7.69 (m, 40H, H_b + H_{BArF}), 7.54 (s, 16H, H_{BArF}), 7.52 – 7.45 (m, 16H, H_d + H_c), 7.42 (m, 8H, H_f), 7.00 (d, J = 1.3 Hz, 8H, H_e), 3.74 (s, 24H, H_g) ppm.

^{13}C NMR (126 MHz, CD_3CN) δ 162.82 (q, J_{C-B} = 49.8 Hz, C_{BArF}),141.00, 140.59, 135.67 (C_{BArF}), 133.06, 131.46, 130.72, 130.64, 130.1 – 129.7 (m, C_{BArF}), 128.83, 125.48 (q, J_{C-F} = 272.4 Hz, C_{BArF}), 123.00, 119.04, 118.73 – 118.62 (m, C_{BArF}, partially overlaps with the CD_3CN signal), 98.48, 75.46, 34.33 ppm.

^{13}C NMR (126 MHz, CD_2Cl_2) δ 162.08 (q, J_{C-B} = 49.8 Hz, C_{BArF}), 140.14, 138.49, 135.22 (C_{BArF}), 131.32, 131.18, 130.28, 130.15, 129.64 – 128.88 (m, C_{BArF}), 124.93 (q, J_{C-F} = 272.4 Hz, C_{BArF}), 121.21, 120.70, 117.98 – 117.85 (m, C_{BArF}), 100.31, 72.79, 34.49 ppm.

^{19}F NMR (471 MHz, CD_2Cl_2) δ -62.73 ppm.

^{1}H DOSY NMR (500 MHz, CD_2Cl_2) 4.11×10^{-10} m^2/s, hydrodynamic radius: 12.9 Å.

ESI TOF HRMS m/z: Found 1694.3635 $[M–2BArF]^{2+}$, calculated for $[C_{160}H_{96}B_2F_{48}N_{16}Pd_2]^{2+}$ 1695.28. Found 841.8502 $[M–3BArF]^{3+}$, calculated for $[C_{128}H_{84}BF_{24}N_{16}Pd_2]^{3+}$ 841.50. Found 415.6259 $[M–4BArF]^{4+}$, calculated for $[C_{96}H_{72}N_{16}Pd_2]^{4+}$415.60.

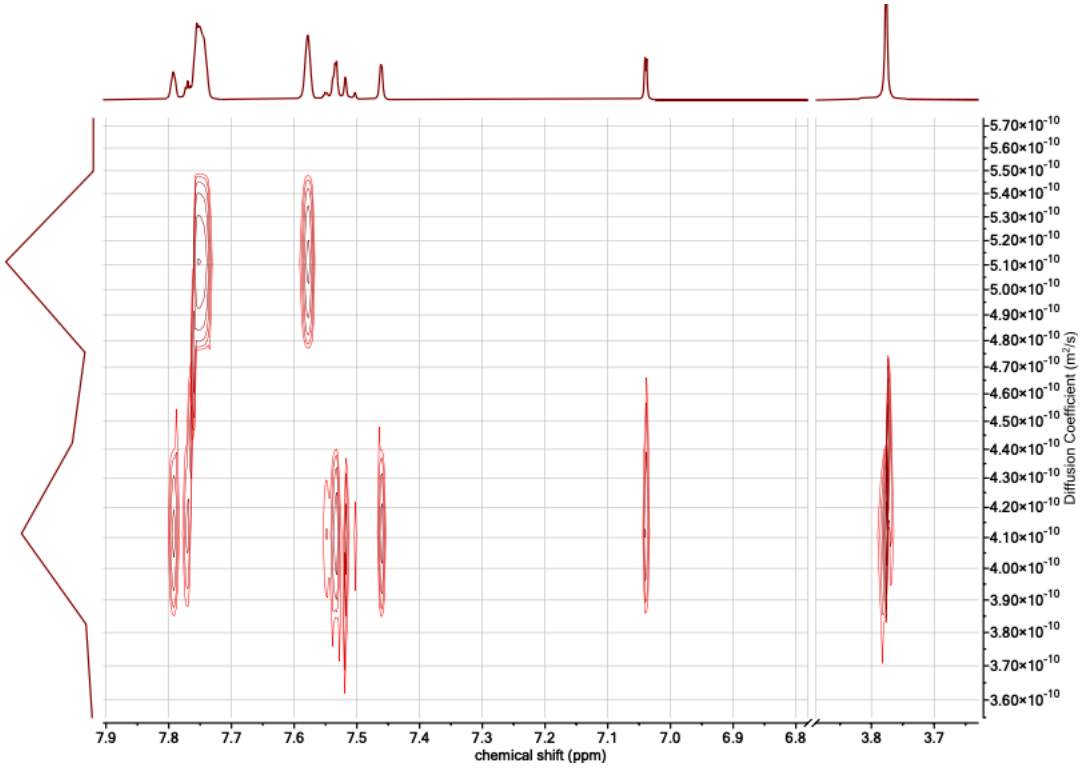

*Figure 4-23. ^{1}H DOSY NMR (500 MHz CD_2Cl_2) spectrum of **C4**.*

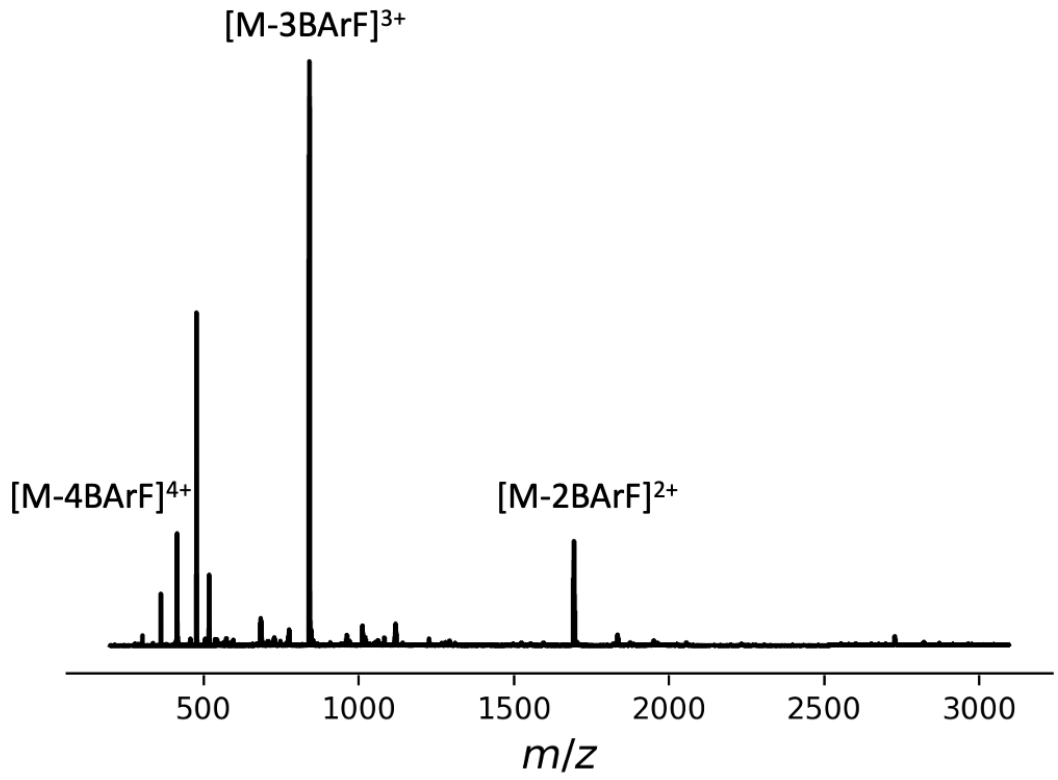

*Figure 4-24. ESI TOF HRMS of **C4**.*

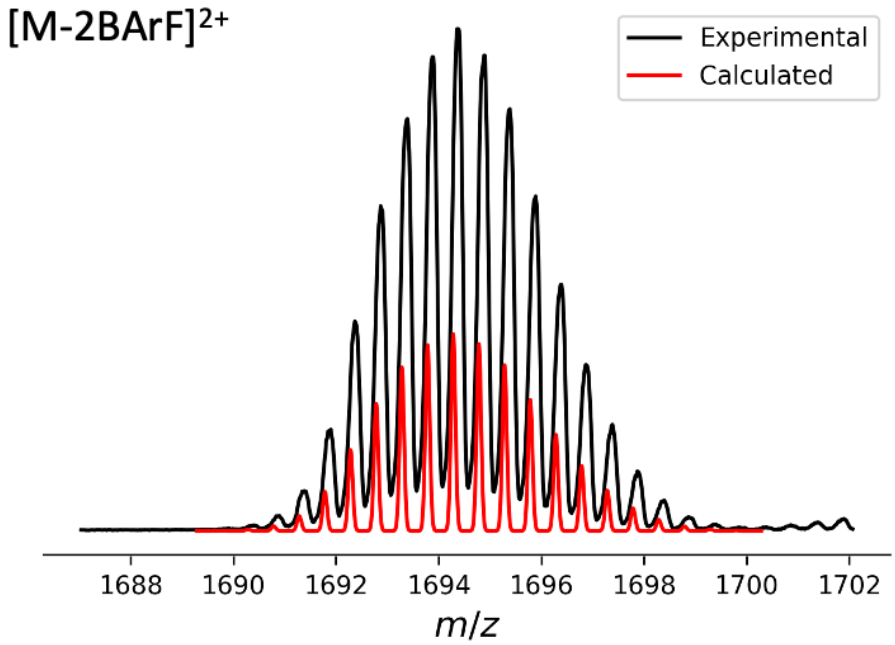

*Figure 4-25. ESI TOF HRMS of **C4** [M-2BArF]$^{2+}$.*

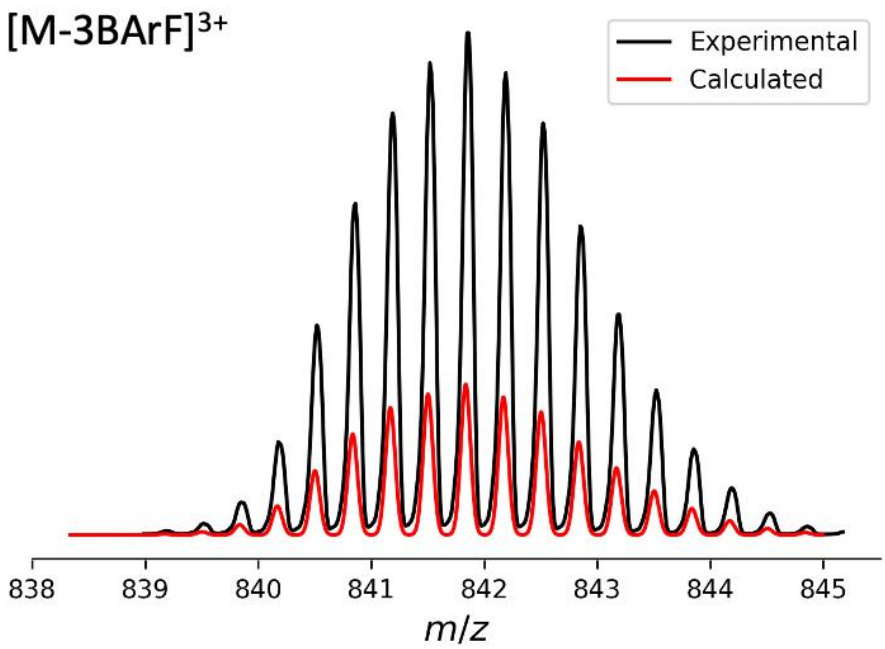

*Figure 4-26. ESI TOF HRMS of **C4** [M-3BArF]$^{3+}$.*

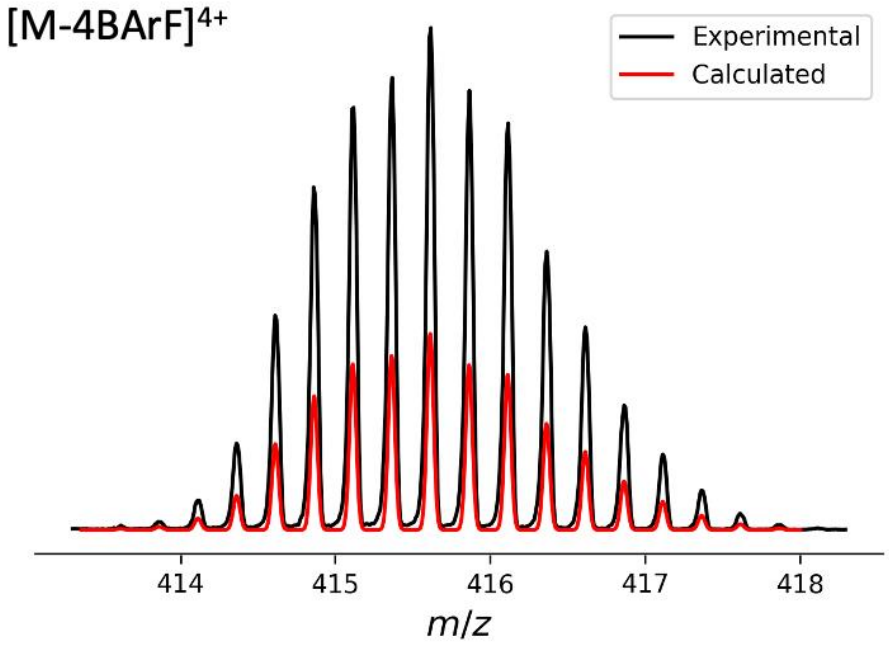

*Figure 4-27. ESI TOF HRMS of **C4** [M-4BArF]$^{4+}$.*

4.8.5 Crystallographic data

4.8.5.1 Crystallographic data of C3

Experimental: Single colourless block crystals of **C3** were recrystallised from a mixture of dichloromethane and toluene by solvent layering. A suitable crystal with dimensions 0.10 × 0.08 × 0.05 mm^3 was selected and mounted on a MITIGEN holder in perfluoroether oil on a Rigaku Oxford Diffraction SuperNova diffractometer. The crystal was kept at a steady T = 120.00(10) K during data collection. The structure was solved with the 2018/2 version **ShelXT**[37] solution program using dual methods and by using **Olex2**[38] as the graphical interface. The model was refined with the 2018/3 versioin **ShelXL**[39] using full matrix least squares minimisation on $\boldsymbol{F^2}$.

Crystal data: $B_4C_{315.5}F_{96}H_{180}N_8Pd_2$, M_r = 6162.70, triclinic, *P*-1 (No. 2), a = 17.3436(5) Å, b = 18.2267(6) Å, c = 24.6561(7) Å, α = 78.320(2)°, β = 74.689(2)°, γ = 75.592(3)°, V = 7202.7(4) $Å^3$, T = 120.00(10) K, Z = 1, Z' = 0.5, μ(Cu K_α) = 2.058, 116495 reflections measured, 29694 unique (R_{int} = 0.0990) which were used in all calculations. The final wR_2 was 0.2066 (all data) and R_1 was 0.0729 (I≥2 σ(I)).

Structure:

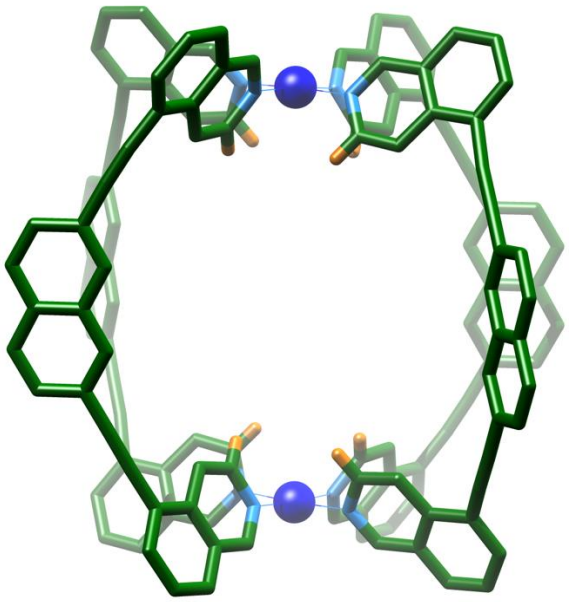

4.8.5.2 Crystallographic data of C4

Experimental: Single colourless plate crystals of **C4** were recrystallised from a mixture of toluene and dichloromethane by solvent layering. A suitable crystal with dimensions 0.31 × 0.24 × 0.06 mm^3 was selected and mounted on a MITIGEN holder in perfluoroether oil on a Rigaku Oxford Diffraction SuperNova diffractometer. The crystal was kept at a steady T = 120.01(10) K during data collection. The structure was solved with the 2018/2 version **ShelXT**[37] solution program using dual methods and by using **Olex2**[38] as the graphical interface. The model was refined with the 2018/3 version **ShelXL**[39] using full matrix least squares minimisation on $\boldsymbol{F^2}$.

Crystal data: $B_4C_{258}Cl_{12}F_{96}H_{164}N_{16}Pd_2$, M_r = 5993.48, orthorhombic, *Pbcn* (No. 60), a = 40.0161(7) Å, b = 19.3641(2) Å, c = 33.2437(4) Å, $\alpha = \beta = \gamma = 90^{\circ}$, V = 25759.7(6) $Å^3$, T = 120.01(10) K, Z = 4, Z' = 0.5, μ(Cu K_α) = 3.406, 509454 reflections measured, 26911 unique (R_{int} = 0.1827) which were used in all calculations. The final wR_2 was 0.2729 (all data) and R_1 was 0.0923 (I≥2 σ(I)).

Structure:

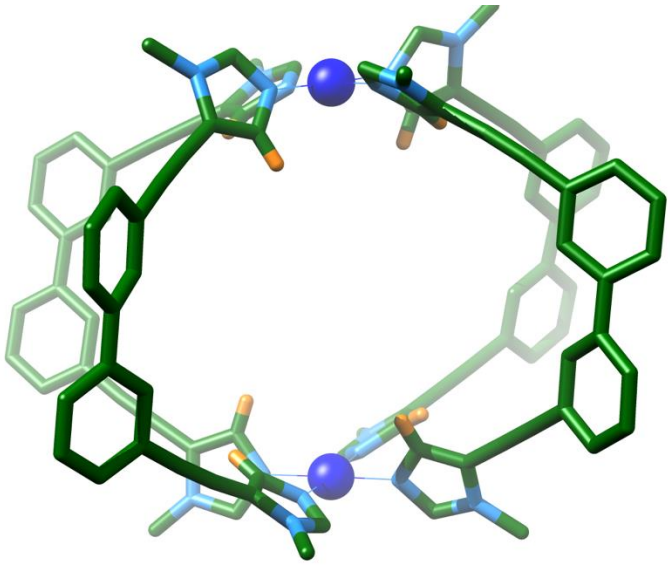

4.8.5.3 Crystallographic data of C1

Experimental: Single colourless block crystals of **C1** recrystallised from a mixture of dichloromethane and diethyl ether by slow evaporation. A suitable crystal with dimensions 0.43 × 0.23 × 0.20 mm^3 was selected and mounted on a MITIGEN holder in Paratone oil on a Bruker D8 VENTURE diffractometer. The crystal was kept at a steady T = 100.0 K during data collection. The structure was solved with the 2018/2 version **ShelXT**[37] solution program using dual methods and by using **Olex2**[38] as the graphical interface. The model was refined with the 2018/3 version **ShelXL**[39] 2018/3 using full matrix least squares minimisation on $\boldsymbol{F^2}$.

Crystal Data. $C_{218}H_{116}B_4Cl_{20}F_{96}N_8Pd_2$, M_r = 5636.22, monoclinic, $P2_1/c$ (No. 14), a = 21.0751(12) Å, b = 39.726(2) Å, c = 28.1176(18) Å, β = 99.867(2)°, $\alpha = \gamma$ = 90°, V = 23193(2) $Å^3$, T = 100.0 K, Z = 4, Z' = 1, μ(Mo Kα) = 0.517, 974085 reflections measured, 57345 unique (R_{int} = 0.0467) which were used in all calculations. The final wR_2 was 0.2116 (all data) and R_1 was 0.0724 (I≥2 σ(I)).

Structure:

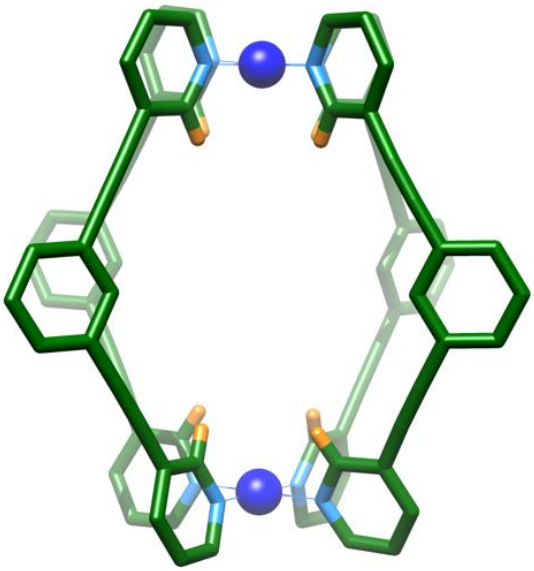

4.8.5.4 Full crystallographic data of all the compounds

Compound	**C3**	**C4**	**C1**
Formula	$B_4C_{315.5}F_{96}H_{180}N_8Pd_2$	$B_4C_{258}Cl_{12}F_{96}H_{164}N_{16}Pd_2$	$C_{218}H_{116}B_4Cl_{20}F_{96}N_8Pd_2$
$D_{calc.}$/ g cm^{-3}	1.421	1.545	1.614
μ/mm^{-1}	2.058	3.406	0.517
Formula Weight	6162.70	5993.48	5636.22
Colour	colourless	colourless	colourless
Shape	block	plate	block
Size/mm^3	0.10×0.08×0.05	0.31×0.24×0.06	0.43×0.23×0.20
T/K	120.00(10)	120.01(10)	100.0
Crystal System	triclinic	orthorhombic	monoclinic
Space Group	P-1	$Pbcn$	$P2_1/c$
a/Å	17.3436(5)	40.0161(7)	21.0751(12)
b/Å	18.2267(6)	19.3641(2)	39.726(2)
c/Å	24.6561(7)	33.2437(4)	28.1176(18)
α/°	78.320(2)	90	90
β/°	74.689(2)	90	99.867(2)
γ/°	75.592(3)	90	90
V/Å^3	7202.7(4)	25759.7(6)	23193(2)
Z	1	4	4
Z'	0.5	0.5	1
Wavelength/Å	1.54184	1.54184	0.71073
Radiation type	Cu K_α	Cu K_α	Mo K_α
Θ_{min}/°	3.621	3.443	2.128
Θ_{max}/°	76.290	77.584	28.265
Measured Refl's.	116495	509454	974085
Indep't Refl's	29694	26911	57345
Refl's I≥2 σ(I)	22896	19505	47624
R_{int}	0.0990	0.1827	0.0467
Parameters	2193	1875	3333
Restraints	498	317	162
Largest Peak	0.895	0.749	4.539
Deepest Hole	-1.451	-1.816	-1.831
GooF	1.027	1.014	1.032
wR_2 (all data)	0.2066	0.2729	0.2116
wR_2	0.1888	0.2472	0.1974
R_1 (all data)	0.0909	0.1153	0.0860
R_1	0.0729	0.0923	0.0724

4.8.6 Determination of binding constants via ^{1}H NMR titration

4.8.6.1 General procedure of ^{1}H NMR titration with C3

For each titration, a solution containing cage (0.25 mM or 0.5 mM) and guest (1 mM, 50 mM or 25 mM) was titrated to a 500 µL solution containing only cage (0.25 mM or 0.5 mM), maintaining the concentration of the cage species throughout. ^{1}H NMR spectrum was recorded at each titration point. Unless specified, the peak positions of the internal pyridyl hydrogens were plotted against the concentration of guests, shown in blue in Figure 4-28. The experimental data was fitted to a 1:1 fast exchange binding model (Equation 4-2) using the Levenberg-Marquardt Nonlinear Least-Squares Algorithm built in the R software and the RStudio software interface.

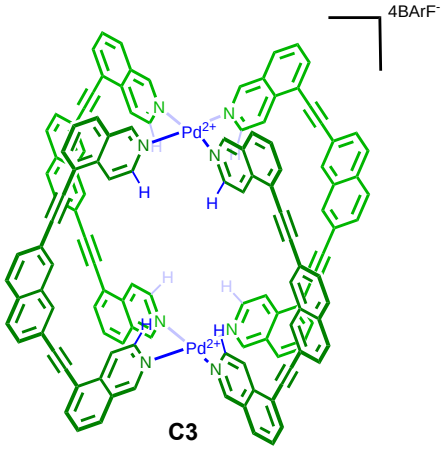

*Figure 4-28. Peak positions of the protons ortho to the N-Pd^{2+} bond (blue) were monitored during NMR titrations, exemplified with **C1**.*

$$\delta = \delta_0 + \frac{\Delta\delta_{Max}}{2}\left(\frac{C_{Guest}}{C_{Host}} + \frac{1}{C_{Host}\cdot K_{Ass}} + 1 - \sqrt{\left(\frac{C_{Guest}}{C_{Host}} + \frac{1}{C_{Host}\cdot K_{Ass}} + 1\right)^2 - \frac{4\cdot C_{Guest}}{C_{Host}}}\right)$$

Equation 4-2.

4.8.6.2 Pseudo ^{1}H NMR titration with C4

For each pseudo titration, guests were added as solids to a **C4** solution (0.5 mM). See Figure 4-10 for NMR spectra.

4.8.6.3 ^{1}H NMR titration data of 4.1 in C3

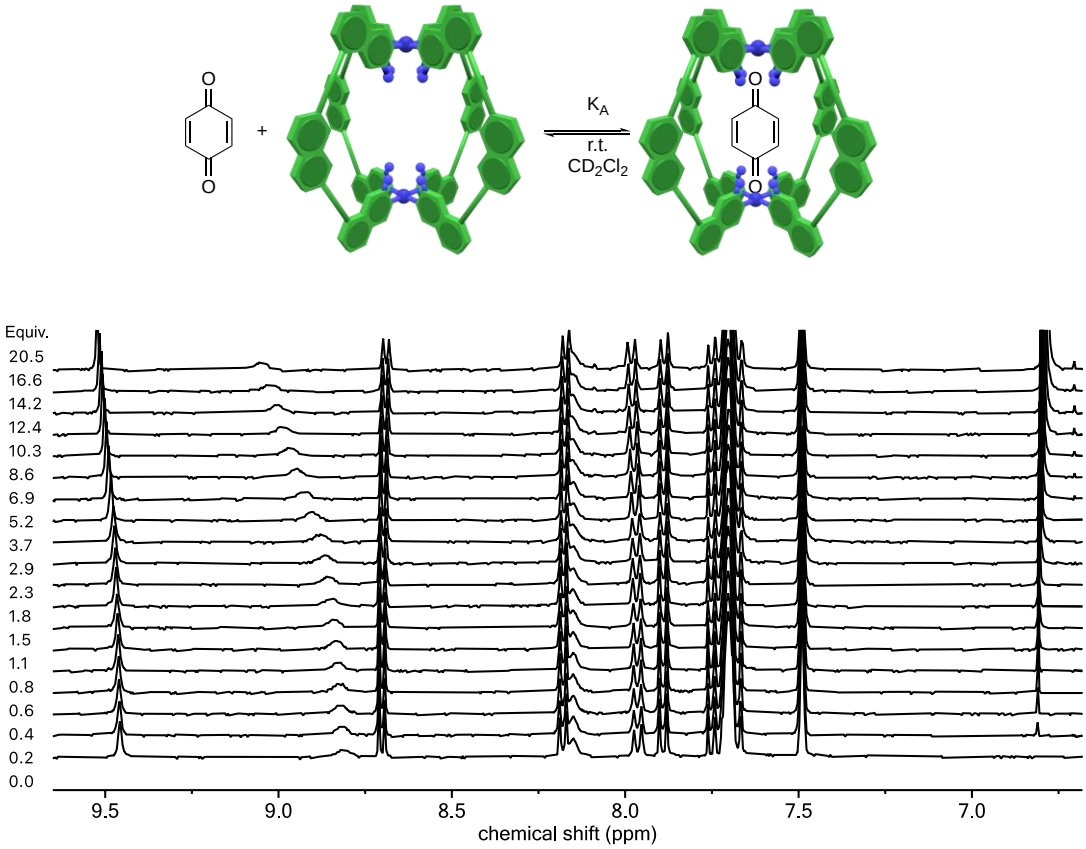

*Figure 4-29. ^{1}H NMR (400 MHz, CD_2Cl_2) spectroscopic data for titration of **4.1** into **C3**.*

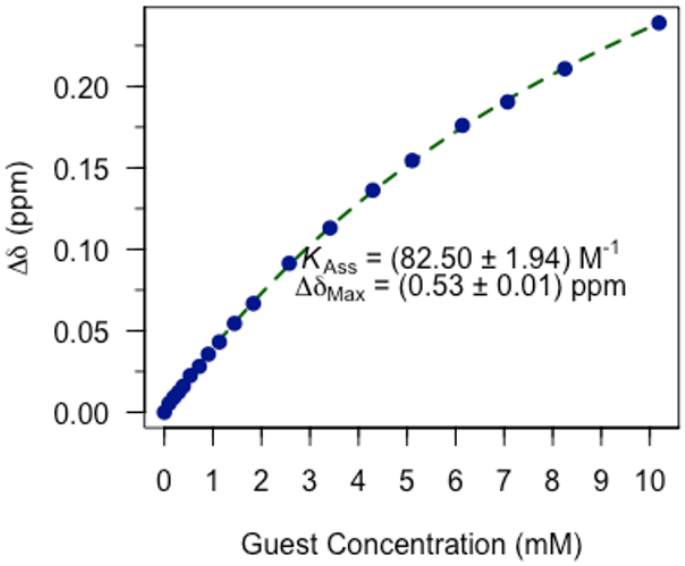

*Figure 4-30. Fitted data for change in peak position with increasing **4.1** concentration.*

4.8.6.4 ^{1}H NMR titration data of 4.4 in C3

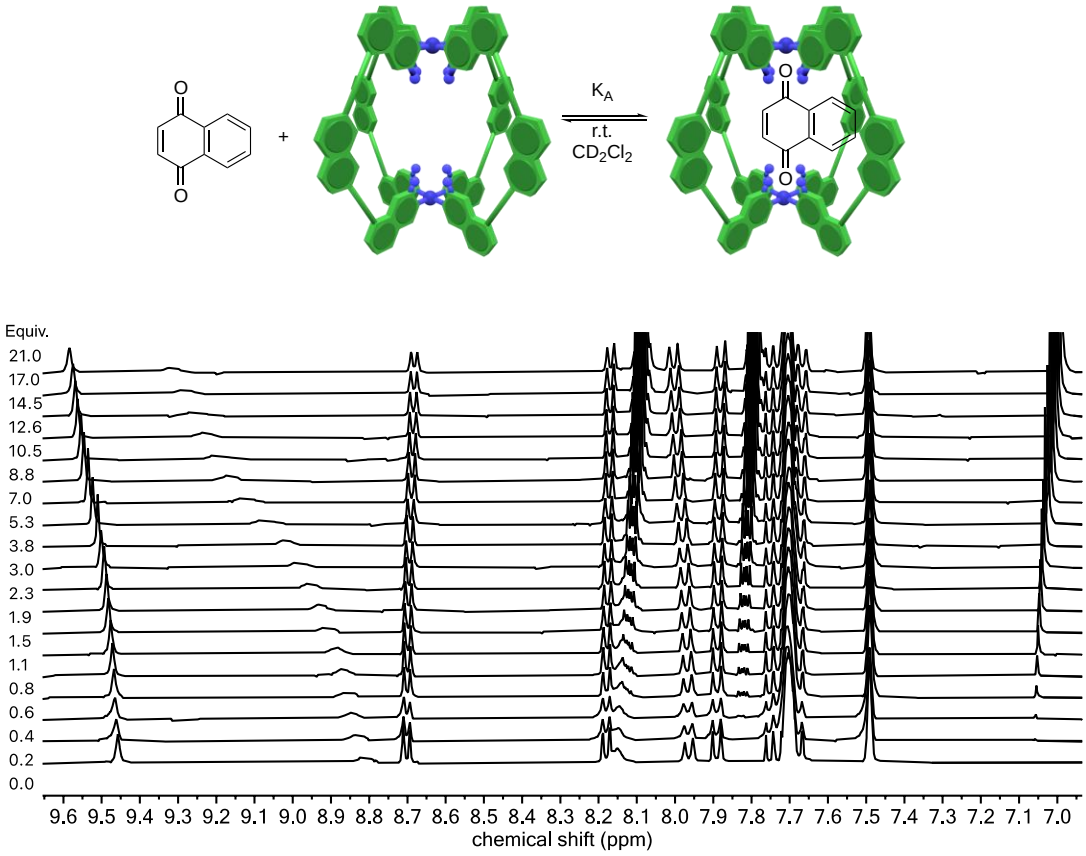

*Figure 4-31. ^{1}H NMR (400 MHz, CD_2Cl_2) spectroscopic data for titration of **4.4** into **C3**.*

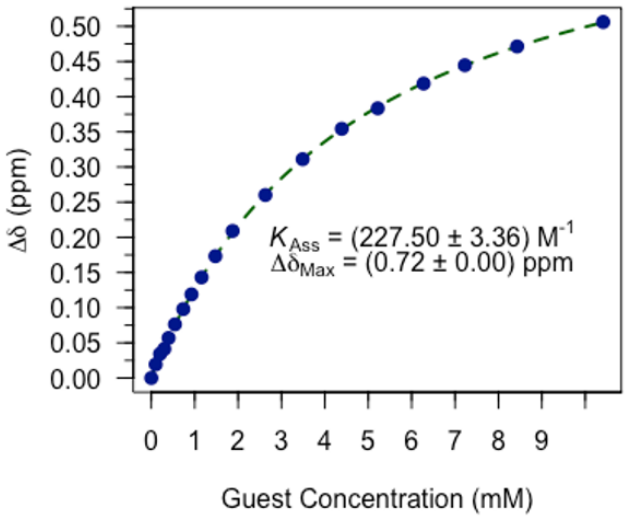

*Figure 4-32. Fitted data for change in peak position with increasing **4.4** concentration.*

4.8.6.5 ^{1}H NMR titration data of 4.6 in C3

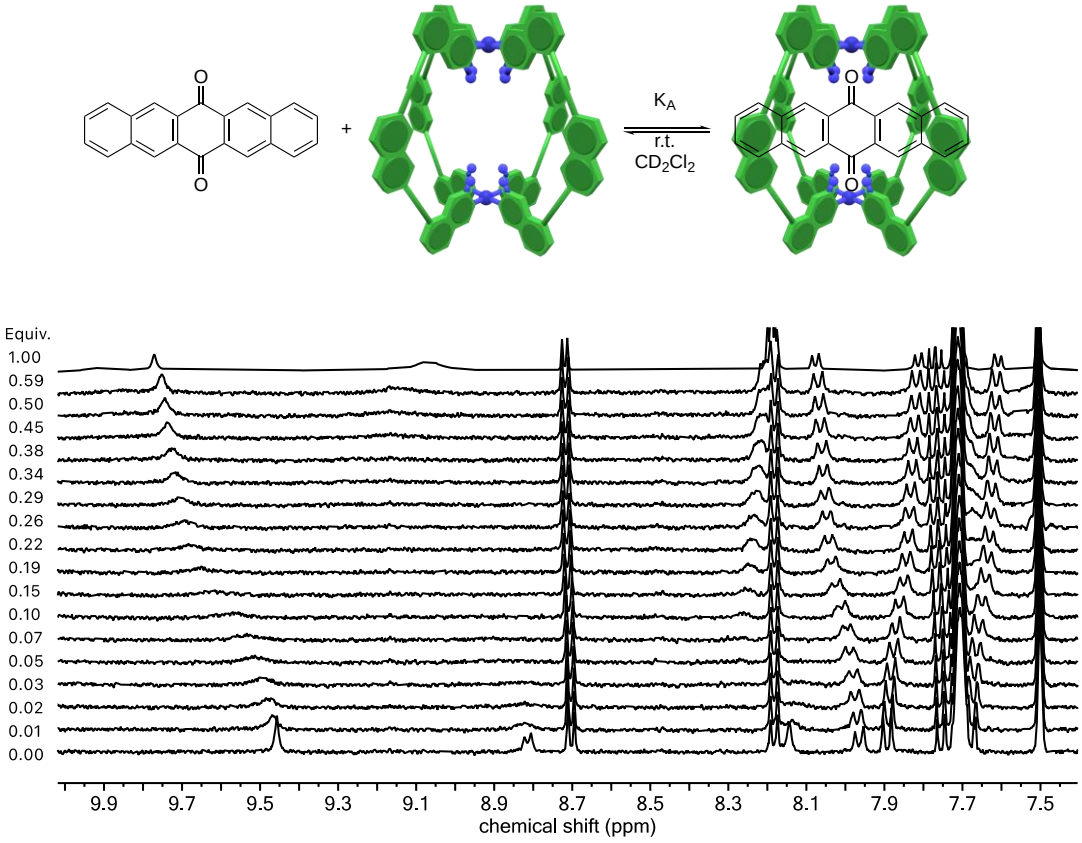

*Figure 4-33. ^{1}H NMR (400 MHz, CD_2Cl_2) spectroscopic data for titration of **4.6** into **C3**. The binding of **4.6** in **C3** fall in the intermediate exchange range in comparison to the NMR time scale. Hence the internal binding proton (δ_0 = 8.81) disapears and reapears through the course of titration. The proton at δ_0 = 7.97 was monitored instead.*

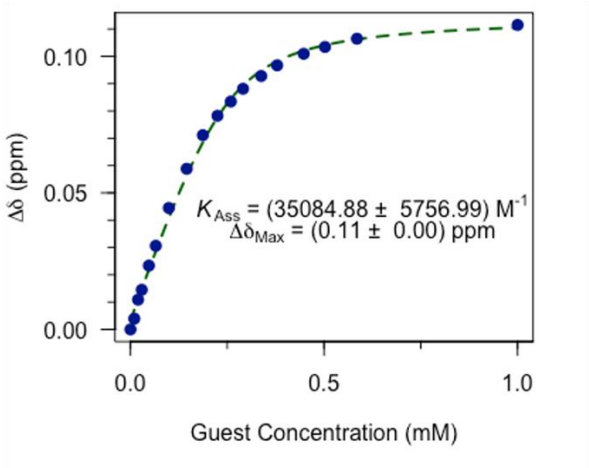

*Figure 4-34. Fitted data for change in peak position of proton at δ_0 = 7.97 with increasing **4.6** concentration.*

4.8.6.6 ^{1}H NMR titration data of 4.3 in C3

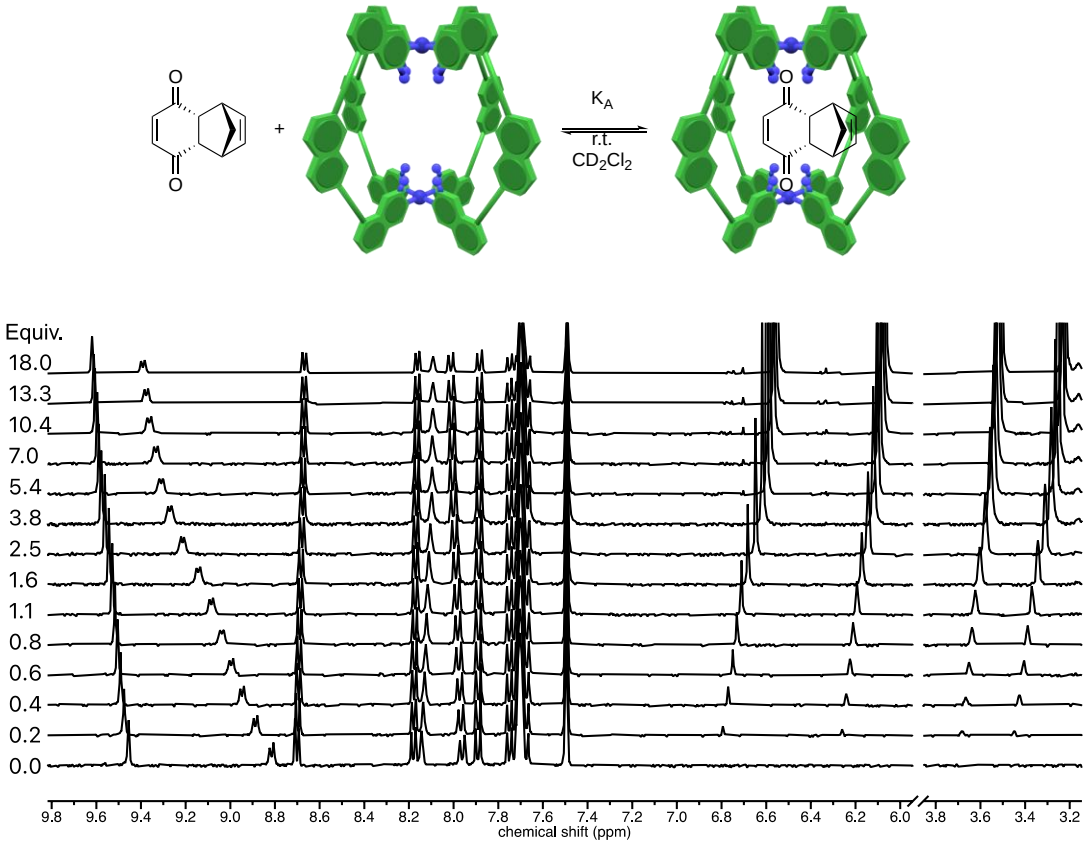

*Figure 4-35. ^{1}H NMR (400 MHz, CD_2Cl_2) spectroscopic data for titration of **4.3** into **C3**.*

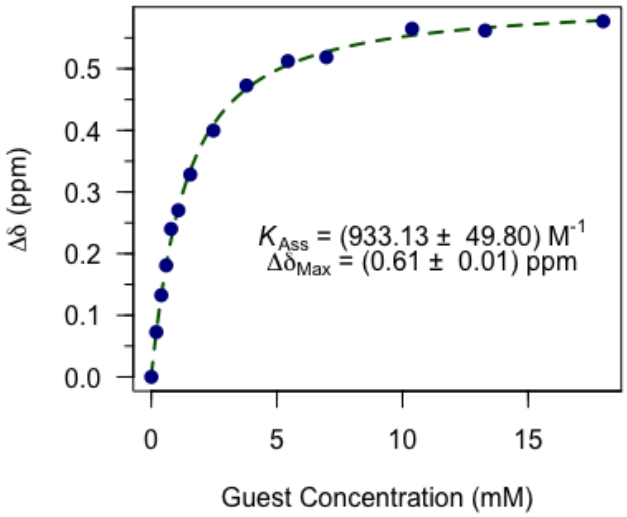

*Figure 4-36. Fitted data for change in peak position with increasing **4.3** concentration*

4.8.7 Kinetic parameter fitting for Diels-Alder reactions

4.8.7.1 The Diels-Alder reaction between 4.1 and 4.2

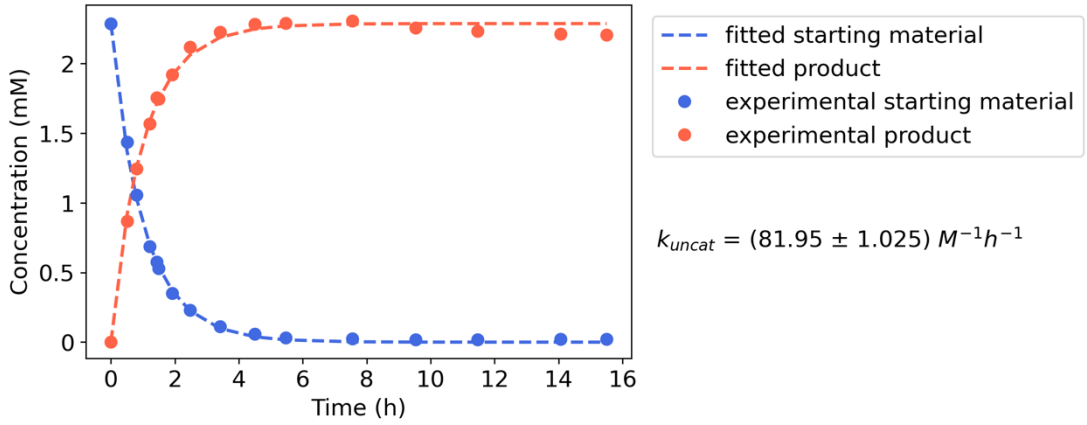

*Figure 4-37. Kinetic fitting for the uncatalysed Diels-Alder reaction between **4.1** (2.5 mM) and **4.2** (12.5 mM).*

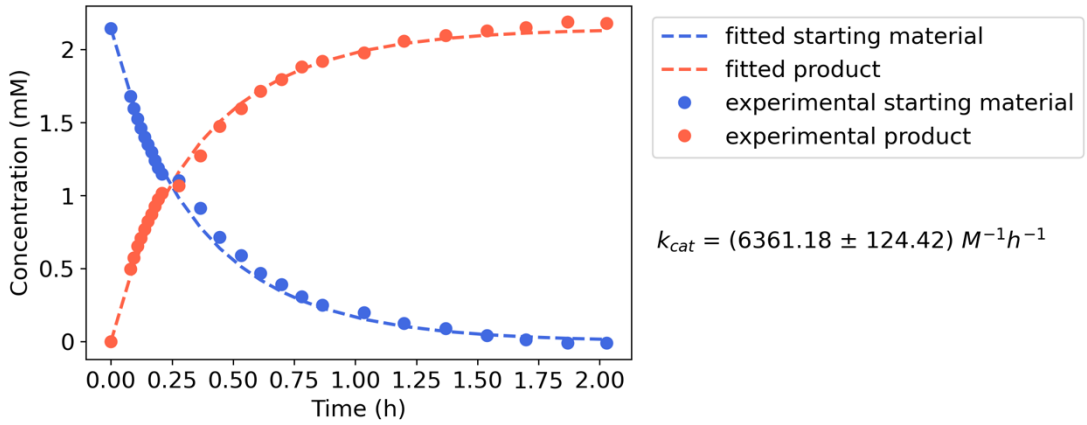

*Figure 4-38. Kinetic fitting for the catalysed Diels-Alder reaction between **4.1** (2.5 mM) and **4.2** (12.5 mM) with **C3** (0.5 mM).*

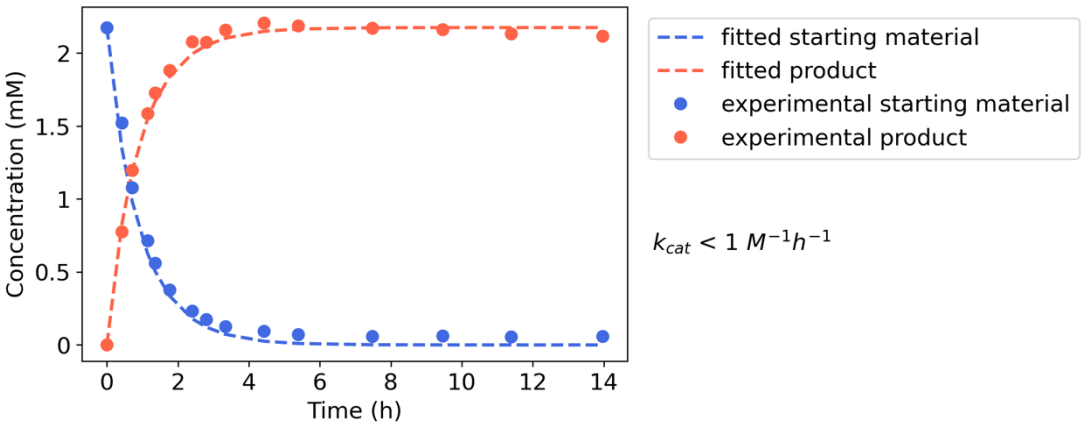

*Figure 4-39. Kinetic fitting for the catalysed Diels-Alder reaction between **4.1** (2.5 mM) and **4.2** (12.5 mM) with **C4** (0.8 mM).*

4.8.7.2 The Diels-Alder reaction between 4.1 and 4.7

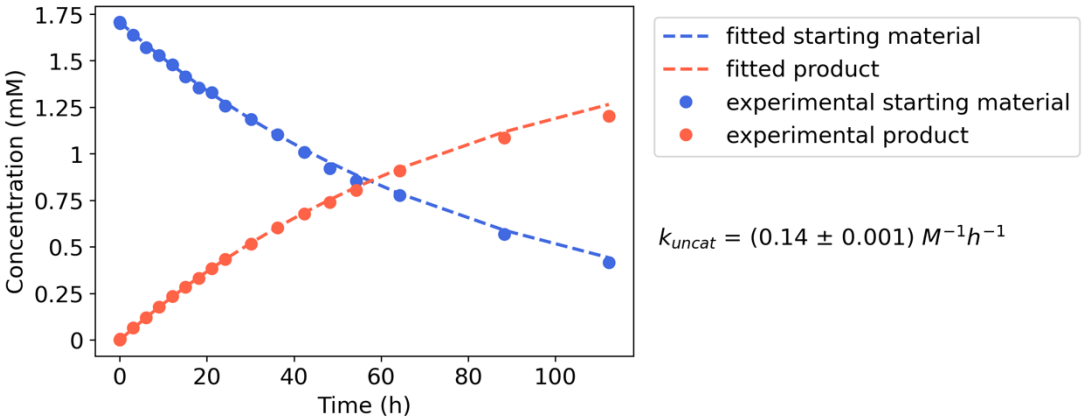

*Figure 4-40. Kinetic fitting for the uncatalysed Diels-Alder reaction between **4.1** (1.8 mM) and **4.7** (85 mM).*

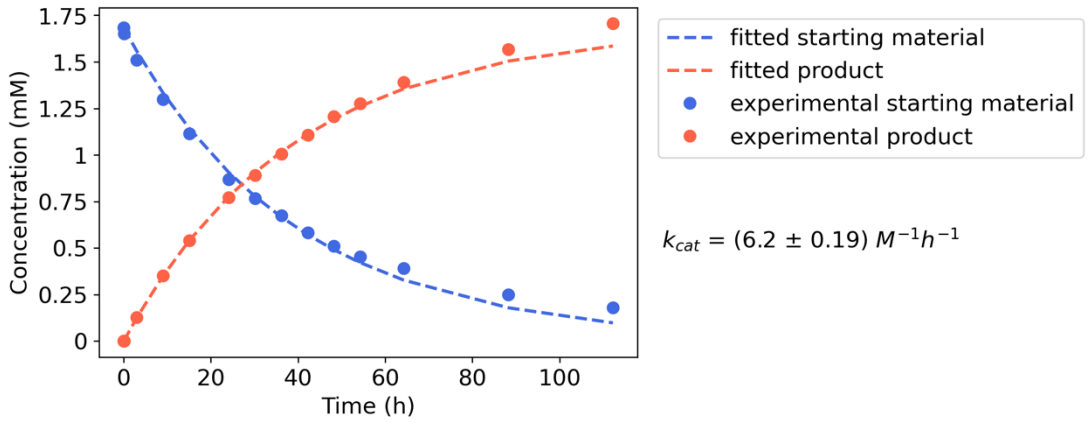

*Figure 4-41. Kinetic fitting for the catalysed Diels-Alder reaction between **4.1** (1.8 mM) and **4.7** (85 mM) with **C3** (0.4 mM).*

4.8.7.3 The Diels-Alder reaction between 4.1 and 4.8

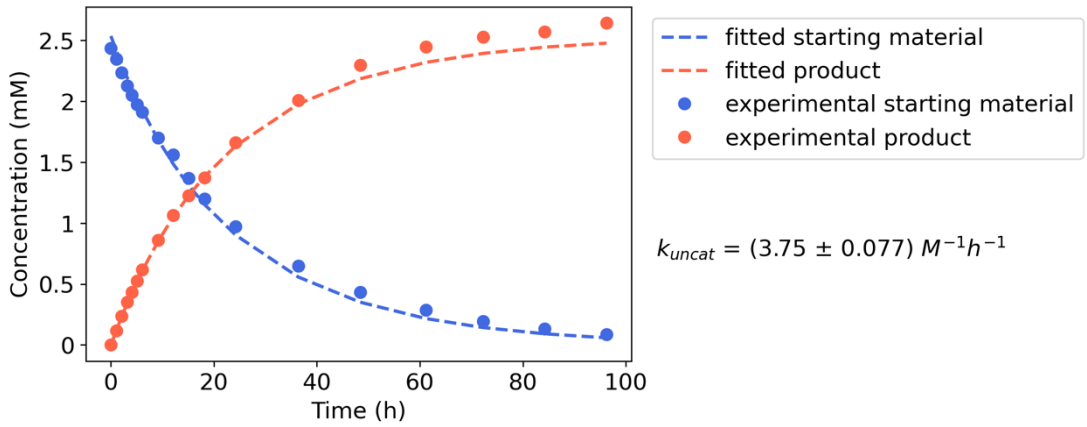

*Figure 4-42. Kinetic fitting for the uncatalysed Diels-Alder reaction between **4.1** (2.5 mM) and **4.8** (12.5 mM).*

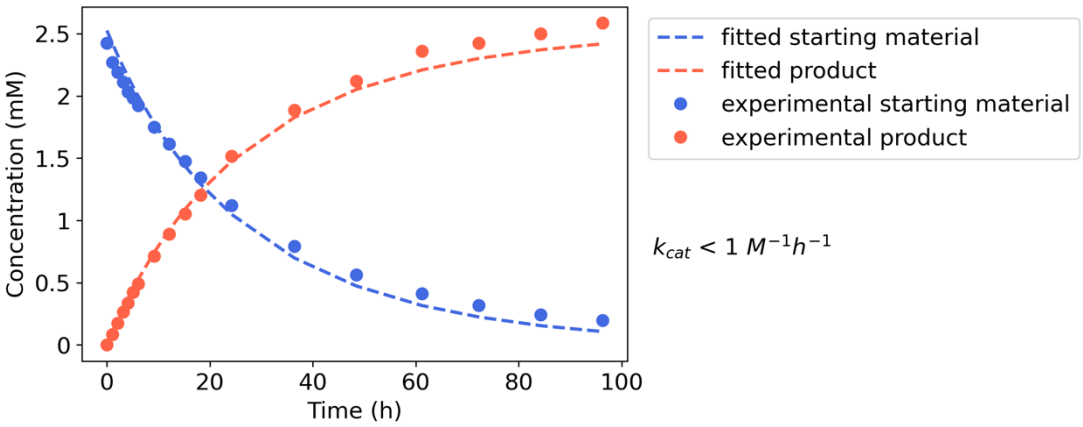

*Figure 4-43. Kinetic fitting for the catalysed Diels-Alder reaction between **4.1** (2.5 mM) and **4.8** (12.5 mM) with **C3** (0.75 mM).*

4.8.8 Kinetic profiles for Michael additions

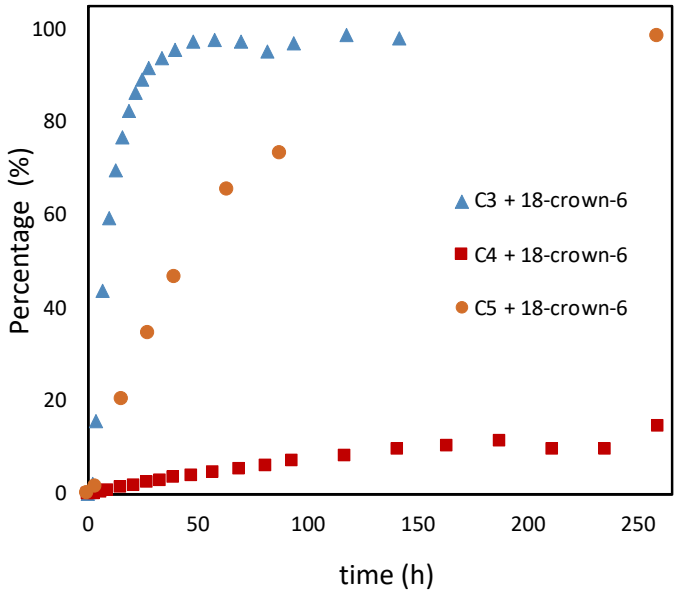

*Figure 4-44. Kinetic profile for the cage catalysed Micheal addition between **4.12** (2.5 mM) and **4.11** (12.5 mM) with 18-crown-6 (2.5 mM) with **C3** (0.5 mM) (blue triangle), **C4** (0.5 mM) (red square) or **C5** (0.5 mM) (orange circle).*

See Chapter 2 for the **C1** and **C2** catalysed reaction of **4.12** and **4.11**.

See Figure 4-15 for the reaction of **4.11** and **4.14**.

4.9 References

[1] R. Chakrabarty, P. S. Mukherjee, P. J. Stang, *Chem. Rev.* **2011**, *111*, 6810–6918.
[2] T. R. Cook, P. J. Stang, *Chem. Rev.* **2015**, *115*, 7001–7045.
[3] M. Yoshizawa, M. Tamura, M. Fujita, *Science* **2006**, *312*, 251–254.
[4] T. Murase, S. Horiuchi, M. Fujita, *J. Am. Chem. Soc.* **2010**, *132*, 2866–2867.
[5] T. Murase, Y. Nishijima, M. Fujita, *J. Am. Chem. Soc.* **2012**, *134*, 162–164.
[6] D. Fiedler, R. G. Bergman, K. N. Raymond, *Angew. Chem. Int. Ed.* **2004**, *43*, 6748–6751.
[7] D. M. Kaphan, F. D. Toste, R. G. Bergman, K. N. Raymond, *J. Am. Chem. Soc.* **2015**, *137*, 9202–9205.
[8] C. J. Hastings, M. D. Pluth, R. G. Bergman, K. N. Raymond, *J. Am. Chem. Soc.* **2010**, *132*, 6938–6940.
[9] W. Cullen, M. C. Misuraca, C. A. Hunter, N. H. Williams, M. D. Ward, *Nat. Chem.* **2016**, *8*, 231–236.
[10] M. D. Pluth, R. G. Bergman, K. N. Raymond, *Science* **2007**, *316*, 85–88.
[11] M. D. Pluth, R. G. Bergman, K. N. Raymond, *J. Org. Chem.* **2009**, *74*, 58–63.
[12] C. G. P. Taylor, A. J. Metherell, S. P. Argent, F. M. Ashour, N. H. Williams, M. D. Ward, *Chem. – Eur. J.* **2020**, *26*, 3065–3073.
[13] D. Samanta, S. Mukherjee, Y. P. Patil, P. S. Mukherjee, *Chem. – Eur. J.* **2012**, *18*, 12322–12329.
[14] W. M. Hart-Cooper, C. Zhao, R. M. Triano, P. Yaghoubi, H. L. Ozores, K. N. Burford, F. D. Toste, R. G. Bergman, K. N. Raymond, *Chem. Sci.* **2015**, *6*, 1383–1393.
[15] C. M. Hong, M. Morimoto, E. A. Kapustin, N. Alzakhem, R. G. Bergman, K. N. Raymond, F. D. Toste, *J. Am. Chem. Soc.* **2018**, *140*, 6591–6595.
[16] V. Martí-Centelles, F. Duarte, P. J. Lusby, *Isr. J. Chem.* **2019**, *59*, 257–266.
[17] T. A. Young, V. Martí-Centelles, J. Wang, P. J. Lusby, F. Duarte, *J. Am. Chem. Soc.* **2020**, *142*, 1300–1310.
[18] S. Saha, I. Regeni, G. H. Clever, *Coord. Chem. Rev.* **2018**, *374*, 1–14.
[19] T. Fu, Y. Li, H. D. Thaker, R. W. Scott, G. N. Tew, *ACS Med. Chem. Lett.* **2013**, *4*, 841–845.
[20] N. A. Thompson, H. Barbero, E. Masson, *Chem. Commun.* **2019**, *55*, 12160–12163.
[21] C. M. Lombardo, S. J. Welsh, S. J. Strauss, A. G. Dale, A. K. Todd, R. Nanjunda, W. D. Wilson, S. Neidle, *Bioorg. Med. Chem. Lett.* **2012**, *22*, 5984–5988.
[22] D. P. August, G. S. Nichol, P. J. Lusby, *Angew. Chem. Int. Ed.* **2016**, *55*, 15022–15026.
[23] V. Martí-Centelles, A. L. Lawrence, P. J. Lusby, *J. Am. Chem. Soc.* **2018**, *140*, 2862–2868.
[24] P. Liao, B. W. Langloss, A. M. Johnson, E. R. Knudsen, F. S. Tham, R. R. Julian, R. J. Hooley, *Chem. Commun.* **2010**, *46*, 4932–4934.
[25] T. R. Schulte, J. J. Holstein, L. Schneider, A. Adam, G. Haberhauer, G. H. Clever, *Angew. Chem. Int. Ed.* **2020**, *59*, 22489–22493.
[26] H. M. O'Connor, M. Coletta, A. Etcheverry-Berríos, G. S. Nichol, E. K. Brechin, P. J. Lusby, *Chem. Commun.* **2020**, *56*, 11799–11802.

[27] M. Han, D. M. Engelhard, G. H. Clever, *Chem. Soc. Rev.* **2014**, *43*, 1848–1860.
[28] I. Regeni, B. Chen, M. Frank, A. Baksi, J. J. Holstein, G. H. Clever, *Angew. Chem. Int. Ed.* **2021**, *60*, 5673–5678.
[29] I. R. Kleckner, M. P. Foster, *Biochim. Biophys. Acta BBA - Proteins Proteomics* **2011**, *1814*, 942–968.
[30] M. P. Latham, G. R. Zimmermann, A. Pardi, *J. Am. Chem. Soc.* **2009**, *131*, 5052–5053.
[31] V. Martí-Centelles, R. L. Spicer, P. J. Lusby, *Chem. Sci.* **2020**, *11*, 3236–3240.
[32] R. Hoffmann, R. B. Woodward, *Acc. Chem. Res.* **1968**, *1*, 17–22.
[33] V. K. Yadav, in *Steric Ster. Eff. Org. Chem.* (Ed.: V.K. Yadav), Springer, Singapore, **2016**, pp. 127–146.
[34] S. D. Banister, M. Manoli, M. R. Doddareddy, D. E. Hibbs, M. Kassiou, *Bioorg. Med. Chem. Lett.* **2012**, *22*, 6053–6058.
[35] M. D. Eastgate, F. G. Buono, *Angew. Chem. Int. Ed.* **2009**, *48*, 5958–5961.
[36] S. Fukuzumi, T. Okamoto, *J. Am. Chem. Soc.* **1993**, *115*, 11600–11601.
[37] G. M. Sheldrick, *Acta Crystallogr. Sect. Found. Adv.* **2015**, *71*, 3–8.
[38] O. V. Dolomanov, L. J. Bourhis, R. J. Gildea, J. A. K. Howard, H. Puschmann, *J. Appl. Crystallogr.* **2009**, *42*, 339–341.
[39] G. M. Sheldrick, *Acta Crystallogr. Sect. C Struct. Chem.* **2015**, *71*, 3–8.

Conclusion and Outlook

The field of coordination cage catalysis is predominated by unimolecular transformations and bimolecular reactions relying on the co-binding paradigm which often leads to product inhibition. This thesis describes a significant shift away from this previous research and instead focuses on the use of coordination cages to promote different chemical transformations using mechanisms that involve the electrostatic stabilisation of transition and/or intermediate states. The supramolecular catalysts described in this thesis work by harnessing and maximising polar interactions with various reactive species similar to how enzymes deliver catalysis.

The Pd_2L_4 systems investigated herein efficiently catalyse the Michael addition of substrates with alpha acidic protons by coulombically enhancing their pro-nucleophilicity and recognising the reaction TS and/or intermediates. This method is further enhanced by using crown ethers to synergistically stabilise the charge separated state. This work has laid the foundation of using not only Pd_2L_4 structures but also a plethora of cationic coordination cages to catalyse numerous C-C bond formation reactions that involve carbanions intermediates. Future work can also focus on compartmentalised catalysis where the separately stabilised charged species can simultaneously undergo/promote reactions that are otherwise incompatible in the bulk phase.

The H-bond binding sites of the Pd_2L_4 cages have shown to exert non-coulombic electrostatic interactions that are capable of influencing neutral TS. The studies on the Diels-Alder catalysis revealed that both rate acceleration and enhanced diastereoselectivity stem from the recognition of TS by the cage cavities. Structural modification of the Pd_2L_4 cages demonstrated that the balance needs to be maintained between the cages' flexibility to distort to accommodate TS and their rigidity, which facilitates pre-organisation for guest binding. This work should inspire future methods to systematically design and optimise supramolecular cage catalysts.

While this work used highly symmetrical cages, interesting diastereoselectivity was proven possible for both Michael and Diels-Alder reactions, due to the selective TS and/or intermediate stabilisation. Future work should expand to the investigations of structures with lower symmetry such as those possessing chirality, furthering the selectivity of coordination cage catalysis.